PhD. THESIS OF THE UNIVERSITY OF LYON

Performed at
INSA DE LYON

Doctoral school N°162
Mécanique, Énergétique, Génie Civil, Acoustique (MEGA)

Speciality:
MECHANICAL ENGINEERING

Publicly defended on June 28th 2019

By
Thibault Beyer
Mechanical Engineer of INSA Lyon

Semi-analytical modeling of damage under contact loading: Application to heterogeneous materials

---

Jury

FARSHID SADEGHI	Professor, Purdue University
PHILIPPE DUFRENOY	Professor, Univ. Lille
CAROLINE RICHARD	Professor, Univ. Tours
JULIEN LEROUX	PhD, Engineer, Safran Aircraft Engines
THIBAUT CHAISE	Ass.-Professor, INSA Lyon
DANIEL NÉLIAS	Professor, INSA Lyon

Département FEDORA – INSA Lyon - Ecoles Doctorales – Quinquennal 2016-2020

SIGLE	ECOLE DOCTORALE	NOM ET COORDONNEES DU RESPONSABLE
CHIMIE	**CHIMIE DE LYON** http://www.edchimie-lyon.fr Sec. : Renée EL MELHEM Bât. Blaise PASCAL, 3e étage secretariat@edchimie-lyon.fr INSA : R. GOURDON	M. Stéphane DANIELE Institut de recherches sur la catalyse et l'environnement de Lyon IRCELYON-UMR 5256 Équipe CDFA 2 Avenue Albert EINSTEIN 69 626 Villeurbanne CEDEX directeur@edchimie-lyon.fr
E.E.A.	**ÉLECTRONIQUE,** **ÉLECTROTECHNIQUE,** **AUTOMATIQUE** http://edeea.ec-lyon.fr Sec. : M.C. HAVGOUDOUKIAN ecole-doctorale.eea@ec-lyon.fr	M. Gérard SCORLETTI École Centrale de Lyon 36 Avenue Guy DE COLLONGUE 69 134 Écully Tél : 04.72.18.60.97 Fax 04.78.43.37.17 gerard.scorletti@ec-lyon.fr
E2M2	**ÉVOLUTION, ÉCOSYSTÈME,** **MICROBIOLOGIE, MODÉLISATION** http://e2m2.universite-lyon.fr Sec. : Sylvie ROBERJOT Bât. Atrium, UCB Lyon 1 Tél : 04.72.44.83.62 INSA : H. CHARLES secretariat.e2m2@univ-lyon1.fr	M. Philippe NORMAND UMR 5557 Lab. d'Ecologie Microbienne Université Claude Bernard Lyon 1 Bâtiment Mendel 43, boulevard du 11 Novembre 1918 69 622 Villeurbanne CEDEX philippe.normand@univ-lyon1.fr
EDISS	**INTERDISCIPLINAIRE** **SCIENCES-SANTÉ** http://www.ediss-lyon.fr Sec. : Sylvie ROBERJOT Bât. Atrium, UCB Lyon 1 Tél : 04.72.44.83.62 INSA : M. LAGARDE secretariat.ediss@univ-lyon1.fr	Mme Emmanuelle CANET-SOULAS INSERM U1060, CarMeN lab, Univ. Lyon 1 Bâtiment IMBL 11 Avenue Jean CAPELLE INSA de Lyon 69 621 Villeurbanne Tél : 04.72.68.49.09 Fax : 04.72.68.49.16 emmanuelle.canet@univ-lyon1.fr
INFOMATHS	**INFORMATIQUE ET** **MATHÉMATIQUES** http://edinfomaths.universite-lyon.fr Sec. : Renée EL MELHEM Bât. Blaise PASCAL, 3e étage Tél : 04.72.43.80.46 infomaths@univ-lyon1.fr	M. Luca ZAMBONI Bât. Braconnier 43 Boulevard du 11 novembre 1918 69 622 Villeurbanne CEDEX Tél : 04.26.23.45.52 zamboni@maths.univ-lyon1.fr
Matériaux	**MATÉRIAUX DE LYON** http://ed34.universite-lyon.fr Sec. : Stéphanie CAUVIN Tél : 04.72.43.71.70 Bât. Direction ed.materiaux@insa-lyon.fr	M. Jean-Yves BUFFIÈRE INSA de Lyon MATEIS - Bât. Saint-Exupéry 7 Avenue Jean CAPELLE 69 621 Villeurbanne CEDEX Tél : 04.72.43.71.70 Fax : 04.72.43.85.28 jean-yves.buffiere@insa-lyon.fr
MEGA	**MÉCANIQUE, ÉNERGÉTIQUE,** **GÉNIE CIVIL, ACOUSTIQUE** http://edmega.universite-lyon.fr Sec. : Stéphanie CAUVIN Tél : 04.72.43.71.70 Bât. Direction mega@insa-lyon.fr	M. Jocelyn BONJOUR INSA de Lyon Laboratoire CETHIL Bâtiment Sadi-Carnot 9, rue de la Physique 69 621 Villeurbanne CEDEX jocelyn.bonjour@insa-lyon.fr
ScSo	**ScSo*** http://ed483.univ-lyon2.fr Sec. : Viviane POLSINELLI Brigitte DUBOIS INSA : J.Y. TOUSSAINT Tél : 04.78.69.72.76 viviane.polsinelli@univ-lyon2.fr	M. Christian MONTES Université Lyon 2 86 Rue Pasteur 69 365 Lyon CEDEX 07 christian.montes@univ-lyon2.fr

*ScSo : Histoire, Géographie, Aménagement, Urbanisme, Archéologie, Science politique, Sociologie, Anthropologie

Acknowledgements

Ces années de thèse auront été riches en apprentissages, rencontres, voyages et défis. Mais le résultat final présent dans ce manuscrit ne rend pas compte des multiples rebondissements au cours de ces années. Je tiens donc à remercier les personnes sans qui ce travail n'aurait pas été possible.

En premier lieu, je tiens à remercier Thibaut Chaise pour m'avoir accompagné et initié à la recherche depuis le master jusqu'à la fin de cette thèse. Je souhaite aussi particulièrement remercier mon directeur de thèse, Daniel Nélias, pour m'avoir confié ce sujet et m'avoir fait confiance pour que je réalise une grande partie de ces trois ans hors des murs du laboratoire, que cela soit à Safran Aircraft Engines ou à Purdue. Enfin et surtout, je vous suis très reconnaissant à tous les deux pour vos conseils et votre aide sur tous les aspects de cette thèse.

Je souhaite aussi remercier Julien Leroux de m'avoir accueilli pendant la majeure partie de cette thèse au sein de l'équipe des méthodes de Safran Aircraft Engines à Villaroche ainsi que les opportunités offertes pour mieux appréhender les matériaux composites. De façon générale, un grand merci à toute l'équipe des méthodes pour son ambiance, sa bonne humeur et les bons moments passés ensemble (merci à Fabien, Didier, Christian, Raul, Adrien, Battista, Loïc, Maxime, Erwann, Caroline, Florence, Arnaud, sans oublier les autres membres que j'ai pu croiser). Une pensée toute particulière pour les autres thésards de Safran: Aude, Cécile, Wafaa, Besnik, Étienne, les différents évenements (séminaires PRC, R&T Day, JDD) auront toujours été de bons moments avec vous.

Je remercie l'ensemble de mes collègues du LaMCoS, passés et présents. Mes séjours au laboratoire étaient toujours très plaisants grâce à vous et votre bonne humeur. Je tiens aussi à remercier le gang des pancakes pour m'avoir toujours accueilli lors de ces séjours lyonnais.

I wish to thank Professor Farhsid Sadeghi for receiving me at his METL laboratory and for being the chairman for my defense. My time at Purdue gave a new dimension to my work thanks to his time and advices. I also thank all the METL students for welcoming me and helping me on my experimental work: Akhil, Kushagra, Akshat, Wyatt, Xin, Arman, Dallin, Ben, David, Zamzam, I trully thank all of you for your friendship.

Je remercie sincèrement Caroline Richard et Philippe Dufrénoy pour avoir accepté de rapporter ce travail et pour leurs contributions à son amélioration.

Mes derniers remerciements vont à mes parents et à ma soeur pour leurs encouragements et leur soutien. A Léa, qui plus que toute autre personne, a vécu ces années de thèse avec moi, merci pour ta présence.

Résumé

Les pieds d'aubes de soufflantes de turboréacteurs étant soumis à des sollicitations de type fretting, l'introduction de matériaux composites dans la nouvelle génération de moteur d'avion a rendu nécessaire le développement d'outils permettant de modéliser le contact entre des matériaux hétérogènes. En particulier, le comportement tribologique et l'endommagement de ces matériaux est encore mal compris. La mise en place de méthodes numériques capable de prédire les endommagements dans le contact permettrait de mieux prédire la durée de vie des pièces en service et de garantir la sécurité des passagers.

Cette thèse porte sur le développement de méthodes semi-analytiques pour la modélisation de l'endommagement dans des conditions de fretting et de roulement. Ceci est stratégique vu les temps de calculs prohibitifs des méthodes plus conventionnelles de type éléments finis. La méthode de l'inclusion équivalente d'Eshelby est utilisée pour modéliser des matériaux hétérogènes, de la présence de défauts jusqu'aux structures complexes des matériaux composites. Cette technique est aussi utilisée afin de représenter les dégradations des propriétés matériaux survenant au cours de l'endommagement. La méthode permet de prendre en compte plusieurs inclusions simultanément et les temps de calculs sont réduits grâce à l'utilisation massive de transformées de Fourier rapides (FFT). De premiers résultats permettent de montrer la capacité de cette méthode à représenter les endommagements apparaissant lors d'une sollicitation de fretting : l'usure et l'amorçage de fissures. Des applications aux matériaux revêtus sont proposées et la méthode est comparée à une méthode plus classique de modélisation de l'usure. Une bonne corrélation entre les deux approches a permis de valider la méthode. Dans un second temps, cette technique est adaptée à la modélisation de transformations microstructurales apparaissant dans les roulements autour de défauts proches de la surface de contact. Une campagne d'essais sous sollicitations de contact sur un matériau tissé 2D a permis de mieux comprendre son comportement tribologique. En particulier, l'effet des propriétés de chaque constituant sur le coefficient de frottement et sur l'évolution de l'usure dans le matériau est étudié. Finalement, une technique de discrétisation est utilisée afin de représenter la structure complexe des matériaux composites tissés dans le code de calcul semi-analytique. L'effet de la structure hétérogène sur la solution du contact est établi et la nécessité de représenter les matériaux hétérogènes à la bonne échelle est soulignée. Une application de cette technique à la microstructure des matériaux métalliques permet de prédire la durée de vie des aciers utilisés dans les roulements.

MOTS CLÉS : Simulation numérique, contact, fretting, mécanique de l'endommagement, usure, fatigue de roulement, microstructure, matériaux composites

Contents

Nomenclature

$\Delta\tau$ Shear stress reversal

δD Damage increment

ΔN Increment in number of cycles

$\Delta x, \Delta y, \Delta z$ Mesh size

δ_{ij} Kronecker symbol

γ Ratio between the inhomogeneity and the matrix Young's modulus

ν^M, ν^I Poisson's ratio of the matrix M and the inclusion I

ϕ, Ψ Harmonic and biharmonic potentials of mass density ε_{ij}^*

σ^n Normal pressure due to the summation of both symmetric inclusions

σ_{ij} Stress tensor components

σ_{ij}^0 Stress corresponding to an infinite applied strain ε_{ij}^0

σ_r Resistance stress

τ Shear stress

$\tau_{alternating}$ Amplitude of alternating shear stress during a cycle

τ_{mean} Mean shear stress during a cycle

τ_r Fatigue limit

$\tilde{\sigma}$ Effective stress

$\tilde{\varepsilon}$ Equivalent strain

$\tilde{E}$ Effective Young's modulus

ε_{d0} Strain at elastic limit

ε_{ij} (Elastic) strain tensor components

ε_{ij}^* Eigenstrain due to the presence of inhomogeneities

ε_{ij}^0 Infinite applied strain

ε_R Strain at macroscopic fracture

$\widehat{B}_{ijkl}$ Frequency response of coefficients B_{ijkl} in the frequency domain

$\widehat{M}_{ij}$ Frequency response of coefficients M_{ij} in the frequency domain

a^* Contact radius

B_{ijkl}^* Influence coefficients are relating the stress σ_{ij} at point (x,y,z) to the constant eigenstrain at the point (x^k, y^k, z^k)

C_{ijkl}^M, C_{ijkl}^I Elastic constants of the matrix and the inhomogeneity

D Damage variable

d_{inc} Inclusion diameter

E Initial (undamaged) Young's modulus of the inhomogeneity

E^I Young's modulus of the inhomogeneity

FFT^{-1} Inverse FFT operation

H Hardness of the material

h Distance between the two surfaces of the contacting bodies

I_{ijkl} Fourth-order identity tensor

K^n Coefficients of the normal displacement at the contact surface due to the contact pressure

m Damage law exponent

M_{ij} Influence coefficients relating the stress σ_{ij} at the point (x,y,z) to the normal traction σ^n within a discretized area centered at $(x^k, y^k, 0)$

N Number of cycles

n_x, n_y, n_z Grid sizes in the half-space along the Cartesian directions x, y, z, respectively

$N_{appearance}$ Number of cycles for butterfly appearance

N_i Number of inclusions in the enrichment along direction i.

P Contact pressure distribution

P_0 Maximum Hertzian pressure

R Indenter radius

S_{ijkl} Components of the Eshelby's tensor

S_{ut} Ultimate tensile stress

u_i Displacements of the contact surface

u_i^* Displacements corresponding to an eigenstrain ε_{ij}^*

u_i^0 Displacements corresponding to an infinite applied strain ε_{ij}^0

W Normal applied load

$x^I = (x^I, y^I, z^I)$ Cartesian coordinates of the inclusion center

z_c Thickness of the coating.

z_{inc} Inclusion depth

2D-FFT   Two-dimensional Fast Fourier Transform

3D-FFT   Three-dimensional Fast Fourier Transform

Introduction

Contact between parts is the main way of transmitting load in mechanical systems. These parts can be subjected to cyclic loading and large loads that can strongly affect their lifetime. Moreover, the presence of heterogeneities inside the material can increase the risk of early failure of the materials. The two dominant damage phenomena observed in contact area are wear and crack initiation. Therefore problematic of contact damage is of major interest for many industrial applications such as the blade/disk interface in aircraft engines, bolted joints, wind turbine bearings and wheel-rail contact. Safran Aircraft Engines, a leader company in the design and production of aircraft engines (CFM-56, LEAP) introduced composite materials in the LEAP aircraft engines in order to increase engine's performance and decrease its weight. Because of the vibrations and aerodynamic forces, fan blades are subjected to fretting loading. In particular, fan blades are made of a 3D woven composite and due to their heterogeneous composition, prediction of the damage phenomena in the contact is very difficult. Existing results are available in the literature for modeling a fretting contact. However these results are based on isotropic material definitions and hence do not account for any heterogeneities near the contact surface. Because of the localized character of contact solicitation, classical homogenization theory can not be easily applied and up to date none of the proposed homogenization model is adapted to consider the presence of a free surface. Furthermore, hybrids bearings with ceramic rolling elements have also been introduced in the new generation of aircraft engines. Presence of manufacturing byproducts like carbides or voids with rolling elements may affect the bearing life. Therefore, introduction of new materials in mechanical systems is pushing forward the need for adapted simulation tools.

The purpose of this work is the development of the Semi-Analytical Method (SAM) for the simulation of machine components damage under contact loading. The present study focuses on fretting wear and rolling contact fatigue phenomena through the introduction of continuum damage mechanics based models coupled with a heterogeneous contact solver. Furthermore, experiments are conducted on woven composite materials which indicate the need for a representative model of material microstructure. Capacity of SAM to model their complex structure is introduced and an application on bearing steel is proposed. Influence of the material structure on the contact solution is also emphasized.

The first chapter presents the background and the industrial context of the study. The context linked to the application to blade/disk interfaces and rolling element bearings in aircraft engines are first introduced along with contact damage phenomena during Fretting and Rolling Contact Fatigue. A brief history and classical formulae of Continuum

Damage Mechanics are presented for a better understanding of the next chapters. Then, a literature review is presented on the modeling and damage in heterogeneous materials and on the numerical methods in contact mechanics. The second chapter briefly discusses the semi-analytical heterogeneous contact model based on the work of former researchers. The third chapter introduces a method to couple a continuum damage mechanics model with the semi-analytical solver. Results with fretting loading in gross slip and partial slip conditions are investigated. An application of the method for coated materials is introduced. A model from the literature is also implemented and results validate our approach. Finally, results obtained with the damage model and a classical wear model based on the dissipated energy in the contact area are compared. The problem of butterfly wings formation around a nonmetallic inclusion in rolling contact fatigue is discussed in the fourth chapter. Introduction of small cuboidal heterogeneities allow to reproduce the effects of microstructural alterations around a spherical inclusion. Experimental results from fretting tests are presented in the fifth chapter and allow to better understand the tribological behavior of composite materials. In the last chapter, a method is proposed to model complex structure of heterogeneous materials using the semi-analytical method. Applications to woven composite materials and to bearing steels to study the fatigue life of rolling elements are presented.

Chapter 1

Context and Background

This chapter aims at introducing the contact problems arising in today's aircraft engines. In particular, some issues due to heterogeneous materials are briefly explained. A focus is made on surface damage phenomena due to contact and on way of modeling both the contact problem, surface and subsurface damage and heterogeneous materials in numerical simulations.

Contents

1.1 Industrial context

The last few decades have seen a steady rise in the number of flights per year. Nowadays over 2 billion people travel around the world every year with 360 000 airplanes [ATA 10]. Consequently, CO_2 emissions due to air travel have considerably increased and are expected to increase in the next decades if nothing is done. The aviation sector signed a declaration to reduce emission by 50% before 2050 (see Fig. 1.1). To achieve this goal, four different areas of improvement have been identified: technology, operations, infrastructure and economic measures. Advance in technology has resulted in the use of composite materials allowing to reduce the weight of the aircrafts. Today they account for almost 50% of the structure of an aircraft (see Fig. 1.2). Compared to traditional aluminum alloy, composite materials can represent a weight saving of 20% and can be formed in more complex forms.
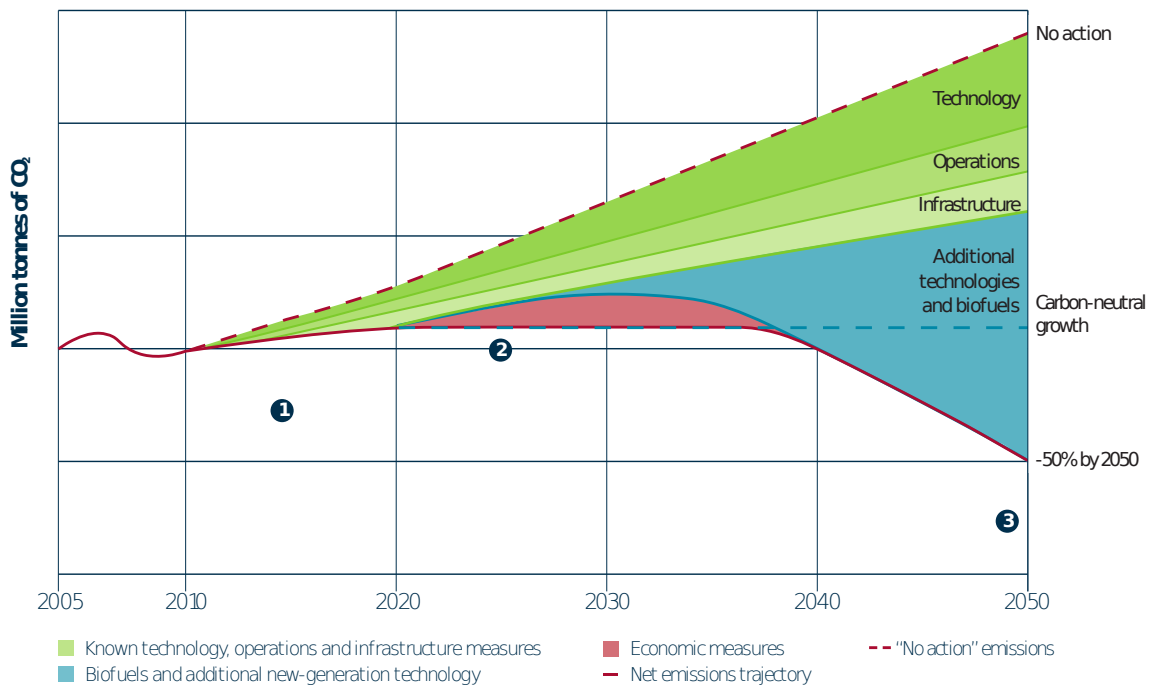
Figure 1.1: Emissions reduction roadmap [ATA 10].

Furthermore, as soon as the function of carrying or transmitting load is needed in a system, contact problems are arising. Thus, the impact of friction and wear on energy consumption and CO_2 emissions have been studied at the global scale by Holmberg and Erdemir [HOL 17]. According to their study, tribological contact issues represent almost 23% of the world's energy consumption. Some of this energy consumption is used to reduce friction or in replacement of worn parts. Developing new technologies to reduce friction and increase life of contacting parts presents a great challenge for industry and could represent short term energy savings up to 25% in the transportation industry.

In the aeronautic sector, engineers have to predict the contact behavior and the damage mechanisms, such as wear or cracks, to adapt their design and calculate the life of the system components. In particular, aircraft engines has a key role in the aircraft CO_2 emissions and fuel efficiency and the new generation of aircraft engines called LEAP achieves excellent performance by using composites materials. In operation, composite materials are subjected to cyclic contact loading. Therefore, the ability of calculating the contact in heterogeneous materials is needed and development of robust and accurate computational method is necessary to guarantee the safety of the system and of the passengers.

In a first part of this chapter, aircraft engine principles are briefly explained. In the subsequent sections, two main contact interfaces in aircraft engines are presented: the blade-disk interface and rolling element bearings. The damage phenomena associated with these contact interfaces are also presented.
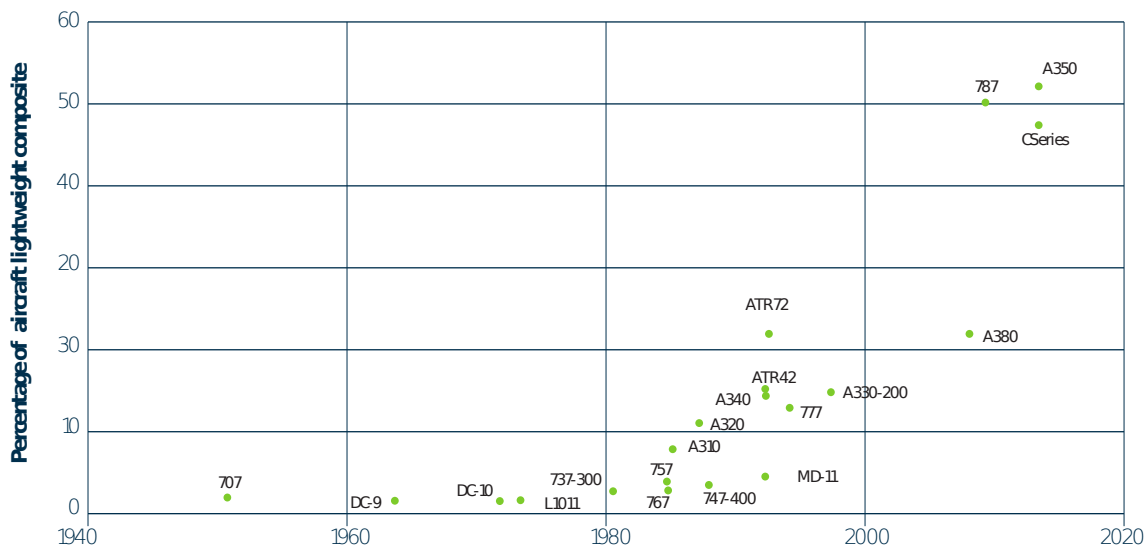
Figure 1.2: Growth in the use of composites in commercial aircraft [ATA 10].

1.1.1 Aircraft engines

Airbreathing jet engines are used for aircraft propulsion since the late 1930s for both civil and military applications. This system is based on the acceleration of the air flow passing through the engine using the mechanical energy from combustion to create the thrust. The airflow enters the engines through an inlet and enters a compressor. In the combustion chamber, fuel is mixed with compressed air and resulting hot gases expand through the turbine. The compressor is powered by the energy extracted by the turbine. In modern engines, a two spool configuration with concentric rotating shafts is often used for improved efficiency. A first shaft runs a low pressure spool (compressor and turbine) and a second shaft runs a high-pressure spool at higher speed. Simple flux engines, where

all the air flow is passing through the combustion chamber have a good efficiency for speed above Mach 1 and are usually used in military applications.

Actual turbofan are a modification of the original turbojet adding a ducted fan (see Fig. 1.4). Some of the entering flow bypasses the core and is accelerated only by the fan using energy from the turbine. Fan dimensions are much more larger than the main core to increase the accelerated airflow. Around 80 % of the thrust is ensured by the bypass flow. The ratio between the air bypassing the core and the air entering the core is called the bypass ratio (BPR). A high BPR is useful to reduce fuel consumption and noise. As BPR increases, the radius of the fan blades increases and the rotating speed of the low pressure turbine decreases needing more stage to extract the energy from combustion. New configurations sometimes introduces a planetary gear box to allow the fan and the turbine to spin at different velocities increasing efficiency of both components. The most recent commercial aircraft engines (CFM Leap, Pratt&Whitney PW1000G) are double core and double flux with a BPR around 11.
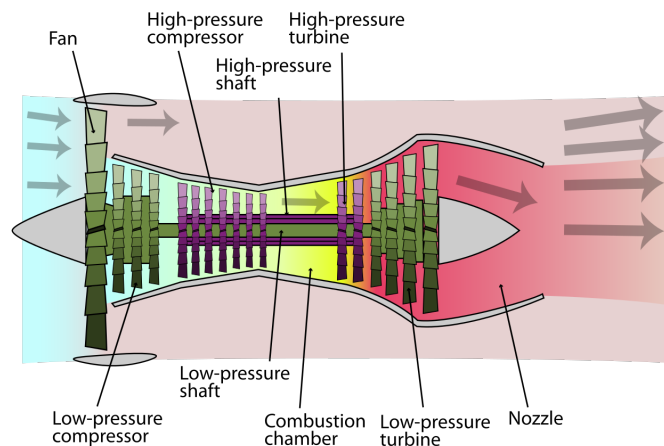
Figure 1.3: Schematic diagram of a high-bypass turbofan engine.

The new generation of aircraft engines commercialized by CFM (joint venture of General Electrics and Safran Aircraft Engines) uses composite materials resulting in a 450kg weight loss. Compared to the previous generation of engines (CFM56) the specific consumption is reduced by 16 %. CO_2 and NO_x emissions are respectively reduced by 16% and 50 % and noise decreases by 15 dB.

1.1.2 Blade / Disk interface

Fan blades are mounted on a disk fixed on the rotating shaft using a dovetail joint (see Fig. 1.5). The joint is made of two interfaces between the blade's foot and the disk and its main goal is to ensure a good transmission of tangential forces and the radial retention of the blade. The disk is made of a metallic alloy and fan blades is typically made of either a metallic alloy with a coating ($Ti - 6Al - 4V$ in CFM-56) or a composite materials (3D woven composites in CFM Leap). During take-off, centrifugal forces lead

Figure 1.4: LEAP fan blades in RTM woven composite materials.
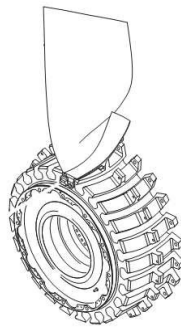
Figure 1.5: Dovetail joint at the blade disk interface.

to a radial displacement of the blade entering in contact with the disk interfaces (see Fig. 1.6). The reverse phenomenon occur during the landing phase. These kind of phenomena are characterized by a low frequency but a high amplitude of blade displacement (around 5Hz and 100μm). During the flight, structural vibrations and aerodynamical forces are resulting in high frequency and low amplitude displacement at the blade/disk interface (around 200 Hz and 10 μm) also called fretting. Loading phases observed at the blade disk interface during a flight cycle are summarized in Fig. 1.7.
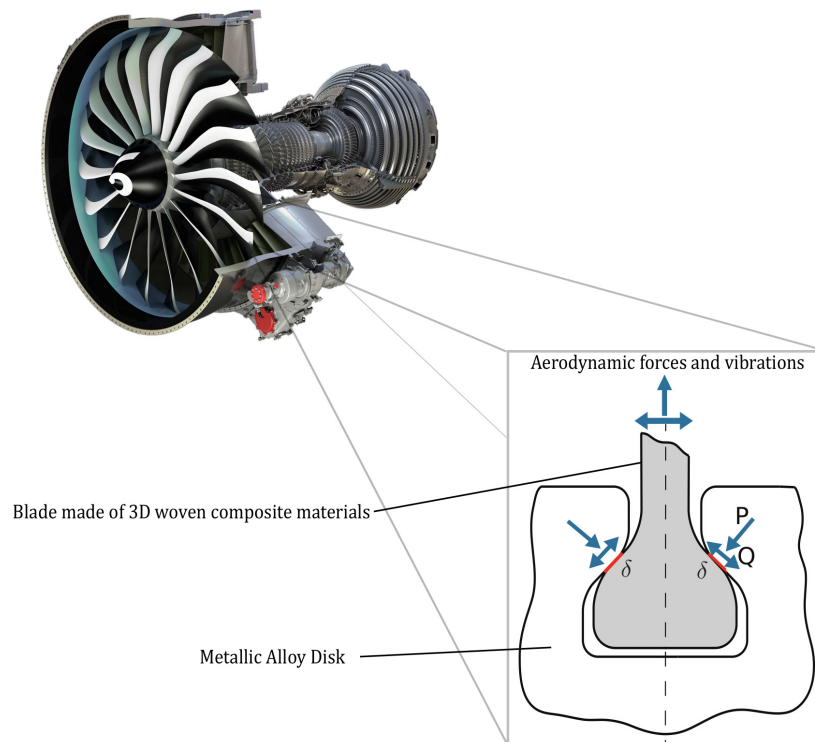
Figure 1.6: LEAP-1A engine with Fan blades in RTM woven composite materials.
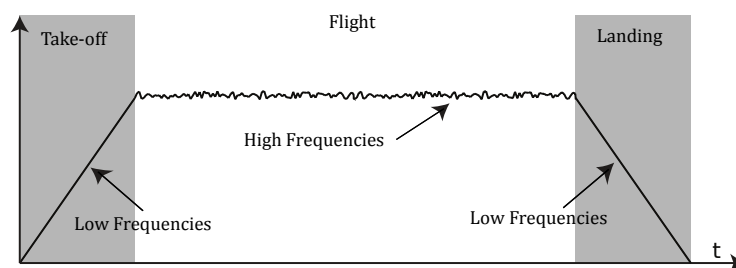
Figure 1.7: Evolution of solicitation frequencies and amplitude during a flight cycle.

1.1.3 Bearings in aircraft engines

Bearings are often used in the aircraft engines to transmit load and reduce friction between moving parts (see Fig. 1.8). With the new generation of aircraft engines with high BPR, fan blades size and weight have increased. This is resulting in the need of transmitting higher load and reducing weight together with a very long lifetime. To respond these challenges, new hybrid bearings made of ceramic balls (Si_3N_4) and high performance steel (M50, M50NiL) have been developed. Ceramic's elements have very good material's properties but their damage phenomena are not well investigated. Furthermore, presence of materials defects such as inclusions and voids after the manufacturing process can strongly modify the fatigue behavior and service life of contacting elements. Same kind of defects have also been found in titanium alloy used for blades like Ti-6Al-4V. Therefore, contacts between blade and disk or between rolling element and bearings races can no longer be considered homogeneous. Reproducing and modeling the behavior of these materials under contact is paving the way to more reliable design of mechanical's systems.

Figure 1.8: Bearings in aircraft engines

1.2 Contact damage phenomena

1.2.1 Fretting

Fretting is defined as a low amplitude repeated relative motion between two surfaces in contact. The sliding between two surfaces in contact can lead to different surface damage phenomena such as wear (fretting-wear), crack (fretting-fatigue) and corrosion (fretting-corrosion). Magnitude of the motion is generally in the order of micrometers. Real contact area can be hard to reproduce experimentally and, most of the time, simplified geometries are used to study fretting. The three most common geometries are :

- Contact between a sphere and a flat surface.

- Contact between a cylinder and a flat surface.

- Contact between two flat surfaces.

The two first configurations were analytically described by Hertz [HER 82] and can be used to described the contact occurring in the blade-disk interface or between the rolling elements and the races of a bearing. The last configuration is more complex due to discontinuity in the pressure and shear stress fields at the edge of the contact area. Complete description of the stress field in elastic contact can be found in the books of Johnson [JOH 85] and Hills [HIL 93]. Three modes of fretting for a sphere on a flat contact were defined by Mohrbacher [MOH 95] are represented in Fig. 1.9. The first mode corresponds to a constant normal force and an oscillating tangential displacement creating slips along one direction, the second mode represents an oscillating normal forces creating radial slips and the third mode corresponds to a constant normal load with a variable moment around z.
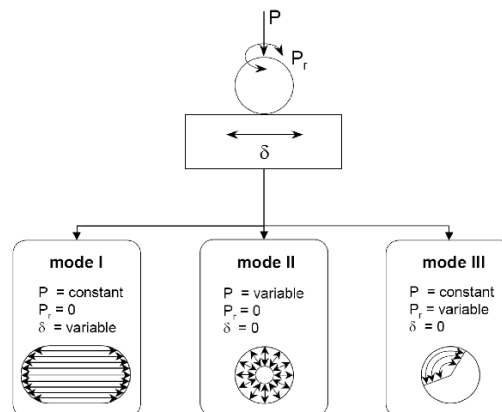
Figure 1.9: Fretting modes [MOH 95]

The first mode is the most investigated due to its simplicity and reasonable accuracy in modeling fretting loading in the blade disk interface. A sphere or a cylinder is pushed in contact on a flat with a constant normal load N and a tangential displacement δ is imposed on one of the solids. A parameter e can be defined comparing the relative displacement and the contact radius a^* [FOU 96]:

$$e = \frac{\delta}{a^*} \tag{1.1}$$

When $e < 1$, a part of the initial contact area is always in contact and never exposed to external environment. This is called fretting. If $e > 1$, the contact is in reciprocating sliding (see Fig. 1.10).

1.2.1.1 Fretting regimes

Based on the amount of stick and slip that occurs in the contact, two fretting sliding conditions can be identified, namely gross slip and partial slip conditions [VIN 88].

- Gross slip condition: according to Coulomb's law, the shear distribution Q is equal to the coefficient of friction μ times the pressure P along the contact surface : $Q = \mu P$ and the whole contact surface is sliding.

- Partial slip condition: the local tangential force is locally reaching Coulomb's threshold even if the macroscopic tangential force $Q < \mu P$ resulting in a stick zone at the center of the contact surface and a slip annulus appearing at the edge of the contact surface [MIN 49].

Transition between the two conditions can be determined using the fretting loop plot $(Q(\delta))$. In stick-slip condition, fretting loop has an elliptical form due to the local slip at the edge of the contact surface while in full sliding condition, fretting loop has a parallelogram form because the tangential force is equal to Coulomb's threshold throughout the tangential displacement.

To calculate the dissipated energy E_d during a fretting cycle and the tangential stiffness of the system $\frac{dQ}{d\delta}$, the tangential displacement δ^*, the maximum tangential force Q^* and the cycle aperture δ_0 can be identified on the fretting loop. For a rectangular cycle, $E_d = 4\delta_0 Q^*$. Several criteria for the transition between different fretting conditions have been proposed by Fouvry [FOU 97] in a sphere/plane configuration.
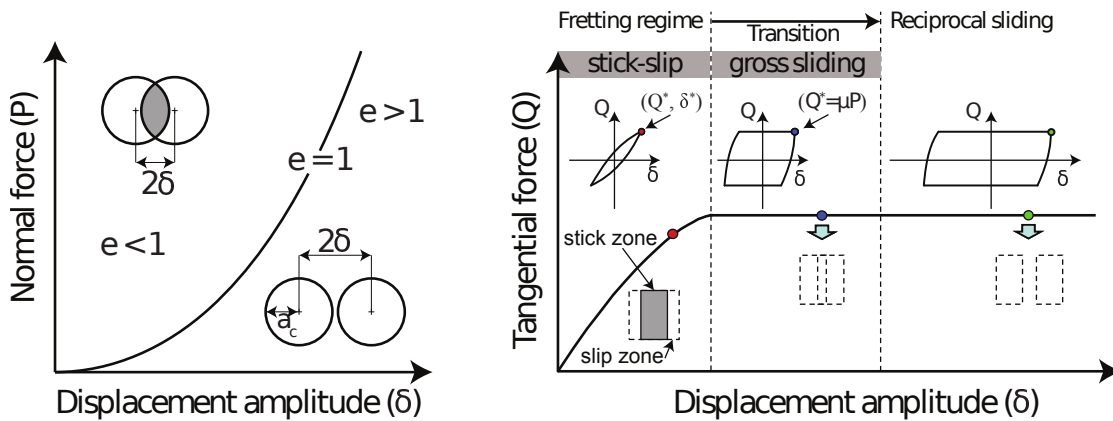
Figure 1.10: Fretting regimes [MON 15]

To study the evolution of contact condition with time, Zhou and Vincent [ZHO 93b] have established three fretting regimes based on experimental results : the partial slip regime, the gross slip regime and the mixed fretting regime which corresponds to sliding conditions evolving from gross slip to partial slip due to a modification of the contact conditions. Generally, the partial slip regime is associated with high normal load and low displacements, while gross slip regime is typically associated with lower normal load

and higher displacements. The mixed regime corresponds to a transition between the two aforementioned regimes. Wear is generally associated with the gross slip regime while the partial slip regime to cracks [VIN 92] and both damage phenomena compete in the mixed regime. Material response fretting map (see Fig. 1.14) associated with each fretting regime map has been proposed in [BLA 91].
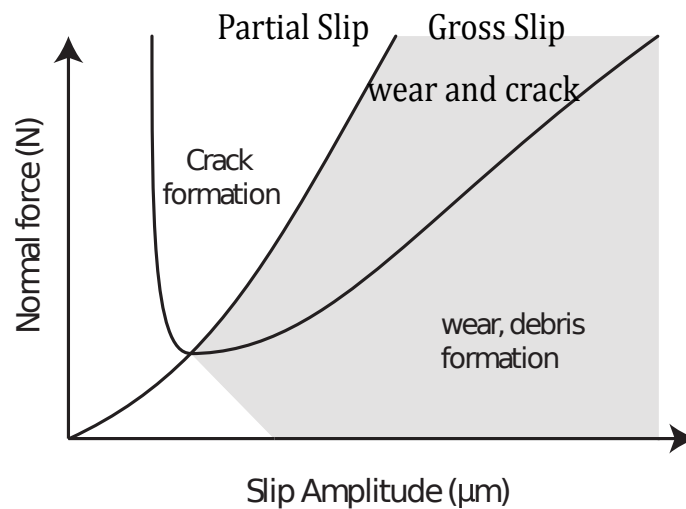
Figure 1.11: Material Response Fretting Map

1.2.1.2 Surface damages

Under fretting loading, cracks and surface degradations appears as a result of fatigue phenomenon, void nucleation and sub-surface crack propagation [SCO 67, SUH 73]. Due to friction and stress gradient in the contact, the two main phenomena, namely wear and crack initiation, are surface originated. Details on these two damage phenomena are briefly recalled in the following subsection.

Wear

Wear in the blade-disk interface is mostly due to friction. Wear by friction can be classified as: adhesive wear (transfer of material due to local overstress), abrasive wear (hard material is plastically deforms a softer one), corrosive wear and fatigue wear. Fatigue wear would be caused by the cyclic shearing of material in the contact region followed by the initiation, propagation and intersections of cracks. During fretting, most of the wear debris are retained in the contact area. Furthermore, several wear mechanisms are often coupled. A summary of different approaches found in the literature to describe friction wear are listed:

- Archard's wear law [ARC 53] defines the wear volume V_W as a function of the sliding distance s, the normal load F and H the hardness of the softer material in contact. K is dimensionless and is called the Archard wear coefficient.

$$V_W = K.\frac{F.s}{H} \qquad (1.2)$$

One should noticed that Archard's law is independent of the coefficient of friction. In experimental results, the hardness of the material may be unknown and a dimensional Archard coefficient (or specific wear rate) is used [WIL 99]:

$$\frac{K}{H} \ \# \ mm^3.N^{-1}.m^{-1} \qquad (1.3)$$

- Third body concept proposed by Godet [GOD 84, BER 90] takes into account the interface between the contacting bodies. According to this concept, wear is governed by three phenomena: detachment, flow and ejection of wear particles. Numerical simulation of wear debris in contact is very expensive in terms of computational time and are only used for qualitative analysis.

- Energetic approach developed by Fouvry [FOU 96, FOU 03] links the wear volume to the dissipated energy in the contact during a fretting cycle. The dissipated energy during a fretting cycle is the sum of the dissipated energy during each part of the load path:

$$E_d = \sum Q.\delta \approx 4Q\delta^* \qquad (1.4)$$

The dissipated energy is a function of the normal load, the coefficient of friction and the tangential displacement. The wear volume can then be computed as the sum of the dissipated energy for every fretting cycles:

$$V_W = \alpha \sum_{k=1}^{N} E_d(k) \qquad (1.5)$$

Because there are not depending on the displacement amplitude, energetic approaches are widely used in the literature. Moreover, these approaches provides an accurate estimation of the wear in sliding contact without representing local mechanisms occurring in the contact area.

When studying contact of materials, one should be careful because the coefficient of friction, friction phenomena, and wear are not material properties but depend on the whole tribological system properties.

Cracks

In the partial slip regime, crack initiation and propagation appears at the edge of the contact area as a result of damage accumulation by cyclic shearing of material in the slip region [BRY 88]. Initiation steps described by Lemaitre and Chaboche [LEM 90] are:
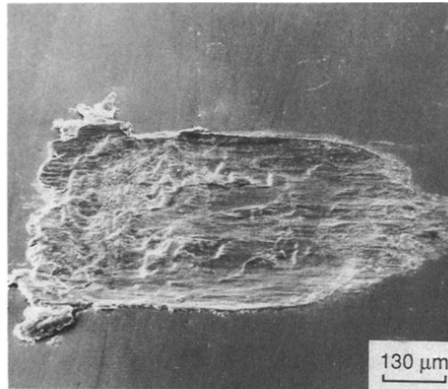
Figure 1.12: Wear scar from fretting [BRY 88].

1) Accommodation phase: stress concentration leads to plastic micro-strains.

2) Initiation phase: plastic strain accommodation leads to a short crack initiation. Crack follows the path maximizing the shear stress with an angle around 45 degrees with the contact surface.

3) Propagation phase: short crack becomes a long crack following the linear elastic fracture mechanics theory [FOR 61, NIX 88, LIS 03].

During the initiation phase, crack path may be influenced by the microstructure of the material because the crack size is around the same size as those of grains [PAN 18]. Multiple initiation criterion have been proposed in the literature based on Tresca stress [FIN 58, MAT 77], Von Mises stress [SIN 59, CRO 56] and mesoscopic approach [DAN 93]. Also, numerical simulations of the initiation and propagation of cracks in blade-disk contact have been investigated by several authors [DIC 06a, MER 11, MON 15].
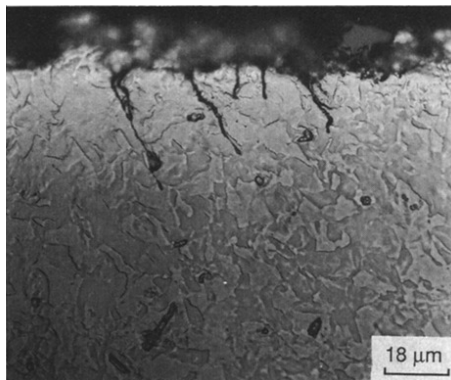
Figure 1.13: Crack initiation in partial slip fretting regime [BRY 88].

Finally, in some contact conditions, wear and cracks can compete in the tribological system. Crack initiation points are also subjected to wear, limiting crack nucleation.
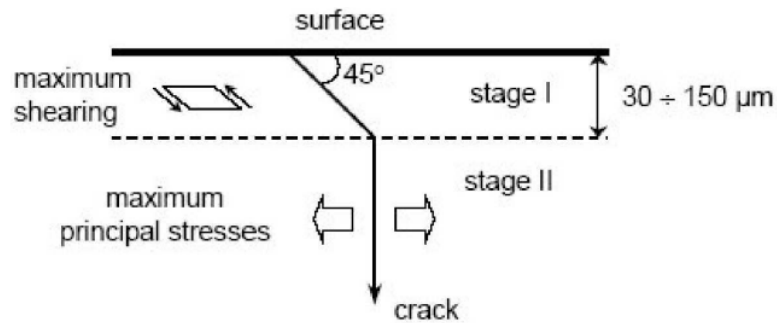
Figure 1.14: Crack initiation and propagation in partial slip fretting regime [FOR 61].

Now that the damage mechanisms occurring during fretting loading have been presented. The damage phenomena due to rolling contact loading are detailed in the next section. One should note that fretting damage phenomena are friction originated while damage phenomena in RCF are mainly due to the reversal of the shear stress during a loading cycle.

1.2.2 Rolling Contact Fatigue (RCF)

Considering good lubrication, installation and operating conditions, life of bearings is only limited by rolling fatigue mechanisms [HAR 01, SAD 09]. Rolling Contact Fatigue (RCF) is a phenomenon due to a repeated rolling loading over a surface. RCF strongly depends on the tribological conditions (lubrication, surface roughness etc.) and the materials properties. Classical fatigue theory can not be applied here due to some major differences with RCF recalled here:

- Stress state in Hertzian contact is multi-axial.

- The maximum stress location is moving during a loading cycle (Fig. 1.15).

- RCF's phenomenon occurs in a very localized volume (contact areas are about a tenth of a millimeter).

- Loading path is not proportional: component of the stress field are not evolving in the same way (even more with plasticity or heterogeneity under the surface).

- Principal stress axes moves during the loading path, making harder to find the plane of maximal shear stress.

- High negative hydrostatic stress due to applied compression limits crack propagation in mode I.

- RCF is mainly due to the reversal of the shear stress [JAL 11] (see Fig. 1.16).
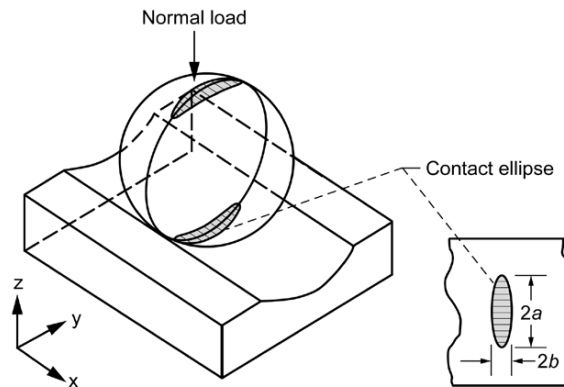
Figure 1.15: Rolling Element Bearing
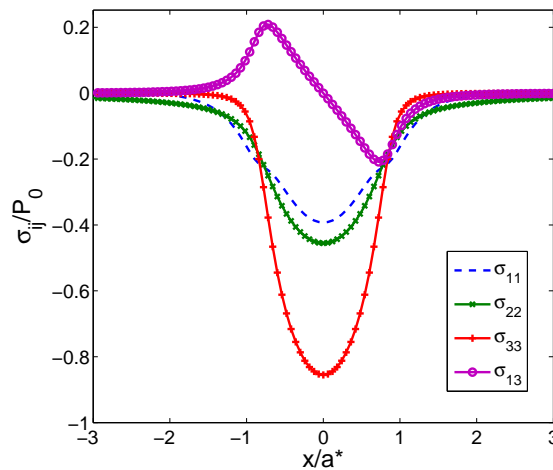
Figure 1.16: Stress history of a point located at $0.5a^*$ in the subsurface of the material as the Hertzian load passes over.

The two different phenomena leading to RCF failure are surface originated pitting and subsurface originated spalling [LIT 66, TAL 99]. Pitting is mainly due to surface defects or insufficient lubrication while spalling is due to subsurface cracks initiating at material imperfections like voids, dislocations and inclusions.

1.2.2.1 Surface initiated damage

Pitting is a phenomenon corresponding to a loss of a chunk of material due to a surface initiated crack (see Fig.1.17). Those cracks are mainly due to low quality surface finishing, debris denting or wear [NEL 99, NEL 00, RYC 17]. Moreover, the approximate thickness of a pit is about 10 μm [DIN 03] and pitting occurs when one of the cracks is reaching the surface. The crack trajectory depends on the shear stress acting on it during the loading path and on the grain boundary stiffness and orientation.
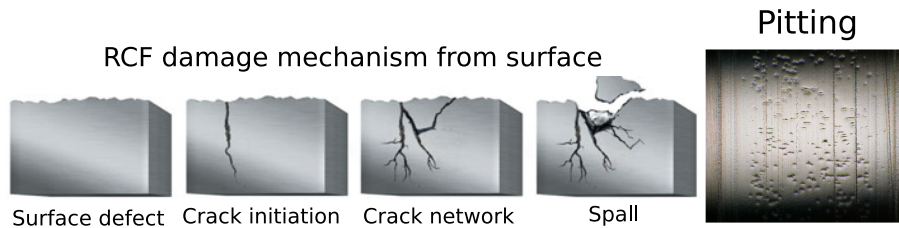
Figure 1.17: Surface initiated damage from RCF [ZAR 12] and illustration of pitting [RYC 12].

1.2.2.2 Subsurface initiated damage

In contrast to pitting, spalling phenomena corresponds to subsurface originated cracks reaching the surface and leading to a loss of a chunk of material [TAL 99, JIN 89]. The subsurface cracks are initiated around heterogeneities close to the surface. This phenomenon can be overcome with the use of coatings or by improving manufacturing processes. Finally, the main difference with pitting is the bigger size of the chunk, called spall. The average thickness of a spall is around $0.25a^*$ to $0.35a^*$ [DIN 03] and can lead to the failure of the rolling element.
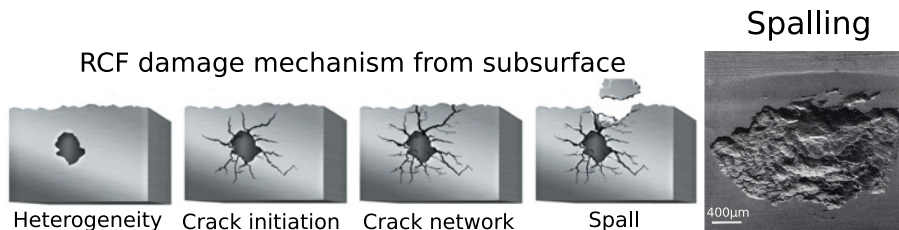
Figure 1.18: Subsurface initiated damage from RCF [ZAR 12] and illustration of a spall [TAL 92].

1.2.2.3 Microstructural alterations due to RCF

This section briefly discusses some additional failure phenomena associated with microstructural changes during the fatigue process. These phenomena are typically revealed by microscopic analysis of etched steel microstructure. According to Zwirlein and Schlicht [ZWI 82], microstructural alterations occur in the following order:

- Butterflies wings are formed of two white etching areas around hard inclusions present in the bearing steel. Wings develop in two main directions depending on the over rolling direction and with an angle of around 45 degrees with respect to the contact surface. Cracks form at the top part of the upper wing and at the bottom part of the lower wing and grow to reach the surface leading to the failure of the bearing. [STY 51, GRA 10, MOG 16a, ALT 18]. The question whether the crack or the wings happen first is still not clearly answered. Some authors believe that wings

form first [MOG 15b, EVA 12] because of wings experimentally observed without cracks and the lack of butterfly wings on the other side of the crack [MOG 16b]. Other authors believe that cracks are already present in the material due to heat treatment or debonded inclusion and then wings appear by rubbing and collision of crack faces [SOL 14].

- Dark etching region (DER) forms and expands with loading cycles just under the raceway, in the region of maximum shear stress but with no preferential orientation. It is characterized by its dark appearance and has been associated with high microplastic strain [GRA 10, BHA 12, WAR 13].

- White etching bands (WEB) appear inside the dark etching region and along specific angles from the over rolling direction. A first band is forming with an angle of about 30 degrees called flat white bands and followed by a 80 degrees bands called steep white band [MAR 66, ZWI 82, POL 95, KAN 13].

- White etching cracks (WEC) are part of a 3D crack network appearing under very high load and are surrounded by white etching microstructure (or layer). Hydrogen embrittlement in the steel is the most common theory used to explain WEC appearance [EVA 13a, RUE 14]. There is still no clear consensus on the origins of these phenomena [BLA 16, SOL 14]. Recently, Manieri et al. [MAN 19] showed that WECs are a consequence of a specific high stress history. Moreover, WEC represents very high costs in wind turbine maintenance and is still an unsolved problem.

In order to achieve better design and to determine a better prediction of component life, several numerical methods have been proposed in the literature to simulate damage of materials under contact loading [MOG 15a, MOR 18b]. These methods are often based on the continuum damage mechanics theory briefly discussed in the following section.

(a)

(b)

(c)

(d)
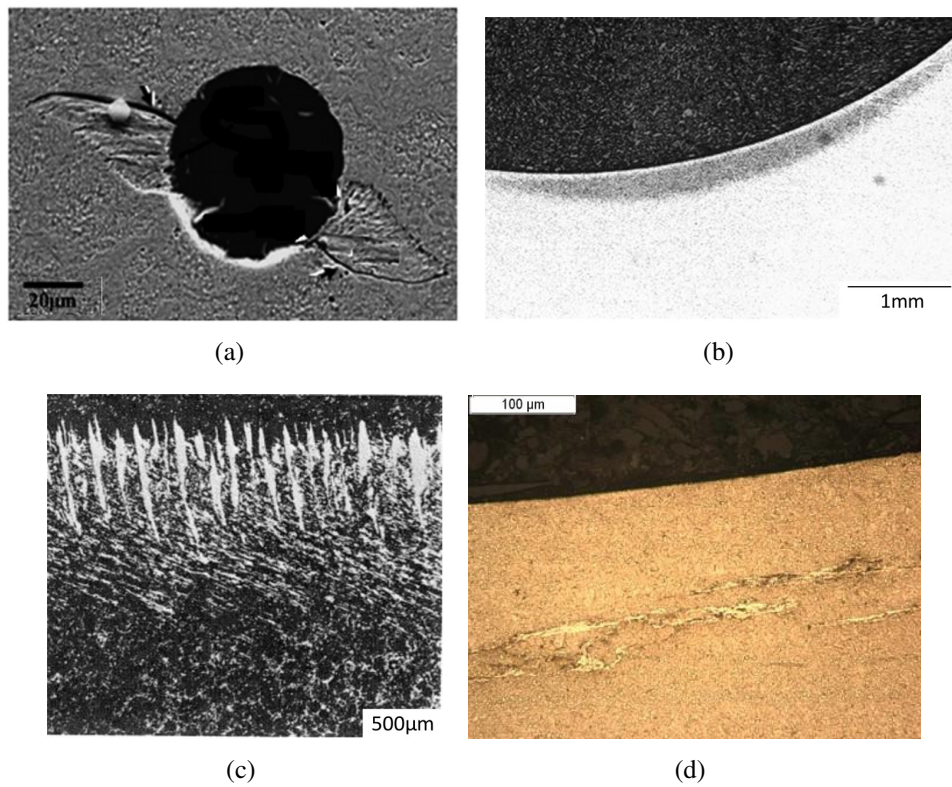
Figure 1.19: Damage mechanisms in Rolling Contact Fatigue (a) Butterfly wings around an inclusion [GRA 10] (b) Dark Etching Region in axial cross section (c) White Etching Flat and Steep Bands [ZWI 82] (d) White Etching Cracks in axial cross section [RUE 14].

1.3   Continuum Damage Mechanics

Continuum damage mechanics (CDM) describes the initiation and evolution of degradation in materials at the microscale such as micro cracks and voids. Study of the CDM originated from efforts to model creep phenomena in USSR. In 1958, Kachanov introduced a scalar variable associated with damage [KAC 58] and his student, Rabotnov, defined the concept of effective stress [RAB 69]. Following this preliminary work, continuum damage concepts have been enriched by the works of Lemaitre. They coupled CDM with both elasticity [LEM 77] and plasticity [LEM 84] and introduced a thermodynamics framework [CHA 74]. Links with ductile fracture have also been proposed by Leckie and Hayhurst [LEC 74]. Advances in CDM modelling has enabled the study of phenomena like micro defects closure in compression, fatigue or anisotropic damage. Moreover, CDM has been applied to different materials like concrete [ORT 85, MAZ 89] and composite materials [MAI 97b, MAI 97a]. Thus, CDM is able to model the alteration of a virgin material until the initiation of a mesoscopic crack in the volume element. Damage is defined through the use of an internal variable called D. In quasi-brittle materials, damage is mostly due to debonding but in ductile materials, damage mechanisms are strongly linked to plasticity and voids coalescence.

Building a model to represent damage in a material requires the definition of a damage variable, an evolution law and a coupling with the constitutive equation of the material [MAR 85]. Appearance of micro cracks is followed by an irreversible alteration of the material characterized by a decreasing material stiffness. Instead of representing micro cracks and voids geometrically in the material, CDM only model their effects on the mechanical properties. Kachanov [KAC 58] defines the damage variable D as the density of micro cracks and voids in the cross sectional area of the representative elementary volume (REV). With $\tilde{S}$, the effective area that carries the load and S, the original undamaged area in the REV, D may be interpreted physically as the ratio of damaged surface area over total surface area:
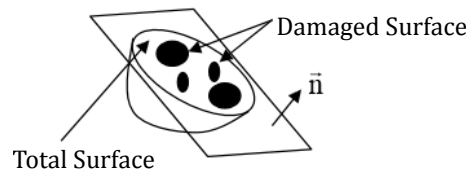
Figure 1.20: Cross sectional area of the RVE with a damaged area.

$$D = \frac{S - \tilde{S}}{S} = \frac{S_D}{S}$$

Considering no healing of the material, D is monotonically increasing from $D = 0$, the undamaged state, to $D = 1$ the complete local rupture of the material. D is defined in
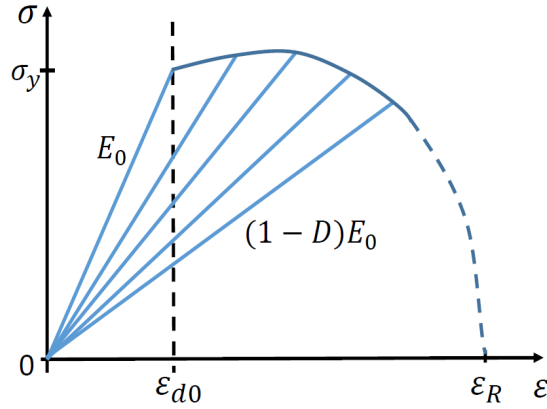
Figure 1.21: Stress strain curve with damage

every point of the solid and represents the alteration level of the REV in this point. In the general case of anisotropic damage, D is a tensor.

The state of stress in the damaged material can be described by the effective stress introduced by Rabotnov [RAB 69]:

$$\tilde{\sigma} = \frac{F}{\tilde{S}} = \frac{F}{S}\frac{S}{\tilde{S}} = \frac{\sigma}{(1-D)} \tag{1.6}$$

Lemaitre [LEM 85] introduced the following hypothesis that the strain behavior is modified by damage only through the effective stress. Hence, the strain associated with a damaged state under the applied stress is equivalent to the strain associated with its undamaged state under the effective stress. Applying the Hooke's law with E, the modulus of elasticity for the undamaged material, the elastic strain in the material becomes:

$$\varepsilon = \frac{\tilde{\sigma}}{E} = \frac{\sigma}{(1-D)E} \tag{1.7}$$

Using the effective stress and the strain equivalence, it yields that the damage variable affects the linear elasticity modulus. An effective elasticity modulus linking the damage parameter evolution with the material deterioration is defined:

$$\tilde{E} = E(1-D) \tag{1.8}$$

Increase in the damage reduces the modulus of elasticity as shown in Fig.3.1. In order to measure the damage variable, D can also be defined as:

$$D = 1 - \frac{\tilde{E}}{E} \tag{1.9}$$

Now that the method to model the degradation of material has been recalled, the next section will focus on the description of composite materials behavior and damage phenomena.

1.4 Modeling and damage in composite materials

1.4.1 Composite materials: structure and composition

Composite materials are made of an assembly of at least two different materials with a goal of obtaining a material with better mechanical, thermal or chemical properties than each material used alone. Composite materials allow complex geometries, low weight and designed properties for specific application that make them very interesting in the aeronautic industry. The main structure of composite materials can be decomposed into the matrix and the reinforcements:

- The matrix surrounds the reinforcement materials and insuring the composite material cohesion. Depending on the application, matrix can be made of polymer (aerospace structure, RTM fan blades), metal (disk of engines) or ceramic (for high temperature application like turbine nozzles).

- The reinforcements improve the matrix mechanical properties. They can be in the form of particles, short fibers or long fibers (see Fig. 1.23).
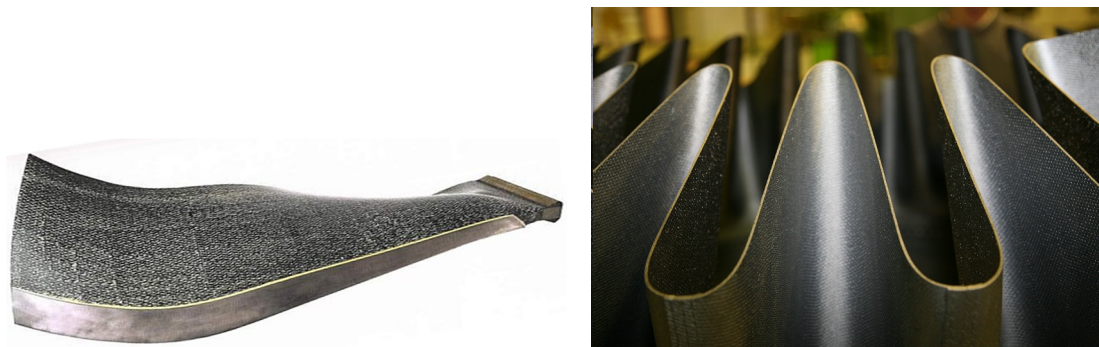
Figure 1.22: Parts in composite materials with (a) Organic matrix (b) Ceramic matrix.
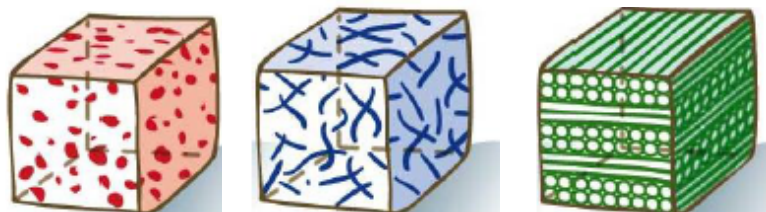
Figure 1.23: Reinforcements in form of (a) Particles (b) Short fibers (c) Long fibers.

Matrix functions are mainly to give the general shape of the part, to transmit the load into the fibers and to protect the fibers from the environment. In addition to its constituents, structure of composite materials play a major role on their mechanical behaviors. Composite made of particles or short fiber reinforcements are generally randomly

distributed inside the matrix and do not have any specific structure. In contrast, long fiber composites usually have specific geometries that are briefly described here:

- Laminated structures are made of plies with different orientation. Each ply is made of yarns (bundles of fibers) with a plane orientation inside the ply. Individual layers are often orthotropic. Modification of the ply order and orientation allow to design the mechanical properties of the composite laminate to its application. Their main damage behavior called delamination corresponds to the separation of the layers at the interface.

- Sandwich structures are made of two thin plates glued to a thick lightweight core. Usually the core material has low stiffness compared to the plates. This kind of structure allows the fabrication of very low density materials with good mechanical properties for bending and torsion.

- Woven structures are made of fibers weaved together in a complex structure called preform and introduced into a resin. Different kind of weaving and knitting are possible to get the desired mechanical properties.

Fan blades of the LEAP engine are 3D interlock woven composites made of a polymer matrix and a carbon fibers preform. 3D woven composites have good performances when out-of-plane loading is applied on the part [PEA 07]. A Resin Transfer Molding (RTM) process is used to develop this material: a fiber preform is introduced into a mold and a heated resin is injected that transforms into a continuous solid matrix.

Understanding and modeling the behavior of this kind of material is very complex. Depending on the kind of problem that need to be represented, three scales of representation can be used: microscopic scale (scale of fibers), mesoscopic scale (yarns are considered homogeneous) and macroscopic scale (the part is considered homogeneous). In contact conditions, validity of the macroscopic scale may not be the most appropriate scale due to the very local solicitations in regard to the material structure. One should be careful about the sensibility of contact mechanics to scale effects of the materials.

1.4.1.1 Behavior of composite materials

Behavior of woven composite depends on the materials used for the matrix, the fibers and the weaving structure. Most of the time, the macroscopic homogeneous behavior is considered as orthotropic. Considered separately, the polymer matrix has a viscoelastic behavior and the yarn has a brittle linear elastic behavior. For a 3D woven material, the behavior in tension in the direction of the yarn is found to be brittle non linear elastic and the behavior of the whole material in out-of-plane tension is found to be non linear with presence of residual strain due to damage [BOR 04]. Fracture of carbon fibers is brittle [TAN 00] and load-unload experimental results show the damage behavior of the material with solicitation in the different directions of the material (weft direction, warp direction and 45 degree out-of-plane) [SCH 08]. Hurmane [HUR 15] observed that in

tension, yarns realign in the direction of the tension loading leading to an hardening of the material behavior. Thus, complete behavior of a 3D woven composite in tension along the warp direction can be described in three steps (see Fig. 1.25):

(a)   (b)
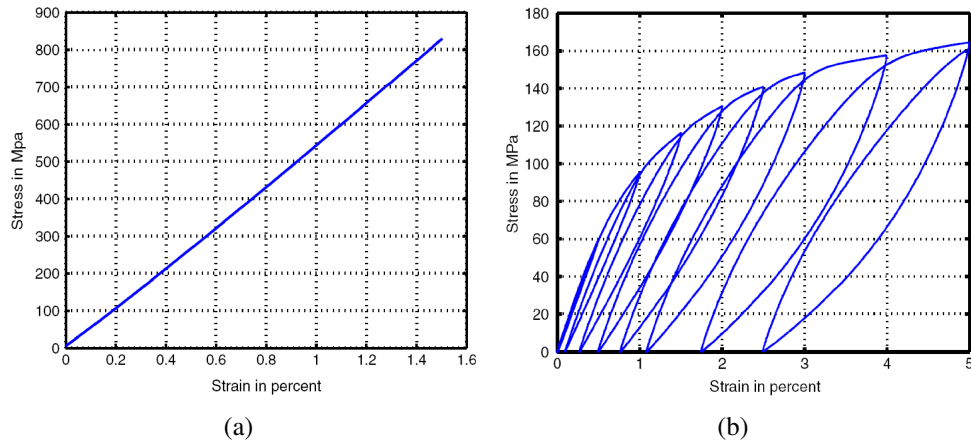
Figure 1.24: Mechanical behavior of a 2D woven composite in (a) traction along the fibers (b) plane shears [BOR 04].

1) Viscoelastic behavior.

2) Damage due to matrix cracks and debonding between yarns and matrix.

3) Yarn failure.
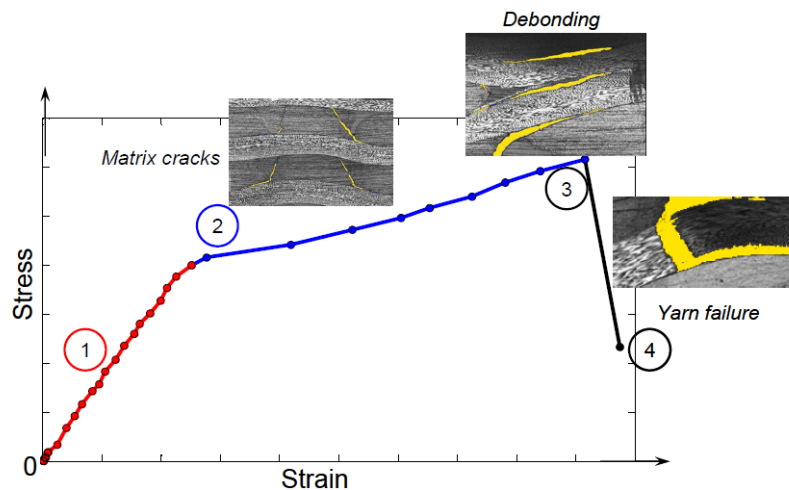
Figure 1.25: Behavior of a 3D woven composite in tension along the warp direction [HUR 14].

1.4.1.2 Damage phenomena in composite materials

After forming, 3D woven composites with polymer matrix have a very low porosity level and no apparent damage (see Fig.1.26). Moreover, polymer matrix has a very low Young modulus compared to the Young modulus of the fibers. Hence, yarns are transmitting most of the load. A lot of studies have been done on the damage mechanisms of woven composite materials and mostly focusing on traction loading [COU 08, KER 14, GRA 13a, LI 15, DOI 15a]. Only a few studies have investigated compression loading [COX 92, HUR 15, ELI 15, ELI 17, MBA 13]. Behaviors in flexion [MAR 10], torsion [SCH 09b] and in fatigue [HEN 11, HEN 13, RAK 13, ANG 16] have also been studied by some authors.

Figure 1.26: Initial state of 3D woven polymer matrix composite [COU 08].

Due to their structures, mechanical behavior of woven composites highly depends on the direction of loading in respect to the direction of the yarns (warp, weft and out-of-plane directions). Common damage mechanisms can be described at three different scales:
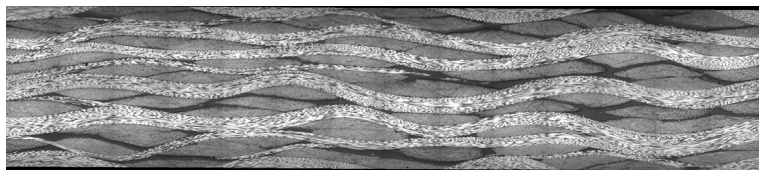
- Microscopic damage mechanisms: fibers-matrix debonding and matrix micro-cracks inside the yarn (see Fig. 1.27(a)). No notable effects on the global behavior have been observed.

- Mesoscopic damage mechanisms: cracks in matrix pockets between the yarns. Cracks are deviated by materials interface (see Fig. 1.27(b)). Effects are mainly observed on the behavior in the warp direction [HUR 15].

- Macroscopic damage mechanisms: Fracture and failure of the material.

When every matrix pockets have been fully damaged, damage is reaching saturation and load is only transmitted through the yarn leading to the hardening of the material [HUR 15].

In compression, only a few damage mechanisms occur before finale failure of the material [HUR 15]. Compression loading is increasing the ripple of the yarns resulting in the softening of the material in the weft direction. Some microscopic damage phenomena appear due to out-of-plane deformation coming from Poisson's effect. Ripples of the yarns leads to debonding and fracture of the fibers as in Fig. 1.28. Couegnat [COU 08] measured the acoustic emissions of a 2.5D epoxy composite material in tension loading. No damage have been detected for loading below 300 MPa. Above this threshold, first

(a)   (b)
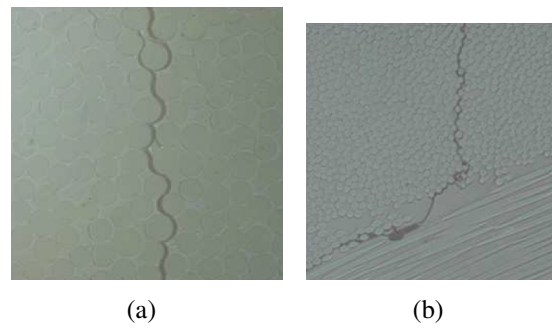
Figure 1.27: Damage mechanisms at the microscopic level [COU 08].
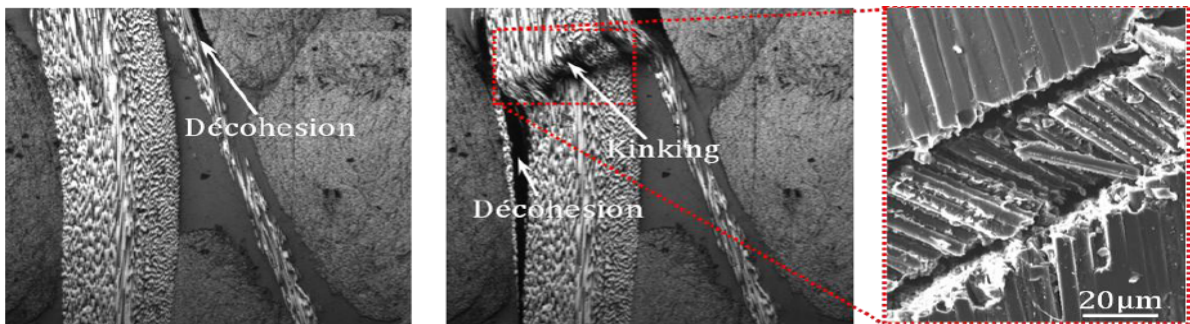
Figure 1.28: Debonding of the yarn followed by kinking fracture in compression [HUR 15].
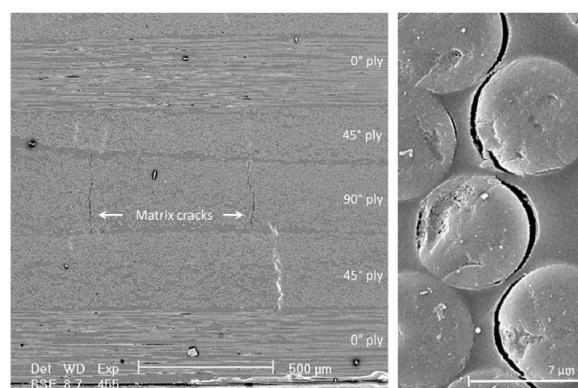
Figure 1.29: Matrix fracture in tension along the yarns at $0 \deg$ [ROM 15].

(a)   (b)
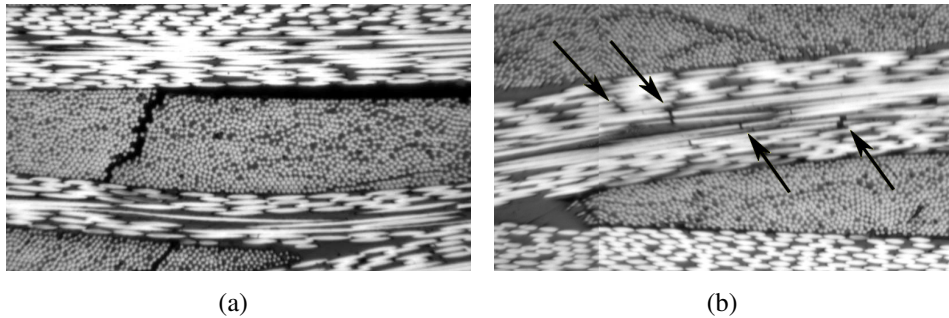
Figure 1.30: Damage of 2.5D-C/epoxy (a) Transverse crack and debonding of the yarn (b) Longitudinal crack of the yarn [COU 08].

fibers failure appears and transverse failures initiate from 475 MPa (see Fig. 1.30(b)). Exact values may depend on the considered material but give a first idea of the damage threshold in polymer woven composite materials. For 3D woven materials, a small non linearity is observed in the yarn direction due to the presence yarns in the third direction. Yarns parallel to the loading direction are in tension and damage the material. Due to the complex stress field appearing under contact loading, comparison with existing work on pure tension and compression damage mechanisms is limited. Elias [ELI 15] observed the damage mechanisms during low speed impact on a 3D woven polymer matrix composite with a spherical projectile. The stress field under low speed impact is close to the one in normal load contact conditions [CHA 11c]. Elias performed some optic microscope observation and found the same kind of damage as already described (yarns debonding and matrix cracking). He compared the localization of the experimentally observed damage with an elastic finite element simulation of impact and found that most damaged zones are in the zone of shear stress while less damaged zone (just under the impact) are zone of high hydrostatic stress. Non damaging effect of hydrostatic stress has already been observed for laminated composite [CAR 12]. Some recent works on the tribological behavior of carbon-reinforced polymer composite against titanium alloy have been done by Li et al. [LI 18b] and showed that the main fretting wear mechanisms are carbon fiber wear, fiber-resin debonding and matrix cracking. Due to friction, wear debris migrate out of the contact area and pile-up at the border of the contact. The kind of wear associated with the carbon fibers is abrasive with creation of small wear particles while the resin has brittle fracture and adhesive wear behavior. Finally, this section presented the main damage phenomena occurring in woven composite materials. In the next section, some existing damage models for composite materials are presented.

1.4.1.3 Damage models for composite materials

Damage prediction and simulation in composite materials is very important in the aeronautic industry with the introduction of the LEAP engine. Different approaches have been proposed depending on the kind of mechanisms to model and at which scale the material

is modeled.

At the microscopic scale, two main methods have been proposed:

- Implicit representation through the rigidity reduction of the mesh grid [SCI 99].

- Explicit representation of the crack by introduction of new nodes in the mesh.

At the mesoscopic scale, the work of Daggumati [DAG 10] and Lomov's team [LOM 00, LOM 07a] with WiseTex software allow to fully mesh the woven pattern. Damage is represented by degrading the mechanical properties of the yarns. Another approach has been proposed by Doitrand et al. [DOI 17a, DOI 17b] to introduce cracks inside the yarn at the mesoscopic scale.

At the macroscopic scale, the complex geometry of the material is not represented but only the effects of the different damage mechanisms on the overall behavior are described. One can cite the work of the LMT Cachan [CHA 95, ALL 93, LAD 94] on an anisotropic damage model with closure effect [MAI 97b] at the macroscopic scale. A specific focus is made on ceramic composite materials and the damage variable can be a scalar, a 2nd order tensor or a 4th order tensor. This model has been coupled with micro mechanics models to take into account self healing and fiber damage [HIL 96, LET 06].

Another damage model for composite material has been developed at Onera for 20 years firstly for ceramic composites [MAI 97a, AIE 01, LAU 07, SAL 18] and later for polymer composites with the work of Marcin [MAR 10]. The "Onera Damage Model" (ODM) has been continuously improved and adapted to different loadings and physics. One can cite the work of Rakotoarisoa and Angrand on fatigue [RAK 13, ANG 16, KAM 15]. Recently Hurmane adapted this model to study compression [HUR 15] and Elias [ELI 15] for low speed impact. Garcia [GAR 17] adapted the model for contact loading in landing systems. Moreover, in the ODM, the composite material is assumed to be homogeneous with a damageable orthotropic behavior. The ODM is made of different damage variables for each scale of damage phenomena and coupled together. Microscopic damage variables are calculated and linked to mesoscopic and macroscopic damage variables through different evolution laws traducing the different scales of damage and finally affecting the macroscopic behavior of the material.

1.4.2   Homogenization of heterogeneous materials

The homogenization theory is used to simplify the simulation of heterogeneous materials by defining a homogeneous twin material. The macroscopic response of the homogeneous material and of the real heterogeneous material should be the same. Homogenization is based on several assumptions that are recalled here:

The representative elementary volume

In the continuum mechanics theory, the representative elementary volume (REV) is defined as the minimum volume allowing to obtain a homogenized behavior independent of

the considered volume size. The size of the REV is often dependent of the size of the microstructure of the material. In periodic materials like woven composite materials, the presence of the woven pattern is used to defined the size of the REV and in metallic alloy, the size of the REV will depend of the grain size distribution in the material.

Scale changes: fine scale and coarse scale

From the definition of the REV, two different scales can be defined. A fine scale associated with the REV dimension l and a coarse scale, associated to the macroscopic structure L. The homogenization theory hypothesizes the separation of scales : $l \ll L$. Therefore, the structure can be considered as a continuum medium and the REV is considered as a material point at the structure scale. Finally, the aim of homogenization is to define a material response independent of the local scale of the material.

Localization

The macroscopic stress and strain are respectively called Σ and E. One can define the localization tensor $A(x)$ as the relationship between the local strain in the material and the macroscopic strain and concentration tensor $B(x)$ as the relationship between the local stress to the macroscopic stress.

$$\varepsilon(x) = A(x) : E \tag{1.10}$$

$$\sigma(x) = B(x) : \Sigma \tag{1.11}$$

Effective properties

The main goal of the homogenization process is to define the macroscopic behavior of the material through effective material properties. The effective stiffness tensor is defined as the tensor linking the macroscopic stress Σ to the macroscopic strain E in the heterogeneous material:

$$\Sigma = C^{eff} : E \tag{1.12}$$

The macroscopic stress and strain are defined as the mean value over the volume of material V of the local stress $\sigma(x)$ and $\varepsilon(x)$:

$$\Sigma = <\sigma(x)> = \frac{1}{V} \int_V \sigma(x) dV \tag{1.13}$$

$$E = <\varepsilon(x)> = \frac{1}{V} \int_V \varepsilon(x) dV \tag{1.14}$$

In the linear elasticity framework, considering an applied strain E, one can obtain the relationship between $\varepsilon(x)$ and $\sigma(x)$:

$$\sigma(x) = C^i(x)\varepsilon(x) \tag{1.15}$$

with $C^i(x)$ the local stiffness tensor.

$$\Sigma = <\sigma(x)> = <C^i(x):\varepsilon(x)> = <C^i(x):A(x):E> \tag{1.16}$$

$$\Sigma = <C^i(x):A(x)>:E \tag{1.17}$$

The homogenized stiffness tensor can be defined as:

$$C^{eff} = <C^i(x):A(x)> \tag{1.18}$$

Some of the different possible methods to define the localization and concentration tensors are recalled in chapter 6.

1.5 Methods in contact mechanics

1.5.1 Analytical solution

The first theory of contact mechanics was proposed by Heinrich Hertz [HER 82] in 1882. Hertz found the solution of the contact between two elastic solids assuming that:

- The contacting surfaces are continuous and non-conforming.

- The contact zone is elliptical

- No friction is occurring in the contact zone

- Contacting solids are elastic half-spaces: the size of the contact zone is small enough compared to the characteristic length of the solids. It means that contact stresses are not altered by the boundary conditions of the solids.

Even if the hypotheses of the Hertzian theory are restrictive, it is still widely used and give a good description of the contact solution.

Contact mechanics theory was later extended to non-Hertzian geometry [JOH 85]. In particular the work of Aleksandrov [ALE 86] on the contact between a punch and a half-space and the work of Westergaard on sinusoidal rough contact [WES 39] can be cited as example. Cattaneo [CAT 38] and Mindlin [MIN 49] proposed a solution for sliding contact using Coulomb's law for friction.

1.5.2 Numerical methods

Finite element

The finite element method is the most common numerical method in solid mechanics. This method is very powerful to find approximate solutions of partial differential equations (PDE). Numerous commercial softwares use this method to solve complex problems (thermal fields, dynamic, plasticity, viscosity, magnetic fields etc.). For 3D contact problem, the geometrical non-linearity can lead to algorithm convergence issues and a very fine mesh is needed in the contact area to have a good accuracy leading to a high computation cost. Recent works on numerical techniques by Yastrebov [YAS 11] investigated the contact between rough surfaces. Extensive information is available in the books of Wriggers [WRI 06] and Laursen [LAU 03] for synthesis of contact simulation with finite element method.

Multigrid

This method is based on the work of Brandt, Lubrecht and Venner [BRA 90, LUB 91, VEN 00] to discretize and solve Lamé equations using finite differences and innovative numerical tools. The computation speed is considerably decreased by solving the equation at different grid refinements depending on the local error (V-cycle strategy). This method has been applied for heterogenenous materials and moving heat source by Boffy et al. [BOF 12, BOF 14, BOF 15] and to composite material modeling [GU 16]. Computation of EHL contact solution on rough surface with presence of a heterogeneity has also been studied recently [MOR 17].

Semi-analytical

Semi-analytical methods are based on the numerical summation of analytical solutions to elementary problems. In contact mechanics, they have been developed by several authors [BEN 67, JOH 85, PAU 81] and one can refer to the work of Kalker [KAL 90]. Originally Kalker's work was based on the use of the Newton-Raphson algorithm which was replaced later by the Gauss-Siedel method by Jaeger [JAE 04]. Finally, the Fast Fourier Transform has been massively used to increase the speed of the method [POL 00, LIU 01].

Nelias and co-workers have been developing a code to solve a three dimensional contact problem [GAL 06, GAL 07a, GAL 10, DON 17] based on the semi-analytical method (SAM) initially proposed by Jacq et al. [JAC 02]. SAMs have been continuously developed and applied to several problems such as thermo-elasto-plastic contact modeling [BOU 05], modeling plasticity and accumulation of plastic strains [BOU 05, WAN 05], running-in [NEL 07], simulation of single impact [CHA 11a], shot peening [CHA 12] and low plasticity burnishing [CHA 11b, NEL 07, CHE 08a], modeling of cuboidal inclusions [ZHO 09, ZHO 11a, ZHO 11b, ZHO 12, FUL 10, ZHO 16], ellipsoidal inclusions [LER 10, LER 11, KOU 14b], heterogeneous viscoelastic behavior [KOU 14a, KOU 15a], heterogeneous elastoplastic behavior [AMU 16, DON 16], as well

as to account for material or coating anisotropy [BAG 12, BAG 13]. The method has also been extended to ultraspeed impact [TAR 14] and contact on dented surface [ANT 08]. Recently, development of solutions for thermal inclusion [LI 19], application to functionally graded thin film [ZHA 18] and imperfect interface conditions [LI 18a] have been proposed. Some applications to lubricated contact for rough contact [REN 09] and a coupled heterogeneous EHL solver [WAN 13, SHE 14, ZHO 16] have been introduced. Finally, semi-analytical methods are very fast and allow to obtain very accurate solution to complex contact problems like plasticity or heterogeneity. Solutions developed in the following work are based on this approach.

### 1.5.3   Simulation of Blade/Disk contact

The blade/disk interface has been studied by several researchers based on 2D analytical solutions [NOW 98, HIL 88]. Contact geometry is often assumed to be equivalent to a punch contact with rounded edges (see Fig. 1.31). Simulations with the Finite Element Method (FEM) have been proposed in [MON 15, DIC 06b, YAS 11] but in order to simulate the contact between a composite blade and a metallic disk, the scale of representation of the composite may strongly affects the contact solution and the capacity to represent the damage occurring inside the material. Previous work of Leroux [LER 13] showed the effects of the presence of heterogeneities on the contact pressure fields. He also used the Wisetex software to obtain a composite geometry description and converted the yarn in a series of ellipsoidal inclusions in the semi analytical solver (Fig. 1.32). Recent work on the meshing of woven composite structure from tomography have been proposed by Naouar et al. [NAO 15b] and is illustrated in Fig. 1.33. One should note that no contact loading simulations has been performed on these kinds of mesh. Finally, the ability of solving the contact problem on a composite material at the mesoscopic scale is still a scientific challenge for the industry.
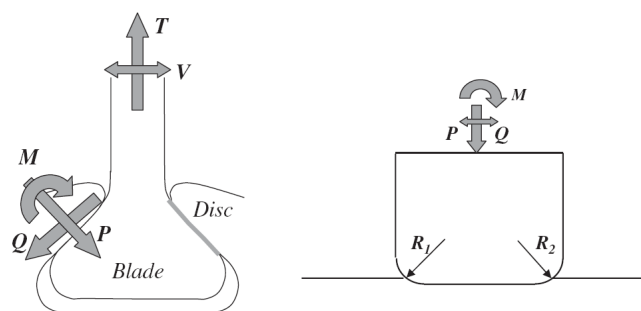
Figure 1.31: Geometrical approximation of the blade disk contact [RAJ 06]
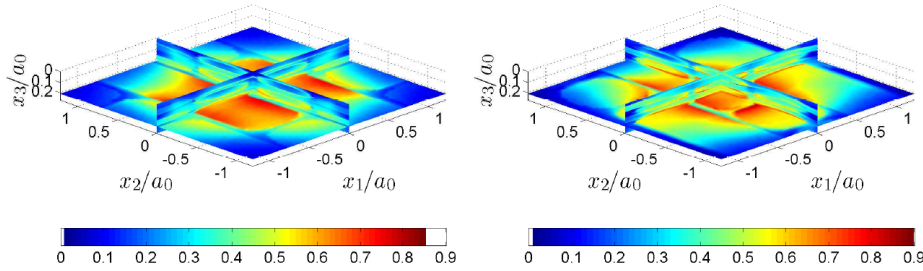
Figure 1.32: Von Mises stress during indentation of 2D composite material with semi-analytical method [LER 13].
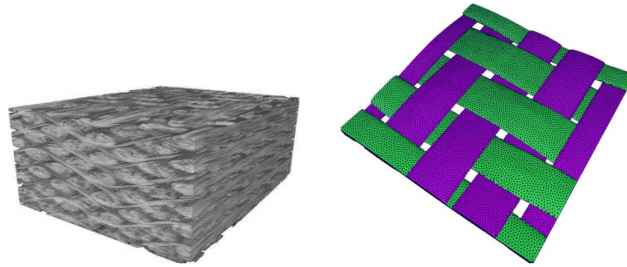
Figure 1.33: (a) Tomography of a Woven composite material 3D (b) Mesh of the woven composite material from tomography [NAO 15b].

1.6 Synthesis and Outline

This section introduced the industrial challenge of the prediction of damage at the blade/disk interface and in rolling element bearings in aircraft engines. Damage phenomena arising with contact loading are presented and the Continuum Damage Mechanics background is briefly described. Mechanical behavior and damage phenomena associated with woven composite materials are introduced. Additionally, challenges in the modeling of heterogeneous composite materials used for the fan blades of the LEAP engines have been highlighted. Subsequently, a summary of different numerical modeling methods for contact simulation are presented. Finally, the main goal of this work is identified to be the development of a contact model for surface and subsurface damage while including the effects of complex geometry of composite materials. Because of the difficulty of modeling heterogeneous materials in contact loading, the semi-analytical method is used in this study due to the low memory needed and high computation speed. Results presented in the following chapter are based on the PhD work of Fulleringer [FUL 11], Leroux [LER 13], Koumi [KOU 15b] and Jerbi [JER 16] on semi-analytical methods. The basics of this method are summarized in the next chapter.

Chapter 2

Semi-analytical method for contact on heterogeneous material

In this chapter, a numerical contact solver based on analytical solution summation and numerical acceleration technique is detailed. Presence of a heterogeneity is taken into account using the Eshelby's equivalent inclusion method. A coupling between the contact problem and the heterogeneous problem is described allowing to solve the heterogeneous contact problem. Influence of multiple heterogeneities is numerically solved using conjugate gradient algorithm.
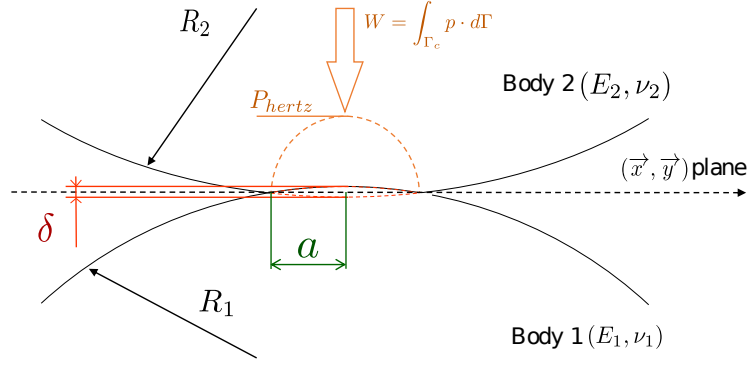
Contents

Figure 2.1: Description of the contact problem.

2.1 Theoretical background of the contact algorithm

2.1.1 Elastic contact problem equations

2.1.1.1 Normal Contact

Let's consider two elastic bodies B_1 and B_2 defined by their undeformed surfaces in the orthogonal basis *Oxyz*. The applied load W is transmitted into the contact through the contact zone Γ_c. Resulting contact pressure field p must verify the equilibrium equation as following:

$$W = \int_{\Gamma_c} p(x,y)d\Gamma \tag{2.1}$$

The gap between the two surfaces at each point (x,y) of the computation domain is equal to the summation of the initial distance between the contacting surfaces h_i, the rigid body displacement δ and the normal component of the elastic displacements of the two bodies $u_z^{B_1+B_2}$.

$$h(x,y) = h_i(x,y) + u_z^{B_1+B_2}(x,y) - \delta \tag{2.2}$$

The distance $h(x,y)$ is always positive to ensure the non-interpenetration of contacting bodies. The contact conditions are defined by the following inequalities:

$$\begin{aligned} \text{When } h(x,y) = 0 \text{ and } p(x,y) > 0 \ &\rightarrow \ \text{contact} \\ \text{When } h(x,y) > 0 \text{ and } p(x,y) = 0 \ &\rightarrow \ \text{separation} \end{aligned} \tag{2.3}$$
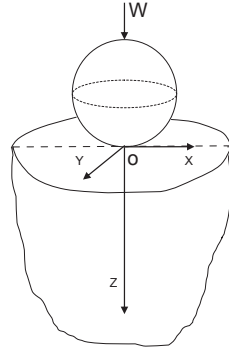
Figure 2.2: Contact of a sphere over an elastic half-space.

Finally, solving the normal contact problem between the two bodies can be resumed to simultaneously solving a system of equations and inequations traducing the boundary conditions of the contact interface. For a load imposed problem, the normal loading W is known.

$$p(x,y) > 0 \qquad\qquad \forall (x,y) \in \Gamma_c \qquad (2.4)$$

$$h_i(x,y) + u_z(x,y) - \delta = 0 \qquad\qquad \forall (x,y) \in \Gamma_c \qquad (2.5)$$

$$p(x,y) = 0 \qquad\qquad \forall (x,y) \ni \Gamma_c \qquad (2.6)$$

$$h_i(x,y) + u_z(x,y) - \delta > 0 \qquad\qquad \forall (x,y) \ni \Gamma_c \qquad (2.7)$$

$$\sum_{\Gamma_p} p(x,y) \cdot S = W \qquad\qquad (2.8)$$

where $u_z(x,y)$ is representing the total elastic displacement of the two bodies at the point (x,y). The variables $p(x,y)$ and $u_z(x,y)$ are the two unknowns of the system.

In the case of two elastic elastic materials, the analytical relationship between the two variables was found by Love [LOV 52].

$$u_z(x,y) = \frac{(1-\nu^2)}{\pi E} \int_{-\infty}^{+\infty} \int_{-\infty}^{+\infty} \frac{p(\xi,\eta)\, d\xi d\eta}{\sqrt{(\xi-x)^2 + (\eta-y)^2}} \qquad (2.9)$$

2.1.1.2 Tangential Contact

When the tangential displacements are not nil, a new set of conditions is needed to solve the tangential contact problem. The tangential contact conditions can be written using the Coulomb's friction law to express the shear stresses q_τ in the contact. The tangential load Q and the contact zone Γ_c are known from the solution of the normal problem. The following system of equation needs to be solved to determine the sticking region Γ_{st} and

the slipping region Γ_{sl}.

$$q_\tau(x,y) = -\mu \cdot p(x,y) \cdot \frac{\Delta s_\tau(x,y)}{\parallel \Delta s_\tau(x,y) \parallel} \qquad \forall(x,y) \in \Gamma_{sl} \qquad (2.10)$$

$$\Delta u_\tau(x,y) - \Delta \delta_\tau = \Delta s_\tau(x,y) \qquad \forall(x,y) \in \Gamma_{sl} \qquad (2.11)$$

$$\parallel q_\tau(x,y) \parallel < \mu \cdot p(x,y) \qquad \forall(x,y) \in \Gamma_{st} \qquad (2.12)$$

$$\Delta u_\tau(x,y) - \Delta \delta_\tau = 0 \qquad \forall(x,y) \in \Gamma_{st} \qquad (2.13)$$

$$\sum_{\Gamma_p} q(x,y)S = Q \qquad (2.14)$$

$$\Gamma_{sl} \cup \Gamma_{st} = \Gamma_c \qquad (2.15)$$

δ_τ is the tangential rigid body displacement and s_τ is the relative slip amplitude. The tangential surface displacement u_τ is the result of the displacements coming from both the shear stresses and the normal pressure field.

2.1.1.3 Coupling between the normal and the tangential problem

Now that the equations characterizing the contact conditions have been set, an iterative method is used to solve the normal and tangential contact problems one after the other.

1. The normal problem is solved assuming no shear tractions. The contact area Γ_c and the pressure field p are found

2. The tangential problem is solved considering the pressure field p found previously. Shears q, slips s and sticking area Γ_{st} are found.

3. If shears are not equal to zero, the normal problem must be solved again considering the shear field q.

This iterative loop must be repeated until both of the problem converged (process of Panagiotopoulos [PAN 85].

The problem is considered fully coupled when normal tractions induce radial shears like in the second mode of fretting (spherical indentation) or when two dissimilar materials are in contact.

$$u_x = u_x^p + u_x^{q_x} + u_x^{q_y}$$
$$u_y = u_y^p + u_y^{q_x} + u_y^{q_y} \qquad (2.16)$$
$$u_z = u_z^p + u_z^{q_x} + u_z^{q_y}$$

When a sphere is moving only along the x-direction (first mode of fretting), one can assume that shears along the x-direction only depend on the tangential force or displacement in this direction. This simplification allow to reduce the computation time of the contact solution.
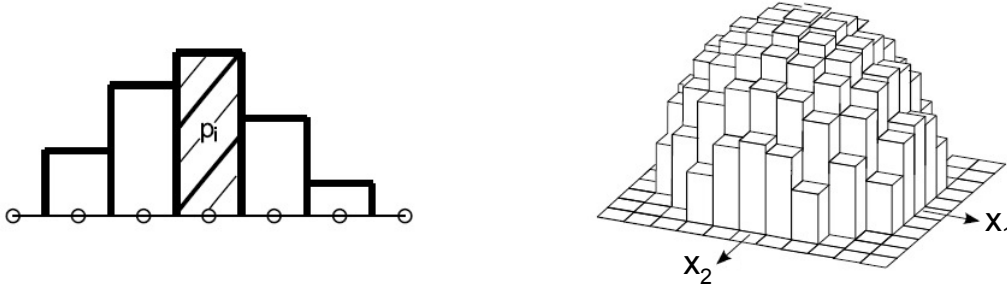
Figure 2.3: Discretizaton of the contact loading in N_p rectangles of uniform pressure and shears.

2.1.2   Numerical discretization

The principle of the semi-analytical problem is to use analytical solution to solve Neumman's problem. The aforementioned problem consists in finding the elastic deflections u and stresses σ in the half-space. Boussinesq [BOU 85] solution is giving the normal displacement at any point of a surface subjected to a unit force. Love [LOV 52] proposed a similar solution for a rectangle on which a uniform pressure is applied and Cerruti [CER 82] for a tangential load. These elementary solutions are known as Green's functions or influence coefficients. Finally, a coupling between the normal and tangential loadings is needed to find the shear distribution in frictional contact [CIA 98a, CIA 98b].

To numerically solve the set of equation for the contact problem, the pressure distribution will be discretized into $N_p = N_x \times N_y$ rectangles of uniform pressure and shears. Distance between each computation point along the x-direction is Δ_x and along the y-direction Δ_y.

According to linear elasticity theory, the surface normal displacement of the half-space at any point (x,y) is found by adding the contribution of each rectangle of uniform pressure p.

$$u_z(i,j) = \sum_{k=1}^{N_x} \sum_{l=1}^{N_y} K_z^p(i-k,j-l)\, p(k,l) \tag{2.17}$$

$$+ \sum_{k=1}^{N_x} \sum_{l=1}^{N_y} K_z^{q_x}(i-k,j-l)\, q_x(k,l) \tag{2.18}$$

$$+ \sum_{k=1}^{N_x} \sum_{l=1}^{N_y} K_z^{q_y}(i-k,j-l)\, q_y(k,l) \tag{2.19}$$

The matrix K_z here represent the effects of a uniform pressure or a uniform shear applied on a patch located at (x',y') on the normal displacements u_z at (x,y)

The subsurface stress field is mandatory to study damage phenomena or plasticity in the material and can be determined by using the same discretization and summation technique. The volume is discretized in many cubes in the same manner than the surface

and stresses are considered uniform in each element of the discretization.

$$\sigma_{ij}(x,y,z) = \sum_{l=1}^{N_x} \sum_{m=1}^{N_y} p(l,m)(C_{ij}^p(x-l,y-m,z,\nu_2)) \qquad (2.20)$$

$$+ \sum_{l=1}^{N_x} \sum_{m=1}^{N_y} q_x(l,m)(C_{Ij}^{q_x}(x-l,y-m,z,\nu_2)) \qquad (2.21)$$

$$+ \sum_{l=1}^{N_x} \sum_{m=1}^{N_y} q_y(l,m)(C_{Ij}^{q_y}(x-l,y-m,z,\nu_2)) \qquad (2.22)$$

2.1.3 Discrete Convolution Fast Fourier Transfrom (DC-FFT)

Surface displacements and subsurface stresses are calculated using influence coefficients (corresponding to the Green functions in their discretized form) and expressed as discrete convolution products between influence coefficients and the perturbation. These convolution products are then computed by switching to the frequency domain using the Fast Fourier Transforms (FFT) where it becomes a simple matrix multiplication. This method was proposed by Ju and Farris [JU 96] and allow to compute a double summation in only $O(N+3N\log N)$ operations instead of $O(N^2)$ for a computation zone size of N points. It should be noted that for contact problem, functions are not periodic and a numerical error is appearing. A numerical method called DC-FFT (Discrete Convolution and Fast Fourier Transform) need to be used to avoid the numerical error. This method is using the 'zero-padding' and the 'wrap-around order' techniques (recalled in Appendix D).

The DC-FFT Method
The technique of zero padding and wrap-around order are the necessary treatments for properly converting the linear convolution into the cyclic convolution. The DC-FFT (Discrete Convolution and Fast Fourier Transform) method presented by Liu [LIU 00] is recalled here

1. Find the influence coefficients, $\{K_j\}_N$;

2. Expand $\{K_j\}_N$ into $\{K_j\}_{2N}$ with wrap-around order;

3. Apply FFT to $\{K_j\}_{2N}$ and obtain $\{\hat{K}_s\}_{2N}$;

4. Input the pressure, $\{p_j\}_N$;

5. Expand the pressure with zero padding, $p_j = p_j$, $j \in [0, N-1]$, $\quad p_j = 0$, $j \in [N, 2N-1]$;

6. Apply FFT to obtain $\{\hat{p}_s\}_{2N}$;

7. Make the element-by-element product of the complex numbers, and obtain the frequency response, $\{\hat{u}_s\}_{2N}$;

8. Apply the IFFT to obtain $\{u_j\}_{2N}$;

9. Discard the spoiled terms and keep $\{u_j\}_{2N}$, $j \in [0, N-1]$.

The DC-FFT method can be extended to 2D and 3D by repeating the Fourier transform for each direction. The 2D DC-FFT is used for surface source like:

$$u_z(i,j) = \sum_{k=1}^{N_x} \sum_{l=1}^{N_y} K_z^p(i-k, j-l) \, p(k,l) \tag{2.23}$$

The 3D-DC-FFT method consists in applying the DC-FFT along the three directions x, y and z. It is commonly used for volume source and volume image calculations.

2.1.4 Contact solver algorithm

2.1.4.1 Weak formulation and constrained optimization

The unique solution of the contact problem can be found by minimizing the strain energy (or complementary energy) of the problem and considering that one body can not interpenetrate the other one. The contact pressures p are positive and the contact shears q are bounded by the Coulomb's law. The strain energy is divided in two part corresponding to the normal and tangential loading:

$$\min\left(\frac{1}{2}\mathbf{p}^T \mathbf{A}_z^p \mathbf{p} + \mathbf{h}^{*T}\mathbf{p} + c_\tau - \sum \lambda_{ij} p_{ij}\right) \Leftrightarrow \mathbf{A}_z^p \mathbf{p} + \mathbf{h}^{*T} - \lambda = 0, \tag{2.24a}$$

$$p_{ij} > 0, \quad \lambda_{ij} = 0, \tag{2.24b}$$

$$p_{ij} = 0, \quad \lambda_{ij} \geq 0. \tag{2.24c}$$

where h^* is the distance between undeformed geometries including the initial separation and the rigid body displacements.

$$\min \left(\frac{1}{2} \mathbf{q}^T \mathbf{A}_\tau^q \mathbf{q} + \mathbf{W}^{*T} \mathbf{q} + c_p + \sum \lambda_{ij} \left(\frac{q_{x\,ij}^2 + q_{y\,ij}^2}{2\mu p_{x\,ij}} - \frac{\mu p_{x\,ij}}{2} \right) \right) \tag{2.25a}$$

$$\Leftrightarrow \mathbf{A}_\tau^q \mathbf{q} + \mathbf{W}^* + \begin{pmatrix} \vdots \\ \lambda_{ij} \frac{q_{xij}}{\mu p_{ij}} \\ \vdots \\ \lambda_{ij} \frac{q_{yij}}{\mu p_{ij}} \\ \vdots \end{pmatrix} = 0, \tag{2.25b}$$

$$\left|\left| \mathbf{q}_{ij} \right|\right| < \mu p_{ij}, \quad \lambda_{ij} = 0, \tag{2.25c}$$

$$\left|\left| \mathbf{q}_{ij} \right|\right| = \mu p_{ij}, \quad \lambda_{ij} \geq 0. \tag{2.25d}$$

with $\mathbf{W}^*$ the tangential displacement tensor induced by rigid body displacements.

In the normal problem, the constraint is linear and λ_{ij} is the gap g_{ij} between two surfaces. For the tangential contact problem λ_{ij} is the slip amplitude. Solving this kind of equation correspond to a constrained optimization problem and a conjugate gradient algorithm is used [POL 99]. Furthermore, DC-FFT techniques are used to reduce the computation cost of the method.

2.1.4.2 Conjugate Gradient Algorithms (CGM)

The conjugate gradient algorithm is an iterative method which generates a sequence of approximations of the solution starting from an arbitrary initial approximation. This method was initially proposed by Hestenes and Stiefel [HES 52, HES 80] and based on Lanczos method and Krylov subspaces to find orthogonal residuals. The minimization problem can be expressed like a linear system of equation where A is a positive defined symmetric square matrix:

$$Ax = b \tag{2.26}$$

Algorithm
Choose an initial value of x_0;
Initialization of the variables: $r_0 \leftarrow Ax_0$, $p_0 \leftarrow -r_0$, $k \leftarrow 0$;

while $r_k \neq 0$

$$\alpha_k \quad \leftarrow \quad \frac{r_k^T r_k}{p_k^T A p_k}; \tag{2.27}$$

$$x_{k+1} \quad \leftarrow \quad x_{k+1} + \alpha_k p_k; \tag{2.28}$$

$$r_{k+1} \quad \leftarrow \quad r_{k+1} + \alpha_k A p_k; \tag{2.29}$$

$$\beta_{k+1} \quad \leftarrow \quad \frac{r_{k+1}^T r_{k+1}}{r_k^T r_k}; \tag{2.30}$$

$$p_{k+1} \quad \leftarrow \quad -r_{k+1} + \beta_{k+1} p_k; \tag{2.31}$$

$$k \quad \leftarrow \quad k+1; \tag{2.32}$$

end while

Because only the last iteration of the variable p_{k-1} is needed to compute p_k, this method is known to be very fast at solving big linear system without using a lot of memory. One of the limitation of the algorithm is the convergence issue if A is not a positive defined and symmetric matrix.

2.1.5   General algorithm of the contact solver

A general flowchart of the semi-analytical contact solver with a coupling between normal and tangential contact is presented in Fig. 2.4.
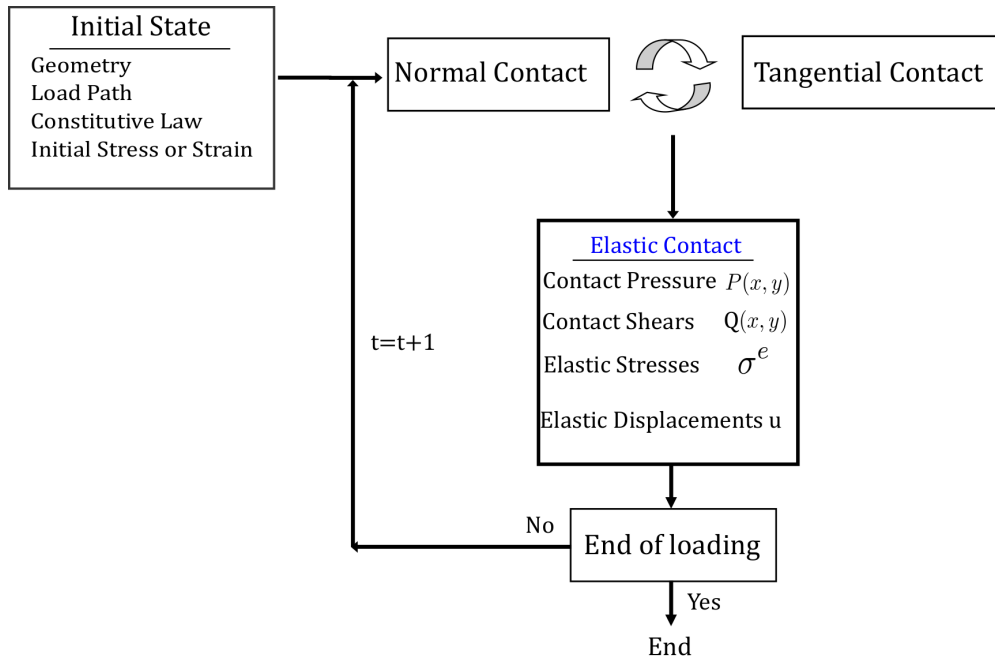

Figure 2.4: Flow Chart of fully coupled semi-analytical elastic contact solver

2.2 Theoretical background of the heterogeneity contribution

2.2.1 Heterogeneity in an infinite solid

A finite subdomain having different elastic properties than the surrounding matrix is called an inhomogeneity (or heterogeneous inclusion). Applied stresses will be disturbed by the existence of the inhomogeneity in the solid. Eshelby [ESH 61] proved that the disturbed stress field can be simulated by considering a fictious eigenstrain inside the domain of the inhomogeneity considering the solid as homogeneous. Eigenstrain is a name given to nonelastic strains (thermal expansion, plastic strains, misfit strains) and traducing the incompatibility between the heterogeneity and the surrounding matrix. The equivalence between an heterogeneous inclusion problem and an homogeneous inclusion problem plus an eigenstrain ε^* is called Eshelby's equivalent inclusion method. When an external load is applied, the disturbance in the stress field caused by the presence of the heterogeneity is called eigenstress σ^*. To determine the eigenstrain, a process to transform a single heterogeneity into an inclusion has been defined by Eshelby and is showed in Fig. 2.5.
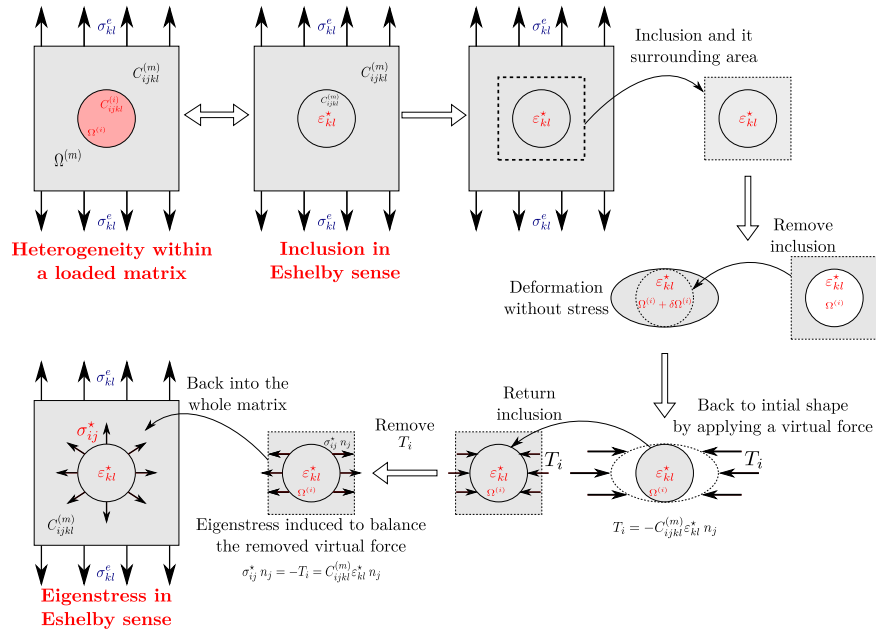
Figure 2.5: Single heterogeneity transformation into inclusion in the sense of Eshelby and subsequent eigenstress

2.2.1.1 Eshelby's equivalent inclusion method

An infinite matrix M with the elastic stiffness tensor C^M_{ijkl} containing an ellipsoidal domain Ω with the elastic stiffness tensor C^I_{ijkl} is submitted at infinity to a uniform strain ε^0. The strain field is disturbed by the presence of the inhomogeneity.

In the case of linear isotropic elasticity, the relationship between the elastic strain ε_{kl} and the elastic stress σ_{ij} is expressed by the Hooke's law:

$$\sigma_{ij} = C_{ijkl}^I \left(\varepsilon_{kl}^0 + \varepsilon_{kl} \right) \ \text{in} \ \Omega^I$$

$$\sigma_{ij} = C_{ijkl}^M \left(\varepsilon_{kl}^0 + \varepsilon_{kl} \right) \ \text{in} \ \Omega^M$$

(2.33)

The Eshelby's equivalent inclusion method (EIM) consists in representing the ellipsoidal inhomogeneity as an inclusion having the same elastic properties C_{ijkl}^M as the matrix but being subjected to an additional imaginary strain called eigenstrain ε^* giving:

$$C_{ijkl}^I (\varepsilon_{kl}^0 + \varepsilon_{kl}) = C_{ijkl}^M (\varepsilon_{kl}^0 + \varepsilon_{kl} - \varepsilon_{kl}^*) \quad \text{in} \ \Omega \tag{2.34}$$

The necessary and sufficient condition for the equivalence of the stresses and strains in the two above problems of inhomogeneity and inclusion is provided by Eq. (2.34). In particular, the eigenstrain ε_{ij}^* is related to compatibility strain ε_{ij} by:

$$\varepsilon_{ij} = S_{ijkl} \times \varepsilon_{kl}^*, \tag{2.35}$$

where S_{ijkl} is the Eshelby's tensor.

Substitution of Eq. (2.35) into Eq. (2.34) leads to:

$$\Delta C_{ijkl} S_{klmn} \varepsilon_{mn}^* + C_{ijkl}^M \varepsilon_{kl}^* = -\Delta C_{ijkl} \varepsilon_{kl}^0 \tag{2.36}$$

where

$$\Delta C_{ijkl} = C_{ijkl}^I - C_{ijkl}^M$$

Eshelby's tensor and influence coefficients are analytically known for some particular geometries (ellipsoids [ESH 57] and cuboids [MAC 58, CHI 78]) using harmonic potential function recalled in Appendix A.

Eshelby's method considers only a uniform applied strain but in contact problem, strains are not uniform. Moschovidis and Mura [MOS 75] extended Eshelby's work for non homogeneous applied strain. If the applied strain has a polynomial form of degree n, the corresponding eigenstrain has also a polynomial form of degree n.

In all this thesis a strong hypothesis is made that the eigenstrain is constant inside the inclusion. This simplification only hold if the applied field around the heterogeneity is also constant. It means that the inclusion should be small enough compared to the radius of contact a^*. To take into account possible gradient of eigenstrain inside the inclusion, eigenstrain development to first and second order polynomials have been proposed by Leroux [LER 13] but are greatly increasing the computation cost of the method without improving significantly the quality of the solution. An other technique consists in representing the inclusion as a cluster of multiple cuboid with the same size as the computation discretization and with each heterogeneous cuboids having a constant eigenstrain. This technique allow to represent complex geometries of heterogeneity through a voxelization technique (see chapter 6).

## 2.2.2 Heterogeneity in a half-space

2.2.2.1 Decomposition method

Three dimensional contact problems involve a half-space that is bounded by the surface plane $z = 0$ in the cartesian coordinate system (x, y, z) as shown in Fig. 2.2. Jacq et al. [JAC 02] and later Zhou et al. [ZHO 09] proposed a method allowing to extend previous solution, valid only for infinite spaces, to half spaces. The solution for an isotropic half space consists in decomposing the problem into three subproblems (Fig. 2.6), known as Chiu's decomposition [CHI 78].

(1) An inclusion with the prescribed eigenstrain $\varepsilon^* = (\varepsilon_{xx}^*; \varepsilon_{yy}^*; \varepsilon_{zz}^*; \varepsilon_{xy}^*; \varepsilon_{xz}^*; \varepsilon_{yz}^*)$ in an infinite space.

(2) A symmetric inclusion with a mirror eigenstrain $\varepsilon_s^* = (\varepsilon_{xx}^*; \varepsilon_{yy}^*; \varepsilon_{zz}^*; \varepsilon_{xy}^*; -\varepsilon_{xz}^*; -\varepsilon_{yz}^*)$ in the same space.

(3) A normal traction distribution $-\sigma^n$ at the surface of the half space ($z = 0$) which is a function of the eigenstrains ε^* and ε_s^*.
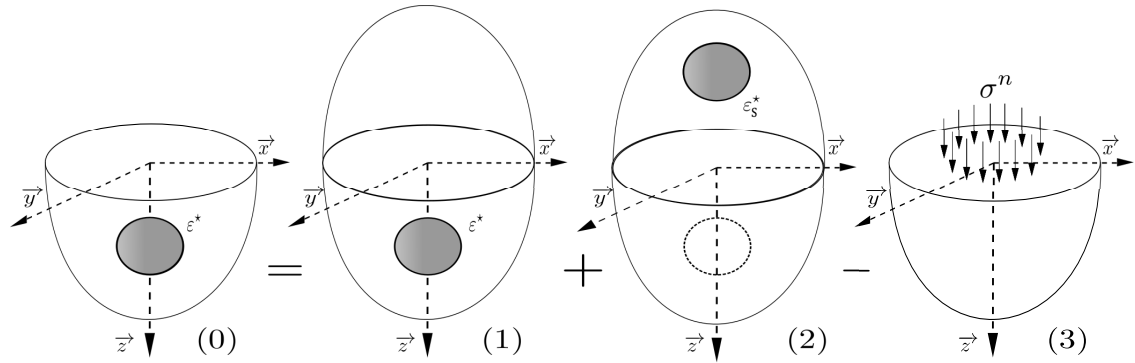
Figure 2.6: Decomposition of the half-space solution into three sub-problems

The summation of the two solutions (1) and (2) leaves the plane of symmetry ($z = 0$) free of shear tractions. By adding an opposite normal stress σ^n, the condition of free surface traction is obtained.

A new method of decomposition was proposed by Zhou et al. [ZHO 14] to avoid the use of the mirror eigenstrain and save computation time.

2.2.2.2 Determination of the eigenstress and surface eigen-displacement

The stress at any point of the domain meshed with $n_x \times n_y \times n_z$ cuboids is given by:

$$\sigma_{ij}(x,y,z) = \sum_{x^I=0}^{n_x-1}\sum_{y^I=0}^{n_y-1}\sum_{z^I=0}^{n_z-1} B_{ijkl}(x-x^I,y-y^I,z-z^I)\varepsilon_{kl}^*(x^I,y^I,z^I)$$

$$+ \sum_{z^I=0}^{n_z-1}\sum_{y^I=0}^{n_y-1}\sum_{x^I=0}^{n_x-1} B_{ijkl}(x-x^I,y-y^I,z+z^I)\varepsilon_{skl}^*(x^I,y^I,-z^I) \qquad (2.37)$$

$$- \sum_{y^I=0}^{n_y-1}\sum_{x^I=0}^{n_x-1} M_{ij}(x-x^I,y-y^I,z)\sigma^n(x^I,y^I,0)$$

where B_{ijkl} are the influence coefficients that relate the constant eigenstrain at the point (x^I,y^I,z^I) which is the inclusion center in an infinite space to the stress σ_{ij} at the point (x,y,z). M_{ij} represent the influence coefficients relating the normal traction σ^n within a discretized area centered at $(x^I,y^I,0)$ to the stress σ_{ij} at the point (x,y,z).

$$B_{ijkl}(x) = C_{ijmn}^M D_{mnkl}(x) \quad \text{for } x \text{ in } D-\Omega \qquad (2.38)$$

$$B_{ijkl}(x) = C_{ijmn}^M(D_{mnkl}(x) - I_{mnkl}) \quad \text{for } x \text{ in } \Omega \qquad (2.39)$$

where $I_{ijkl} = \frac{1}{2}(\delta_{il}\delta jk + \delta_{ik}\delta jl)$ is the fourth-order identity tensor.

The expression for D_{ijkl} is given in Mura [MUR 87] and recalled for simple geometries in Appendix B.

$$D_{ijkl} = \frac{1}{8\pi(1-\nu)}[\Psi_{,ijkl} - 2\nu\delta_{kl}\phi_{,ij} - (1-\nu)(\delta_{kl}\phi_{il} + \delta_{ki}\phi_{,jl} + \delta_{jl}\phi_{,ik} + \delta_{li}\phi_{,jk})] \quad (2.40)$$

For a single inclusion centered at (x^I,y^I,z^I) in the half-space, the normal traction σ^n at the surface point $(x^,y^,0)$ is obtained as:

$$\sigma^n(x',y',0) = - B_{33kl}(x'-x^I,y'-y^I,-z^I,)\varepsilon_{kl}^*(x^I,y^I,z^I)$$
$$- B_{33kl}(x'-x^I,y'-y^I,z^I,)\varepsilon_{skl}^*(x^I,y^I,-z^I) \qquad (2.41)$$

In Eq. (2.37), each component $M_{ij}()$ is obtained by a double integration of the function $F_{ij}()$ over a discretized surface area $2\Delta x \times 2\Delta y$ centered at $(x^I,y^I,0)$, see appendices A and B.

$$M_{ij}(x-x^I,y-y^I,z) = \int_{x^I-\Delta x}^{x^I+\Delta x}\int_{y^I-\Delta y}^{y^I+\Delta y} F_{ij}(x-x',y-y',z)dx'y' \qquad (2.42)$$

The 3D-FFT is used to accelerate the calculation of the first (1) and second terms (2) and the 2D-FFT for the third term (3).

The surface normal 'eigen-displacements' can be obtained when inserting the eigenstrain into the total strain. They are generated by the pressure field σ^n only. The normal displacements are calculated as:

$$u_z^*(x,y) = \sum_{y'=0}^{n_y-1} \sum_{x'=0}^{n_x-1} K^n(x-x',y-y')\sigma^n(x',y') \qquad (2.43)$$

To solve the equation above numerically, the surface in contact is discretized into $n_x \times n_y$ rectangular elements of uniform size $2\Delta x \times 2\Delta y$. Then, pressure and displacement within each discrete patch are treated as constant and their values located at the center. The effect of a uniform pressure on a rectangular area has been given by Love [LOV 52] and Johnson [JOH 85]. K^n denotes the influence coefficients that relate the normal pressure at the surface point $(x',y',0)$ to the normal displacement at the surface point $(x,y,0)$, recalled in Appendix A.

2.2.2.3 Algorithm for heterogeneous contributions in contact solution

The presence of a heterogeneity within one of the bodies in contact is taken into account by adding in Eq. 2.44 the eigen-displacement u_z^* induced by the eigenstresses. Equation 2.2 is then modified as follows:

$$h(x,y) = h_i(x,y) - \delta + u_z(x,y) + u_z^*(x,y) \qquad (2.44)$$

The contact loading stress field inside the material is used as an input load for the computation of the eigenstrain using Eshelby's equivalent inclusion method. The eigenstress generated by the heterogeneity are added to the stress field from the contact loading. The contact surface geometry is updated by adding the eigen-displacements in Eq. 2.44. The modified geometry is used to solve the contact problem and the procedure is repeated until convergence of both the problem as in Fig. 2.7. The heterogeneous problem and the contact problem are fully coupled and has been validated using the Finite Element Method [KOU 14a]. Comparison between a finite element model on Abaqus v6.11 and the semi-analytical method have been realized on the same computer. With a very good agreement between the results in both simulations, Koumi found the semi-analytical solver to be eight times faster than the finite element model. The semi-analytical simulation is computed on a grid of 10^6 computation points while the finite element model has 1.5×10^6 ddls and is fully described in [KOU 14b].
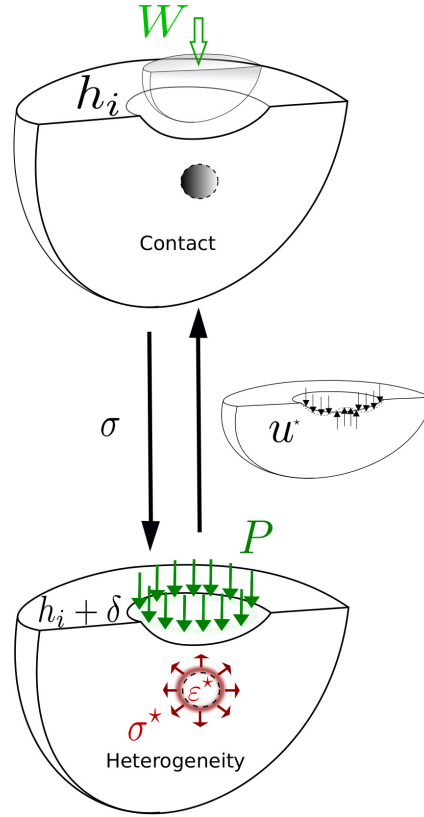
**Figure 2.7:** Iteration between contact problem and heterogeneous problem

2.2.2.4 Mutual influence between close inclusions

Moschovidis and Mura [MOS 75] extended Eshelby's solution to two close ellipsoidal inhomogeneities. In recent work, multiple inclusion problems have been solved by using a conjugate gradient algorithm to determine each unknown eigenstrain [ZHO 11a, ZHO 11b, LER 10].

Let's consider a solid with n heterogeneities Ω_ψ ($\psi = 1, 2, ..., n$) and discretized into $n_x \times n_y \times n_z$ computation points. Each heterogeneity, centered on a point $\left(x^\alpha, y^\beta, z^\gamma\right)$, has an elastic tensor $C^I_{\alpha,\beta,\gamma}$. The Eshelby's equivalent inclusion (Eq. 2.35) for each heterogeneity is recalled:

$$(C^I_{\alpha,\beta,\gamma} C^{M^{-1}} - I^d)\sigma^*_{\alpha,\beta,\gamma} + C^I_{\alpha,\beta,\gamma}\varepsilon^*_{\alpha,\beta,\gamma} = (I^d - C^I_{\alpha,\beta,\gamma} C^{M^{-1}})(\varepsilon^0_{\alpha,\beta,\gamma}),$$
$$With\,(0 \leq \alpha \leq n_x - 1, 0 \leq \beta \leq n_y - 1, 0 \leq \gamma \leq n_z - 1) \qquad (2.45)$$

The eigenstrain is supposed uniform inside each heterogeneity. The stress field $\sigma_{\alpha,\beta,\gamma}$ at the point $[\alpha, \beta, \gamma]$ is influenced by the contribution of the eigenstrains of each heterogeneity inside the domain.
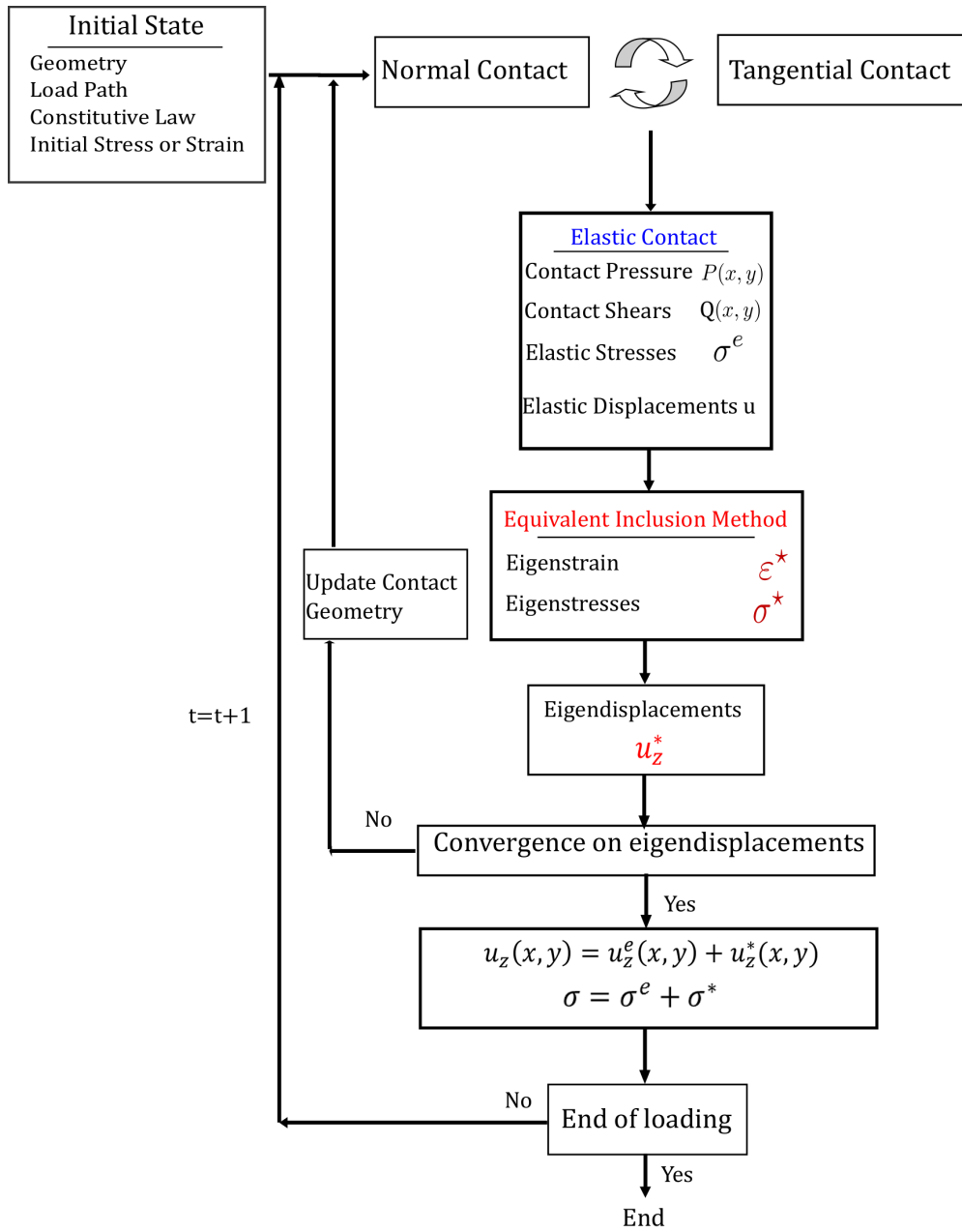
Figure 2.8: Flow chart of fully coupled semi-analytical heterogeneous elastic contact solver

$$\sigma^*_{\alpha,\beta,\gamma} = \sum_{\varphi=0}^{n_z-1} \sum_{\zeta=0}^{n_y-1} \sum_{\xi=0}^{n_x-1} B_{\alpha-\xi,\beta-\zeta,\gamma-\varphi} \varepsilon^*_{\xi,\zeta,\varphi}$$
$$(0 \leq \alpha \leq n_x - 1, 0 \leq \beta \leq n_y - 1, 0 \leq \gamma \leq n_z - 1) \tag{2.46}$$

with $B_{\alpha-\xi,\beta-\zeta,\gamma-\varphi}$ the influence coefficients, function of the elastic properties and of the geometric shape of the considered heterogeneity. They depend on the relative distance between the heterogeneities $\left(x^\alpha, y^\beta, z^\gamma\right)$ and $\left(x^\xi, y^\zeta, z^\varphi\right)$. Eigenstresses are computed for every point inside the domain both inside and outside the heterogeneities.

Equations 2.36 and 2.46 give the relationship between stress and eigenstrain to solve the modified equivalent equation 2.45:

$$\left(C^I_{\alpha,\beta,\gamma} C^{M^{-1}} - I^d\right) \sum_{\varphi=0}^{n_z-1} \sum_{\zeta=0}^{n_y-1} \sum_{\xi=0}^{n_x-1} B_{\alpha-\xi,\beta-\zeta,\gamma-\varphi} \varepsilon^*_{\xi,\zeta,\varphi} + C^I_{\alpha,\beta,\gamma} \varepsilon^*_{\alpha,\beta,\gamma}$$
$$= \left(I^d - C^I_{\alpha,\beta,\gamma} C^{M^{-1}}\right) \varepsilon^0_{\alpha,\beta,\gamma},$$
$$(0 \leq \alpha \leq n_x - 1, 0 \leq \beta \leq n_y - 1, 0 \leq \gamma \leq n_z - 1) \tag{2.47}$$

The equation 2.47 is the general equation to solve the multiple heterogeneity problem. With n heterogeneities, $6n$ equations need to be solved. The system can be see like a linear system to solve:

$$A\varepsilon^* = b \tag{2.48}$$

A conjugate gradient algorithm is used to numerically solve the equation system. The adapted CGM algorithm proposed by Zhou [ZHO 11a] and Leroux [LER 13] is working with defined positive symmetric matrix. In some cases, like the presence of surface traction, the matrix is no longer symmetric and other algorithms have been proposed by Koumi [KOU 15b]: Bi-Conjugate Gradient Stabilized Algorithm (BiCGSTAB) and Orthodir based on the work of Van der Vorst [VOR 92]. They are able to solve non symmetric linear systems and are based on the bi-orthogonalization of Lanczos to solve simultaneously two systems of equations associated with the matrix A and with the transposed matrix A^T. As a consequence, the need in memory is much more important than for the classical CGM.

The proposed method allow to numerically find the eigenstrain of each heterogeneity in the solid. They are used to determine the eigen-displacements u^*_3 at the contact surface and to take into account the presence of heterogeneities in the contact algorithm.

2.3   Partial Conclusion

This chapter presented the semi-analytical method for a contact on a heterogeneous material. The contact problem is solved by summing analytical solutions of simple problems. Solution of the contact problem is used as a loading input to solve the heterogeneous material model based on Eshelby's equivalent inclusion method. Presence of heterogeneity close to the surface is influencing the contact solution. A good agreement has been found with a finite element model by Koumi [KOU 14b] and influence between multiple heterogeneities is taken into account by numerical algorithm like the Conjugate Gradient Method. The next chapter will use the semi-analytical method to model damage phenomena in contact loading by coupling a continuum damage mechanics based model with the heterogeneous contact solver.

Chapter 3

Damage model for fretting

In this chapter, a damage model is proposed to simulate the mechanisms appearing under fretting loading in both gross slip and partial slip regime using semi-analytical method. Application to coated materials is also presented. The proposed damage model is compared to a damage model from the literature using a jump-in-cycle algorithm. Finally, a comparison between the damage law and a wear law based on the dissipated energy is introduced.

Contents

3.1 Continuum Damage Mechanics

3.1.1 History and Background

Continuum Damage Mechanics (CDM) background permits to describe the initiation and evolution of degradation in materials at the microscale such as micro cracks and voids. The damage model used in the current approach is isotropic and based on a single scalar damage variable D introduced by Kachanov [KAC 58]). Considering no healing of the material, D is monotonically increasing from $D = 0$, the undamaged state, to $D = 1$ the complete local rupture of the material.

The state of stress in the damaged material can be described by the effective stress introduced by Rabotnov [RAB 69]:

$$\tilde{\sigma} = \frac{\sigma}{(1-D)} \tag{3.1}$$

Following Lemaitre [LEM 85] strain equivalence hypothesis, the strain behavior is modified by damage only through the effective stress. Hence, the strain associated with a damaged state under the applied stress is equivalent to the strain associated with its undamaged state under the effective stress. Applying the Hooke's law with E, the modulus of elasticity for the undamaged material, the elastic strain in the damaged material becomes:

$$\varepsilon = \frac{\tilde{\sigma}}{E} = \frac{\sigma}{(1-D)E} \tag{3.2}$$

From this equation it can be deduced that an increase in the damage manifests as the reduction in the modulus of elasticity as shown in Fig. 3.1. D characterizes the effect of microscopic phenomenon on the macroscopic behavior of the material as a strength loss. These usually reproduce the presence of micro-cracks within an elastic material. The constitutive equation can be expressed as:

$$\sigma = (1-D)E\varepsilon \tag{3.3}$$

3.1.2 Thermodynamics of damage

In order to verify that the proposed model is in accordance with the law of thermodynamics, one should recall the Clausius-Duhem inequality. The model will consider only elastic strain and a constant temperature during the process. The chosen state variables correspond to the physical mechanisms of deformation and degradation of the material (see Table 3.1.2).

Mechanisms	Observable state variables	Internal state variables	Associated variable
Elasticity	ε		σ
Entropy	T		s
Damage		D	$-Y$

With Y the thermodynamics variable associated with the damage variable. The Helmholtz specific free energy of the system is a function of all the variables:

$$\Psi = \Psi(\varepsilon, D, T) \tag{3.4}$$

When considering no plasticity and no thermal effect, the potential is considered as the Gibbs specific free enthalpy:

$$\Psi^* = \sup_{\varepsilon^e} \left[\frac{1}{\rho} \sigma_{ij} \varepsilon_{ij} - \Psi \right] \tag{3.5}$$

where ρ is the density. Lemaitre [LEM 72] showed that the strain constitutive equation for a damaged material are equivalent that for a undamaged material by replacing the stress by the effective stress.

$$\sigma_{ij} = \rho \frac{\partial \Psi}{\partial \varepsilon_{ij}} = E_{ijkl} \varepsilon_{kl} (1 - D) \tag{3.6}$$

$$Y = \rho \frac{\partial \Psi}{\partial D} = -\frac{1}{2} E_{ijkl} \varepsilon_{ij} \varepsilon_{kl} \tag{3.7}$$

Then, the Clausius-Duhem inequality can be expressed as:

$$-Y.\dot{D} \geq 0 \tag{3.8}$$

with Y a quadratic positive form. This condition should be satisfied by the evolution law for the internal variables for the constitutive model to be thermodynamically admissible.

$$\frac{1}{2} E_{ijkl} \varepsilon_{ij} \varepsilon_{kl}.\dot{D} \geq 0 \quad \rightarrow \quad \dot{D} \geq 0 \tag{3.9}$$

Finally, damage being a dissipative phenomenon, the damage evolution law must be defined accordingly with the fact that damage is always increasing in order to respect the Clausius-Duhem inequality.

3.1.3 Elasticity coupled with CDM

In order to model the damage of concretes, predominant in tension, Mazars [MAZ 89] used the scalar damage parameter D coupled with elasticity in his 3D model. He choosed D as a function of the positive (tensile) strains and to evaluate these strains, he defined the following scalar called equivalent strain:

$$\tilde{\varepsilon} = \sqrt{\sum_{i=1,3} \langle \varepsilon_i \rangle_+^2} \tag{3.10}$$

with

$$\langle \varepsilon_i \rangle_+ = \left(\frac{\varepsilon_i + |\varepsilon_i|}{2} \right) \tag{3.11}$$

and ε_i the principal strains. However, to study the damage of contact under fretting, D needs to take into account tensile, compressive and shear stresses.

An adaptation of the expression of Mazars's equivalent strain is proposed here :

$$\tilde{\varepsilon} = \sqrt{\sum_{i=1,3} \langle \varepsilon_i \rangle_+^2 + \sum_{i=1,3} \langle \varepsilon_i \rangle_-^2} = \sqrt{\sum_{i=1,3} \varepsilon_i^2} \tag{3.12}$$

with

$$\langle \varepsilon_i \rangle_- = \begin{cases} |\varepsilon_i| & if \quad \varepsilon_i \leq 0 \\ 0 & if \quad \varepsilon_i > 0 \end{cases} \tag{3.13}$$

The equivalent strain is now traducing the local three-dimensional state of strain of the solid via a uniaxial scalar variable.

The equivalent strain controls the growth of the damage variable according to an evolving threshold. At the end of every time step and for every point of the discretization of the half-space, the loading function can be defined as :

$$f(\varepsilon, D) = \tilde{\varepsilon} - K(D) \tag{3.14}$$

$K(D)$ takes the largest value of the equivalent strain $\tilde{\varepsilon}$ ever reached by the material during the loading history at the considered point. $K(D = 0)$ is initialized at ε_{d0}, the damage threshold strain, corresponding to the strain at the elastic limit.

$$\begin{cases} K(D) = \varepsilon_{d0} & if \quad D = 0 \\ K(D) = \max_t \tilde{\varepsilon} & if \quad D \geq 0 \end{cases} \tag{3.15}$$

If the threshold is reached, a new increment of damage called δD is added to the damage variable at the considered point. The evolution law for the damage variable is defined as:

$$\begin{cases} \delta D = \dfrac{\tilde{\varepsilon} - K(D)}{\varepsilon_R - \varepsilon_{d0}} & if \quad \tilde{\varepsilon} \geq K(D) \\ \\ \delta D = 0 & if \quad \tilde{\varepsilon} < K(D) \end{cases} \quad \rightarrow D = D + \delta D \tag{3.16}$$

with ε_R the strain leading to a macroscopic crack.
The behavior of the material is linear elastic on the first part of Fig. 3.1. When the equivalent strain reaches the damage threshold, the local elastic properties of the matrix are modified through the presence of micro-cracks which decreases the strength of the material. This local decrease of the modulus of elasticity is irreversible. From ε_{d0}, the damage threshold strain, the damage variable will modified the elastic behavior of the material by decreasing the Young's modulus as illustrated in Fig. 3.1 and until the material strain reaches the macroscopic fracture strain ε_R (see Fig. 3.2(b)).The damage evolution is always increasing and locally linear by pieces (Fig. 3.2(a)).
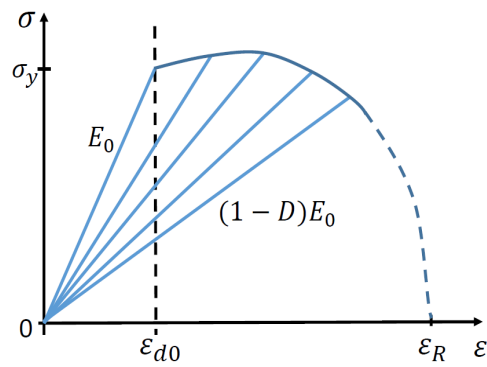
Figure 3.1: Stress-Strain plot with damage evolution.
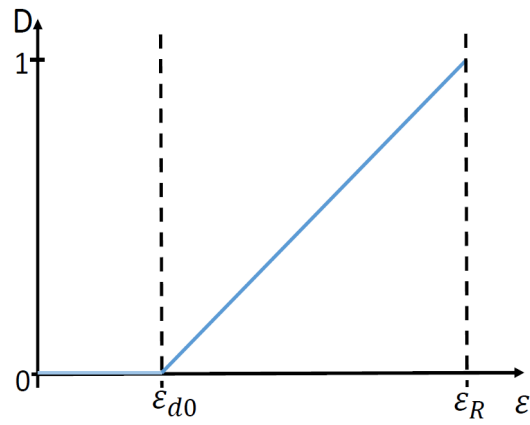
(a)
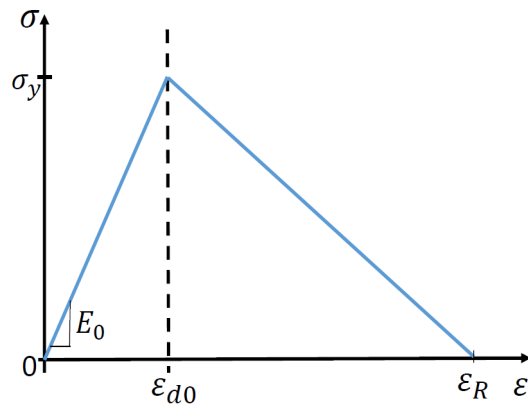
(b)

Figure 3.2: (a) Damage evolution as a function of strain showing the purely elastic domain and the damageable domain. (b) Purely elastic and damageable domains on a stress strain plot.

It should be noted that if the damage threshold is not evolving at each step by replacing ε_{d0} into $max_{\forall t}\left(\tilde{\varepsilon}\left(x,y,z\right)\right)$ in the damage increment computation then every time the equivalent strain $\tilde{\varepsilon}$ is exceeding the threshold the damage increment would correspond to the increment for a pristine material and not for an already equivalent damaged material. Damage evolution would be overvalued.

Moreover, hypothesis is made in the damage evolution law that the evolution of D is linear by pieces. It should be noted that if every computed damage increments are summed then the critical value of the damage variable called D_c must be equal to 1:

$$D_c = \sum_{i=0}^{i=N} \delta D_i = \sum_{i=0}^{i=N} \frac{\tilde{\varepsilon}_{i+1} - \tilde{\varepsilon}_i}{\varepsilon_R - \varepsilon_{d0}} = \frac{\varepsilon_R - \tilde{\varepsilon}_i + \tilde{\varepsilon}_i - \tilde{\varepsilon}_{i-1} + \ldots + \tilde{\varepsilon}_1 - \varepsilon_{d0}}{\varepsilon_R - \varepsilon_{d0}} = 1 \qquad (3.17)$$

3.1.4 Behavior of a representative volume element

The constitutive law is illustrated on a strain-stress curve for a cube in uni-axial tension and compression in Fig. 3.3. The curve is showing a linear elastic behavior curve for strain under the threshold ε_{d0} and becomes non-linear after damage occurs. The material behavior is symmetric in tension and in compression because no conditions on micro-defects closure is introduced [LEM 05].

(a)   (b)
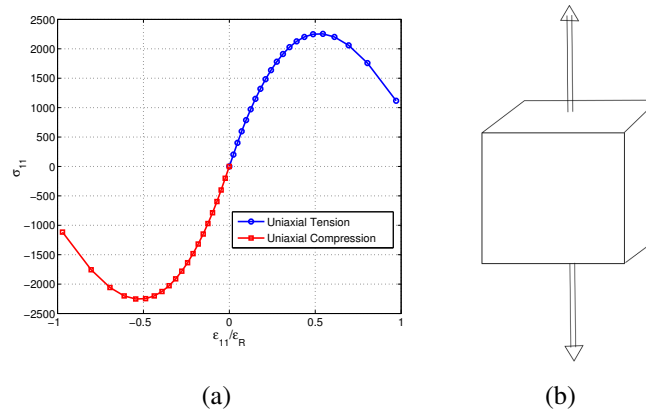
Figure 3.3: Stress-Strain plot with damage evolution for a cube in uni-axial tension and compression.

3.2 Implementation in the semi-analytical method

3.2.1 General algorithm of the coupled damage contact solver

The damage model defined in 3.1.3 is coupled with the semi-analytical contact solver developed by Nelias and co-workers [GAL 10, LER 10]. This method is based on the solution developed by Love [LOV 52] for a rectangular patch of pressure over a homogeneous half space. The Eshelby's equivalent inclusion method is used as an enrichment
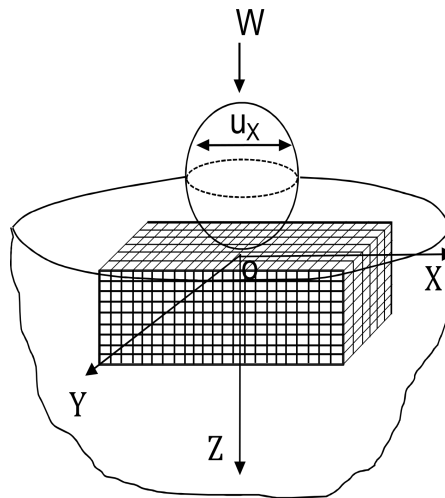
Figure 3.4: 3D view of a sphere on a elastic half-space with multiple cuboidal inclusions superimposition

technique in order to introduce a local modification of the Young's modulus of the material. Multiple cuboidal inclusions with the same size as the discretization of the half-space and initially with the same elastic properties are superimposed on the half-space as presented in Fig. 3.4. The effect of damage on the material is traduced through the modification of the Young's modulus of the inclusions. This enrichment technique has already been validated for coated materials with cuboidal inclusions through comparison with both analytical solution and multigrid method in [KOU 15b].

Leroux et al. [LER 10] and Koumi et al. [KOU 14b] have shown that the contact pressure distribution may be significantly modified by the presence of inhomogeneities close to the surface, which subsequently affect the subsurface stress distribution. The Young's modulus of the inclusions are modified by the damage variable D and hence affect the contact pressure distribution through the contribution of eigenstrains. One of the main advantage of the method is to compute only the stress field in the area around the contact (at the surface but also in depth). It has been observed that damage usually happened just under the contact during fretting [BRY 88]. For sake of computational efficiency, the half-space has been enriched only in this area. Note that no damage occurs far from the contact. When the first element is reaching a damage value equal to 1, the simulation is stopped. It should be noted that in CDM, $D = 1$ means that the element is too damaged to ensure continuity which can lead to the initiation of crack. Depending of the area concerned and of the localization of the damage, it can be interpreted as wear or crack initiation.

One should note that because simulations are stopped when a first element damage value reaches 1, the present model is only simulating the phenomena leading to the first appearance of wear or crack. In order to continue the simulation once an inclusion damage value reaches 1, the contact surface should be modified by removing the considered element.
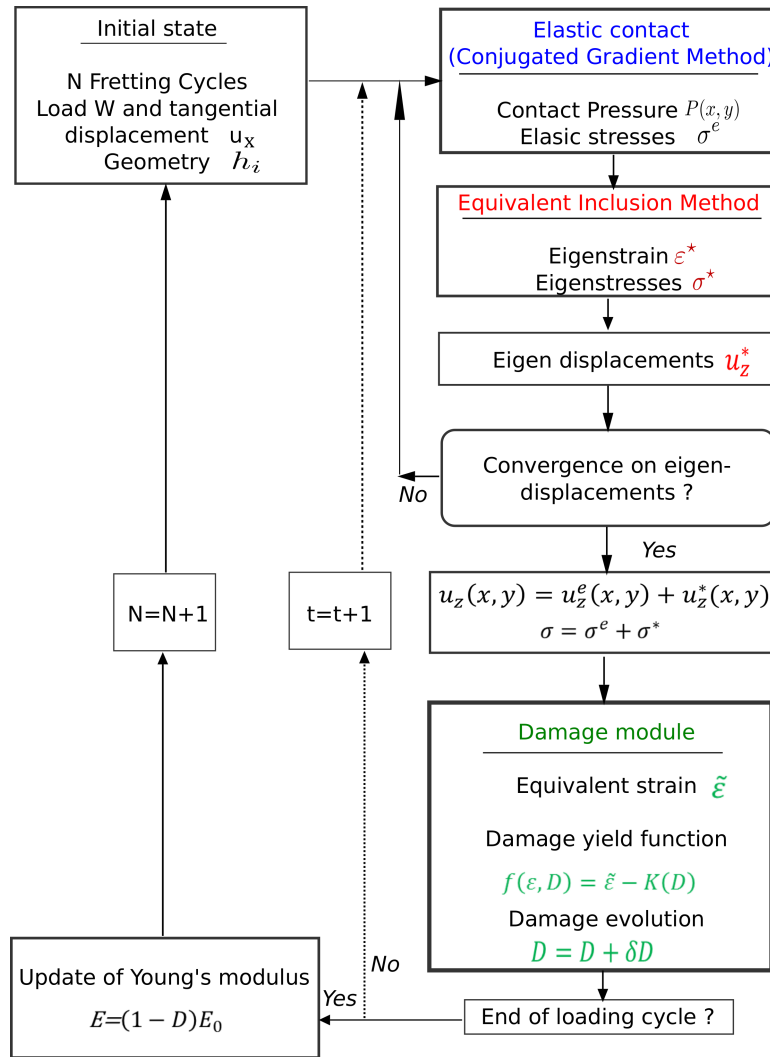
Figure 3.5: Algorithm of Heterogeneous Elastic-Damageable Contact Problem

The main step of the algorithm, summarized on the flowchart in Fig. 3.5 are described here:

1st **Fretting Cycle :**

- **Step1**:
  Enrichment with cuboidal inclusions with the same Young's modulus E_0 than the half-space.
  Solve the elastic contact problem for the initial loading increment, and determine the elastic stresses and strains in the solid.

- **Step2**: Damage module
  Compute the equivalent strains for the current loading increment.
  Test the damage criterion for each inclusion and determine the inclusion's damage

increments δD for the current time step.
Increment the loading and solve the elastic problem again.
Compute the equivalent strains and, after testing the damage criterion, determine the inclusion's damage increment δD.
Repeat until the last loading increment of the loading cycle.

- **Step3**: At end of the cycle:
  Update the corresponding Young's modulus with the damage variable computed during the loading cycle.

i^{th} **Fretting Cycle :**

- Assign to each inclusion the new Young's modulus.

- Repeat the previous steps for the considered loading cycle. Compute elastic stresses, equivalent strains and the damage increments δD for each time step of the cycle.

- At the end of the fretting cycle, if one-or more-of inclusions are totally damaged : stop the calculation.

The damage evolution is computed for each cycle and material's properties are modified at the end of each fretting cycle.

3.2.2   Simulation on a homogeneous solid

Validation of the enrichment technique

For validation purpose of the enrichment technique, a comparison with the analytical Hertzian solution is performed. Note that the heterogeneous semi-analytical method has been compared and validated in previous work with both analytical solutions [LER 10] and finite element simulation [KOU 14b]. A 3D rigid sphere in contact with a heterogeneous half-space has been simulated with the semi-analytical method. The half-space Young's modulus and Poisson's ratio are chosen as $E_0 = 210$ GPa and $\mu_0 = 0.3$, respectively. The normal applied load is $W = 410$ N. For the homogeneous half-space, this load leads to a contact radius $a^* = 0.32$ mm and a maximum contact pressure $P_0 = 1890.8$ MPa. The half-space is discretized in $67 \times 67 \times 51$ computation points such as the space between the constituted is $2\Delta x = 2\Delta y = 2\Delta z = 0.062a^*$. Then the half-space is filled from the free surface to a defined thickness with cuboidal inclusions centered on computation points and having the same dimensions as the discretization. The enrichment is constituted of $62 \times 62 \times 36$ cuboids as illustrated in Fig. 3.4.

A comparison between the analytical Hertzian contact solution and the contact solution founded with the enriched half-space is given for the pressure distribution, for the half space stresses along axis z and axis y at surface ($z = 0$) as shown in Fig. 3.6. A very good agreement is found which in turn validates the numerical enrichment technique.

Simulations with the semi-analytical solver with and without inclusions have been performed. Results show a computation time about 60 times higher with an enriched half-space than without any enrichment. Most of the computation cost is due to the computation of the inclusion stress field.

Description of the problem

In this section the contact simulation between a rigid sphere of radius $R = 25$ mm and a homogeneous half-space is presented. The contacting bodies are subjected to an oscillatory tangential motion. The two bodies are first brought into contact with a normal load $W = 410$ N. A tangential displacement along the x direction is then applied. The half-space Young's modulus and Poisson's ratio are chosen as $E_0 = 210$ GPa and $\mu_0 = 0.3$, respectively. For the homogeneous half-space, this load leads to a Hertzian contact radius $a^* = 0.32$ mm and a maximum contact pressure $P_0 = 1890.8$ MPa. The imposed rigid body displacement is cycling between $u_x = 0.025$ mm and $u_x = -0.025$ mm ($u_x/a^* = 0.078$) to reproduce an entire fretting loop. The fretting cycle is decomposed into multiple time steps as shown in Fig. 3.7.

The half-space has been enriched with damageable elastic cuboidal inclusions with the same properties than the half-space. The damage model, as presented in section 3.1.3 is used with two parameters : $\varepsilon_R = 0.036$ and $\varepsilon_{d0} = 0.003225$. Firstly, results in the case of the gross slip regime are presented, afterwards the partial slip regime is investigated and finally, simulation in the case of coated materials are presented.

3.2.2.1 Gross slip regime

Here are presented the results of contact simulations in gross slip regime. According to Coulomb's law, the shear distribution is equal to the coefficient of friction times the pressure along the contact surface : $Q = \mu \times P$.

For unlubricated contact, the coefficient of friction is generally high [FOU 04] and main phenomena are wear and cracks. That is why all simulations have been performed with a friction coefficient $\mu \geq 0.3$.

A first fretting simulation is presented with a coefficient of friction $\mu = 0.5$. In Fig. 3.8, the distribution of the equivalent strain $\tilde{\varepsilon}$ is shown for normal and tangential loading conditions for the undamaged material. It can be observed that the maximum value of $\tilde{\varepsilon}$ is reached at depth around $z/a^* = 0.5$ under the surface for a normal loading. This localization is the same than the maximum Von Mises stress for a circular Hertzian contact. When a tangential displacement is added, the maximum value of $\tilde{\varepsilon}$ is reached at the surface and is more than 50% higher than with normal load only. All damage simulations have been performed until at least one point reached the critical damage value $D = 1$.

(a)

(b)

(c)
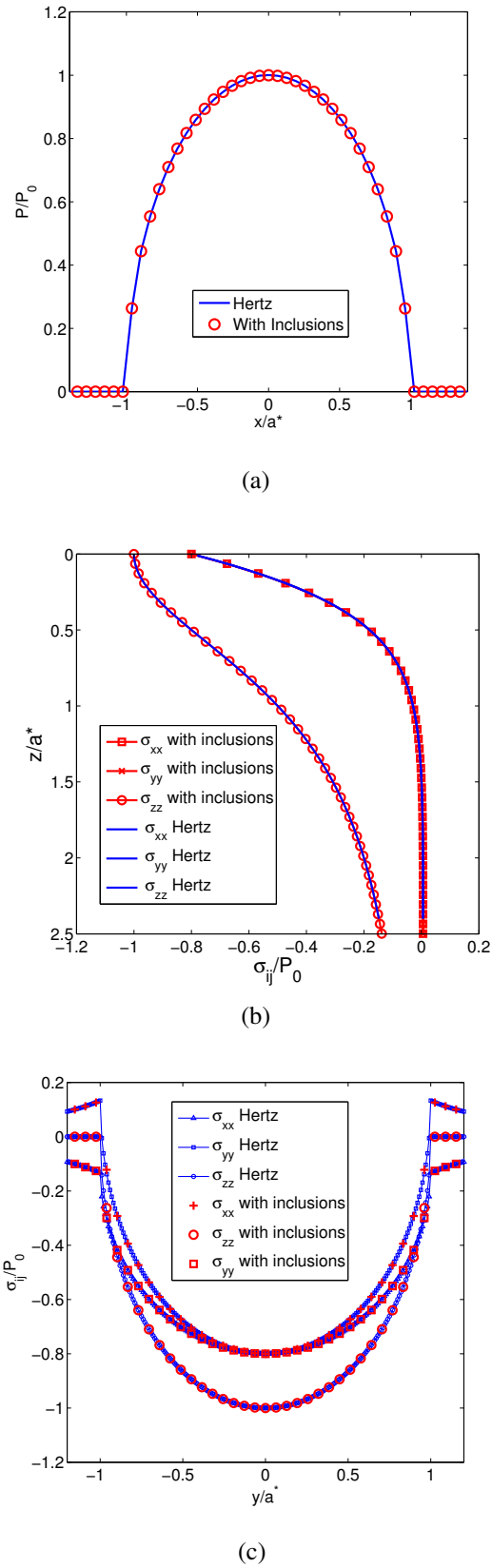
Figure 3.6: Validation of the enrichment technique with Hertzian analytical solution (a) Pressure distribution (b) Stresses along z direction (c) Stresses along y direction
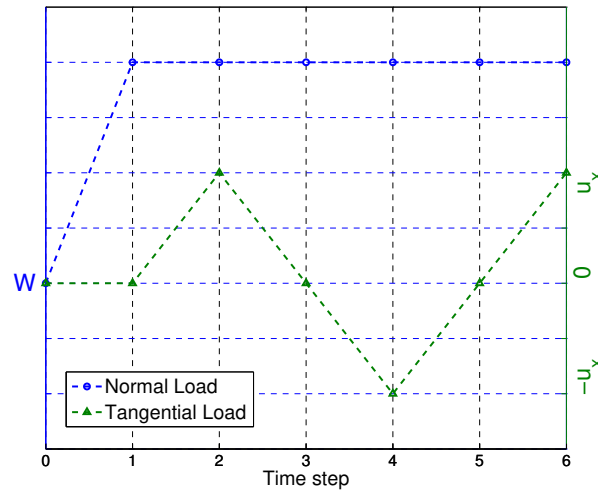
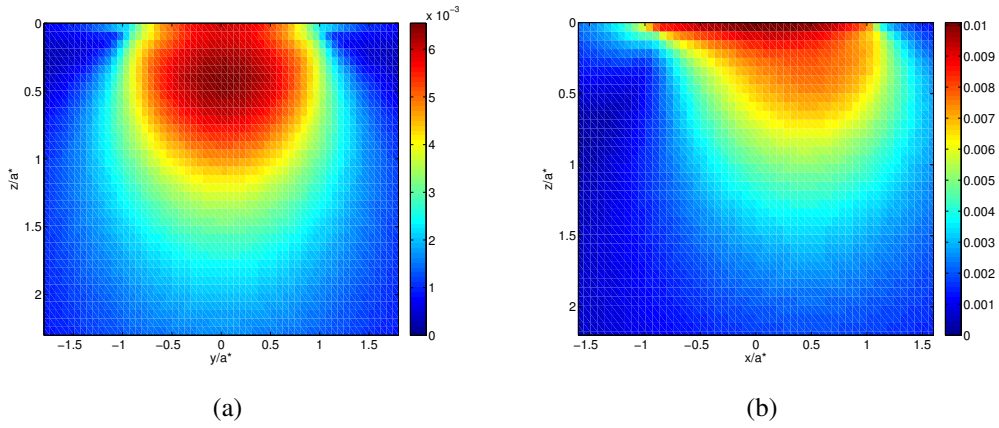**Figure 3.7:** Normal and tangential loads during one fretting cycle

The distribution of the scalar damage variable D at the end of fretting simulation is plotted at the contact surface $z = 0$ and in the plane $x = 0$ in Fig. 3.9(a) and Fig. 3.9(b). It can be observed that the maximum damage is located at the center of the contact surface where the contact pressure is the higher and where the surface has seen the biggest sliding amplitude.

Figure 3.10 represents the evolution of the damage variable and the associated Young's modulus for the most damaged point of the material during fretting cycles. As the Young's modulus is decreasing, the equivalent strain is increasing and the material is becoming more damaged until the damage variable reaches its critical value and the Young's modulus has dropped to 0.

As the damage variable increases, contact pressure decreases (Fig. 3.11) and consequently, the contact area increases to respect the load equilibrium (Eq. 2.1). Moreover, the contact pressure drops locally by almost 40% at the center of the contact, where the surface is the more damaged.

Figure 3.8: Equivalent strain $\tilde{\varepsilon}$ (a) under normal loading in the plane $x = 0$. (b) under normal and tangential loading in the plane $y = 0$ with $\mu = 0.5$ during the first fretting cycle.
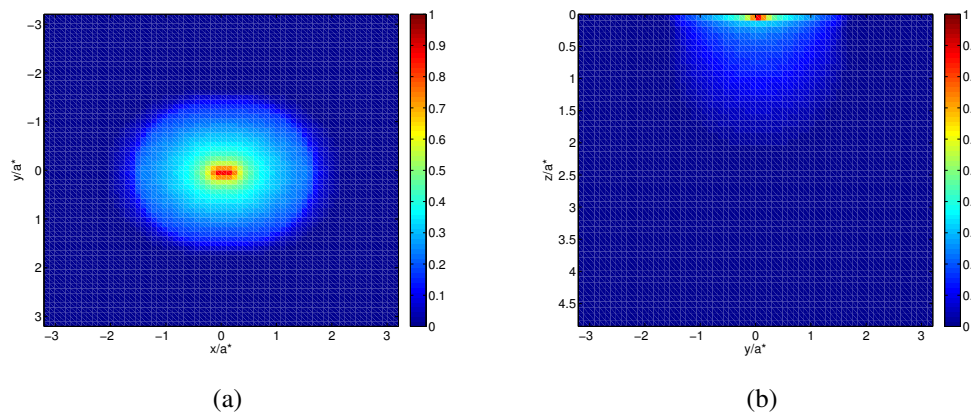
Figure 3.9: Damage variable D with $\mu = 0.5$ (a) in the plane $z = 0$. (b) in the plane $x = 0$ after 17 cycles.
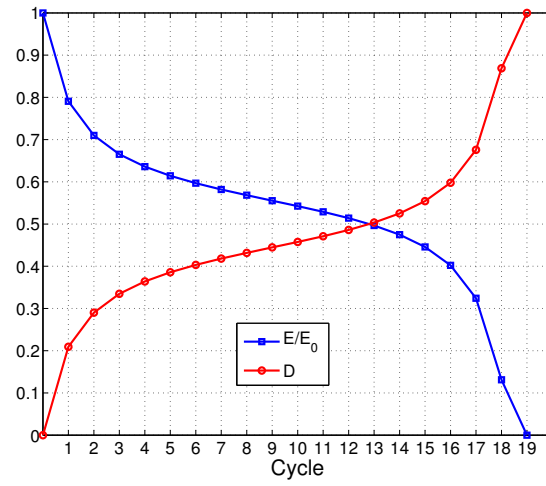
Figure 3.10: Evolution of damage and Young modulus with cycles for $\mu = 0.5$
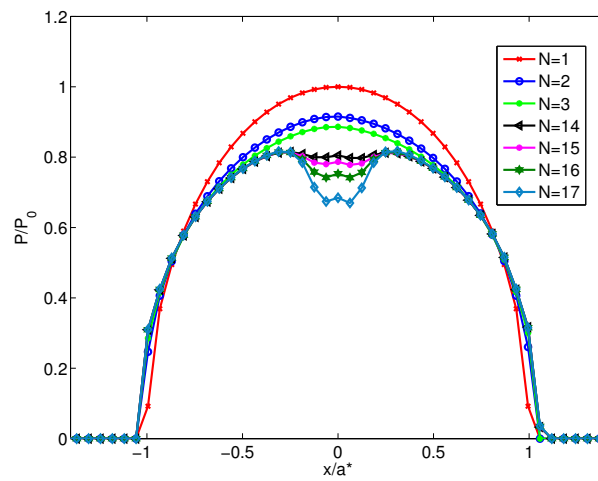
Figure 3.11: Effect of damage on contact pressure for $\mu = 0.5$

Effect of the coefficient of friction

Simulations were then performed in order to identify the influence of the friction coefficient on the model response. Firstly, values of the equivalent strain $\tilde{\varepsilon}$ along direction z for different coefficients of friction are compared in Fig. 3.12. It can be observed that for $\mu < 0.3$, the highest value of $\tilde{\varepsilon}$ is localized in the subsurface under the center of the contact while for $\mu \geq 0.3$, it is localized at the surface $z = 0$. Note that during unlubricated fretting conditions, the friction coefficient is usually high [FOU 04]. The following studies will focus on friction coefficient $\mu \geq 0.3$.

It can be observed in Fig. 3.15 that a higher coefficient of friction leads to an increased surface damage rate. It comes from the fact that, according to Coulomb's law, the higher is the coefficient of friction, the higher are the surface shear stresses. That is why the damage surface is larger with $\mu = 0.7$ (Fig. 3.13(a) and Fig. 3.13(b)) than for $\mu = 0.5$ and the pressure distribution is dropping on a larger surface (see Fig. 3.14). It should be noted that the number of cycles leading to failure is significantly lower than what can be found in literature. The number of damage cycles found in our model is compared to the number of cycles leading to the first appearance of wear, also called the wear initiation period.

Effect of computation discretization on damage evolution

The reference space between the computation point is defined as $2\Delta x = 0.062a^*$ in section 3.2.2. Simulations are performed with different discretization sizes and the damage evolution of the most damaged point is plotted in Fig. 3.16. The enrichment size is kept the same for every simulation. This is leading to a greater number of inclusions to fill the enrichment domain when the discretization size is decreasing. There is no effect of the discretization size on the damage computation at the beginning of the simulation but after a few cycles, damage values are slowly diverging. For an identical damage value, different discretizations are modifying the Young's modulus in a different material volume. In the following cycles, the stress field will not be the same for the different discretizations. Furthermore, discretization size and area must be adapted to the considered loading (rolling contact).

Effect of enrichment size on damage evolution

The half-space is constituted of $N_x \times N_y \times N_z$ cuboids as illustrated in Fig. 3.4. Fretting simulations are performed with $\mu = 0.5$ and with different enrichment sizes and plotted in Fig. 3.17. The enrichment depth in the z direction is corresponding to a distance of $2.23a^*$ and is kept the same for every simulation. Enrichment distances in the x and y directions are equals and vary from $2a^*$ to $4a^*$. One can observe that no effect of the size of the enrichment is observed on the damage evolution nor on contact pressure (see Fig. 3.18).
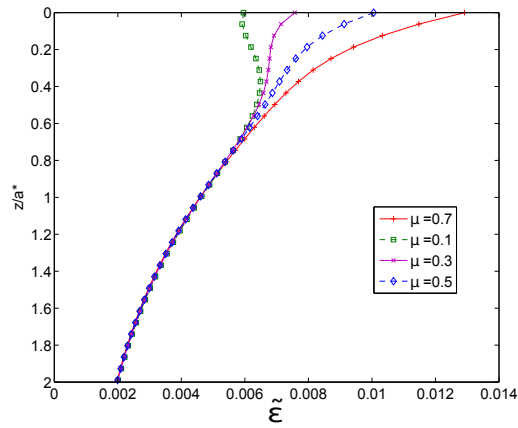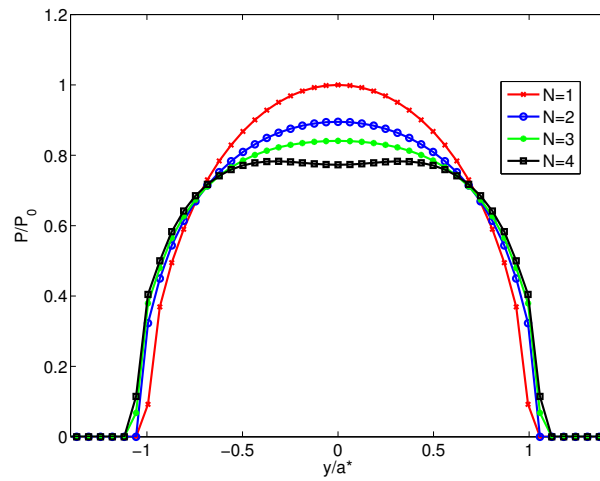
Figure 3.12: Equivalent strain $\tilde{\varepsilon}$ along direction z for different friction coefficients
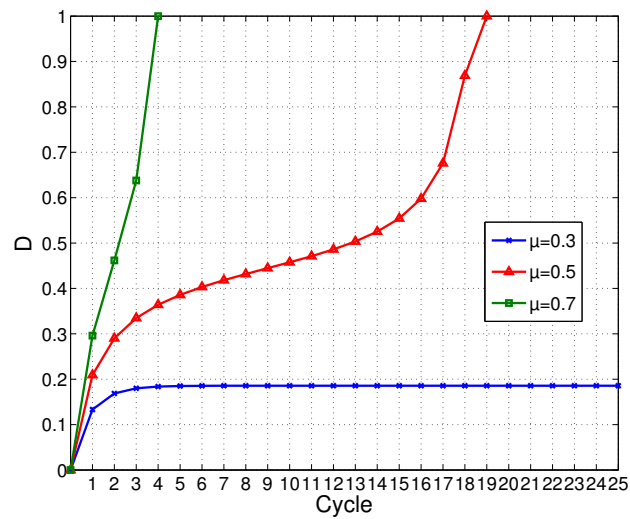

(a)   (b)
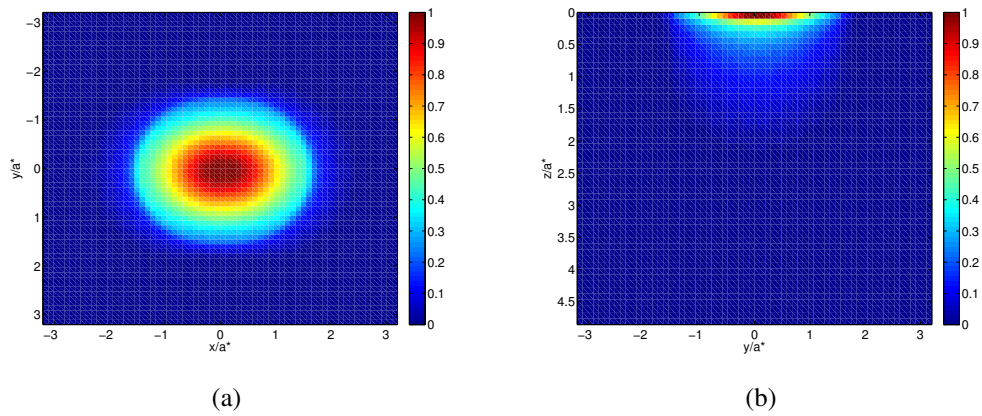
Figure 3.13: Damage variable D with $\mu = 0.7$ (a) in the plane $z = 0$. (b) in the plane $x = 0$ after 4 cycles

Figure 3.14: Effect of damage on contact pressure for $\mu = 0.7$

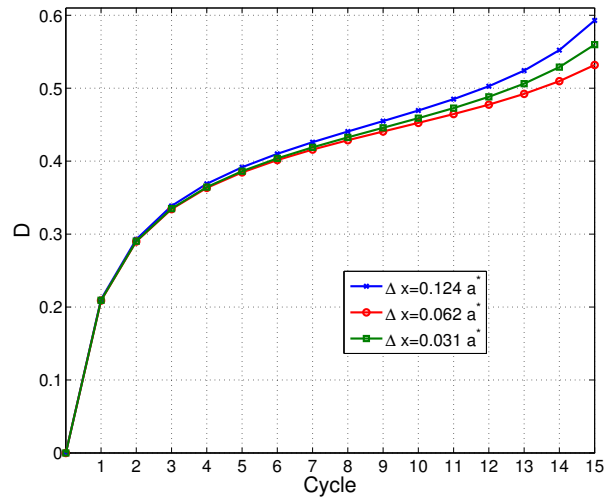**Figure 3.15:** Evolution of damage function of friction coefficient

Figure 3.16: Effect of computation discretization on damage evolution
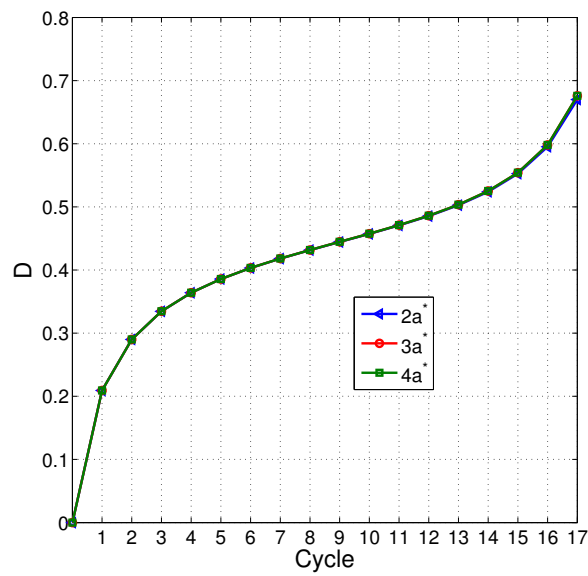
Figure 3.17: Effect of enrichment size on damage evolution
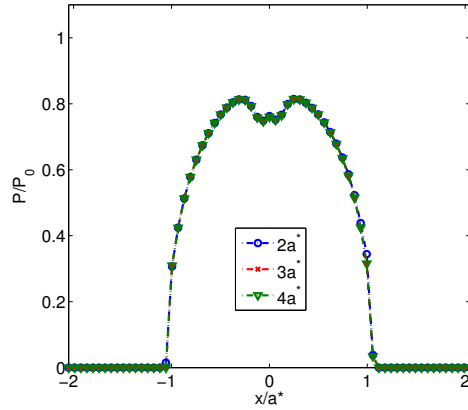
Figure 3.18: Comparison of contact pressure at the end of the damage simulation function of enrichment width

3.2.2.2   Partial slip regime

In this section, the same damage model is used in the partial slip regime. A gross slip fretting loop is associated to wear whereas the partial slip regime is associated to cracking appearance. For the contact between a sphere and a plane in partial slip regime the center of the contact is sticking and an annular slip zone is appearing at the edge of the contact area as shown in [MIN 49]. Accordingly to fretting material response (fretting map), cracking appearance is generally associated with smaller displacement amplitude and higher normal loading than in gross slip conditions [VIN 92].

A simulation is performed using a coefficient of friction of $\mu = 0.7$ and a normal load $W = 900$ N. Accordingly with Hertzian theory, this load leads to a contact radius $a^* = 0.41817$ mm and a maximum contact pressure $P_0 = 2457.386$ MPa. The tangential displacement is imposed with a value of $u_x = 0.001$ mm or $u_x/a^* = 0.0023$. The damage model parameters are kept the same as in section 4.3.1.

The state of the scalar damage variable D at the end of fretting simulation can be observed at the contact surface $z = 0$ and in the plane $x = 0$ in Fig. 3.19(a) and Fig. 3.19(b) after five fretting cycles. The higher damage values are localized in the slip circular zone at the edge of the contact. It is where the material sees the maximum strain during fretting cycles. In agreement to that, the pressure distribution is locally dropping at the contact edge as the damage is increasing (Fig. 3.20). During the damage progression, the contact area is increasing to respect the load equilibrium (Eq. 2.1) and the shear maximum value is moving out of the initial contact area (Fig. 3.21). These results exhibit the same effects of damage on contact pressure that the ones found in Ghosh et al. [GHO 13].

The results obtained in sections 3.2.2.1 and 3.2.2.2 are qualitatively in good agreement with the surface damage phenomenon usually observed in fretting conditions, see for example our experimental results in Figs. 3.22(a) and 3.22(b) – that can be compared to Figs. 3.13 and 3.22 – or to literature data [VIN 92].
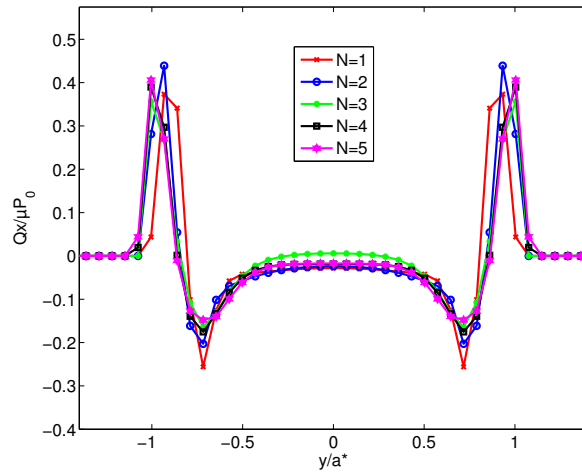
(a)

(b)
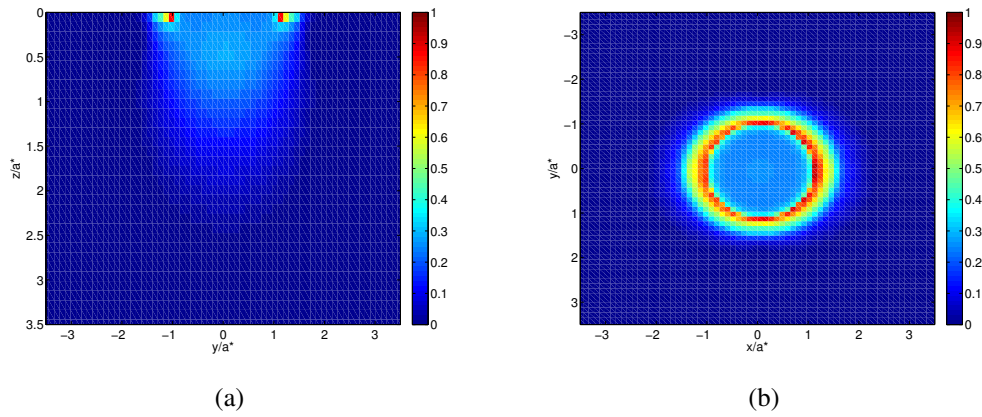
Figure 3.19: Damage variable D with $\mu = 0.7$ (a) in the plane $z = 0$. (b) in the plane $x = 0$ after 5 cycles.
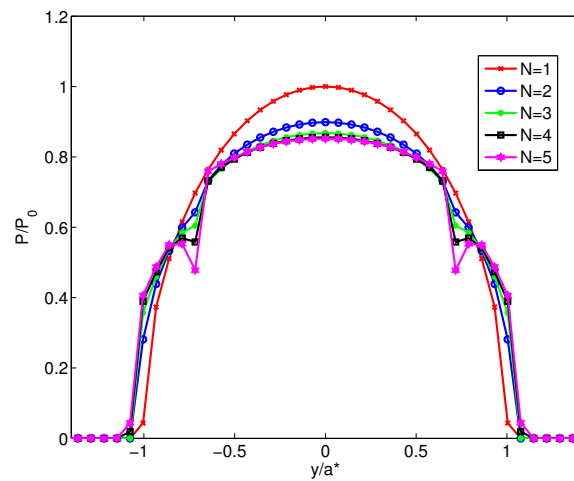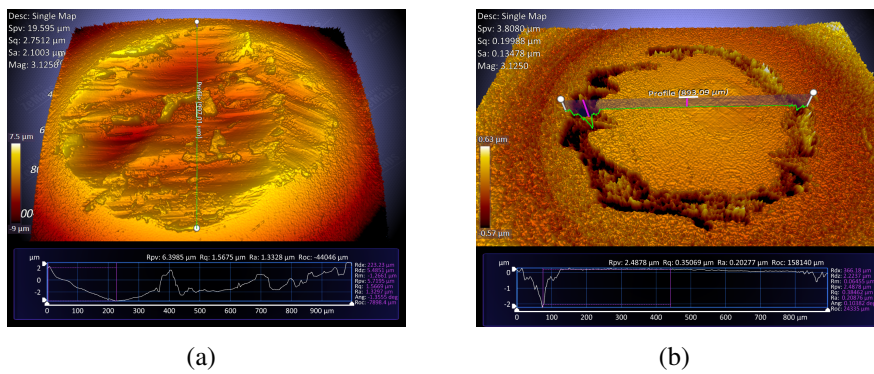

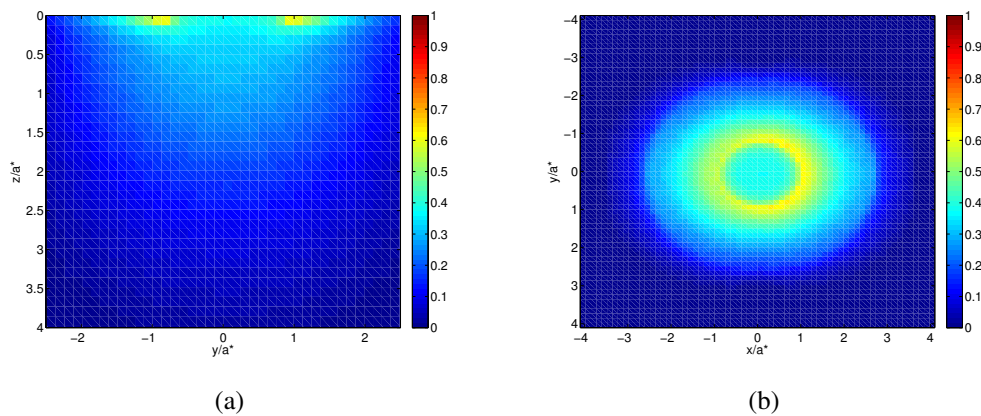**Figure 3.20:** Evolution of contact pressure with damage in the plane $x = 0$ for $\mu = 0.7$
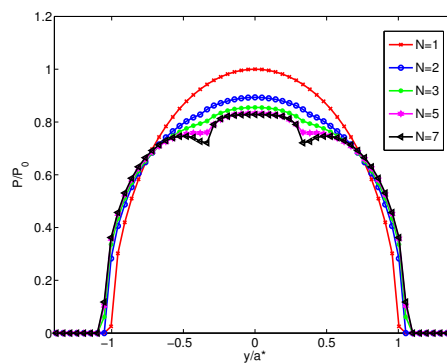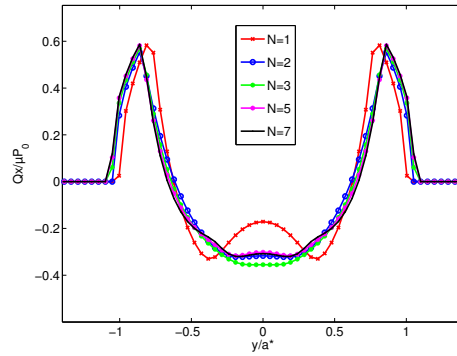
Figure 3.21: Evolution of contact shear distribution with damage in the plane $x = 0$ for $\mu = 0.7$

Figure 3.22: Wear scar of a steel ball (a) under gross slip regime (b) under stick-slip regime.

(a)   (b)

Figure 3.23: Damage variable D with $\mu = 0.4$ (a) in the plane $z = 0$. (b) in the plane $x = 0$ after 7 cycles.

Figure 3.24: Evolution of contact pressure with damage in the plane $x = 0$ for $\mu = 0.4$

Effect of the coefficient of friction

A second simulation was realized with a coefficient of friction $\mu = 0.4$. All other parameters are kept the same than in the previous simulation. In Fig. 3.23, one can observe that the increasing slip zone and vanishing stick zone are leading to an increased surface damage zone. Wear and crack initiation phenomena are competing in the slip zone where the maximum shear stress occur.

Contact pressure in Fig 3.24 and shear stress in Fig. 3.25 show that pressure is locally decreasing at the border of the contact area and the stick zone at the center is less affected by damage. The contact area is increasing with the decreasing pressure to ensure the contact load equilibrium.

Finally, results found with the proposed damage model are in good agreement with the physical phenomena experimentally observed in literature as recalled in Fig 3.26.

Figure 3.25: Evolution of contact shear distribution with damage in the plane $x = 0$ for $\mu = 0.4$
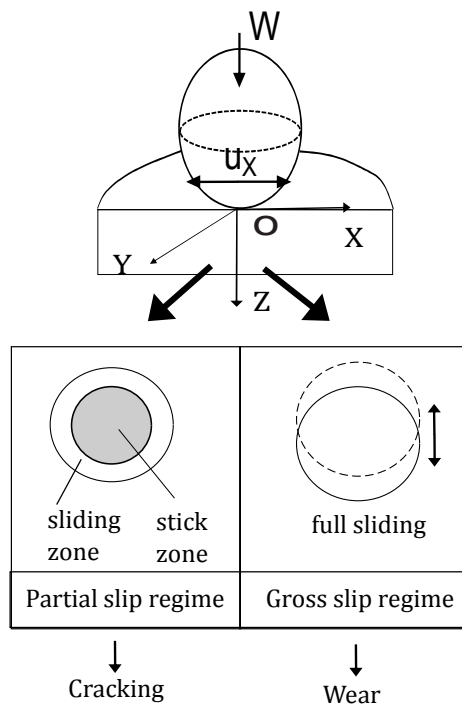
Figure 3.26: Fretting regime and associated damage phenomena

3.2.2.3 Application to coated materials

A lot of materials used in the industry are coated to protect the surface from damage or to help keeping the integrity of the substrate. Hard metallic coatings can mitigate fretting by reducing friction and resisting crack initiation [BEA 87, FOU 97]. Using the same enrichment technique as before gives the possibility to simulate coated materials. From the top surface until a defined thickness z_c cuboidal inclusions with different material properties than the substrate are used. Above this layer, the same material properties than the substrate are used for the inclusions (see Fig. 3.27).

This section only aims to investigate the effects of elastic coatings on the localization of damage in the material. Firstly, only the distribution of equivalent strain $\tilde{\varepsilon}$ is studied. Different coating's stiffnesses (with a Young modulus ratio defines as $\gamma = E/E_0$ with E and E_0 the modulus of the coating and substrate, respectively) and thickness (z_c) are studied and the effect on damage evolution is analyzed.

Two different coating stiffnesses are studied here, a harder one with $\gamma = 2$ and a softer one with $\gamma = 0.5$. The equivalent strain $\tilde{\varepsilon}$ is plotted in order to represent the coating effect on the damage localization. The same parameters as in section 4.3.1 are used for the contact loading.

In Figs. 3.28 and 3.29, the equivalent strain $\tilde{\varepsilon}$ is plotted for the undamaged material during the first cycle in the plane $y = 0$ for four different coating thicknesses z_c and for both coating stiffness ratios γ. These results are compared to the uncoated model along the axe z in Figs. 3.30 and 3.31.

For $\gamma = 0.5$, the maximum equivalent strain $\tilde{\varepsilon}$ is always located in the coated material (see Fig. 3.28) and $\tilde{\varepsilon}$ is very attenuated in the substrate. Moreover, the equivalent strain $\tilde{\varepsilon}$ in the coating is almost twice the value of $\tilde{\varepsilon}$ in the uncoated half-space (Fig. 3.30).

In contrary to soft coatings, the maximum equivalent strain $\tilde{\varepsilon}$ is always located in the substrate material (see Fig. 3.29) for hard coatings ($\gamma = 2$). Moreover, the maximum equivalent strain $\tilde{\varepsilon}$ in the hard coating is almost two times lower than with the uncoated half space (Fig. 3.31). It is important to notice that the maximum of the equivalent strain $\tilde{\varepsilon}$ is located at the interface between the coating and the substrate for a coating thickness $z_c/a^* \approx 0.5$ (close to the maximum shear stress localization). In the case of $z_c = a^*$, there is no high equivalent strain $\tilde{\varepsilon}$ at the interface. The layered structure of hard coatings leads to damage propagation at the interface between the coating and the substrate parallel to the surface as shown in [GOR 79].

The damage variable D is plotted in Fig. 3.32, along the z-axis for the two different coating stiffnesses for a coating thickness $z_c = 0.25a$ after one fretting cycle. A strong hypothesis is made here that the damage parameters are the same for the coating and for the substrate even if there are not from the same material.

It can be observed that, accordingly with what was previously observed with $\tilde{\varepsilon}$, the soft coating is a lot more damaged than the hard one. Moreover, for the hard coating, the maximum damage is located at the interface between the substrate and the coating. But for the soft coating, the maximum of damage is located at the surface and is much higher (around 5 times).
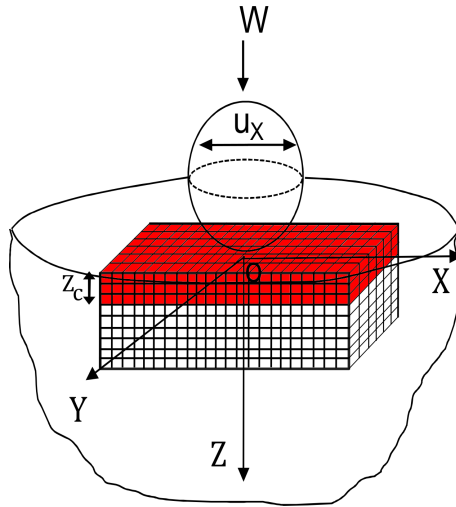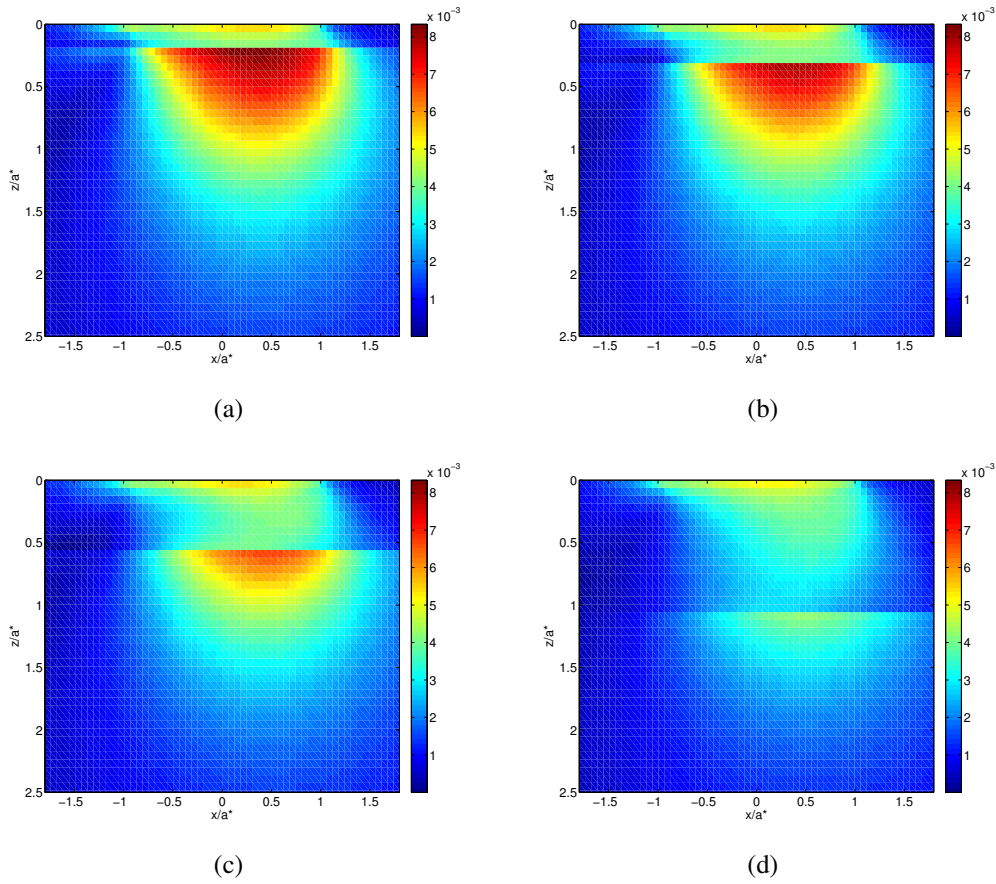
Figure 3.27: Enrichment of the half space with cuboidal inclusions to simulate the effect of coatings.
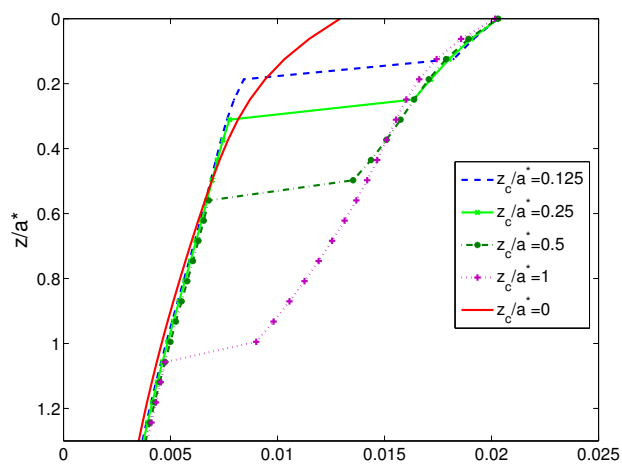

(a)

(b)

(c)

(d)
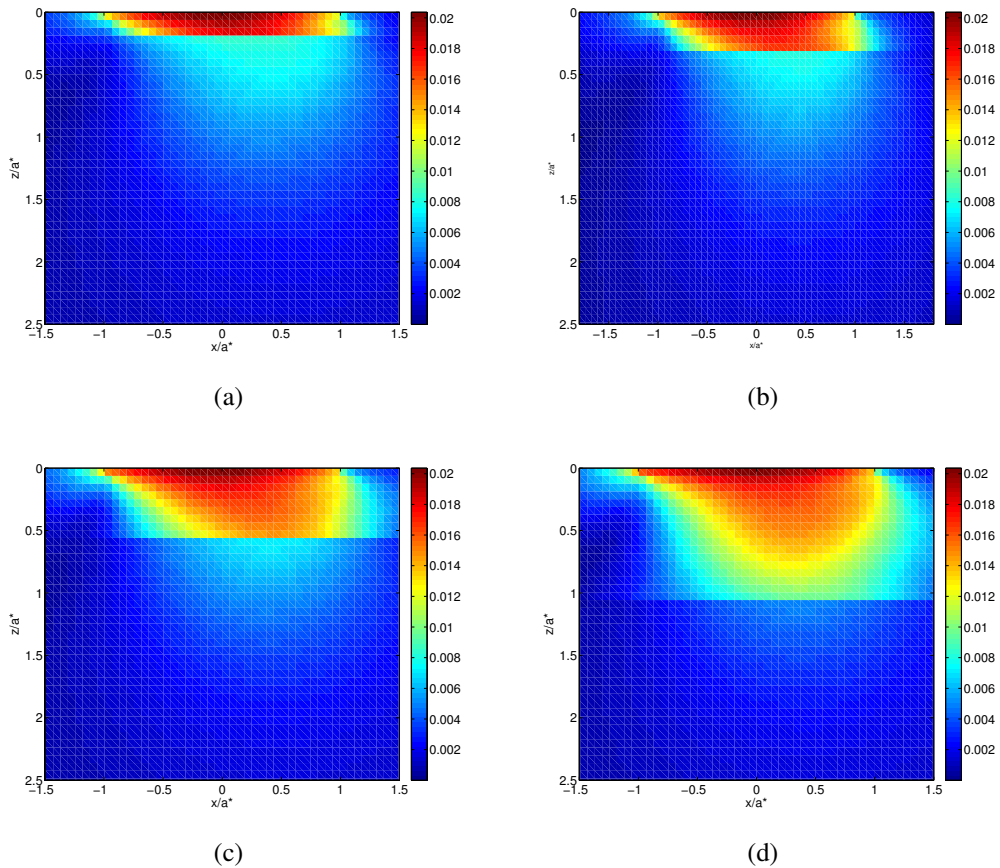
Figure 3.28: Equivalent strain $\tilde{\varepsilon}$ with a soft coating ($\gamma = 0.5$) of thickness (a) $z_c = 0.125a^*$ (b) $z_c = 0.25a^*$ (c) $z_c = 0.5a^*$ (d) $z_c = a^*$
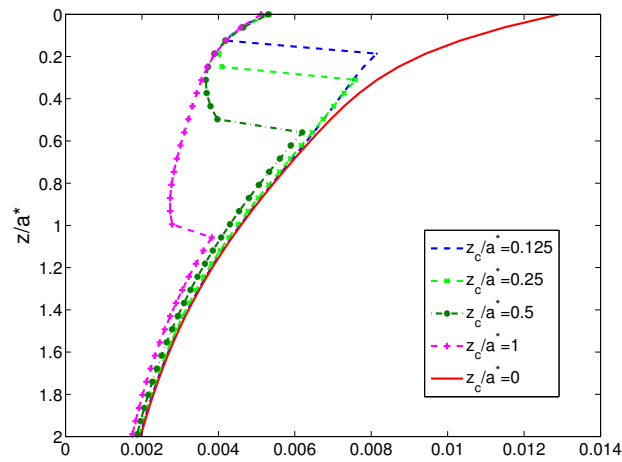
(a)

(b)

(c)

(d)

Figure 3.29: Equivalent strain $\tilde{\varepsilon}$ with a hard coating ($\gamma = 2$) of thickness (a) $z_c = 0.125a^*$ (b) $z_c = 0.25a^*$ (c) $z_c = 0.5a^*$ (d) $z_c = a^*$

**Figure 3.30:** Equivalent strain along z for different thickness z_c and with a soft coating ($\gamma = 0.5$)

Figure 3.31: Equivalent strain along z for different thickness z_c and with a hard coating $(\gamma = 2)$

The results presented here show that hard coatings are effective to protect the material from fretting surface degradations while soft coatings are damaging faster than uncoated material assuming that the damage threshold in term of yield strength (ε_{d0}) and ductility (ε_R) are the same. Finally, soft coatings are accommodating the surface stress field in the contact limiting crack initiation but are more subjected to wear. In contrary, hard coatings are wear resistant but are increasing the surface stresses leading to surface fatigue and pitting.
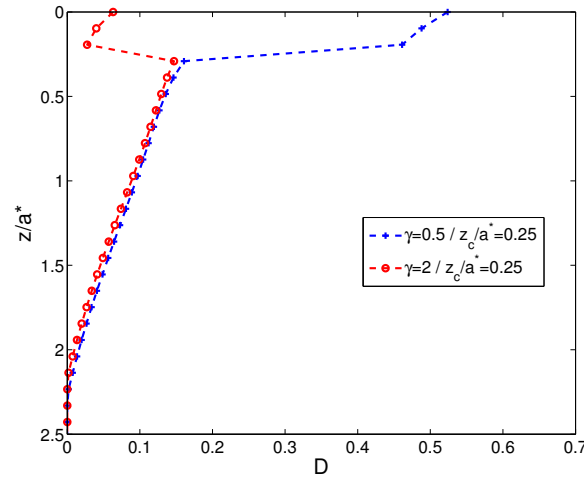
Figure 3.32: Damage after one fretting cycle along z direction for two different coating stiffnesses

3.3 Comparison with another damage model

A damage law used in Ghosh et al. [GHO 13] is presented in this section and implemented into the semi-analytical contact solver. Fretting simulations are performed in gross slip regime and results are compared between the two damage models.

3.3.1 Presentation of the damage model

The theoretical developments leading to the damage wear law presented in Ghosh et al. [GHO 13] are briefly presented in this part. Recalling that fretting wear is caused by micro-cracks growing along weak point in the material due to high contact stresses, a damage evolution law with an isotropic damage variable D based on the work of Chaboche and Lesne [CHA 88] is defined. The evolution of D is a function of the stress level:

$$\frac{dD}{dN} = f(\sigma, D) \tag{3.18}$$

with N the number of stress cycles and σ the stress level at the considered point. Xiao et al. [XIA 98] proposed a damage evolution law of the following form:

$$\frac{dD}{dN} = \left(\frac{\sigma_0}{\sigma_r(1-D)} \right)^m \tag{3.19}$$

with σ_0 the critical stress quantity for the considered damage phenomenon (wear here), σ_r and m are material parameters that need to be determined. As hypothesized for rolling contact fatigue by Raje et al. [RAJ 08a] and extended to fretting wear by Ghosh et al. [GHO 13], it is assumed that shear stress causes surface initiated failure because it un-

dergoes two reversals in an Hertzian contact. Finally one can replace $\Delta\sigma$ by $\Delta\tau$ in Eq. 3.19.

Previous work have shown the importance of coefficient of friction in surface failure mechanisms. In particular, Fouvry et al.[FOU 96] proposed a theory linking the wear volume to the dissipated energy due to friction in the interface. Furthermore, coefficient of friction can be expressed as a function of the softer material shear strength and it penetration hardness.

$$\frac{dD}{dN} = \frac{0.8 S_{ut}}{E} \frac{\Delta\tau}{H(1-D)} \qquad (3.20)$$

with N the number of stress cycles, S_{ut} the ultimate tensile strength of the material, E the Young's modulus and H the hardness of the material. $\Delta\tau$ is the shear stress reversal at the considered point during a fretting cycle. Details leading to this equation can be found in Ghosh et al. [GHO 13].

$$\int_0^N dN = \int_0^1 \left[\frac{E}{0.8 S_{ut}} \frac{H(1-D)}{\Delta\tau} \right] dD, \qquad (3.21)$$

The number of cycles N leading to failure is defined as:

$$N = \frac{E}{0.8 S_{ut}} \frac{H}{2\Delta\tau} \qquad (3.22)$$

The shear stress amplitude during one fretting cycle is calculated using the semi-analytical contact solver and damage evolution is calculated at every point of the material domain using Equation 3.20. For sake of computational efficiency, the number of cycles leading to the first fully damaged element is computed using the jump-in-cycles algorithm proposed by Lemaitre [LEM 92] and already used in finite element simulation by Slack et al. [SLA 10]. This method assumes a linear damage evolution over a block of cycles.

3.3.2 Gross slip regime

Contact between a rigid sphere of radius $R = 25$mm and a homogeneous half-space is simulated using the semi-analytical solver. The same material and loading characteristics than in section 4.3.1 are used with a coefficient of friction $\mu = 0.7$.

The half-space has been enriched with damageable elastic cuboidal inclusions with initially the same properties than the half-space. The damage model proposed in Ghosh et al. [GHO 13] is used with two parameters: $S_{ut} = 2500$ MPa and $H = 1$ GPa. The damage increment used in the jump-in-cycles algorithm is chosen to be $\Delta D = 0.01$. All damage simulations have been performed until at least one point reached the critical damage value $D = 1$. Results in the case of gross slip regime and partial slip regime are investigated. The distribution of the scalar damage variable D at the end of fretting simulation is plotted at the contact surface $z = 0$ and in the plane $x = 0$ in Fig. 3.33. It can be observed that the maximum damage point is located at the center of the contact surface as observed with the previous model in Fig. 3.13. As the damage variable increases, contact pressure

(a)

(b)
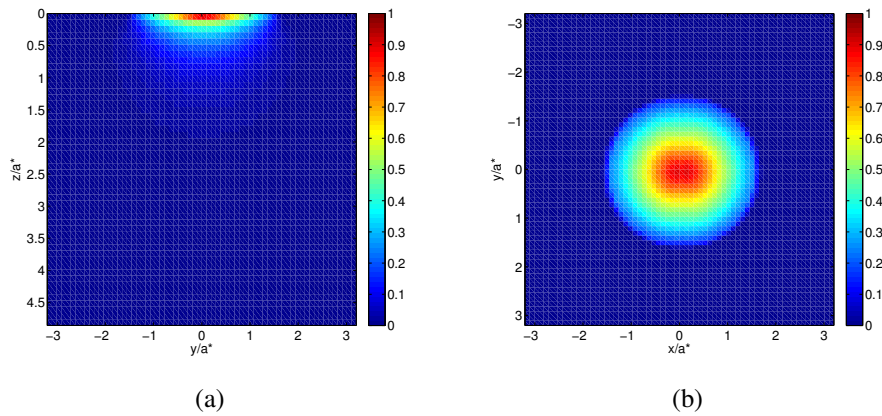
Figure 3.33: Damage variable D with $\mu = 0.7$ (a) in the plane $x = 0$. (a) in the plane $z = 0$ after 28 loading cycles using damage model from Ghosh et al. [GHO 13].

decreases (Fig. 3.34) and consequently, the contact area increases to respect the load equilibrium (see Eq. 2.1). Moreover, the contact pressure found at the last cycle with the two models are similar. A small difference is found between the two pressures due to the fact that simulation is stopped once the damage variable reaches the value $D = 1$ for the first time. The represented contact pressure is computed with the damage state from the previous cycle and depending on the damage evolution law, the damage level at this previous cycle is not exactly the same in the two models.

The number of damage cycles found in this damage model is equal to 28 compared to 4 in the proposed model (see Fig. 3.35). Therefore one damage cycle in our model is equivalent to approximately 7 cycles in the model of Ghosh et al. [GHO 13] in this specific example i.e. with the defined hardness and tensile strength.

3.3.3 Partial slip regime

In this section, simulation with this damage model are realized in the partial slip regime. Simulation parameters are the same than in section 3.2.2.2 and the damage model parameters are kept the same as in section 3.3.2.

The state of the scalar damage variable D at the end of fretting simulation can be observed at the contact surface $z = 0$ in Fig. 3.36 after 34 fretting cycles. The higher damage values are localized in the slip circular zone at the edge of the contact. The present results exhibit the same effects of damage on contact pressure that the ones found with the proposed damage model in section 3.2.2.2 and in Ghosh et al. [GHO 13].
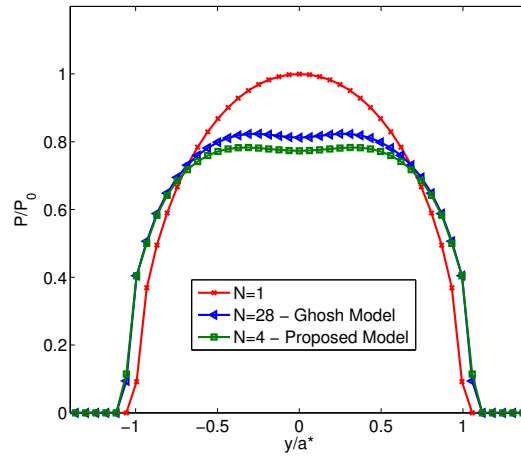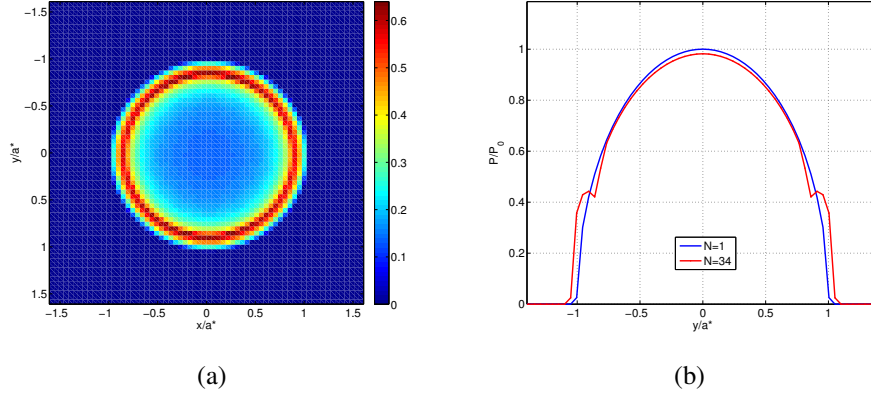
Figure 3.34: Contact pressure with damage in the plane $x = 0$ for $\mu = 0.7$ at the last iteration of the simulation for the two models.
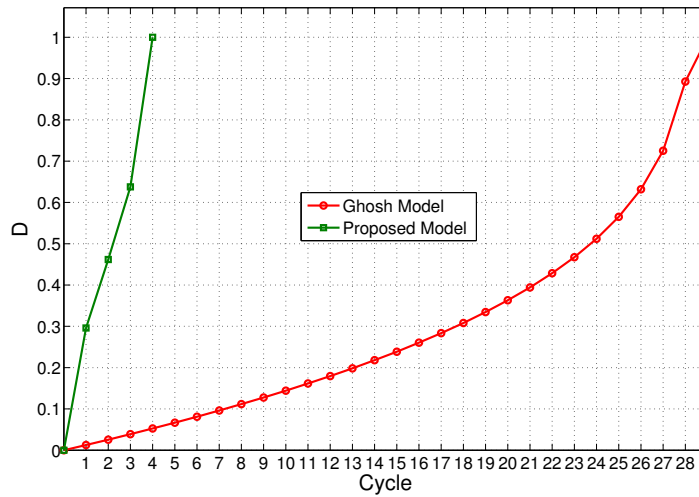
Figure 3.35: Damage evolution with fretting cycles for the two damage models with $\mu = 0.7$.

Figure 3.36: (a) Damage variable D with $\mu = 0.7$ in the plane $z = 0$ in partial slip regime. (b) Contact pressure evolution with fretting cycles in the plane $x = 0$ using damage model from Ghosh et al. [GHO 13].

3.4 Comparison with a wear model.

All the proposed damage models aim at simulate the damage phenomenon leading to wear or crack initiation at the contact surface. In this section, a comparison between the damage model from section 3.1.3 and simulation of wear in the semi-analytical solver is proposed. The wear law used here is based on the quantity of dissipated energy in the contact during each fretting cycle [GAL 07a].

$$V_W = \alpha \sum_{k=1}^{N} E_d(k) \tag{3.23}$$

Following Coulomb's law, one can write the local dissipated energy by friction per surface area, ed, as the product of surface shear and slip:

$$ed = q.s \tag{3.24}$$

The local wear law can then be expressed as:

$$\Delta h = \alpha \sum_{k=1}^{N} \delta_0(N) \sum_{1Cycle} q.s \tag{3.25}$$

In the wear simulation, an increase in the computed wear volume is introduced by modifying the surface geometry of the solid in the contact area. Wear is usually shared by the two materials in contact. To be consistent with our damage simulation, one can consider that only the half-space is going to be wearing. The surface equation is modified considering the number of cycles ΔN and the wear depth Δh. More details can be found in [GAL 07b].

$$f_2(x,y) = f_2(x,y) - \Delta N \Delta h(x,y) \tag{3.26}$$
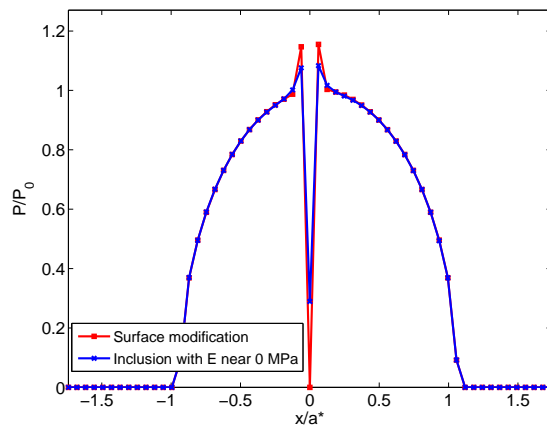
**Figure 3.37:** Contact pressure with one damaged element and with wear surface modification in the plane $x = 0$.

One should notice that the damage model from section 3.1.3 is based on a volume stress computation of a damage variable while the wear model is based on surface stress computation and is not taking into account any subsurface phenomena. The effect on the contact pressure is based on a surface modification in the wear model and on the eigendisplacements coming from the inclusions in the damage model.

In order to easily compare the effects of wear and damage on the contact pressure, a rigid sphere in contact on a half space with only one inclusion almost fully damaged ($E \approx 0$) and tangent to the surface is plotted in Fig. 3.37. It is compared with the contact pressure from a rigid sphere in contact with a half-space where the flat surface have been modified at the same point and by the same size than the previously considered inclusion (no inclusion is present in this case) as if only this point of the surface have been worn off. Both of the contact pressure are dropping to 0 at the considered point and two peaks of pressure due to the discontinuity around the surface modification can also be observed in Fig. 3.37. A very good agreement is found between the two contact pressure confirming the ability of the damage model to represent the phenomena leading to wear without modifying the surface geometry.

Furthermore, fretting simulations have been performed with the wear model and compared to the same simulation but with the damage model from 3.1.3 after 4 fretting cycles. In every simulations, contact conditions and damage parameters are kept the same than in section 4.3.1. For the simulation with the wear model, $\Delta N = 100000$, $\Delta h = 0.0002$ mm and the wear coefficient is chosen arbitrarily. Fretting loops associated with each fretting slip regime are showed in Fig. 3.38.

Contact pressures along the x direction at the last computed cycle are compared for both models in gross slip and partial slip regimes in Fig. 3.39. In every cases, the contact area is increasing while the contact pressure is dropping, at the center of the contact area in full sliding conditions (see Fig. 3.39(a)) and at the border of the contact area in stick
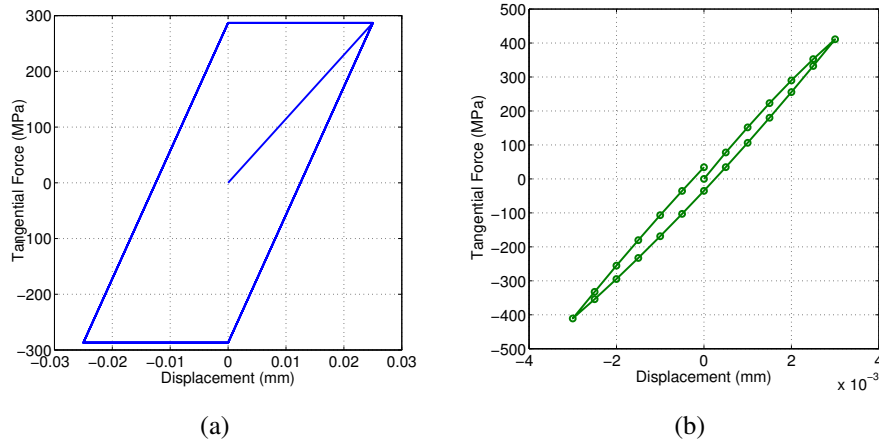
Figure 3.38: Fretting Loops (a) in Gross slip regime (b) in partial slip regime.

slip conditions (see Fig. 3.39(b)).

Wear scars are compared to the level of damage at the surface along the *x* axis in the gross slip regime in Fig. 3.40 and in the partial slip regime in Fig. 3.41. In the gross slip regime, the center of the contact is the most damaged and it is also where the surface is the most worn. No quantitative comparison can be made here because D is a dimensionless variable while the wear scar depth is in mm. In the partial slip regime, the most damaged area and the most worn surface are localized on the edges of the contact area. One should observed that some damage is also localized at the center of the contact area while no wear seems to appear at that time in the center of the contact area. Therefore, a good agreement is found between the results from the damage model and based on a volume stress field computation and a wear model from Gallego et al. [GAL 07a] based on surface stress computation.
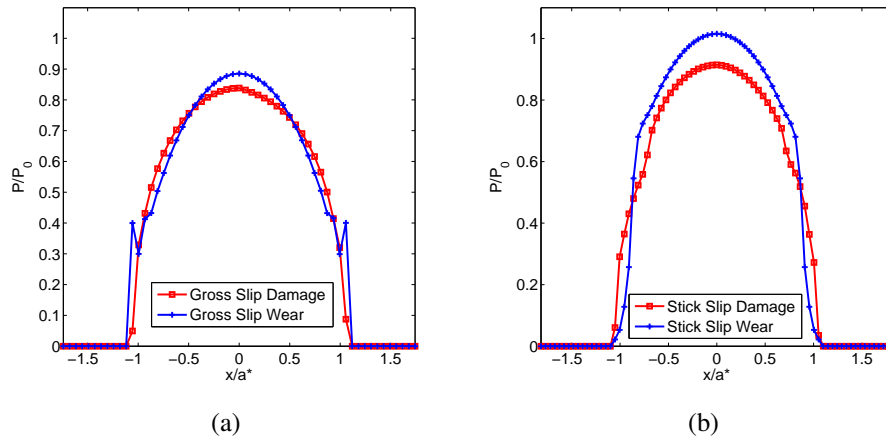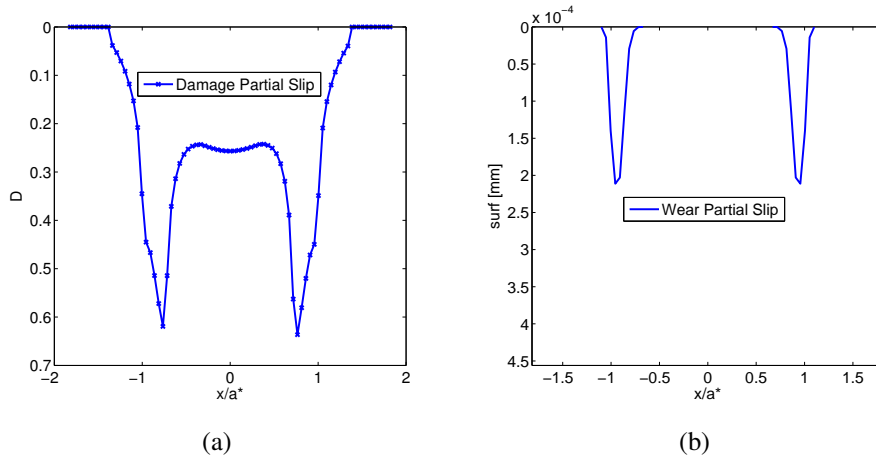
Figure 3.39: Pressure distribution with Wear and Damage (a) in gross slip regime (b) in partial slip regime.
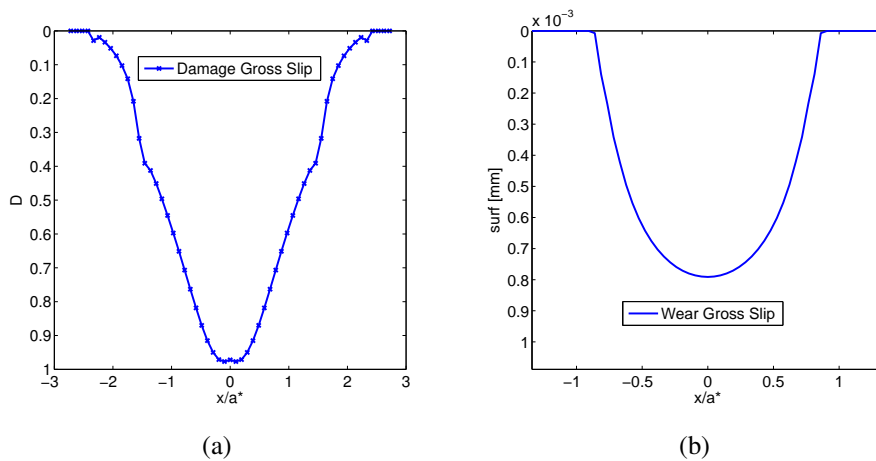
Figure 3.40: (a) Damage at the surface along *x* direction (b) Worn surface along *x* direction in the gross slip regime.

Figure 3.41: (a) Damage at the surface along *x* direction (b) Worn surface along *x* direction in the partial slip regime.

3.5 Partial Conclusion

In this chapter, a numerical method has been proposed to model the effect of fretting on surface damage and contact solution. A three-dimensional contact solver with a heterogeneous elastic damageable model is developed based on the Eshelby's equivalent inclusion method. Multiple cuboidal inclusions are superimposed on the half space solution as an enrichment technique. The model has been validated by performing a comparison with the Hertzian contact solution. The model allow to simulate fretting cycles while taking into account the damage evolution of the surface and his influence on the contact solution. The following major conclusions have been reached :

- The proposed method permits to couple the contact problem, the presence of heterogeneous inclusions and a damage law. The algorithm is very robust and convergence can be easily reached even with high level of damage. Influence of the computation discretization and enrichment size have been performed to proof the accuracy of the simulations.

- Contact pressure and shear distributions have been investigated along with the damage evolution for both gross slip and partial slip regimes.

- The results obtained with our model are in good agreement with the surface damage phenomenon caused by fretting. The proposed method reproduces accurately some classical results of the literature [VIN 92].

- The model proposed in Ghosh et al. [GHO 13] has been implemented in the semi-analytical solver along with the jump in cycle algorithm and a good agreement has been found between the two models.

- The enrichment technique allows to simulate fretting contact on coated material. The influence of these coatings on the damage localization in the material has been highlighted. In agreement with the literature [BEA 87, FOU 97], it is found again that hard coatings are protecting the surface from fretting damage.

- A good agreement between wear simulation model [GAL 07a] through surface geometry updating and damage simulation has been observed.

The present work is made on the assumption of linear elasticity to keep the model simple and demonstrate its capability. To be more realistic, the present model could be improved by taking into account plasticity effects during the fretting cycles. One way of adding the plasticity effect would be to define a second damage evolution law based on the accumulated plastic strain and to take the larger damage increment as the current damage increment as in [WAR 14, SHE 15].

Chapter 4

Damage model for Rolling Contact Fatigue

*In this chapter, the coupling between continuum damage
mechanics based model and the heterogeneous contact solver
is applied to rolling contact fatigue. A first part is focusing on
subsurface microstructural alterations occurring around
nonmetallic inclusions and called butterfly wings. A second
part is considering the application of a damage model to
surface initiated damage on indented surface.*

Contents

4.1 Introduction

Rolling element bearings (REB) are commonly used when a relative rotary motion and a significant amounts of load needs to be transmitted between machine components such as wind turbines, transmission systems and engines. REBs carry the load through contacts between the rolling elements and the races and low friction losses are ensured by lubrication. After a proper installation and under good operating conditions, the main phenomenon limiting the life of the bearings is rolling contact fatigue (RCF) [HAR 01]. In contrast to classical fatigue, RCF is not due to tensile stress but due to the reversal of the shear stress [JAL 11] (see Fig. 4.1). The two different phenomena leading to RCF failure are surface originated pitting and subsurface originated spalling [LIT 66]. Pitting is mainly due to surface defects or insufficient lubrication while spalling is due to subsurface cracks initiating at material imperfections like voids, dislocations and inclusions. Non-metallic inclusions present in the material are byproducts of steel manufacturing process and act as stress raisers in the material [KER 06, SCH 88]. Moghaddam et al. [MOG 16a] reviewed the alterations occurring around these inclusions in rolling contact fatigue.
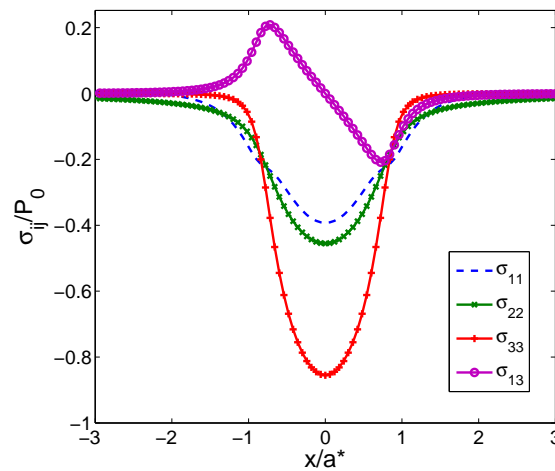

Figure 4.1: Stress history of a point located at $0.5a^*$ in the subsurface of the material as the Hertzian load passes over.

4.1.1 Experimental observations

Kang et al. [KAN 13] have shown that micro-structural alterations occur in the matrix when bearing steel is subjected to RCF loading. One is commonly referred to as "butterfly wings" and is associated with crack initiation in the vicinity of inclusions (Fig. 4.2). This phenomenon was observed for the first time in 1947 by Jones [JON 47] and then by Styri [STY 51] in 1951 and has been continuously investigated since. Butterfly wings are regions where the material is transformed from martensite into ultrafine ferritic grains [BHA 12, BEC 81]. The pair of wings around the inclusion form a 45° angle with the

rolling direction (see Fig. 4.2). Tricot et al. [TRI 72] and Nelias et al. [NEL 99] showed that the wings formation is dependent on the over rolling direction (ORD) (see Fig. 4.3). Furthermore, butterfly wings are often the site of crack initiation, in particular on the top of the upper wing and bottom of the lower wing. These cracks can propagate and lead to the failure of the bearings [GRA 07, EVA 12, EVA 13c].
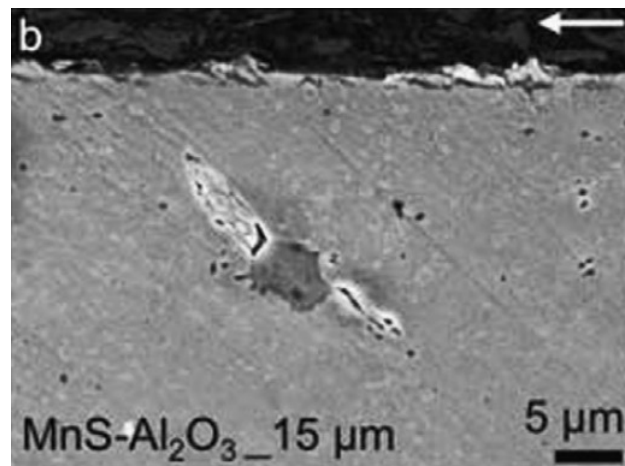
Figure 4.2: Butterfly wings formed around an inclusion [EVA 13b]. The rolling direction is from right to left.
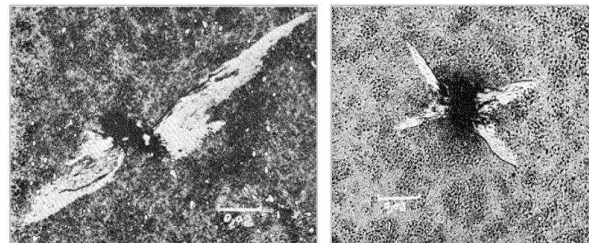
Figure 4.3: Butterfly wings around an inclusion in rolling contact fatigue. Picture on the right is showing a case where the over rolling direction have been inverted. [TRI 72]

Many experimental works have been conducted to investigate the root causes and effects of butterfly wings on RCF failure. Destructive methods provide a good knowledge of the microstructrual alteration that occur in the butterflies [GRA 07, EVA 13c, KRE 16, ALT 18]. On the other hand, non-destructive methods such as acoustic emission and X-ray tomography are able to track the formation of wings and the initiation and propagation of cracks [GUY 97, STI 09, UME 09, RAH 09, KAN 13]. In particular, ultra-sound methods have been used to detect inclusions localization, wings propagation [GUY 97] and the effects of inclusions depth on wing formation [NEL 99].

4.1.2 Numerical model

Numerical models have been developed by some investigators to simulate butterfly wings formation in rolling contact fatigue. Salehizadeh and Saka [SAL 92] computed the residual stress evolution around a circular inclusion. The hydrostatic stress around inhomogeneities with or without the presence of cracks has been investigated by Hirakoa et al.[HIR 06]. Alley and Neu [ALL 10] proposed a model based on the plastic strain accumulation around an inclusion under rolling contact loading. Recently, Cerullo and Tvergaard [CER 15] used the Dang Van criterion to determine the effects of small inclusions on fatigue.

Among the numerical models, some are based on Continuum Damage Mechanics (CDM) to study failure due to fatigue [LEM 92]. Moghaddam et al. [MOG 15b] proposed a damage mechanics approach to simulate butterfly wings propagation using finite element simulation. The model was later extended to crack propagation [MOG 15a] and to 3D simulation [MOG 16b]. In the 3D model, the inclusion is embedded in a half-space discretized using a Voronoi tesselation. This kind of discretization has been used intensively to represent the microstructure of the material [RAJ 08a, VIJ 18]. Guan et al. [GUA 17] used also the Voronoi tesselation to compute the stress intensity factors and the crack propagation around an inclusion. Lately, CDM has also been applied to study the microstructural transformation leading to dark etching layer in the material under Rolling Contact Fatigue [MOR 18b] and coupled with an EHL contact solver [PAU 17a, PAU 17b].

For three-dimensional problem and a moving load, a very fine mesh is required for the contact interfaces and for the inclusion region leading to high computation costs. In order to compute the coupled solution of the contact problem over an heterogeneous material, the numerical method developed by Nelias and co-workers [JAC 02, LER 10, KOU 14b, AMU 16] is used. One should note that the results presented by Moghaddam et al. [MOG 15b, MOG 16b] don't take into account the effect of the heterogeneity on the contact solution. The purpose of the present work is to use the damage mechanics approach to model the phenomenon of butterfly wings formation around nonmetallic inclusions coupled with a semi-analytical heterogeneous contact solver. The subsurface and the contact problem solutions are coupled. The microstructural modifications inside the material are represented by adding cuboidal heterogeneities at the location where the damage occurs.

4.2 Presentation of the damage model

In the elastic heterogeneous contact solver presented in Chapter. 2, a Continuum Damage Mechanics (CDM) based model was implemented in order to describe the degradation of material due to contact loading. Following the same principles that in Chapter. 3 but applied to subsurface damage phenomena, section 4.2.1 recall the basics of CDM and its applications to butterfly formations around nonmetallic inclusions. Sections 4.2.2 present the implementation of the damage model in the heterogeneous contact algorithm.

4.2.1 Continuum Damage Mechanics

The state of stress in the damaged material can be described by the effective stress introduced by Rabotnov [RAB 69]:

$$\tilde{\sigma} = \frac{\sigma}{(1-D)} \tag{4.1}$$

In the present model, it is assumed that D is a scalar representing the alteration of the material behavior during the phase transformation from martensite into ferrite. Thus, an increase in the damage manifests as a reduction in the modulus of elasticity in the constitutive relationship.

$$\sigma = (1-D)E\varepsilon \tag{4.2}$$

Micro indentation tests have shown that the hardness increases during the transformation [BEC 81, EVA 12, UME 09, GRA 10, MOG 15a]. Moghaddam et al. [MOG 15a] used a reverse analysis of his indentation test results to determine the reduced modulus of elasticity in the wings to be $E_{butterfly} = 0.9E_{steel}$ and therefore $D_{butterfly}$ is assumed to be 0.1 in the simulations. After this microstructural transformation, the hypothesis is made that no other transformation will occur and then no more damage will be happening at this location. Furthermore, no damage is applied to the inclusion itself. In order to compute the damage evolution in the material, a stress-based non linear evolution law was proposed by Xiao et al. [XIA 98]:

$$\frac{dD}{dN} = \left(\frac{\sigma_0}{\sigma_r(1-D)} \right)^m \tag{4.3}$$

Where N is the number of stress cycles and σ_0 is a measure of the stress mainly responsible for the fatigue damage. The resistance stress, σ_r, and m are material dependent parameters. A version of the damage evolution law for the modeling of butterfly wings was proposed by Moghaddam et al.[MOG 15b]:

$$\frac{dD}{dN} = \left(\frac{\Delta\tau}{\tau_r(1-D)} \right)^m \tag{4.4}$$

$$With\ \Delta\tau = \tau_{alternating} + |\tau_{mean}| \tag{4.5}$$

Because butterfly wings is assumed to be a shear driven phenomenon, the stress component ($\Delta\tau$) is the sum of $\tau_{alternating}$, the alternating shear stress and $|\tau_{mean}|$ the absolute value of the mean shear stress during one loading cycle. They are the components of the stress tensor mainly responsible for the damage accumulation and the formation of butterfly wings. The resistance stress τ_r represents the ability of the material to resist

fatigue damage accumulation. τ_r and the exponent m are material dependent parameters. An analogy with shear driven fatigue test, torsion test, is used to determine these parameters based on the experimental results obtained by Shimuzu for bearing steel AISI 52100 [SHI 09]. In the following simulations, values of 6.11 GPa and 10.0 will be used for τ_r and m respectively.

4.2.1.1 Jump-in-cycle Algorithm

In order to achieve computational efficiency in high cycle fatigue, the jump-in-cycles procedure is used [LEM 92]. This method assumes that, over a finite number of cycles ΔN, the stress history of a loading cycle remains constant and the increment in damage ΔD is assumed to be constant. The damage evolution is then a piecewise linear function over a block of cycles ΔN as illustrated in Fig. 4.4. Stress computations are performed once for every block of cycles and not for each individual cycle N.
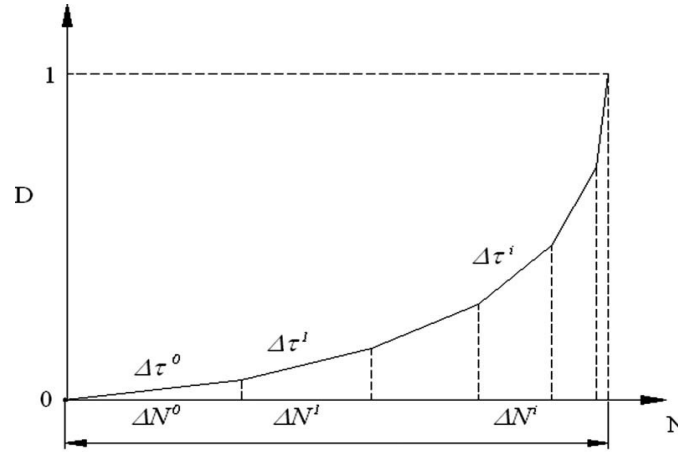
Figure 4.4: Piecewise linear damage evolution with block of cycles in the Jump-in-cycles algorithm [RAJ 08a]

.

The procedure is described below:

1 $N = 0$: for a pristine material domain, the initial damage in each element is assumed to be $D_j^0 = 0, j = 1...n_{elements}$.

2 Stress history $(\Delta\tau)_j^i$ for a loading cycle is computed at each point of the material using the semi-analytical contact solver.

3 The damage evolution rate in each element is evaluated knowing the stress history for the present block and the current state of damage in the element using the following equation:

$$\left(\frac{dD}{dN}\right)_j^i = \left(\frac{\tau_{alternating} + |\tau_{mean}|}{\tau_r(1 - D_j^i)}\right)^m \tag{4.6}$$

4 The element with the maximum damage evolution rate is chosen as the critical element for the current block of cycles:

$$\left(\frac{dD}{dN}\right)^i_{crit} = Max\left|\left(\frac{dD}{dN}\right)^i_j\right| \tag{4.7}$$

5 The number of cycles in the current block of cycles is computed as:

$$\Delta N^i = \frac{\Delta D}{\left(\frac{dD}{dN}\right)^i_{crit}} \tag{4.8}$$

6 The number of cycles elapsed is updated to:

$$N = N + \Delta N^i \tag{4.9}$$

7 The increment in damage for each element during the current block of cycles is then given by:

$$\Delta D^i_j = \left(\frac{dD}{dN}\right)^i_j \Delta N^i \tag{4.10}$$

8 The damage states for each element at the start of the next block of cycles are updated to:

$$D^{i+1}_j = D^i_j + \Delta D^i_j \tag{4.11}$$

9 The elastic moduli are modified at the start of the next block of cycles according to:

$$E^i_j = E_0(1 - D^i_j) \tag{4.12}$$

The value of ΔD is an input of the algorithm and ΔD is the maximum damage increment for each block of cycles. A small value of ΔD will increase the computation time and the accuracy of the method. Moreover, to be in perfect agreement with Moghaddam et al. [MOG 15b], the value of ΔD is set to 0.01. It takes ten loading cycles to transform a first element from martensite to ferrite.

4.2.2 Integration of the damage model in the contact algorithm

The damage model defined in section 4.2 is coupled with the semi-analytical contact solver developed by Nelias and co-workers [GAL 10, LER 10, KOU 14b]. In order to take into account the local damage of the matrix, a cuboidal heterogeneity is added at each damaged location as an enrichment technique as in Chapter 3. The Young modulus of the added heterogeneity corresponds to the locally damaged Young modulus of the matrix and the size of the cuboidal heterogeneity is the same as the discretization of the half-space (see Fig. 4.5). At the beginning of each time step of the loading cycle, Eshelby's equivalent inclusion solution is computed to take into account the modifications of the material parameters on the contact solution. A flowchart of the solver algorithm to explain the coupling between the contact solver and the damage model is presented in Fig. 4.6.
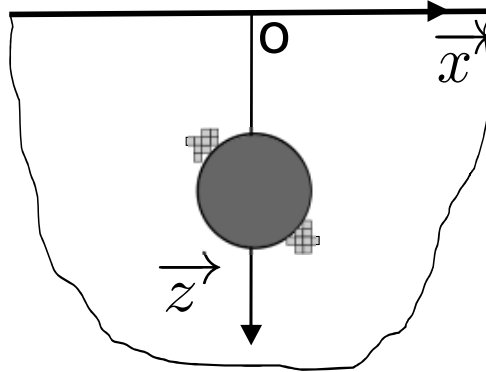
Figure 4.5: Illustration of the enrichment technique using cuboidal inclusion around a central spherical inclusion.
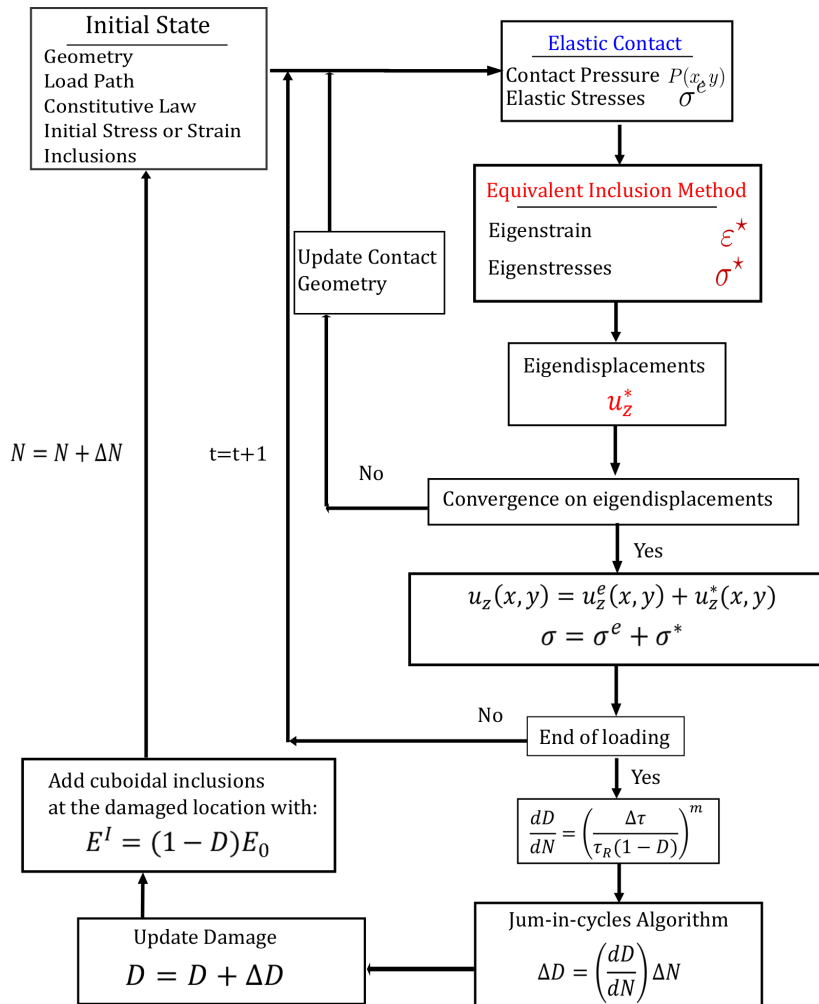

Figure 4.6: Flowchart of the coupled contact solver and damage model

## 4.3 Results

4.3.1 Description of the problem

The rolling of a 3D rigid cylinder on an elastic damageable body with a spherical inclusion is investigated (Fig. 4.7). The radius of the cylinder is $R = 5.5$mm and its length in the Y-direction is $L_Y = 0.16$ mm. A normal load $W = 55$ N is applied on the cylinder. The half-space Young's modulus and Poisson's ratio are chosen as $E_0 = 200$ GPa and $\nu_0 = 0.3$, respectively. For the homogeneous half-space, this load leads to a contact half width $a^* = 0.1$ mm and a maximum contact pressure $P_0 = 2$ GPa. One should note that the dimension of the contact in the Y-direction is approximately 16 times larger than the contact half width. A spherical inclusion with a diameter $d_{inc} = 0.16a^*$ is placed at the center of the domain at a depth $z_I = 0.5a^*$. The inclusion Young modulus is chosen to be $E_I = 300$ GPa and its Poisson's ratio $\nu_I = 0.3$ to be consistent with Al_2O_3 oxide inclusions. The loading moves from left ($x < 0$) to right ($x > 0$), maintaining the normal load constant, on a distance equal to $2a^*$ decomposed into 21 time steps. The tangential displacement at each time step is equal to $0.1a^*$. The value of the coefficient of friction is chosen to be $\mu = 0.05$ and the direction of surface traction is opposite to the over rolling direction (which corresponds to the driven surface). The loading and material parameters are consistent with the ones in Moghaddam et al. [MOG 15b]. Note that the computation being elastic, only the direction of surface traction has an influence on the results. The half-space is discretized in $225 \times 71 \times 45$ computation points such that the space between points is $2\Delta x = 2\Delta y = 2\Delta z = 0.04a^*$. As in Moghaddam et al. [MOG 15b] simulations are stopped when a second pair of wings is appearing. Quiñonez [QUI 19] computed a similar model with a coupled EHL and 3D finite element simulation with a subsurface inclusion. Their model is made of $193 \times 385 \times 129$ points and for every time step, computation time is found to be about 1 hour with a 2.6 Ghz CPU and 16 GB RAM. The proposed method is found to be around 40 times faster at solving the same kind of problem.
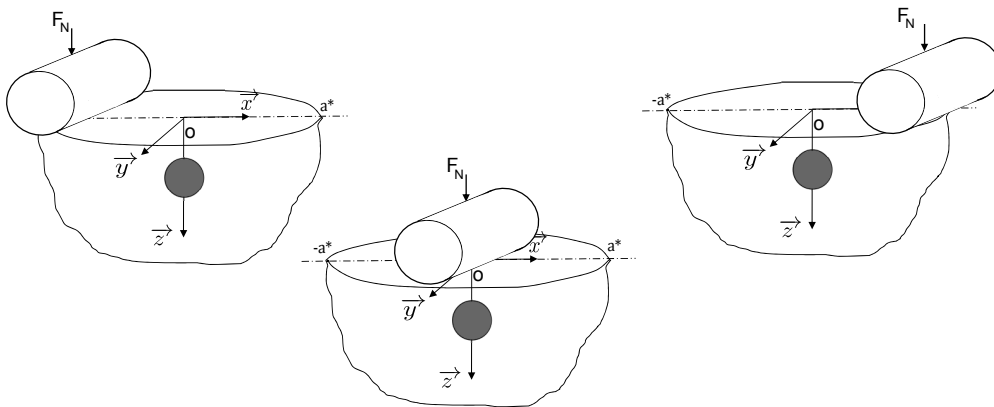
Figure 4.7: 3D view of the rolling of a cylinder on a elastic half-space with a spherical inclusion.

An important difference between the model proposed by Moghaddam et al.

[MOG 15b, MOG 16b] and the results presented here is the presence of a coupling between the contact solver and the heterogeneous material which permit to take into account the effect of the inclusion on the contact pressure [LER 10, LER 11, LER 13, KOU 14b, KOU 14a, KOU 15a, KOU 15b, AMU 16]. Furthermore, the 3D model in Moghaddam et al. [MOG 16b] is using a Voronoi tesselation to represent the microstructure of the material around the inclusion.
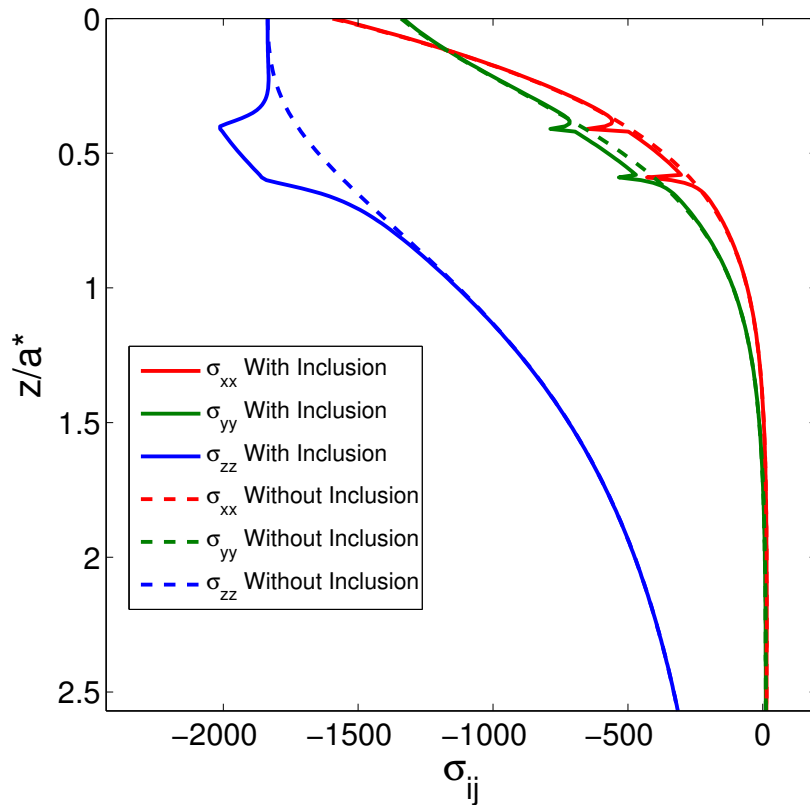
Figure 4.8: Effect of the presence of a spherical inclusion located at $z_{inc} = 0.5a^*$ under the surface on the stresses at the center of the contact. Note that here the inclusion is 1.5 times harder than the matrix: $E_I = 300GPa$, $E_0 = 200GPa$.

Moghaddam et al. [MOG 15b] found that in order to describe butterfly formation as a stress-based fatigue phenomenon, one should take into account the stress history of the material during each loading cycle and, in particular, the alternating shear stresses. In 3D, the value of these stresses should be calculated in all the different planes around the inclusion in order to find the plane of maximum alternative shear stress. But Weinzapfel et al. [WEI 11] have shown that the plane of the maximum shear stress around a spherical inclusion during a rolling cycle is the XZ-plane. In the following simulations, the computation of the alternating shear stress, $\tau_{alternating}$, and of the mean shear stress, τ_{mean}, will use the shear stress in the XZ-plane, τ_{xz}.

The effect of the inclusion on the stress field is decreasing with the distance from its center. Therefore the computation of the alternating shear stress and of the damage evolution will be limited to a square REV with the inclusion in its center and a size $L = 3 * d_{inc}$ (see Fig. 4.9). Other authors studied line contact by periodically duplicated the contact pressure solution in the Y-direction to simulate line contact on rough surfaces [REN 09] and with periodically distributed inclusions [ZHO 16]. One should note that in the present study, dimension of the contact in the Y-direction is more than 30 times the size of a REV side length. Hence no duplicating technique is needed here. The alternating shear stress, the absolute mean stress and the resulting delta stress after one rolling cycle are represented in Fig. 4.10.
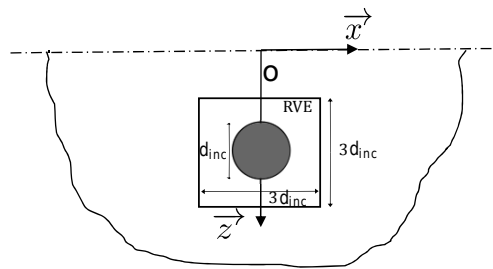
Figure 4.9: View of the REV around the spherical inclusion

The alternating shear stress in Fig. 4.10(a) shows high amplitude in four regions around the inclusion and the absolute mean stress shows two maximum amplitude stress at top left and bottom right of the inclusion (see Fig. 4.10(b)). The absolute mean stress around the inclusion is influenced by the presence of surface traction (see Fig. 4.10(b)).

While the alternating shear is the more critical for butterfly formation, the mean shear stress is influenced by surface traction and therefore is giving the butterfly propagation's direction. One can observe that the sum of these two components is showing two regions with higher amplitude giving the direction of the wing formation as shown in Fig. 4.10(c). These results correlate well with the stress distribution found by Moghaddam et al. [MOG 15b].

4.3.2   Wings initiation and propagation

Most of the previous numerical results of the literature have been done in 2D [ALL 10, CER 15, MOG 15b] but the actual model is in 3D and allows to observe the propagation of the butterfly wings around the inclusion in the same way as in [MOG 16b]. The formation and growth of the wings around the inclusion is shown chronologically in Fig. 4.11. Each red cuboid corresponds to a zone where the microstructural transformation happened and an heterogeneity with a Young's modulus $\tilde{E} = 0.9E$ is introduced. It can be noted that the wings grow both in the planes XZ and XY.

The damage distribution is shown in different planes of the half-space parallel to the rolling direction (see Fig. 4.12). It can be observed that the damage increases out of the
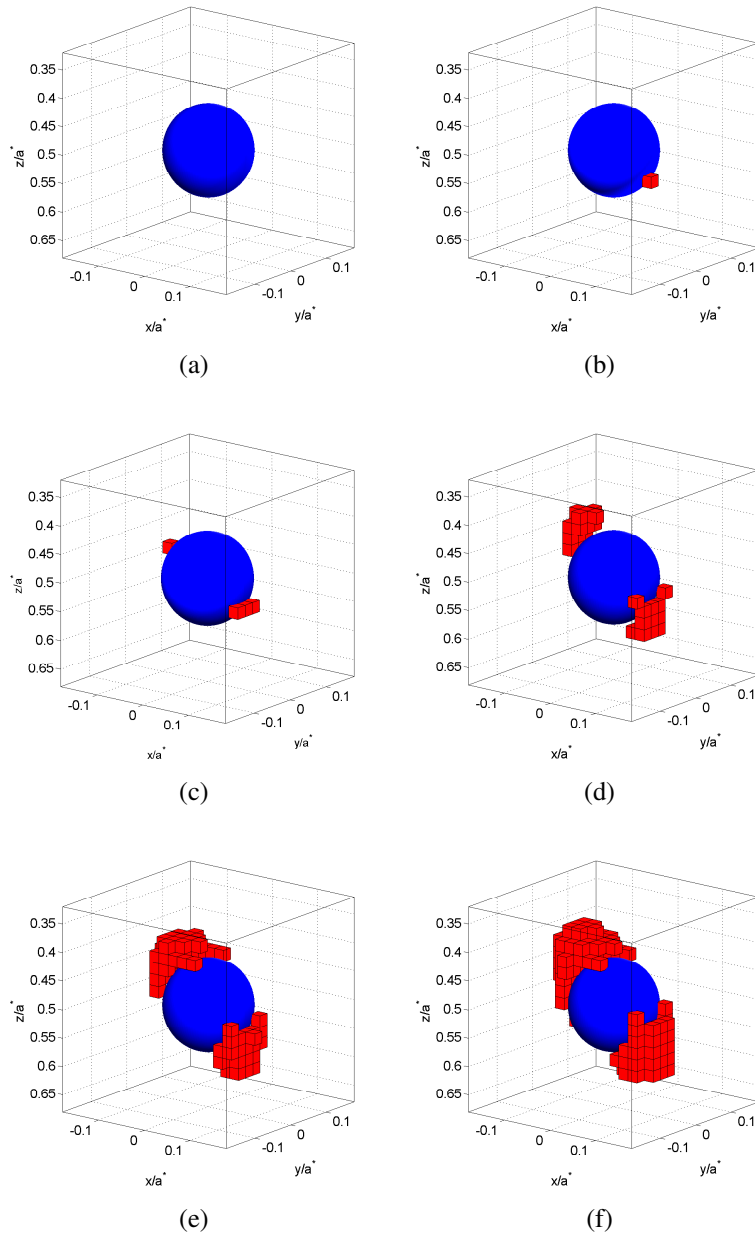
(a)

(b)

(c)
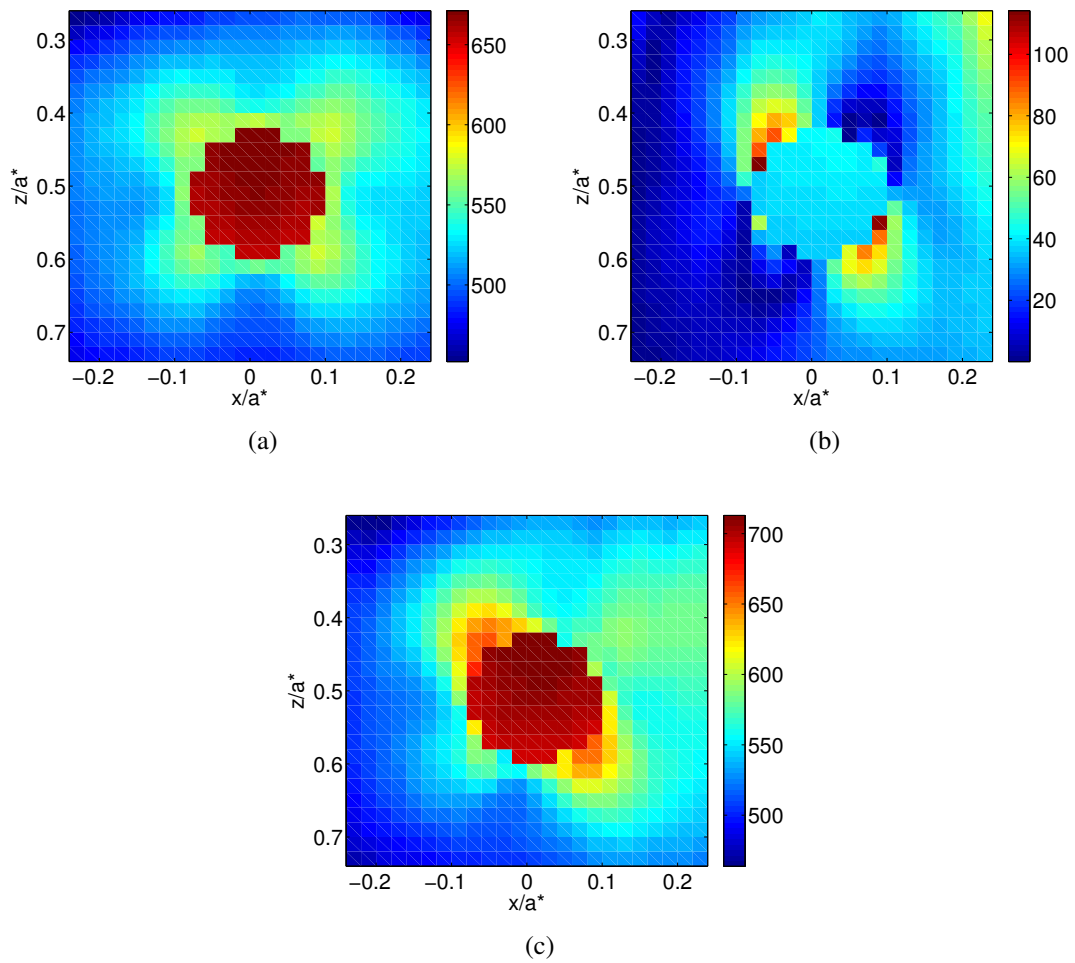
Figure 4.10: Alternating shear stress $\tau_{alternating}$ (a), absolute mean shear stress $|\tau_{mean}|$ (b) and their summation $\Delta\tau$(c) in MPa during one load pass over a half-space in the plane $y = 0$.

Figure 4.11: Chronological order of butterfly initiation and evolution in 3D with inclusion depth $z_{inc} = 0.5a^*$.

plane of maximum alternating shear stress around the inclusion (see Fig. 4.12(d)). As observed in Fig. 4.11 and Fig. 4.12, butterfly wings seem to propagate in a direction transverse to the rolling direction. This phenomenon could explain some experimental observation in the open literature of inclusion-less butterflies [LUN 10].

It should be noted that in the model proposed by Moghaddam et al. [MOG 16b], the volume around the inclusion is discretized using a Voronoi tessellation technique. In the semi-analytical solver, the volume is discretized in small cuboids to compute the stress field. That is why the representation of the damage around the inclusion and the inclusion itself demonstrates a non-smooth interface in Fig. 4.12. In the semi-analytical method, the discretization size needs to be constant in the domain [POL 99] and its size is equal to $0.04a^*$. In the FE model of Moghaddam et al. [MOG 15b], four different mesh densities are used and in the REV of the inclusion, the mesh size is equal to $0.008a^*$. The results obtained are compared with both the experimental results of Takemura [TAK 01] and the results of Moghaddam et al. [MOG 15a] in order to determine when butterflies wings appear during the life of the bearings. Takemura studied fatigue life of bearings made of AISI 52100 steel with more than 400 tests. He reported the life of bearings related to butterfly wings formation around oxide inclusions. Three different loadings corresponding to a maximum Hertzian pressure of 2.0, 3.0 and 4.0 GPa are used to compare the butterfly initiation life with the one in [MOG 15b, TAK 01]. The initiation life is taken when the damage variable reaches for the first time the value $D = 0.1$ and plotted in Fig. 4.13.
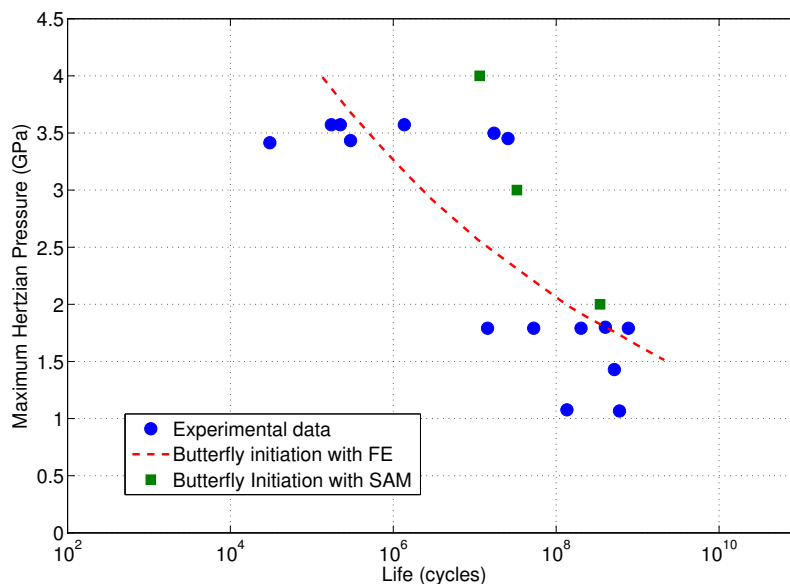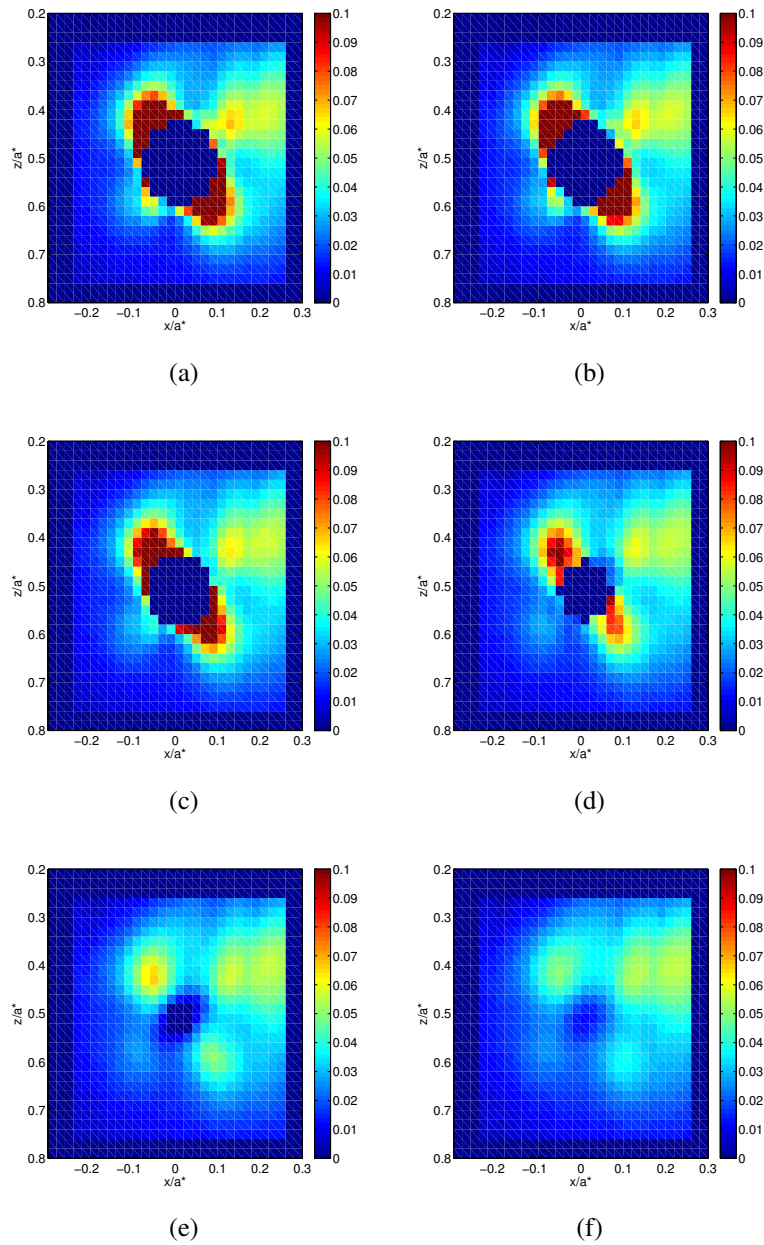

Figure 4.13: S-N curve for butterfly initiation comparing results from experimental data [TAK 01], finite element [MOG 15a] and semi-analytical simulations.

When the maximum Hertzian pressure is increasing, the shear stress becomes larger in the material and the number of cycles leading to initiation of butterfly wings is decreasing.

Figure 4.12: Sectioning of the damage variable D around an inclusion at $z_{inc} = 0.5a^*$ in different planes parallel to the rolling direction. (a) Plane y=0 (b) Plane y=0.04a^* (c) Plane y=0.08a^* (d) Plane y=0.12a^* (e) Plane y=0.16a^* (f) Plane y=0.2a^*.

It can be observed that the model closely matches the results of finite element simulation and the experimental results for load around 2.0 GPa but is less conservative than the numerical results of Moghaddam et al. [MOG 15b] for higher loads. This difference could come from the difference in the discretization between the two simulations. A larger discretization in the simulation results in computing the level of stress on a larger volume of the solid in the semi-analytical method. Stress gradients are averaged in the element volume. Thus the average stress field on the element volume is lower and leads to a larger jump in the cycles and therefore to a larger initiation life as observed in Fig. 4.13. For all loadings, the results obtained with the semi-analytical results are in good agreement with the experimental results of Takemura [TAK 01].

4.3.3 Effect of inclusion depth

The effect of the inclusion depth was investigated experimentally by Lund [LUN 10], Grabulov [GRA 07] and Evans [EVA 13b]. Evans results were compared by Moghaddam et al. [MOG 15b] using the damage FE model. They showed that for an inclusion close to the surface (between $0.2a^*$ and $0.5a^*$), the lower wing is more developed and for an inclusion between $0.5a^*$ and $0.8a^*$, the upper wing is larger. However it should be recalled that in their models it is assumed that the presence of the inclusion does not influence the contact pressure distribution. This hypothesis does not hold when the inclusion is close to the surface, i.e. when $z_{inc} < a^*$ [LER 10, LER 11, LER 13, KOU 14b, KOU 14a, KOU 15b, KOU 15a, AMU 16].

In the current study, five different inclusion depths have been investigated: $0.2a^*$, $0.3a^*$, $0.4a^*$, $0.5a^*$ and $0.6a^*$. The results for the damage distribution shown in Fig. 4.14 are in good agreement with those of Moghaddam et al. [MOG 15b] and the 3D shape of the wings around the different inclusions is shown in Fig. 4.15. For an inclusion stiffer than the matrix and close to the contact surface ($z_{inc} < 0.5a^*$) the lower wing is more developed than the upper wing (see Fig. 4.14(a) and Fig. 4.14(b)). Moreover, it can be noted that when an inclusion is located at $0.3a^*$, no upper wing is appearing during the rolling cycles 4.15(a). For an inclusion at a depth larger than $0.5a^*$, the upper wing is more developed (see Fig. 4.14(d)) and a third wing is appearing on the top of the inclusion. It comes from the fact that the effect of surface traction decreases when the inclusion's depth becomes larger. Thus the alternating shear stress becomes predominant over the absolute mean stress, leading to the appearance of a second pair of wings (see Fig. 4.14(d)). The depth of an inclusion determines how the wings expand and can lead to cracks and damage of the roller bearings.

### 4.3.4 Effect of inclusion stiffness

Simulations have been performed with an inclusion softer than the matrix ($E_I = 10$GPa) and with the same parameters than presented in section 4.3.1. After one rolling cycle, the delta shear stress $\Delta\tau$ is found to be maximum at four localization around the inclusion (see Fig. 4.16) but obtained results show that no damage propagation in the form of butterfly
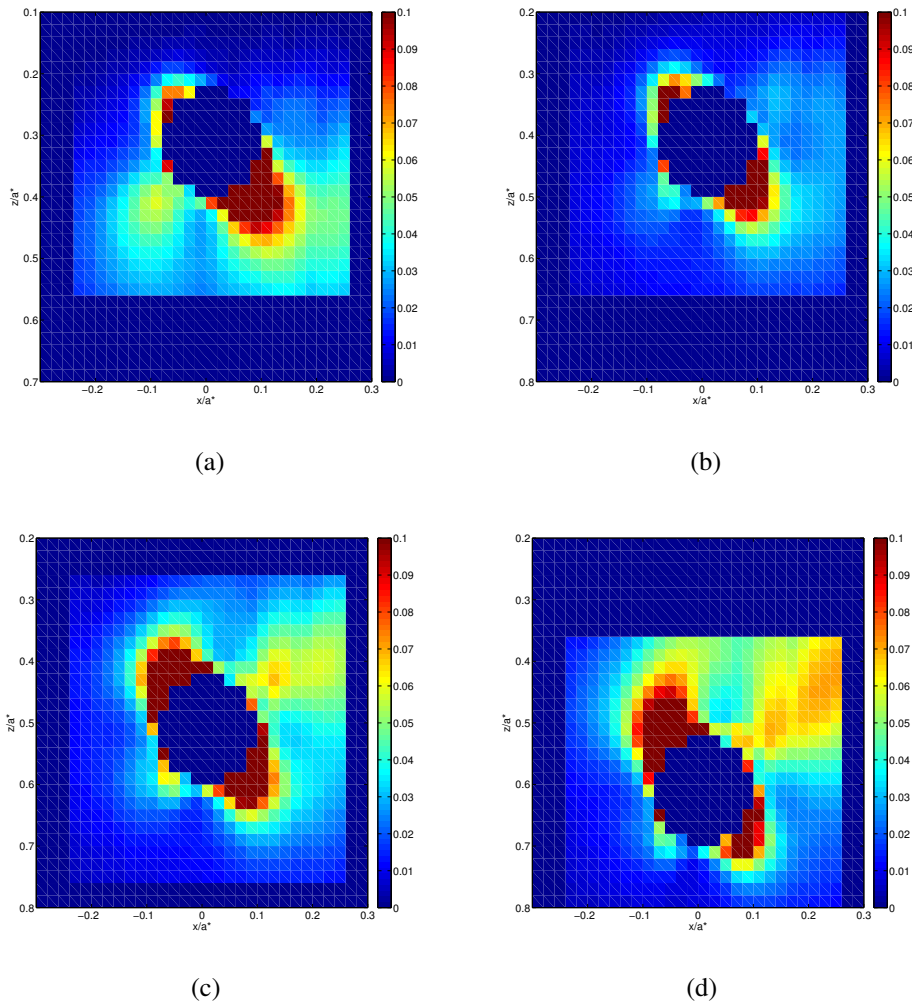
Figure 4.14: Damage variable D in the plane $y = 0$ with inclusion depth (a) $z_{inc} = 0.3a^*$ (b) $z_{inc} = 0.4a^*$ (c) $z_{inc} = 0.5a^*$ (d) $z_{inc} = 0.6a^*$. The inclusion considered is 1.5 times stiffer than the matrix.
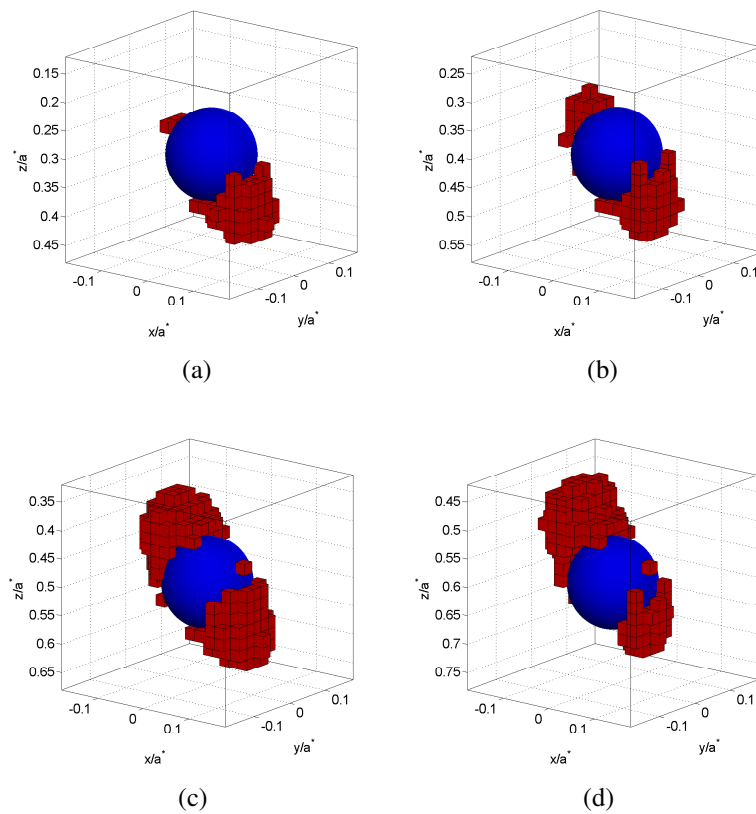
Figure 4.15: Butterfly wings around a spherical inclusion with inclusion depth (a) $z_{inc} = 0.3a^*$ (b) $z_{inc} = 0.4a^*$ (c) $z_{inc} = 0.5a^*$ (d) $z_{inc} = 0.6a^*$. The inclusion considered is 1.5 times stiffer than the matrix.

wings is observed with the model. In fact, the presence of a soft inclusion in the matrix is decreasing the stress in the region around the inclusion while a high stress gradient is appearing at the interface between the inclusion and the matrix. Hence, a debonding phenomenon may occur at this location, not taken into account in the current model.
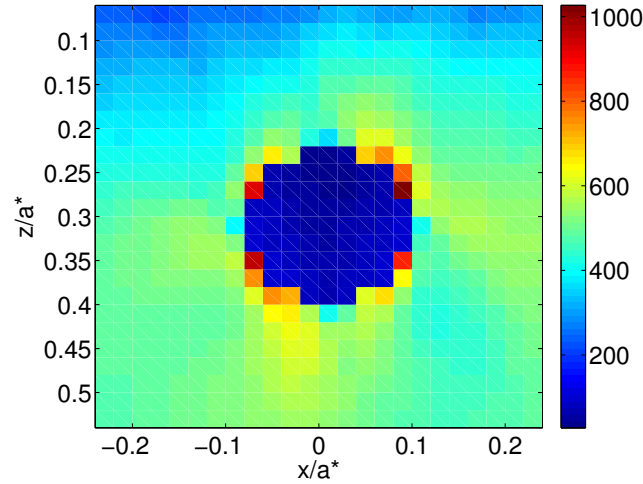
Figure 4.16: Delta shear stress $\Delta\tau$ in MPa in the plane $y = 0$ with a very soft inclusion $E_I = 10\text{GPa}$.

4.3.5 Effect of butterfly initiation on contact pressure

One of the main differences between the FEM simulation proposed by Moghaddam et al. [MOG 16b] and the semi-analytical solver proposed here is the coupling between the contact solver and the heterogeneous half-space. In the model of Moghaddam, a Hertzian contact pressure is imposed as an input of the simulation and no effect of the inclusion nor the damage of the material is affecting the contact solution. Leroux et al. [LER 10, LER 11, LER 13] and Koumi et al. [KOU 14b, KOU 14a, KOU 15a, KOU 15b] have shown that the contact pressure distribution may be significantly modified by the presence of inhomogeneities close to the surface ($z_{inc} < a^*$), which subsequently affects the subsurface stress distribution (see Fig. 4.8 and Fig. 4.17).

In order to highlight the effect of the presence of an inclusion on the contact pressure, simulations have been realized with an inclusion very close to the contact surface ($z_{inc} = 0.2a^*$) and with two different Young's modulus. One can define γ as the ratio between the inclusion and the matrix Young's moduli. A hard inclusion with $\gamma = 1.5$ as in section 4.3.1 is compared to a soft inclusion with $\gamma = 0.05$. Contact pressure when the contact load is just over the inclusion is plotted for both inclusion ratio in Fig. 4.17. In presence of a hard inclusion, a peak of pressure is observed. The maximum contact pressure is around 10% higher than the Hertzian pressure. With a soft inclusion, a local drop of contact pressure of almost 50% is observed. Influence of the depth of the inclusion on the contact pressure is also observed in Fig. 4.18. In the case studied here, it must be noted that inclusions are

really small compared to the contact half width ($d_{inc} = 0.16a^*$) and the contact pressure is affected only when the inclusion is close to the contact surface.
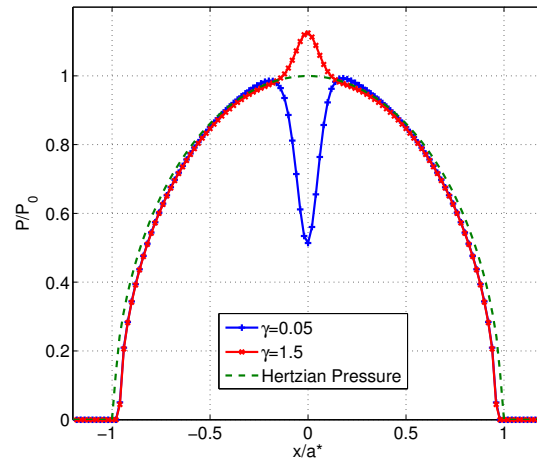

Figure 4.17: Influence of the inclusion stiffness ratio $\gamma = E_I/E_M$ at a depth $z_{inc} = 0.2a^*$ on the contact pressure in the plane $y = 0$. Inclusion's diameter is $d_{inc} = 0.16a^*$.
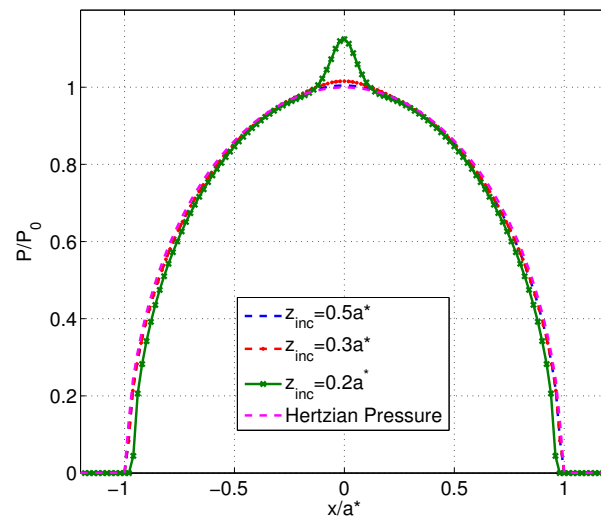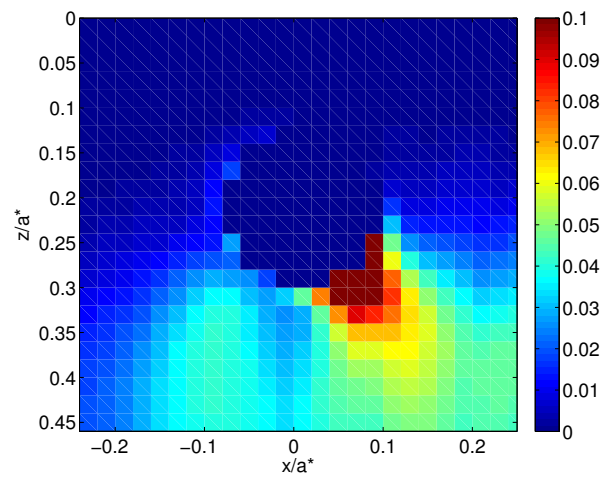

Figure 4.18: Comparison of the contact pressure with a spherical inclusion under the center of the contact for different inclusion's depth. Inclusion's diameter is $d_{inc} = 0.16a^*$ and 1.5 times stiffer than the matrix ($E_I/E_0 = 1.5$).

During the formation of butterfly wings, the microstructural transformation appearance modifies the response of the material when the loading is rolling over the domain. The introduction of small heterogeneities around the inclusion modifies the stress field in

the material. Computation have been performed with a inclusion depth of $z_{inc} = 0.2a^*$. Contact pressure over the damaged area is locally found to be slightly decreasing with the formation of the wings (see Fig. 4.19). This is due to the fact that the metallurgical transformation is associated with a local decrease of the Young modulus (by 10%. This effect is localized due to the small area concerned but is increasing with the evolution of the wings formation. As observed in section 4.3.3, only the lower wing is appearing in this case and consequently a small asymmetry is appearing in the contact pressure (see Fig. 4.19(a)). One can note that due to the small alteration of the material properties in the wings (a 10% decrease), the effect on the contact pressure is limited compared to the effect of the presence of a hard inclusion close to the surface. Finally, results show that the coupling between the heterogeneous contact solver and the damage model is not modifying the ability to predict butterfly formation with the damage model.
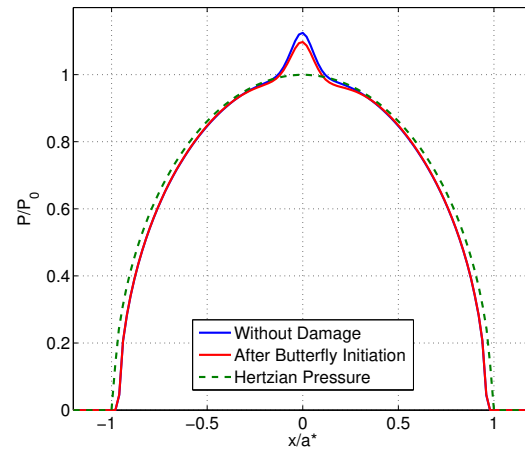
(a)

(b)

Figure 4.19: (a) Comparison of the contact pressure with a spherical inclusion of diameter $d_{inc} = 0.16a^*$ and 1.5 times stiffer than the matrix ($E_I = 300GPa$) under the center of the contact for a inclusion's depth $z_{inc} = 0.2a^*$ before and after wing initiation. (b) Butterfly wing appearance in the plane $y = 0$.

4.4 Application to rolling contact fatigue on indented surface.

The damage model studied in chapter 3 is applied to surface initiated damage during rolling contact fatigue. In particular, this study focus on damage occurring around indent as observed in Fig. 4.21 and called C-cracks. They often lead to the creation of a spall.

The rolling of a 3D sphere on an elastic damageable body with an artificial indent is investigated. The radius of the sphere is $R = 2.78$ mm. The half-space and the sphere are made of the same material with a Young's modulus and Poisson's ratio defined as $E_0 = 210$ GPa and $\nu_0 = 0.3$, respectively. A normal load $W = 25$ N is applied and for a homogeneous half-space, this load leads to a contact radius $a^* = 0.077$ mm and a maximum contact pressure $P_0 = 2027.5$ GPa. The loading moves from left ($x < 0$) to right ($x > 0$), maintaining the normal load constant, on a distance equal to $2a^*$ decomposed into 21 time steps. The tangential displacement at each time step is equal to $0.1a^*$. The value of the coefficient of friction is chosen to be $\mu = 0.05$ and the direction of surface traction is opposite to the over rolling direction (see Fig. 4.20). Note that the computation being elastic, only the direction of surface traction has an influence on the results. The half-space is discretized in $291 \times 121 \times 15$ computation points such that the gap between points is $2\Delta x = 2\Delta y = 2\Delta z = 0.085a^*$. The geometry of the dent is defined by a damped cosinus (see Eq. 4.13) that described a dent of $r = 0.065$ mm radius and of $d = 0.0032$ mm depth. No residual stress or plasticity is considered here.

$$hi(x,y) = hi(x,y) + 35cos\left[2\pi\frac{450}{r}\right]exp\left[-13\frac{r^2}{450^2}\right] \qquad (4.13)$$

The presence of an indent on one of the contacting surface is resulting in peaks of pressure around the indent when the load is moving over the surface (see Fig. 4.4). The corresponding Von Mises stress show high gradient located on the side of the indent (Fig. 4.23). Thus, the equivalent strain is computed during each step of the loading cycle resulting in an increment of damage at the end of every rolling cycle. The local Young modulus of the half-space is modified accordingly. This method has been fully detailed
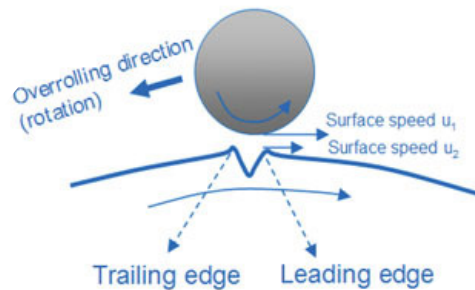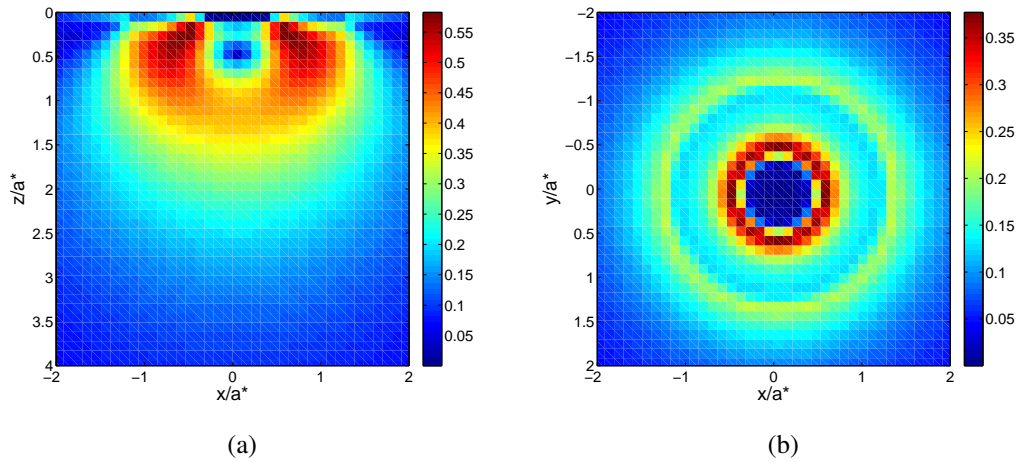

Figure 4.20: Definition of Over Rolling Direction [MOR 15]
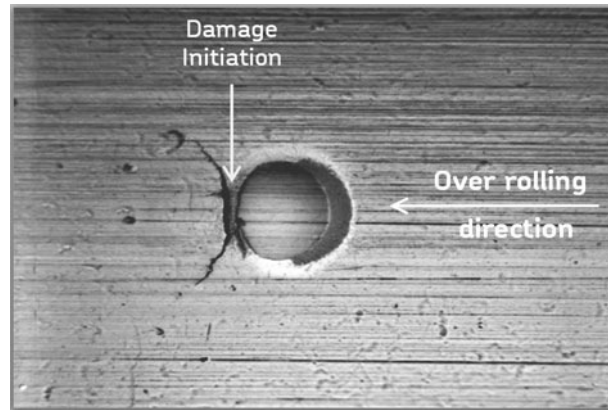
Figure 4.21: C-cracks around indent under rolling condition [MOR 15]
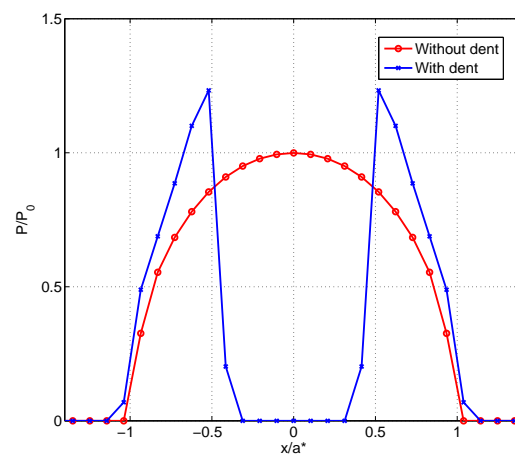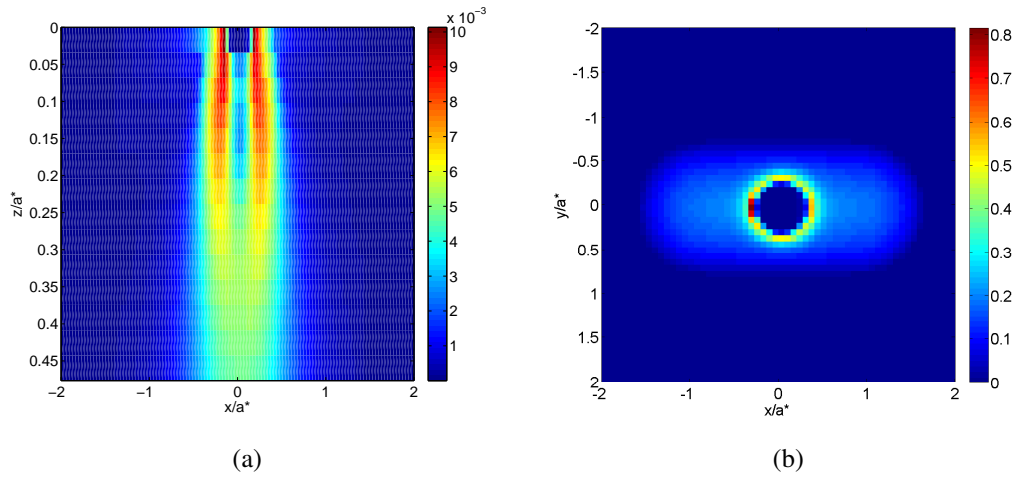

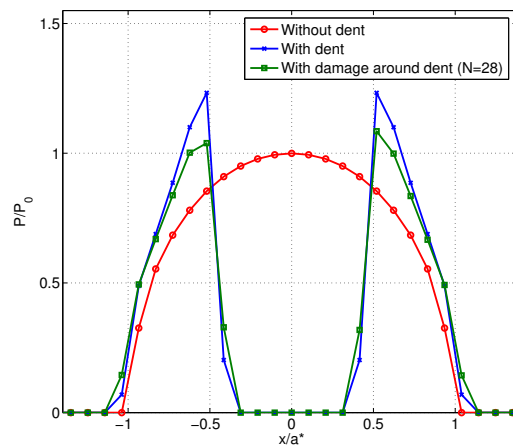**Figure 4.22:** Contact pressure on the indented surface

Figure 4.23: Dimensionless von Mises stress field σ_{VM}/P_0 in the contact over an indent (a) in the subsurface (b) on the top surface

in chapter 3. Equivalent strain when the load is over the indent is plotted in Fig. 4.24(a). Damage parameters are chosen arbitrarily and are equal to the one in chapter 3. Damage variable after 28 rolling cycles in the plane $z = 0$ (Fig. 4.24(b)) show a maximum on the left part of the indent at the same spot than the crack initiation spot in Fig. 4.21. Finally, the influence of damage on the contact pressure in the plane $y = 0$ is observed in Fig. 4.4 and results in a decreasing maximum pressure at the localization of the pressure peaks. Finally, this section suggests a new application of the semi-analytical solver for surface initiated damage in RCF. A good agreement is found between the maximum damage localization and crack initiation spot observed in the literature. Further study should focus on the effect of geometry and plastic strain around real indent.

(a)   (b)

Figure 4.24: (a) Equivalent strain at the end of the first rolling cycle. (b) Damage in plane $z = 0$ after 28 rolling cycles over the indent.

Figure 4.25: Contact pressure on indented surface without damage (blue line) or with damage after N=28 cycles (green line) and compared with contact pressure without presence of the dent.

4.5   Partial Conclusion

In this section, a numerical method has been proposed to model the effect of rolling contact fatigue on butterfly wings formation around a non-metallic spherical inclusion. A three-dimensional contact solver with an heterogeneous elastic damageable model is developed based on the Eshelby's equivalent inclusion method. Cuboidal inclusions are superimposed on the half space solution as an enrichment technique to represent the microstructural alteration around the spherical inclusion. The proposed method allows to couple the contact problem, the presence of heterogeneous inclusions and a stress-based damage evolution law. The computation cost of the damage evolution is improved through the use of a jump-in-cycles algorithm. The shape of the wings in 3D has been investigated for different inclusion depths. Moreover, the effects of the inclusion and of the wing propagation on the contact pressure due to the existence of a coupling in the solver have been highlighted. These effects represent one of the main advantage of the method, especially when inclusions are close to the surface (i.e between the surface and the Hertzian depth). A second section introduced an application of the method to surface initiation rolling contact fatigue. Preliminary results show the capacity of the damage model to predict the crack initiation spot around an artificial indent. The results obtained with both approach correlate well with results in the open literature [MOG 15b, MOG 16b, MOR 15]. The ability of modeling damage using the semi-analytical method has been emphasized. The following chapter presents some experimental work to better understand the tribological behavior of composite materials. The following results are needed to build a damage model adapted to this kind of material.

Chapter 5

Contact experiments on composite materials

In this chapter, several experimental testings on a woven composite material are presented with the aim of achieving a better understanding of their tribological behavior. In a first part, pin-on-disk tests between a composite disk and a steel ball are conducted followed by fretting tests with the same material configuration. In a second part, a few contact experiments at the scale of the macroscopic structure of the composite are presented. Results obtained in this chapter show the different tribological behaviors of each material constituent.

Contents

5.1 Introduction

Tests to identify the experimental behavior of woven composite materials under contact loading have been realized at the Mechanical Engineering Tribology Laboratory (METL) of Purdue University. The METL has developed different kinds of experimental approaches for fretting wear and fretting fatigue [LEO 12b, WAL 14, AHM 18]. Results presented in the previous chapter proved the ability of the semi-analytical method to reproduce damage behavior during fretting and rolling contact fatigue. The aim of these experiments was to understand the contact behavior of woven composite and to identify the damage mechanisms in fretting associated with this kind of materials. A lot of studies already exist on the fretting behavior of metallic alloys in contact [FOU 96, FOU 04, GAR 15, XIN 17]. Whereas most of the experimental studies concerning woven composite materials are realized by tensile tests [LOM 08, DOI 15a] or impacts [ELI 17], only a very few results are available in the literature about contact loading on woven composite materials [MAT 09, HUR 14, LI 18c]. Experiments can be divided in two parts, a first one with existing test rigs to understand the behavior and the damage phenomena of the composite materials and of its constituent under contact loading. Because the REV of the woven pattern is much larger than the REV of metallic alloy, some new experiments are conducted at a larger scale in a second part to better understand the macroscopic behavior of the composite material under contact. The following sections are presenting the different test rigs and the woven composite material used for the tests. Observations and results for pin on disk and fretting tests are presented followed by some preliminary results of contact at a larger scale.

5.1.1 Experimental test rig

Pin-on-Disk and fretting tests between a steel ball and a woven composite flat are conducted on a Bruker UMT Tribolab. A dual-axis force sensor is used to measure the friction force and the normal force simultaneously. The load sensor can measure a force in the range 2-200 N with a resolution of 2.5 mN. A reciprocating linear drive is used to move the flat plate against the stationary ball. For the Pin-on-Disk (see Fig. 5.5), a rotary drive is used that can reach a speed of 5000 rpm for the composite disk. In all the experiments with the Tribolab, rolling bearing balls are used. They have a diameter of half an inch ($\approx$12 mm) and are made in through hardened bearing steel AISI 52100 (with Young's elastic modulus $E = 210$ GPa and Poisson's ratio $\mu = 0.3$). Moreover, wear scars from the ball-on-flat configuration are scanned using an optical surface profilometry (ZeScope, Zygo Corp.).

Figure 5.1: Bruker UMT Tribolab
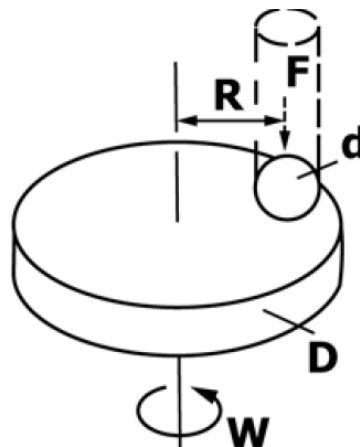
Figure 5.2: Description of Pin-on-Disk parameters

5.1.2   Woven composite sample

A plate of woven composite is used to realize the test. It's a 9 mm thick plate of a 2D woven composite composed of carbon fiber yarns and a polymer matrix. The distribution of yarns in each direction is 50% of yarns in the warp direction and 50% of yarns in the weft direction. Yarns have a width around 2mm and 0.5mm thick. The polymer matrix behavior is visco-elastic with a Young's modulus $E_{Matrix} = 4000$ MPa and a Poisson's ratio $\mu = 0.4$. Yarns are made of thousand of carbon fibers and have a transverse isotropic behavior with $E_{f3} = E_{f2} = 6777$ MPa and $E_{f1} = 186240$ MPa. Shear modulus are equal to $G_{f13} = G_{f12} = 5800$ MPa and $G_{f23} = 5300$ MPa and Poisson's ratio are equal to $\mu_{f13} = \mu_{f12} = 0.269$ and $\mu_{f23} = 0.3349$.
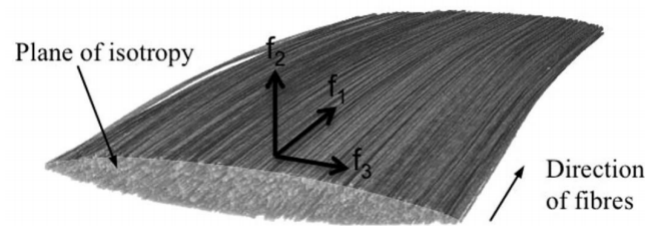
**Figure 5.3:** Transverse isotropy of yarn [NAO 15b].
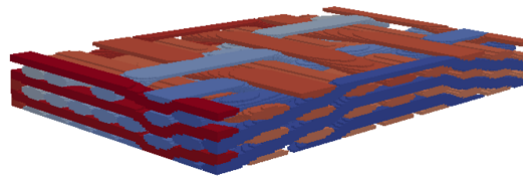
Figure 5.4: View at 45° of the woven composite material without the matrix.

5.2 Pin on disk

5.2.1 Description of the procedure

A pin-on-disk experiment was conducted using the Tribolab test rig. A small disk of composite was cut off the composite plate (see Fig. 5.5) and installed on the rotating driver of the Tribolab. A normal force is applied through the upper ball using a force sensor and the lower composite disk is rotating at a constant speed. Both the rotating speed and normal imposed load are kept constant during the test. This is guaranteed by a control loop of the test rig. Due to the dissimilar material properties of the composite, some jumps in normal load measurement are appearing when the contact area is moving from one phase of the composite to another. To ensure that the load is constant, a small rotating speed is needed to let enough time to the software to adjust the load. As observed in Fig. 5.2, the parameters of the test are the normal force imposed on the ball, the rotating speed and the radius of the track on the disk (distance between the center of the contact and the center of the disk). All experiments were conducted during 5000 cycles and at a linear speed 0.075 m/s. Moreover, experiments were conducted for different normal loads from 10N to 120N. It should be noted that each part of the disk is seeing the load the same number of time for each test but the ball has a different sliding distance for each test radius (see Table 5.1). As a consequence, the ball is more worn off for a bigger radius and the evolution of the contact pressure between the ball and the disk is not the same for every test.
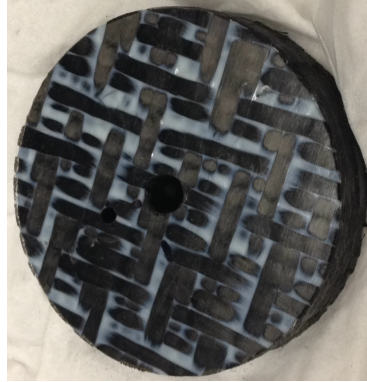
Figure 5.5: Disk made of woven composite material

Test number	Normal Load (N)	Track Radius (mm)
1	10	20
2	15	28
3	20	18
4	30	24
5	40	26
6	50	22
7	60	22
8	80	20
9	120	16

Table 5.1: Experimental settings.

5.2.2   Coefficient of friction

The dual-axis force sensor of the Tribolab allows to measure the friction force and the normal force simultaneously during the experiment. It is possible to determine the macroscopic coefficient of friction between the bearing steel ball and the composite disk and its evolution with cycles using Coulomb's law. The averaged coefficient of friction is plotted in Fig. 5.6 for different normal loads. It can be noted that the coefficient of friction is increasing from a value of $\mu = 0.1 - 0.3$ to a value of $\mu = 0.4 - 0.5$ during the first hundred cycles. It can be explained by the presence of a small coating of polymer matrix on the top surface of the disk that need to be worn off before reaching the normal composite structure. Moreover, the contact radius is predicted by the Hertzian theory to be around 0.9 mm which is much smaller than the yarn width (≈ 2 mm). Finally, results obtained here are giving an average of the coefficient of friction between the steel ball and each constituent of the woven composite.
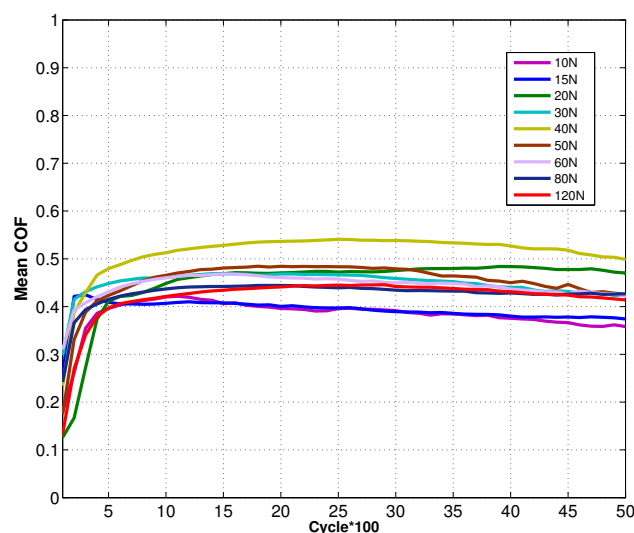

Figure 5.6: In-situ coefficient of friction between AISI 52100 steel ball and woven composite disk for different normal loads.

This macroscopic coefficient of friction is important for the industrial application because in the blade disk contact area both the yarns and the matrix are in contact. The advantage of the pin-on-disk experiment is to cover different zones of the composite surface and therefore to be able to get a good average value of the behavior of the composite. In section 5.3, COF between the steel ball and each constituent are determined.

5.2.3   In-situ wear depth

During the experiment, the normal load is kept constant and the normal position of the ball is measured using a proximity probe. Because of the wear of the surface, the vertical

position of the ball is moving to keep the contact loading constant. The evolution of the normal position corresponds to the in-situ measurement of the scar depth, that is to say the sum of the wear volume on both the ball and the composite disk surfaces. The in-situ scar depth is plotted for different normal loading amplitudes during test cycles in Fig. 5.7. One can note that the scar depth rate has an higher slope when the normal load is increasing.
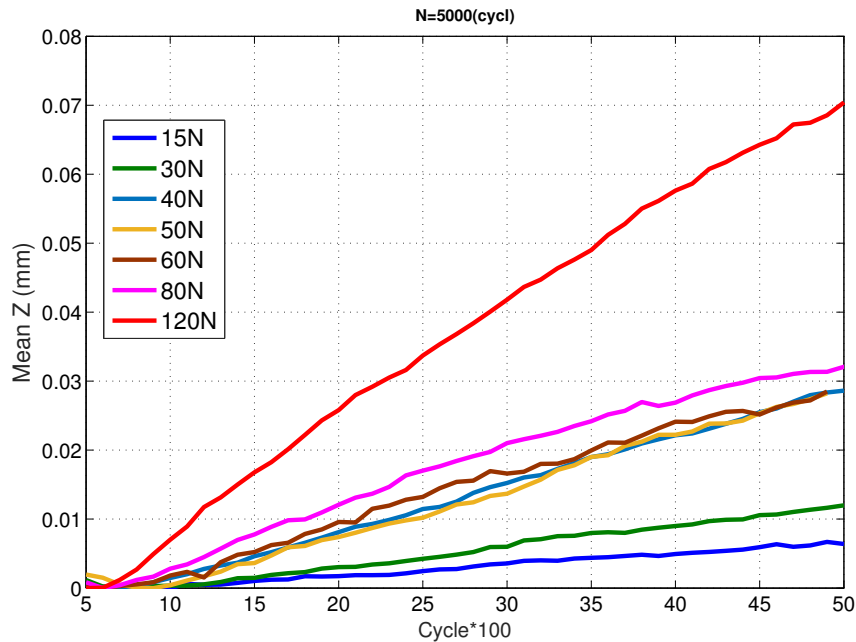
Figure 5.7: In-situ wear depth between AISI 52100 steel ball and woven composite disk for different normal loads.

A strong assumption is made that the different sliding distances seen by the ball has no effect on the results. It should be noted that in contrary to fretting loadings, the sliding direction is always the same during a pin-on-disk experiment. Unidirectional sliding results in a molecular alignment along the sliding direction and increase the wear resistance of the material [BRA 96].

5.2.4 Archard wear law identification

According to Archard's wear law [ARC 57], the wear volume is function of the normal load F, the sliding distance S, hardness of the softest contacting surface H and K a dimensionless constant.

$$V_W = \frac{K}{H}FS \tag{5.1}$$

It is possible to define a specific wear rate K_s in $mm^3.N^{-1}.m^{-1}$ [WIL 99] from the slope of the wear volume curve function of the sliding distance times the normal loading.

The wear volume is computed form the scar depth following the same method than in Ahmadi et al. [AHM 18] based on the ASTM G99 and on the assumption that wear depth is equally distributed between the ball and the composite. In order to identify the specific wear rate between steel and the 2D woven composite, the wear volume evolution is plotted against the normal force times the sliding distance for four different normal loads in Fig. 5.8. A linear regression is performed to obtain the specific wear rate and results are varying between $1.9 \times 10^{-7} < K_s < 5.17 \times 10^{-7} mm^3.N^{-1}.m^{-1}$. Specific wear rates in the literature for contact between steel and polymers are found to be around $9 \times 10^{-6} mm^3.N^{-1}.m^{-1}$ [UNA 04]. The results obtained here have lower specific wear rates due to the wear resistance of carbon fibers in our material [CHE 15]. Optical micrograph observations of the different contact regions are presented in Appendix D. A pin-on-disk test between a steel ball and a steel disk has also been performed and results are presented to validate the approach.

Finally, pin-on-disk experiments allow to obtain the coefficient of friction and wear depth when the ball is moving over matrix and yarn contact areas on the composite disk. Results are based on measurements of each constituent tribological behavior. They allow to obtain an average value of the tribological behavior of the composite material in unidirectional sliding. In the next section, fretting tests on individual composite's constituent are performed to better understand their surface damage mechanisms.
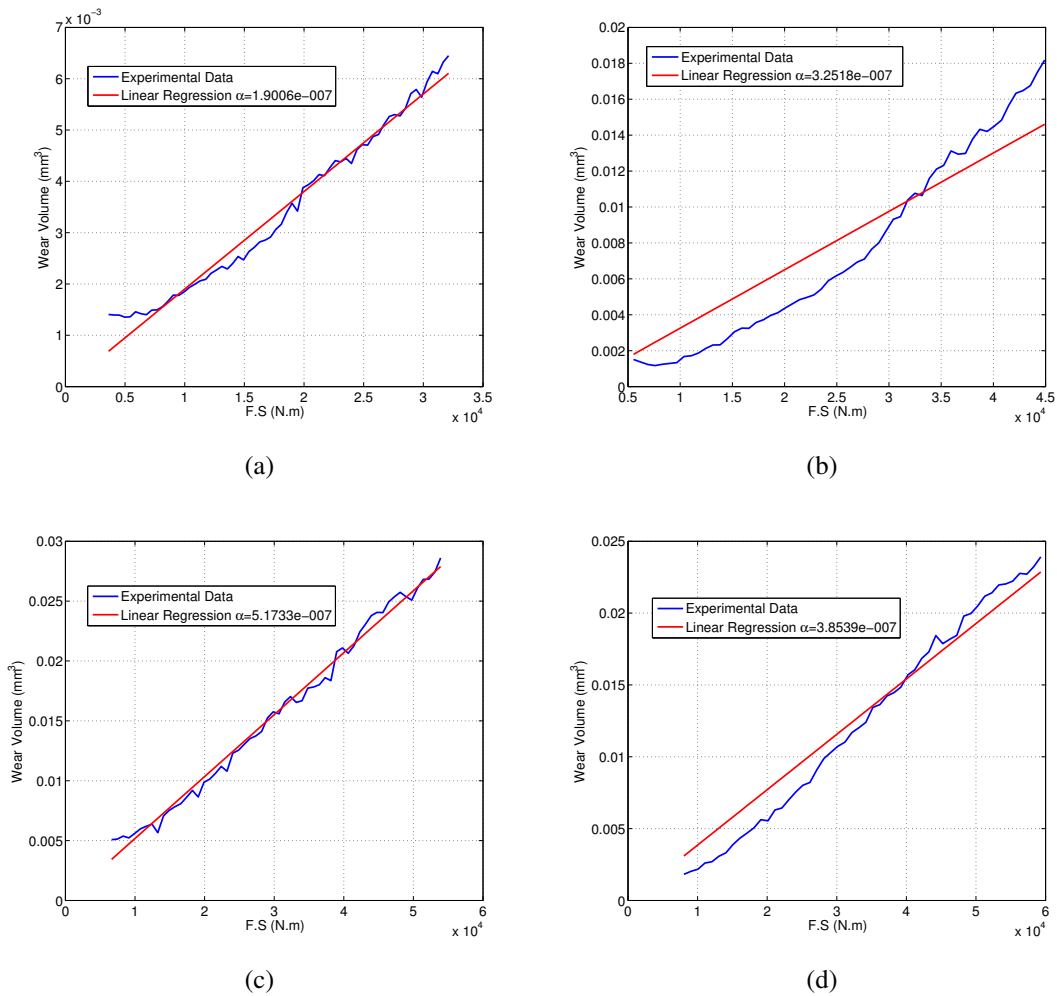
Figure 5.8: Wear Volume between AISI 52100 steel ball and composite disk function of the sliding distance and determination of the wear rate coefficient from a linear regression (α) for (a) 30 N (b) 50 N (c) 60 N (d) 80 N of normal load.

5.3 Fretting tests

5.3.1 Description of the procedure

In order to be closer to the conditions occurring between aircraft engine blade and disk, fretting experiments have been performed with the Tribolab test rig. A reciprocating linear drive is used to move a square part of woven composite against a stationary ball. A zero to peak displacement $\delta = 0.18$mm (stroke length of 0.36 mm) is applied with a frequency $f = 10$ Hz and feedback is ensured by a linear encoder of $1\mu m$ resolution. Experiments are performed for different normal loads but keeping the same tangential displacement. The normal load applied is ranging from 10 N to 40 N and is kept constant during the tests. Friction force and displacement amplitudes are measured during the experiments with a sampling rate of 2000 Hz. Each test is running for exactly 40000 cycles. One should note that performing test in the partial slip regime is very difficult. Imposed small displacements are accommodated by the deformation of the test rig and the contact is found to be only sticking. That's why all tests are performed in the gross slip regime and are performed either on yarn or on matrix surface. Contact radius a^* is around 0.3 mm which is almost ten times lower than a yarn width. Two pictures of the contact region are presented in Fig. 5.10 showing the size of the contact compared to the size of the composite structure. In order to understand the macroscopic behavior of the composite materials, contact experiments should be realized with a contact area containing both matrix and several yarns.
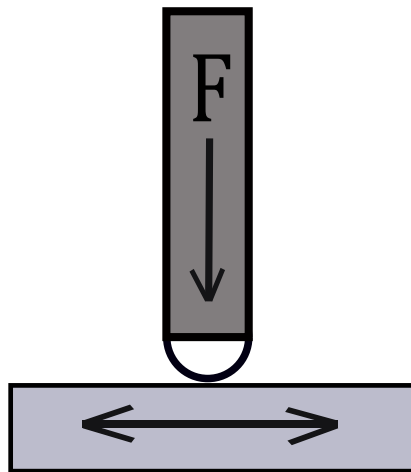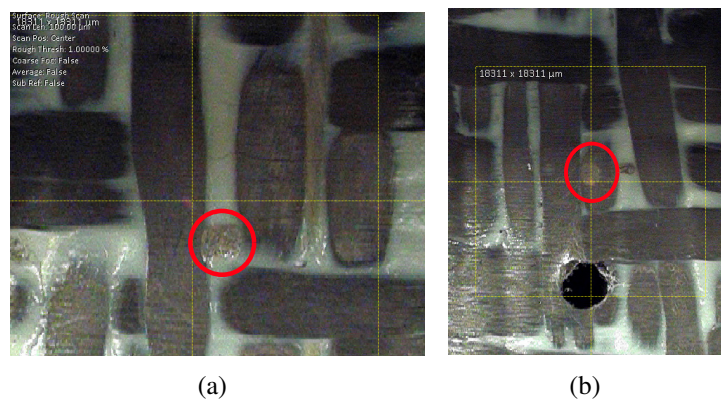

Figure 5.9: Schematic view of the fretting experiment.

| Test number	Contact zone	Normal Load (N)
1	matrix	10
2	matrix	15
3	matrix	20
4	matrix	40
5	yarn	15
6	yarn	20
7	yarn	25
8	yarn	30
9	yarn	40

Table 5.2: Experimental settings for fretting tests.

(a)   (b)

**Figure 5.10:** Fretting zone on composite: N=40000 Cycles and W=40N (a) Contact surface on matrix. (b) Contact surface on yarn.

5.3.2 Coefficient of friction

The coefficient of friction (COF) is plotted for contact on the matrix in Fig. 5.11 and for contact on a yarn in Fig. 5.12. The measured coefficient of friction is found to be $\mu \approx 0.55$ between the matrix and the AISI 52100 steel ball and $\mu \approx 0.25$ between carbon fiber's yarn and AISI 52100 steel. As observed during pin-on-disk tests, the coefficient of friction is increasing during the first thousand fretting cycles until the top surface matrix layer is worn-off. Then the coefficient of friction between the matrix and the steel ball is slowly decreasing after the first 10000 cycles in Fig. 5.11. This is probably a consequence of the increasing temperature in the contact region. In Fig. 5.12, a first phase when the coefficient of frictions between a yarn and the steel ball is stabilized is followed by a second phase starting after around 25000 cycles where the coefficient of friction is unstable. This phenomenon may come from the presence of wear debris in the contact area.

The macroscopic coefficient of friction found during pin-on-disk experiment in Fig. 5.6 is approximately the mean value ($\mu \approx 0.4$) of the two constituent's coefficient of friction. This result is in good agreement with the rule of mixture usually used to predict the COF of heterogeneous materials [TRI 10].One consequence of this result is that both constituents would be equally present on the top surface of the disk.
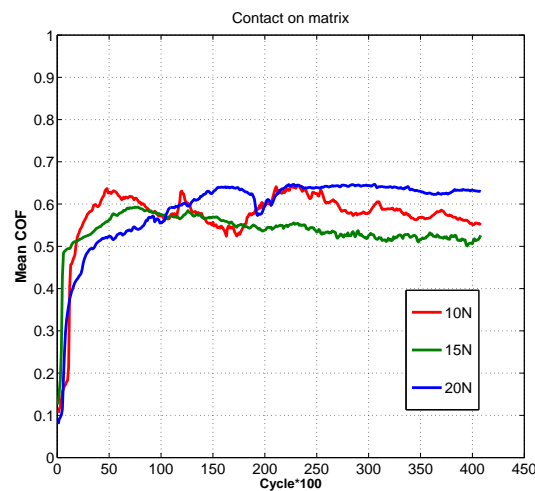
Figure 5.11: In-situ coefficient of friction between AISI 52100 steel ball and composite for different normal load vs. the number of fretting cycles. The contact spot is located on the matrix.
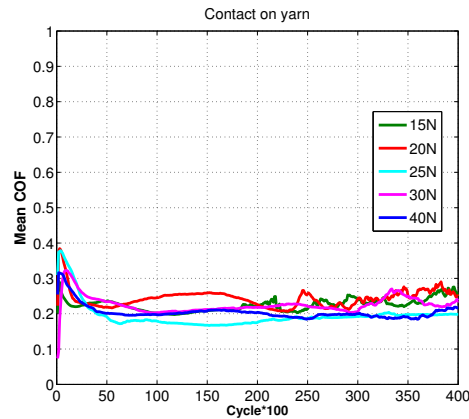
Figure 5.12: In-situ coefficient of friction between AISI 52100 steel ball and composite for different normal load vs. the number of fretting cycles. The contact spot is located on a yarn.

5.3.3 Fretting loops

In this section, fretting loops for a normal load $W = 20$N on a yarn and for $W = 30$N on the matrix are plotted at the beginning and at the end of the test. Measurements show a full sliding hysteresis loop at the beginning of the test but fretting loops are sometimes evolving toward a higher dissipated energy (see Fig. 5.13(a)) and exhibit a peak in the force at the end of the stroke. This phenomenon have been identified to be the consequence of material's build-up at the contact borders [FOU 04]. Sometimes fretting evolving toward a stick contact mode (see Fig. 5.13(b)). This stick mode is only observed when the contact is located on the matrix where the coefficient of friction is higher. One interpretation is that after some fretting cycles, the wear scar is deep enough to trap the steel ball and the tangential displacement is accommodated by the test rig arm deformation.

5.3.4 Optical micrograph observations

Observations with an optical surface profilometer have been performed on the contact surface of the composite and of the steel ball. Differences in the wear mechanisms are observable between the matrix and the yarns in Fig. 5.14 and Fig. 5.15 as in section 6.4. For contact on a yarn, the maximum scar depth is localized at the center of the contact area (see Fig. 5.15(c)) and for contact on the matrix, the maximum scar depth is found at the center of the contact on the composite but a transfer phenomenon of the wear particles on the ball happened. That is why the maximum scar depth on the steel ball is on the side of the contact zone in Fig. 5.14(a). Wear mechanism between steel and matrix seems to be adhesive while the wear mechanism between steel and yarn seems to be abrasive with creation of very thin wear particles. An example of moving from full sliding condition to sticking condition on the matrix is observed in Fig. 5.16. It can be noticed that wear particles are moving out of the contact and are piling-up at the contact edges on the com-
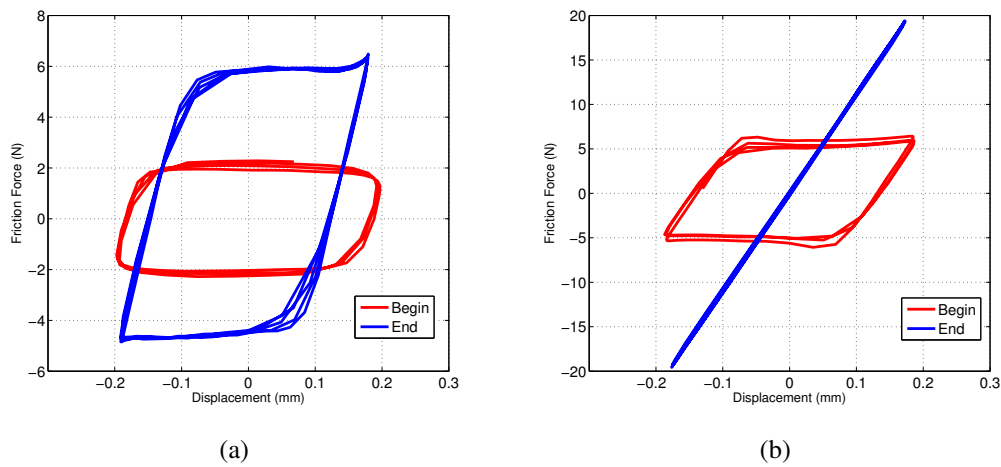
Figure 5.13: Fretting Loops at the beginning and end of the test after (a) W=20N on a yarn (b) W=30N on the matrix.

posite in Fig. 5.16(c). Moreover a wear scar is appearing on the edge of the contact zone on the ball surface in Fig. 5.16(a). This is a characteristic feature of stick-slip contacts for which the wear is localized in the slip annulus. Results presented in this section are giving an overview of the wear mechanisms of each constituent of the composite material during fretting loading. Finally, the results obtained in the previous sections show the differences between the coefficient of friction of each constituent in contact with a steel ball. Micrograph observations also allow to understand the tribological behavior of each constituent of the composite in fretting loading. The next section aims at obtaining the wear kinematics of these two constituents.

(a)

(b)

(c)

(d)
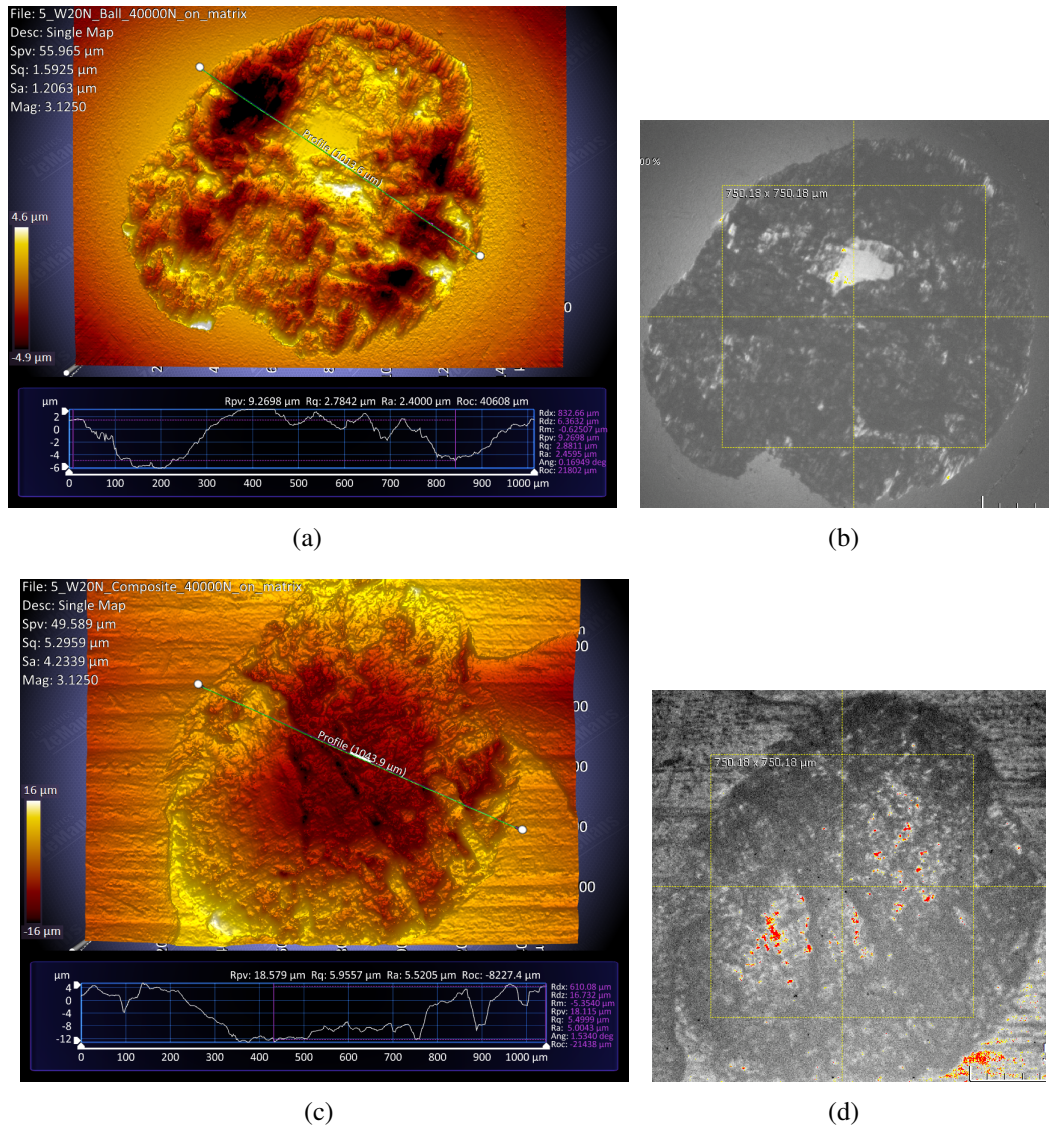
Figure 5.14: Adhesive wear scar showing transfer of material after full sliding fretting cycles on matrix: N=40000 Cycles and W=20N (a) Profilometer view of the contact surface on the steel ball. (b) Picture of the surface. (c) Profilometer view of the contact surface on the composite plate. (d) Picture of the surface.

(a)

(b)

(c)

(d)
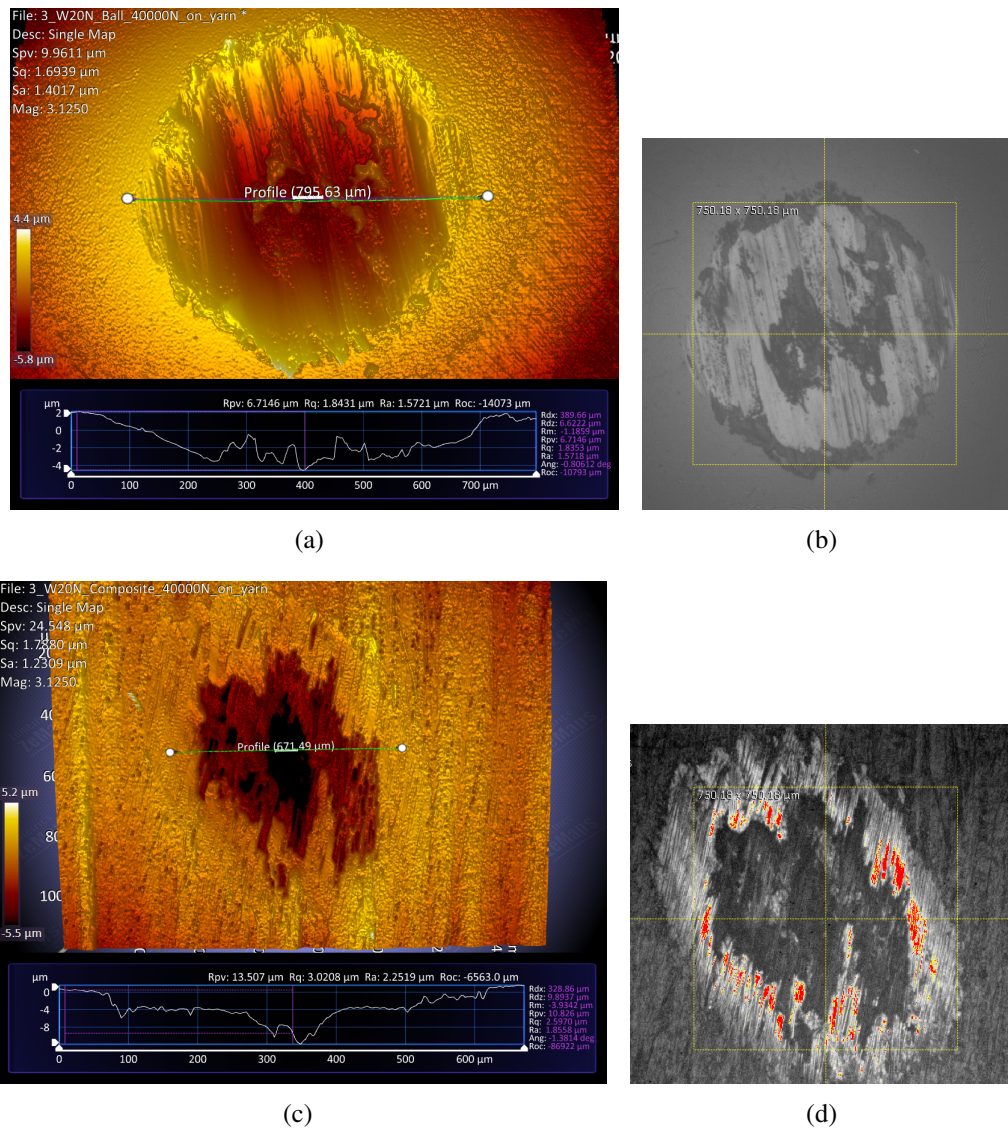
Figure 5.15: Abrasive wear scar showing wear particles at the edge of the contact area after full sliding fretting cycles on a yarn: N=40000 Cycles and W=20N (a) Profilometer view of the contact surface on the steel ball. (b) Picture of the surface (c) Profilometer view of the contact surface on the composite plate. (d) Picture of the surface.

Figure 5.16: Adhesive wear scar with transfer of material at the edge of the contact area after partial slip fretting cycles on matrix: N=40000 Cycles and W=40 N (a) Profilometer view of the contact surface on the steel ball. (b) Picture of the surface. (c) Profilometer view of the contact surface on the composite plate. (d) Picture of the surface.

5.3.5 In-situ wear depth

The wear depth is measured during each experiment following the same technique than in section 5.2.3. The wear depth function of the number of fretting cycles is plotted for different normal loads on the matrix in Fig. 5.17 and on the yarn in Fig. 5.18. Using these data, the specific wear rate can be identified for each constituent of the composite material. It should be noted that the wear depth during the contact with the yarns is very low and close to the resolution of the probe ($\approx 0.1\mu m$) leading to some important noise in Fig. 5.18. It may result in a lack of precision in the identification of the specific wear rate in Fig. 5.20.
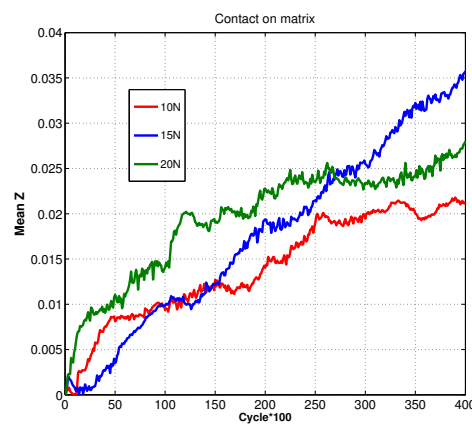

Figure 5.17: In-situ wear depth between AISI 52100 steel ball and composite for different normal load vs. the number of fretting cycles for a contact spot located on the matrix.
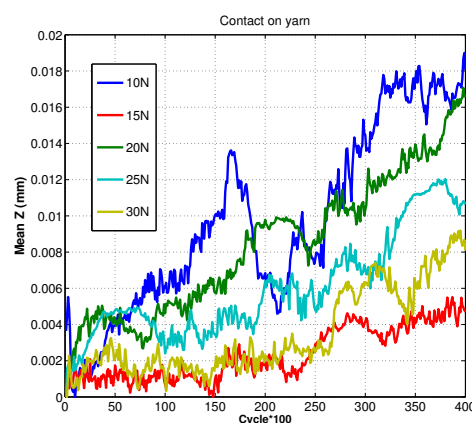
Figure 5.18: In-situ wear depth between AISI 52100 steel ball and composite for different normal load vs. the number of fretting cycles for a contact spot located on a yarn.

5.3.6 Archard wear law identification for yarn and matrix

Using the same method than in section 5.2.4, the specific wear rate is calculated from the measurement of the wear scar depth for each constituent of the matrix. The specific wear rate between the steel and the matrix is obtain from a linear regression in Fig. 5.19 and is found to be in the range $2.19 \times 10^{-4} < K_s < 2.9 \times 10^{-4} mm^3.N^{-1}.m^{-1}$. For the yarn, a specific wear rate in the range $7.27 \times 10^{-6} < K_s < 4.65 \times 10^{-5} mm^3.N^{-1}.m^{-1}$ is calculated from data in Fig. 5.20. As observed in section 6.4, yarns are more wear resistant than the matrix. Thus the specific wear rate is much lower for the yarns than for the matrix.

(a)   (b)
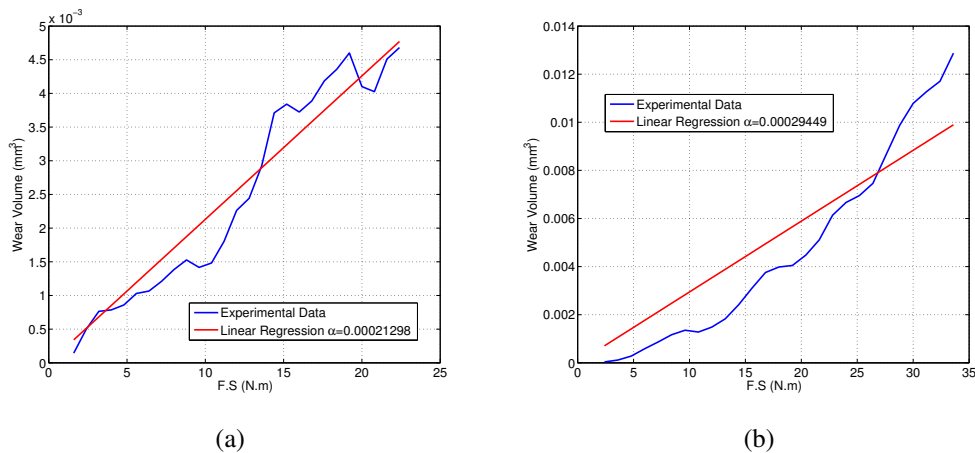
Figure 5.19: Fretting Wear Volume between AISI 52100 steel ball and the matrix of a composite material function of the sliding distance and determination of the wear rate coefficient from a linear regression (α) for a normal load equal to (a) 10 N (b) 15 N.

One should take into account that the contact area considered in these experiments is really small compared to the material structure's scale or RVE (Fig. 5.10). As a consequence, fretting experiments are not representative of the macroscopic behavior of the composite material and experiments with a larger contact area containing enough of both components, yarns and matrix, are necessary to understand the macroscopic fretting behavior between the composite blade and the metallic disk in the industrial application of this work.
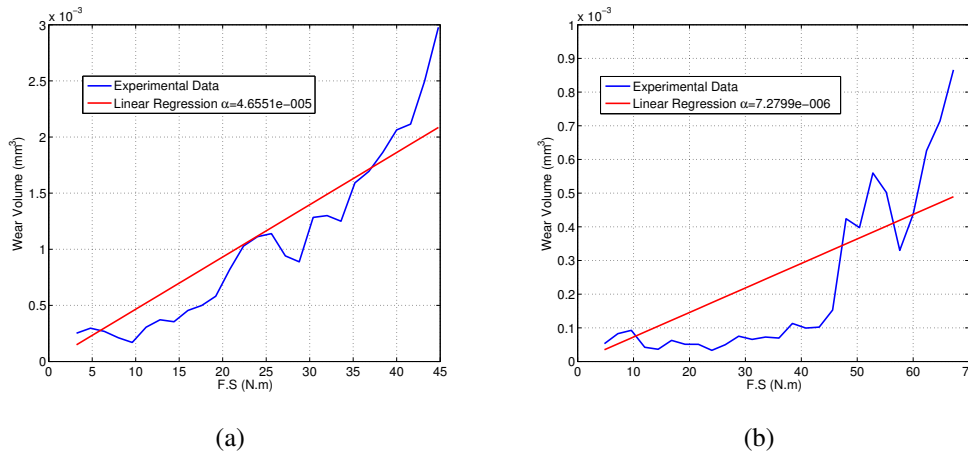
Figure 5.20: Fretting Wear Volume between AISI 52100 steel ball and the yarn of a composite material function of the sliding distance and determination of the wear rate coefficient from a linear regression (α) for a normal load equal to (a) 20 N (b) 30 N.

5.4 Toward tests at the mesoscopic scale

The aim of this part is to realize contact experiments between steel and woven composite at the scale of the RVE of the composite structure. This scale is between fundamental test on a unique component of the composite (see section 5.3), easy to analyze but not representative of the overall behavior of the composite material, and technological experiments on industrial parts which are very costly. A first experiment is proposed to determine the normal behavior of the composite under contact loading and a second experiment is presented to understand its tangential behavior under fretting conditions. Preliminary results are presented in the following section but further tests should be realized to obtain a good understanding of the contact behavior of woven composite materials.

### 5.4.1 Normal load test with MTS test engine

Two steel parts were designed and machined to be used on a MTS (Material Testing System) 810 machine present at the METL laboratory [WAL 14]. A first part was designed only to support a square part of composite material on a flat surface and a second part was designed to apply a normal load on the composite material (see Fig. 5.22 and 5.21). A crowning with a radius of 100 mm was used but only a part of the spherical surface was effectively machined. The roughness of the indent was not considered here but could be of major importance in tangential loading. The MTS machine has hydraulic actuators with a capacity of 100 kN. It is controlled by a computer and a MTS software responsible for data acquisition. A load cell is measuring the axial load applied to the specimen. In all experiments axial displacements were imposed with a resolution of 0.01 mm and around 3 N in the measurements. The aim of the tests was to determine the macroscopic behavior

of the composite under contact loading and to detect the appearance of damage on the force-displacement curve. In Fig. 5.23, results are plotted for a cyclic indentation curve from 0.01 mm displacement to 0.06 mm with an unloading phase between every new increase in the loading. The maximum imposed displacement is increased by 0.01 mm at each step. The maximum imposed displacement is leading to a contact radius $a^* = 1.82$ mm and to a maximum contact pressure of 86 MPa according to the Hertzian theory. Results in Fig. 5.23(a) show that the loading curves are superposing for the loading phases from 0.01 to 0.03 mm displacement. Moreover, in Fig. 5.23(b) the results corresponding to a maximum displacement of 0.04 to 0.06 mm are not superposing on the other curve. This modification in the behavior may come from two different phenomena. The first one is the appearance of damage in the composite material like matrix cracks and fiber debonding while the second one is the yielding of the indenting steel part. One can observe that the slope of the loading phase is decreasing with the increase of the maximum displacement. Based on the fact that yielding is an hardening phenomenon while damage is a softening phenomenon, it is assumed that damage is predominant here. To better understand the damage mechanisms occurring in the material during the normal loading, tomography of the composite parts before and after each loading phase should be realized along with a sectioning and metallurgical observations of the indent.

The preliminary results presented in this section show the effect of damage in the normal contact between a steel indent and a composite part. The contact area is large enough to contain both matrix and yarns. The results show a softening behavior of the contact with increasing normal loading. Further investigations are needed to fully understand this phenomenon.
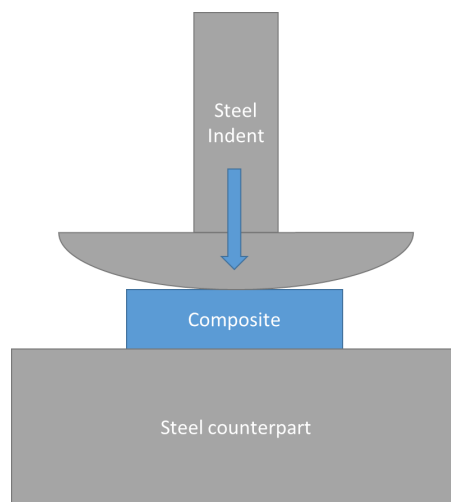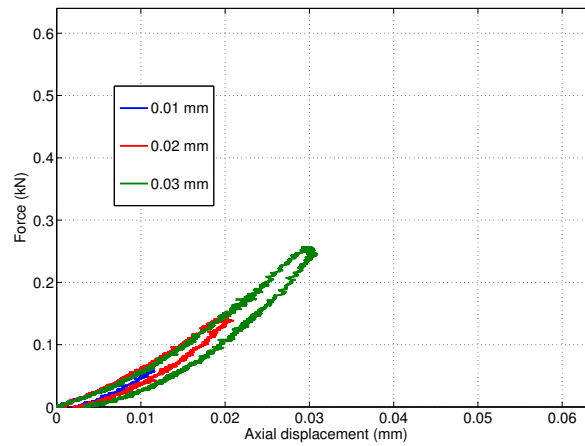

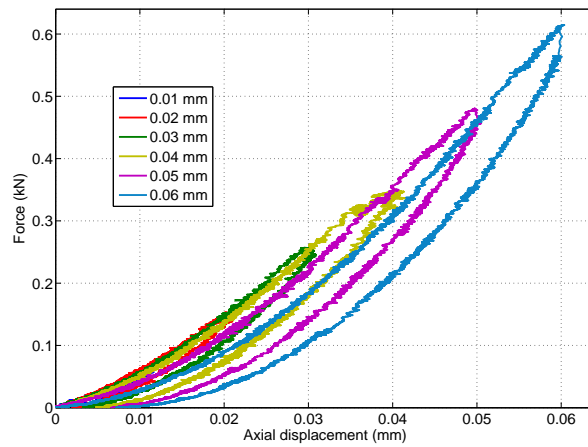**Figure 5.21:** Schematic view of the compression experiment with MTS test rig.

(a)

(b)

(c)
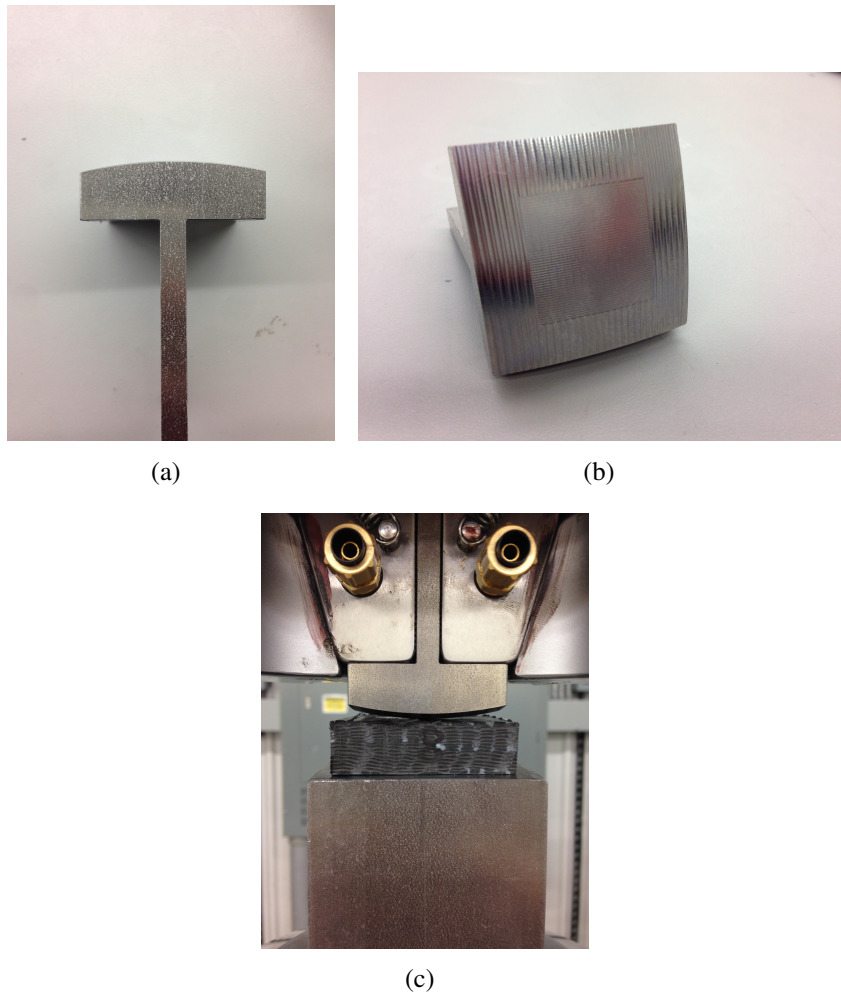
Figure 5.22: Normal test with MTS Engine (a) Indenter side view. (b) Indenter's tip view (c) View of experimental set up.

(a)

(b)

Figure 5.23: Force-Displacement curves of normal tests (a) from 0.01mm to 0.03mm of imposed axial displacement (b) Full cycle loading curves from 0.01mm to 0.06mm.

5.5   Partial Conclusion

The contact behavior under normal and tangential loading of a woven composite material has been investigated. Various tests have been conducted to understand the behavior of each component of the composite material and the effects of the structure of the composite on its macroscopic behavior. Both the coefficient of friction and the wear mechanisms of the material have been investigated during pin-on-disk tests and fretting tests. In-situ measurements of the coefficient of friction and of the scar depth have been compared to observations and measurements with an optical profilometer. Results tend to show that the macroscopic coefficient of friction between steel and composite is an average of the coefficient of friction between steel and matrix materials and between steel and yarn materials. The resulting coefficient of friction would depend of the proportion of each constituent on the contacting surface. A last part consisted in testing the material at a larger scale, closer to the technological application by using a different test rig and steel part specifically designed for the experiment. Results were obtained to show the effect of increasing load on the normal behavior of the material and the appearance of damage as a softening effect. Further experiments are necessary to fully understand and characterize the behavior of woven composite materials and their damage phenomena. But the results presented in this chapter highlighted the effects of the heterogeneous structure of composite materials in contact with a steel part on the tribological behavior of the system. Different coefficients of friction and wear kinematics have been identified for each constituent. In order to take into account these phenomena in our simulations, composite materials need to be modeled by considering their heterogeneous structure.

Chapter 6

Simulation of material heterogeneous structure with voxel

In this chapter, some limitation of the application of homogenization methods in case of contact loading are highlighted. Hence, a voxelization technique is proposed along with numerous inclusions to represent the complex structure of composite materials. A first part focuses on the use of data from the tomography of composite materials and converted into inclusions through the voxelization technique. A second part is dedicated to the representation of the bearing steel microstructure using a Voronoi tessellation algorithm. Finally, an application of this technique is made on the determination of the scatter in the fatigue life of bearing steel.

Contents

6.1 Homogenization of heterogeneous materials with SAM

In most computations of composite materials, the heterogeneous structure of the material is not modeled. Instead an equivalent homogeneous material with effective material properties C^{eff} is considered. Effective properties are defined through an homogenization process of the material Representative Elementary Volume (REV) as defined in section 1.4.2. The size of the REV depends of the woven pattern of the composite material. Homogenization theory assumes that at the scale of the REV, the properties of the material can be averaged. The properties measured are independent of the localization within the material. Design can be realized by considering the structure as homogeneous and having the averaged properties measured on the REV. In the next section, some classical homogenization methods are briefly discussed. Then, the semi-analytical solver is modified to obtain the effective properties of a periodic REV.

One should note that homogenization theory assumes a separation of scales between the scale of the REV and the scale of the structure. Homogenization technique aims at defining a material response independent of the local scale of the material. If the contact area is around the size of the REV, then the hypothesis of scale separation is no more valid. Previous work by Leroux and Nelias [LER 10] showed the effect on contact of the presence of heterogeneities close to the surface. In the next section, contact loadings are applied on both heterogeneous materials and equivalent homogenized materials. The first part of this chapter aims at showing some limitations of the homogenization theory in case of contact loading. The second part presents a technique to model composite material at the scale of the yarns (also called mesoscopic scale). Finally, an application of this technique to model crystalline microstructure of alloy is also introduced.

6.1.1 Homogenization theory

Due to the difficulty of simulating the real structure of composite materials, several homogenization methods have been proposed to establish the macroscopic effective properties and to predict the global stress-strain response of the material. Some of these theories are briefly recalled here. They are all based on the definition of a REV and aim at finding the macroscopic effective properties C^{eff}.

In presence of a material REV of volume V made of n phases of volume V^I, one phase volume fraction can be written $v_f^I = \frac{V^I}{V}$ and the total volume fraction is equal to

$$\sum_{i=1}^{n} v_f^i = 1 \tag{6.1}$$

The effective elastic tensor can then be expressed as:

$$C^{eff} = \sum_{i=1}^{n} v_f^i C^I : A^I \tag{6.2}$$

with A^I the localization tensor of the considered phase.

Assuming a uniform strain on the REV and $A^I = I_d$, the **Voigt bound** [VOI 89] can be determined:

$$C_{Voigt}^{eff} = \sum_{i=1}^{n} v_f^i C^I \tag{6.3}$$

Following the same idea and considering the concentration tensor, one can express the effective elasticity tensor as:

$$C^{eff} = \left(\sum_{i=1}^{n} v_f^i C^I : B^I \right)^{-1} \tag{6.4}$$

Assuming a uniform stress on the REV and $B^I = I_d$, the **Reuss bound** [REU 29] is defined as:

$$C_{Reuss}^{eff} = \left(\sum_{i=1}^{n} v_f^i C^I \right)^{-1} \tag{6.5}$$

The Voigt and the Reuss bound only take into account the elastic properties of each volume fraction as a rule of mixtures. They represent the lower and upper bound for the homogenized behavior of the composite. These bounds don't take into account the geometry of the phases and the mutual influence between those different phases.

In a multi-phase material, the **Mori-Tanaka method** [MOR 73, BEN 87] considers the behavior of non-dilute heterogeneities as if each heterogeneity is embedded and submitted to the mean strain field in the matrix ε^m. The mean stress field is influenced by the presence of other heterogeneities. Therefore, this method is taking into account the mutual influence between heterogeneities by averaging their effect.
The strain field inside the heterogeneity α can be expressed as:

$$\varepsilon^\alpha = A_{Eshelby}^\alpha : \varepsilon^m = A_{Eshelby}^\alpha : A_{MT}^\alpha : E \tag{6.6}$$

With A_{MT}^α the pseudo localization tensor linking the total strain field in the heterogeneity α to the mean strain field of the matrix.

$$A_{MT}^\alpha = A_{Eshelby}^\alpha \left(v_f^m I_d + \sum_{i=1}^{n} v_f^i A_{Eshelby}^i \right)^{-1} \tag{6.7}$$

$$C_{MT}^{eff} = C^M + \sum_{i=1}^{n} v_f^i \left(C^i - C^M \right) A_{MT}^i \tag{6.8}$$

The Mori-Tanaka method is giving a good prediction for the effective stiffness tensor if the heterogeneity volume fraction is not over 30%.

The presented method are based on the assumption that the REV is duplicated in every direction to reconstitute the material macroscopic structure. Periodic boundary conditions need to be imposed on the borders of the REV to numerically compute the effective properties of the material. The following sections aim at showing the capacity of obtaining effective material properties with the semi-analytical solver. Firstly, a numerical technique is proposed to simulate periodic boundary conditions. Secondly, examples with a REV composed of one hard inclusion embedded in a matrix are compared with analytical homogenization solution.

6.1.2 Periodic boundary conditions

In order to represent boundary conditions on the edge of the computed REV in the semi-analytical solver, a modified DC-FFT algorithm called DCD-FFT (Discrete Convolution Duplicated) is used. DCD-FFT has been firstly used to compute contact solution on rough surface without knowing the frequency response functions of the surface [CHE 08b, REN 09] and for lubricated contact on heterogeneous material [ZHO 16]. The main idea of the algorithm is to duplicate the excitation variable (the eigenstrain here) in every direction and to compute the product with the influence coefficients to get the stress field coming from the presence of inclusions inside the Fourier domain. Finally, only the stress field inside the original REV is kept but this field is taking into account the presence of similar REV all around (see Fig. 6.1). In Fig. 6.2, the duplicated padding is illustrated in the case of REV with one spherical inclusion in 2D (eight inclusions are added to simulate the periodic boundary conditions). In 3D, the algorithm is creating 27 inclusions in the three directions to simulate the periodic boundary conditions.
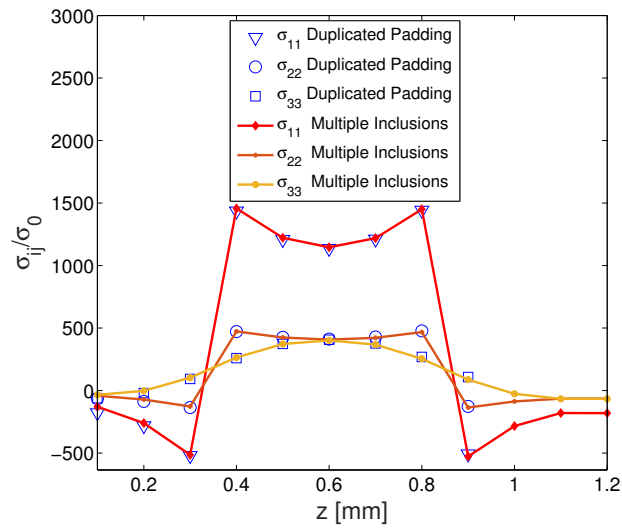
The semi-analytical solver is used to simulate an infinite solid with one spherical inclusion and using the DCD-FFT algorithm. The stress field inside and around the inclusion along z axis is compared with the stress field obtained by effectively adding 27 inclusions in the domain and without using the duplicated padding algorithm. A very good agreement is found in Fig. 6.3 between the two stress fields and confirms the ability of the algorithm to simulate periodic boundary conditions. This new technique is now used to perform numerical homogenization of the heterogeneous solid.
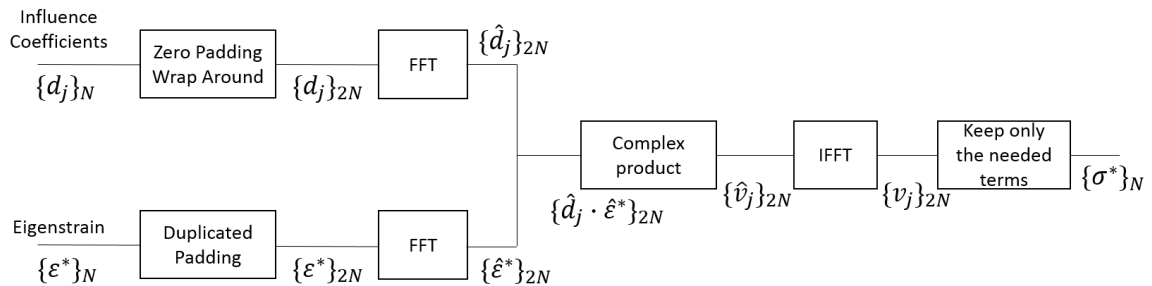
Figure 6.1: DCD-FFT Algorithm applied on the heterogeneous subsurface problem
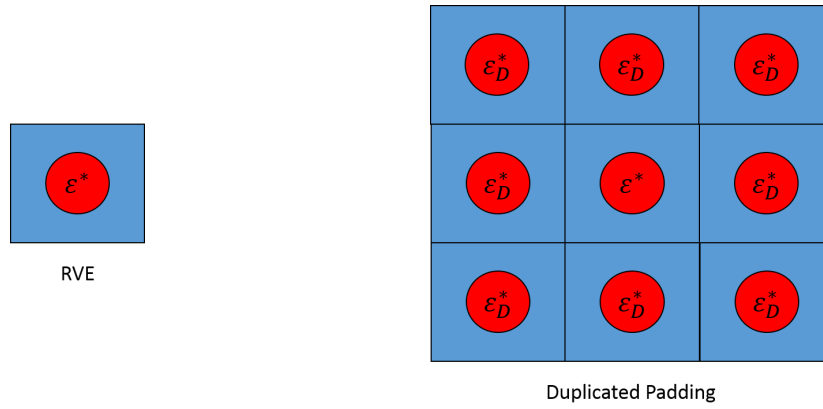
Figure 6.2: Illustration of the duplicated padding in 2D

Figure 6.3: Stress field in the REV with duplicated padding and with representation of the inclusions.

6.1.3   Heterogeneity in infinite solid

The elastic stress and strain fields computed with the semi-analytical solver are used to determine the effective Young modulus of the material using the duplicated padding algorithm. Solutions are compared with the predictions obtained with classic homogenization methods. Firstly, the effective Young modulus for a domain with a unique spherical inclusion (Fig. 6.4) and with a volume fraction varying between $0.1 \leq V_f \leq 0.5$ is computed. It should be noted that the volume fraction of the sphere is limited by the geometry of a sphere inside a cubic REV (V_f can not exceed 0.52). The Young modulus ratio between the inclusion and the matrix is set to $\gamma = \frac{E_I}{E_M} = 23.3$.

Moreover, the effective Young modulus is calculated for a domain with a cuboidal inclusion (Fig. 6.5) and with the same Young modulus ratio $\gamma = 23.3$ than in the previous example. In this case, the volume fraction V_f is varying between $0.1 \leq V_f \leq 0.9$.

For both inclusion shapes, the effective Young modulus curve is following the results found using the Mori-Tanaka theory [MOR 73, BEN 87]. Such result can be explained by the fact that as in the Mori-Tanaka method, the semi-analytical solver is also taking into account the mutual influence between heterogeneities in the duplicated padding algorithm through a mean stress field.

### 6.1.4   Indentation on homogenized solids

The previous section showed the capacity of the heterogeneous solver to obtain homogenized properties for a material with periodic boundary conditions. The present section is focusing on the limitation of applying homogenization theory in presence of a contact loading. A contact between a rigid sphere of radius $R = 35.0mm$ and a heterogeneous domain is compared with the contact between the same rigid sphere and the homogenized domain assigned with the effective elastic properties. The homogenization technique with the semi-analytical solver presented in the previous section is used here. The applied normal load is increasing from $W = 1N$ to $W = 100N$ in 22 time steps. At the end of the loading phase, the contact radius is found to be $a^* = 1.17mm$. Two examples are presented with a hard cuboidal inclusion in a matrix and a Young modulus ratio $\gamma = 23.3$ as in 6.1.3. Volume fractions of the inclusion are equal to $V_f = 0.7$ and $V_f = 0.1$ respectively. Comparison between indentation curves and contact pressure fields are presented in Fig. 6.6 and Fig. 6.7. One should note that the contact area is about the same size than the REV in these two examples. It is consistent with the contact conditions in the experimental results presented in chapter 5 when the size of the yarn is about the same size than the area of contact. Results when the heterogeneous phase volume fraction is $V_f = 0.7$ are showing that the homogenization method over estimates the effective material properties resulting in a contact pressure almost 40% higher than the contact pressure with the heterogeneous domain. The slope of the indentation curve is also higher than the one obtained with the heterogeneous domain. With a heterogeneity volume fraction $V_f = 0.1$, homogenization under estimates the effective properties resulting in a maximum pressure lower than the one in the heterogeneous domain and a lower indentation curve
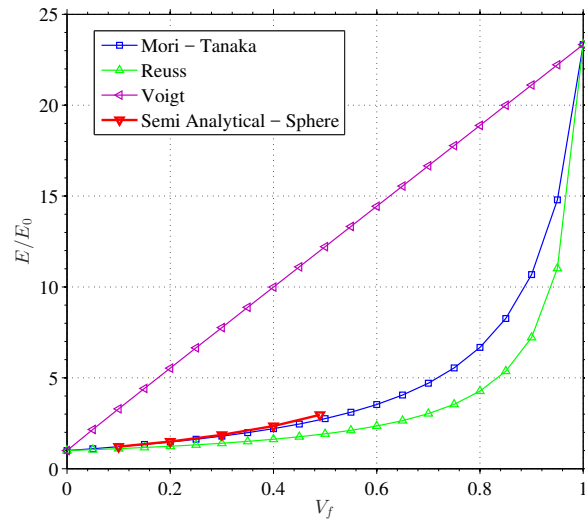
Figure 6.4: Effective Young modulus comparison with classic homogenization methods for one spherical inclusion embedded in a matrix with periodic boundary conditions. The Mori-Tanaka and the numerical technique curves match exactly.
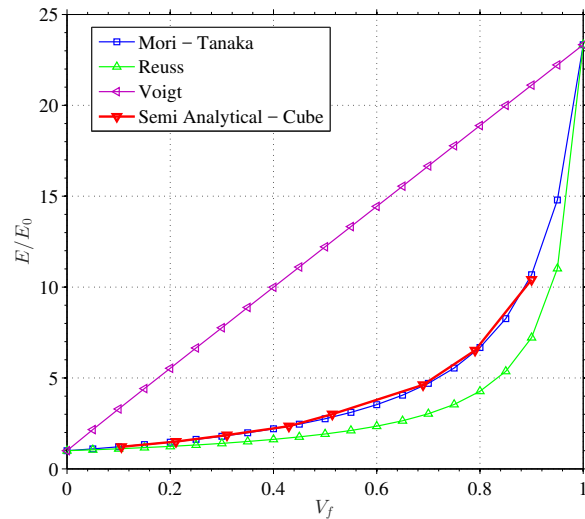

Figure 6.5: Effective Young modulus comparison with classic homogenization methods for one cuboidal inclusion embedded in a matrix with periodic boundary conditions. The Mori-Tanaka and the numerical technique curves match exactly.

slope. Another example is proposed in Fig. 6.8 where the contact radius is around five times the REV. Indentation curves between homogenized and heterogeneous domains are showing only small differences while the contact pressure exhibits peaks due to the presence of heterogeneities close to the surface. The maximum pressure in the heterogeneous material is 20% higher than in the homogenized domain. Moreover, the stress field in the subsurface is considerably disturbed by the presence of heterogeneities (see Fig. 6.9). Finally, results in this section show the limitation of the homogenization theory for contact mechanics due to incompatibility in the boundary conditions between both theories. One should note that contact loading is often a very localized solicitation. There is a coupled effect between the scale of the material and the scale of the contact loading. In particular, due to the size of yarns, scale's separation hypothesis can not be ensured in the contact on woven composite materials. In case of contact loading, this kind of material can not be represented by its equivalent homogeneous effective properties. The following section present a way of representing the heterogeneous structure of composite materials in the semi-analytical solver.
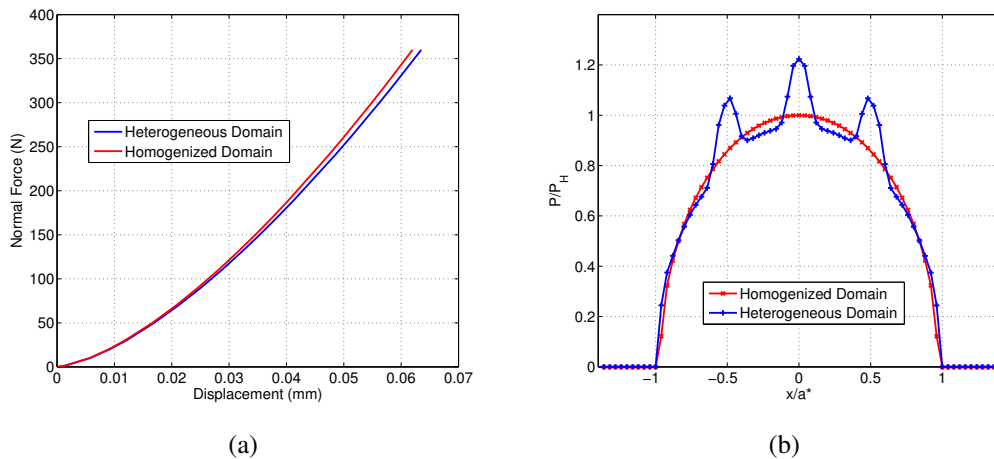

(a)   (b)
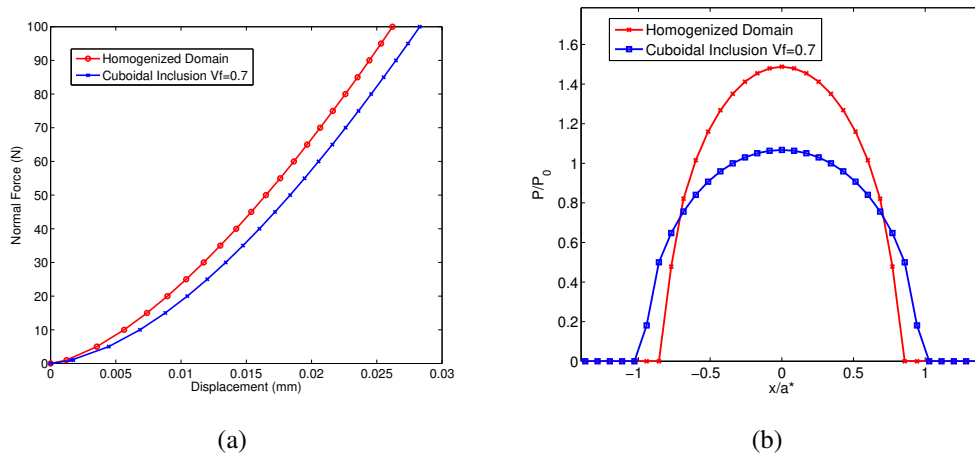
Figure 6.6: Comparison of the indentation curve (a) and of the dimensionless contact pressure with a normal load $W = 100N$ (b) for a half space with one inclusion ($V_f = 0.7$) in the REV and the corresponding homogenized domain.
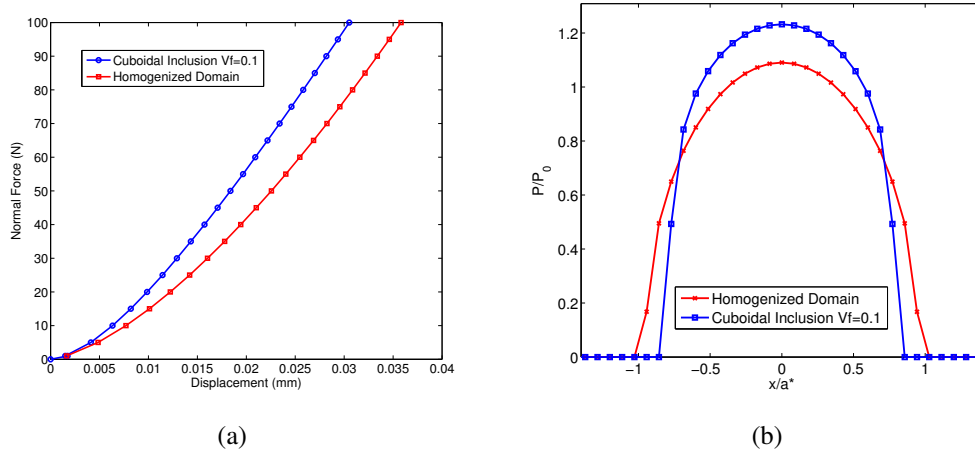
Figure 6.7: Comparison of the indentation curve (a) and of the dimensionless contact pressure P/P_0 (b) for a half space with one inclusion ($V_f = 0.1$) in the REV and the corresponding homogenized domain.

Figure 6.8: Comparison of the indentation curve (a) and of the dimensionless contact pressure P/P_0 (b) for a half space with a periodic structure of cuboidal inclusions ($V_f = 0.1$) and the corresponding homogenized domain.

(a)

(b)

(c)
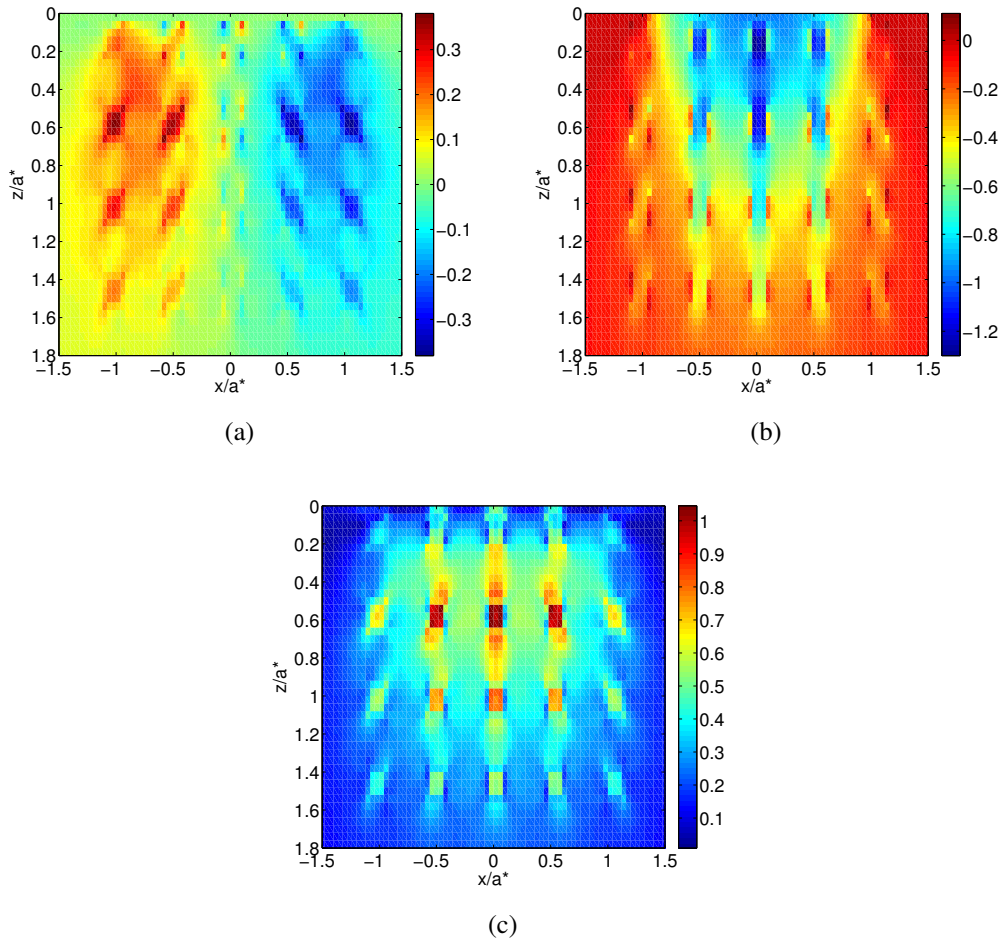
Figure 6.9: Dimensionless stress field (a) σ_{13}/P_0 (b) σ_{33}/P_0 (c) σ_{VM}/P_0 in the plane $y = 0$ for a half space with a periodic structure of cuboidal inclusions ($V_f = 0.1$).

6.2   Contact on composite materials

Results obtained in section 6.1.4 have shown the necessity of representing the heterogeneous structure of the material to obtain accurate pressure fields in the contact. In this section, a voxelization method is proposed to accurately reproduce materials microstructure in the semi-analytical solver. In a first part, a 2D woven composite material is modeled using data from tomography to reproduce the woven structure of the material. Yarns are considered orthotropic and the matrix is considered isotropic. This scale of representation is called mesoscopic. In a second part, the polycrystalline microstructure of a metallic alloy is modeled using a Voronoi tessellation technique. Effects of the structure representation on the rolling contact fatigue life is investigated.

6.2.1   Modeling of the structure of woven composites at the mesoscopic scale

In order to model the behavior of a woven composite material in the semi-analytical solver, composite materials are represented at the scale of the yarns also called mesoscopic scale. Yarns have a complex microstructure made of carbon fiber filaments entangled in a matrix. Each carbon fiber has a few μm diameter and a yarn is around 2 mm width and 0.5 mm thick. The REV of the considered composite is around $28mm \times 17mm \times 10mm$. Durville [DUR 10] proposed a method to simulate the fibers position in the yarn (at the microscopic scale) but due to the high number of fibers to represent (more than three hundred in [DUR 07]), this kind of simulation is very time consuming. To simulate the structure of the composite in the semi-analytical solver and to reduce the computation cost, yarns will be considered homogeneous in the model, however orthotropic (mesoscopic scale). The effective properties of the yarns are obtained through the homogenization of an elementary cell. In order to obtain information on the weaving pattern, two different methods can be used: a geometrical description of the weaving and experimental data of the real weaving from X-ray tomography.

Geometrical model of woven composites

A first method to know the geometry of a woven composite is based on a geometrical description of the yarns. A software developed by the team of Lomov at the Katholieke Universiteit Leuven called Wisetex [LOM 00, LOM 07b, LOM 07a] generates the geometry of the yarns by minimizing the energy of deformation of each fiber to get a static equilibrium. This method models the yarn trajectory and the size of yarn sections. Some difficult experimental identification to avoid any yarn interpenetration are also needed by the method [LOM 07b, COU 08]. Another software called TexGen developed at the university of Nottingham [SHE 07] allows to easily realize some woven geometrical elementary cells without any mechanical consideration. Both of these methods are considering a constant and idealized form of the yarns. A woven structure from Wisetex has already been used in the semi-analytical solver using ellipsoidal inclusion by Leroux [LER 13].

Yarns are modeled by placing ellipsoidal inclusions along the mean line of the yarn profile.
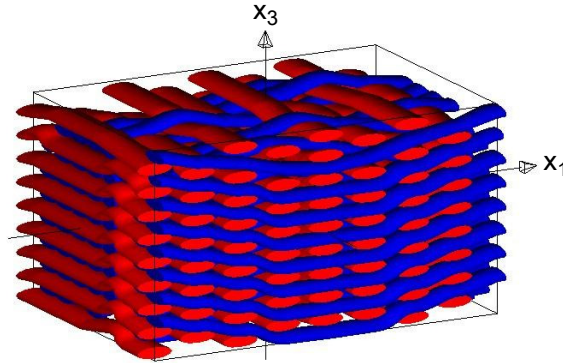

Figure 6.10: 2D woven composite geometry from WiseTex [LER 13].

Tomography of woven composites

X-ray tomography is a non destructive method to build a 3D view of an object. It measures the attenuation of the X-ray beam through the object reflecting the density of the material. A large number of beam angles are used to collect enough data to reconstruct the structure of the body in grey scale. X-ray tomography has a lot of applications in material's science [SAL 03]. Tomography resolution is around 10 μm to 30 μm and is good enough to allow the observation of the material at the mesoscopic scale [SCH 06]. Naouar et al. [NAO 14, NAO 15b] proposed a method to build a finite element mesh of the composite based on the real geometry using data from a computed tomography. More recently, computed tomography have been used with digital volume correlation on a 3D woven composite material to detect differences between two samples and find missing yarns [MEN 19]. In the next section, tomography results are used to model realistic geometry of the composite in the semi-analytical solver using a voxelization technique.

6.2.2   Voxelization of the composite structure

Representing the structure of woven composite materials in numerical simulation is very complex. Grail et al. [GRA 13b] proposed a method to create a conformal mesh of woven composites taking into account the contact between the yarns. But due to its complexity, this kind of method is not widely used in the industry. A more straight-forward method to translate the geometrical characteristic of the weaving into input data for the semi-analytical solver is based on the use of a voxel mesh [IAR 09, DEC 11, POT 12, SCH 09a]. A voxel can be defined as a cube and is the 3D equivalent of a pixel. The principle of the method is to decompose the solid into a grid of small voxels and to assign mechanical properties to each voxel. Mechanical properties of each constituent are assigned to each voxel depending on their position. If the

(a)   (b)
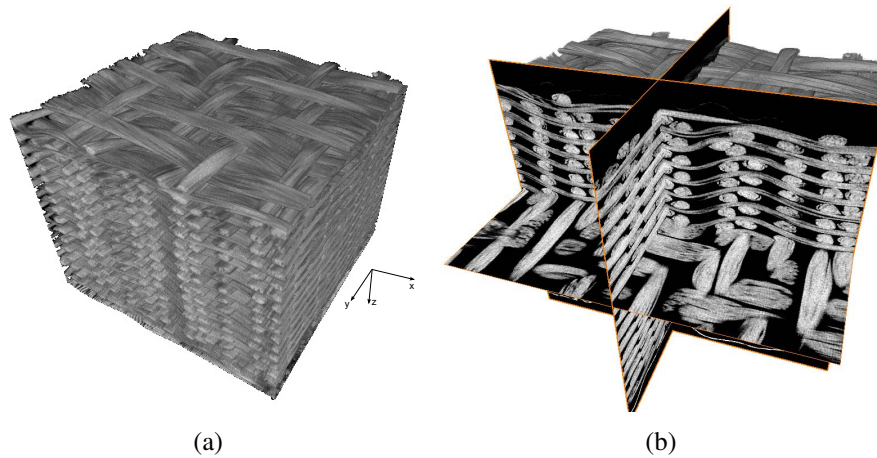
Figure 6.11: Computed tomography of an interlock composite and plane cuts [NAO 15a].

voxel belongs to a yarn, mechanical properties of the yarn are assigned to the voxel. If the voxel belongs to the matrix, mechanical properties of the matrix are assigned to the voxel. The perfect contact between the yarns is one of the main advantage of the method but some local artificial stress appears at the interface due to the non-smooth interfaces [DOI 15b]. Voxel meshing method has also been used to model damage in woven composites [KOU 14c, WAR 16]. An internal numerical tool of Safran Aircraft Engines called REVoxel is used in this part to traduce geometrical data from the material REV into voxels. Voxelisation data are used in the semi-analytical solver through the introduction of orthotropic heterogeneous cuboids. One cuboidal heterogeneity is assigned to each voxel with its material properties. Orthotropic material properties and orientations of the heterogeneities are obtained by the voxelization process. Cuboidal inclusions are superimposed on the half-space to represent the structure of the composite material as an enrichment technique. Mutual influence between close inclusions is computed using a modified conjugate gradient algorithm called Orthodir as in [KOU 15b]. One should note that only voxel representing the yarns are converted into inclusions in the solver and the matrix material's data are assigned to the half space.

## 6.2.3   Results and comparison with homogeneous materials

A sample of 2D woven composite have been voxelized using REVoxel, the resulting voxelized yarns are represented in Fig. 6.12(a). The size of the voxelized domain is 28.8 mm $\times 16.96$ mm $\times 3.5$ mm. The domain is discretized into small voxel of size $2\Delta x = 0.1$ mm. The volumic fraction of yarns in the considered material is around $V_f = 0.8$. A contact simulation between a steel sphere and a voxelized composite material using the semi-analytical solver is performed. The contact area position is represented on the voxelized structure in Fig. 6.12(b). The contact area ($a^* = 1.50$ mm) is about the size of a yarn ($\Delta x = 0.033a^*$). Matrix and Yarn material properties from chapter 5 are used in

the simulation. Surface stress fields on the voxelized microstructure are presented in Fig. 6.13 and are compared to the same simulation with a homogeneous material in Fig. 6.14. The surface stress field is disturbed by the presence of yarns close to the contact area. Stress field in the plane $z = 0$, $x = 0$ and $y = 0$ for a larger contact radius ($a^* = 2.59$ mm and $\Delta x = 0.019a^*$) are presented in Fig.6.15, Fig. 6.16 and Fig. 6.17. The corresponding pressure field is compared to the pressure field on a homogeneous material with elastic material properties of the matrix in Fig. 6.18. Size of the yarn is around the size of the contact radius a^*. Presence of the yarn in the contact is disturbing the contact pressure. The maximum pressure on the composite is found to be around 50% higher than the maximum pressure found on the homogeneous material. When comparing stress field for both contact radii, one can observe that the maximum dimensionless von Mises stress is almost twice larger when the contact area is localized on a yarn. Hence, the solution of the contact problem is depending on both the scale of the material structure and on the size of the contact area. In every case, stress fields in the heterogeneous simulation are showing strong gradient at the surface and in the subsurface at the interface between the yarns and the matrix. These gradients are not present in the homogeneous simulation and may be responsible for the appearance of damage in composite materials. Some of these gradients are product of the non-smooth interface between yarns and matrix (see Fig. 6.16(d)). It is an artifact of the voxelization technique as explained in [DOI 15b]. Finally, results observed in this section show the need of modeling composite materials at the mesoscopic scale to predict their behavior and damage phenomena. Moreover, the ability of the semi-analytical solver to model contact on composite materials at the mesoscopic scale have been highlighted. The following section present an extension of the damage model proposed in chapter 3 to the damage of yarns in composite materials.
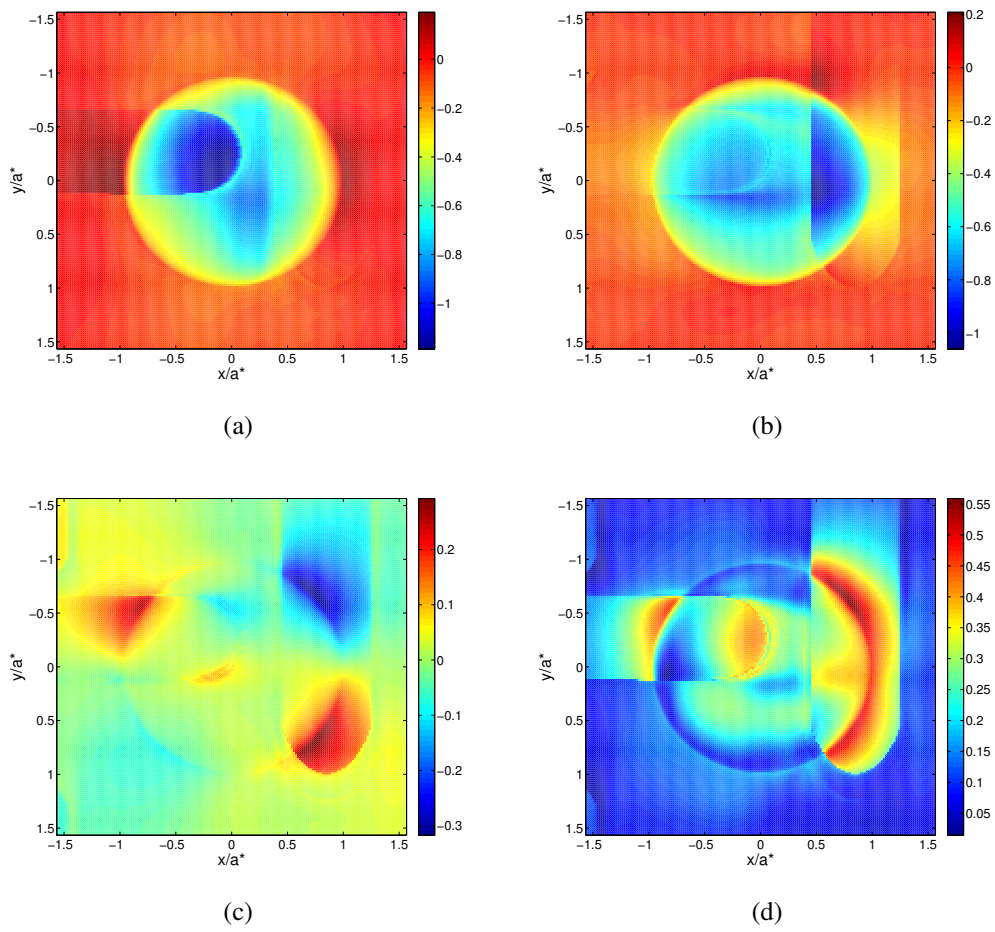
(a)

(b)
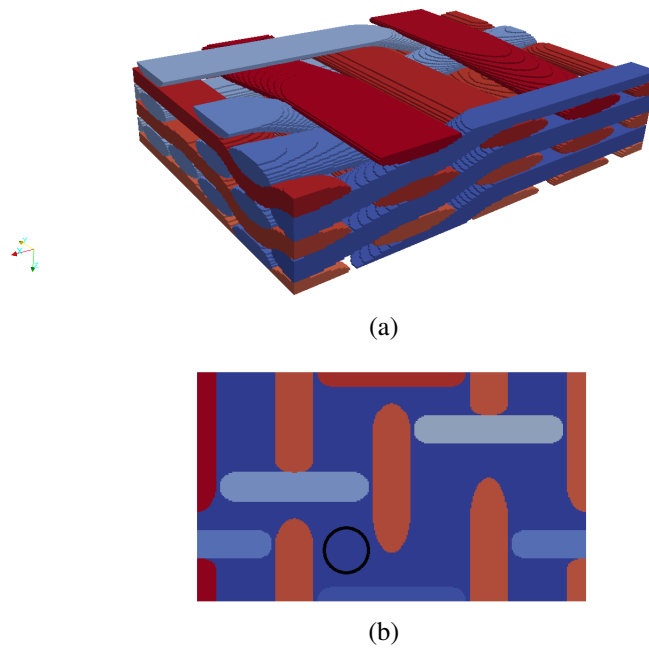
**Figure 6.12:** (a) Voxelized view of the woven yarns. (b) Contact area on the composite structure.
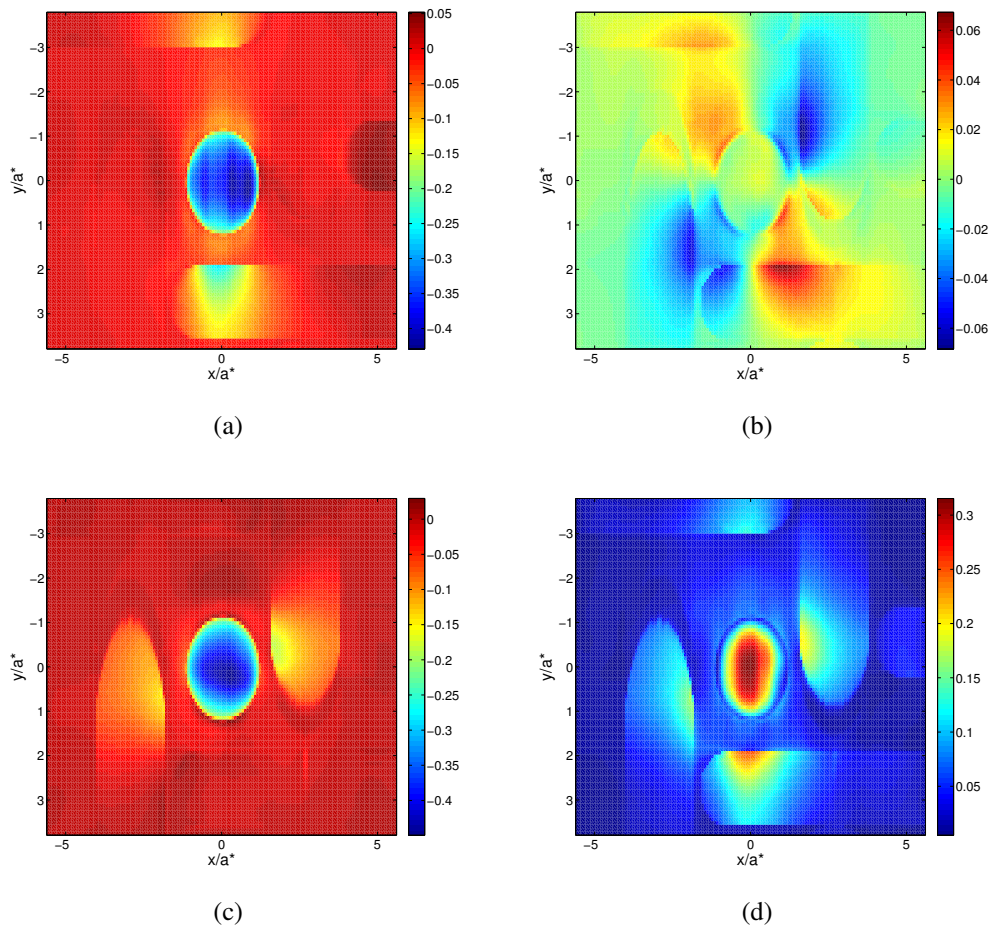
Figure 6.13: Dimensionless stress field in the plane $z = 0$ of a voxelized composite (a) σ_{11} (b) σ_{12} (c) σ_{22} (d) σ_{VM}
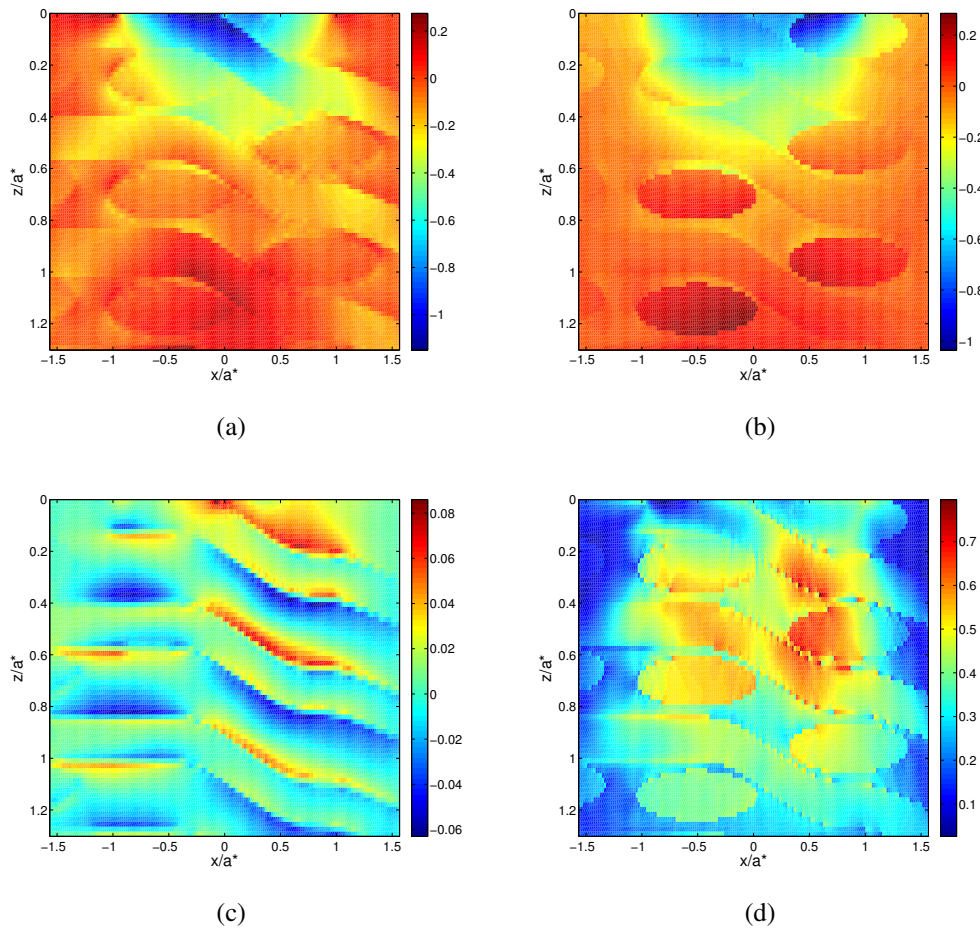
(a)

(b)

(c)
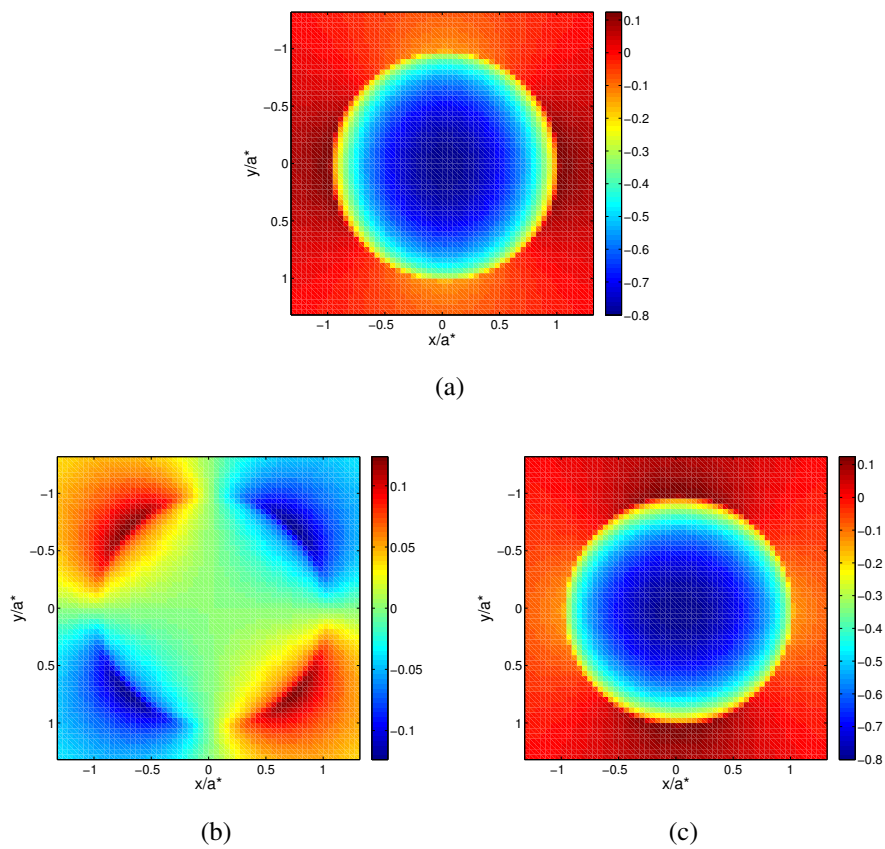
Figure 6.14: Dimensionless stress field in the plane $z = 0$ of a homogeneous material (a) σ_{11} (b) σ_{12} (c) σ_{22}
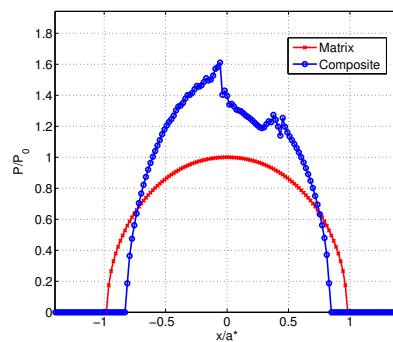
(a)

(b)

(c)

(d)

Figure 6.15: Dimensionless stress field in the plane $z = 0$ of a voxelized composite (a) σ_{11} (b) σ_{22} (c) σ_{12} (d) σ_{VM}
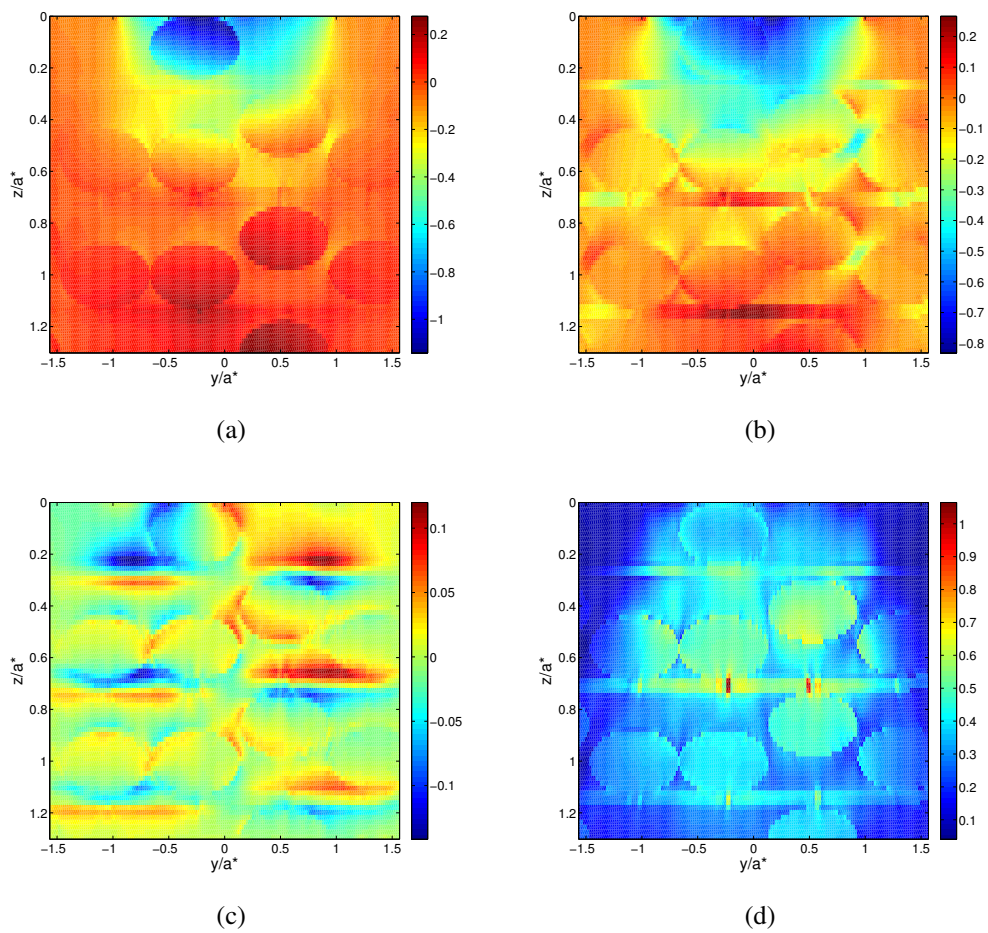
Figure 6.16: Dimensionless stress field in the plane $x = 0$ of a voxelized composite (a) σ_{11} (b) σ_{22} (c) σ_{12} (d) σ_{VM}

(a)

(b)

(c)

(d)

Figure 6.17: Dimensionless stress field in the plane $y = 0$ of a voxelized composite (a) σ_{11} (b) σ_{22} (c) σ_{12} (d) σ_{VM}

Figure 6.18: Contact pressure on the voxelized composite material (blue line) and on a homogeneous material with matrix elastic properties (red line).

6.2.4 Towards a damage model for woven composite materials

The previous section has shown the ability of the semi-analytical solver to represent composite materials at the mesoscopic scale. This section aims at proposing a modification of the damage model presented in chapter 3 considering the fact that yarns have a transverse isotropic behavior (see Fig. 6.19). Some preliminary results are presented. Future work would need experimental results to identify the model parameters. The equivalent strain is decomposed in two parts corresponding to the equivalent strain in the direction of the yarn called fiber direction (with subscript F) and the equivalent strain in the direction orthogonal to the yarn called transverse direction (with subscript T). Expressions of these two equivalent strains are defined below:
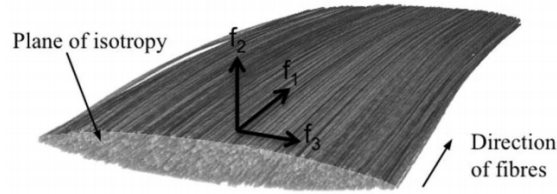
Figure 6.19: Transversely Isotropic directions of the yarn

$$\tilde{\varepsilon}_{Fiber} = \sqrt{\langle \varepsilon_F \rangle_+^2} \tag{6.9}$$

$$\tilde{\varepsilon}_{Transverse} = \sqrt{\langle \varepsilon_{T1} \rangle_+^2 + \langle \varepsilon_{T2} \rangle_+^2} \tag{6.10}$$

In order to accurately compute those expressions, one should apply the Maccauleigh brackets $\langle \rangle_+$ in the reference frame using the eigen-vectors matrix P and then transfer back the field in the frame of the yarn following these steps:

- Compute the equivalent strain in the principal frame:

$$\sigma_{ij} \to P^{-1} \sigma_{ij} P \to \sigma_I \to \varepsilon_I \to \langle \varepsilon_I \rangle_+ \tag{6.11}$$

- Transfer in the yarn's reference frame:

$$P \langle \varepsilon_I \rangle_+ P^{-1} \to \{ \tilde{\varepsilon_T}, \tilde{\varepsilon_F} \} \tag{6.12}$$

Using the same model than for an isotropic material in Chapter. 3, two damage evolution laws of the yarn corresponding to the fiber direction and to the transverse directions can be defined with two different thresholds functions K_F and K_T:

$$\begin{cases} f_F(\varepsilon_F, D_F) = \tilde{\varepsilon}_F - K_F(D_F) \\ f_T(\varepsilon_T, D_T) = \tilde{\varepsilon}_T - K_T(D_T) \end{cases}$$

Yarns having a transversely isotropic behavior, damage phenomena may apply differently in the two transverse directions. The coupled elastic damage constitutive law can be expressed through the compliance tensor:

$$
\begin{pmatrix} \varepsilon_{11} \\ \varepsilon_{22} \\ \varepsilon_{33} \\ 2\varepsilon_{23} \\ 2\varepsilon_{31} \\ 2\varepsilon_{12} \end{pmatrix} = \begin{pmatrix} \frac{1}{(1-D_F)E_F} & \frac{-\nu_{TF}}{(1-D_T)E_T} & \frac{-\nu_{TF}}{(1-D_T)E_T} & 0 & 0 & 0 \\ \frac{-\nu_{FT}}{(1-D_F)E_F} & \frac{1}{(1-D_T)E_T} & \frac{-\nu_{TT}}{(1-D_T)E_T} & 0 & 0 & 0 \\ \frac{-\nu_{FT}}{(1-D_F)E_F} & \frac{-\nu_{FF}}{(1-D_T)E_T} & \frac{1}{(1-D_T)E_T} & 0 & 0 & 0 \\ 0 & 0 & 0 & \frac{2(1+\nu_{TT})}{(1-D_T)E_T} & 0 & 0 \\ 0 & 0 & 0 & 0 & \frac{1}{G_{FT}} & 0 \\ 0 & 0 & 0 & 0 & 0 & \frac{1}{G_{FT}} \end{pmatrix} \begin{pmatrix} \sigma_{11} \\ \sigma_{22} \\ \sigma_{33} \\ \sigma_{23} \\ \sigma_{31} \\ \sigma_{12} \end{pmatrix}
$$

Four different coefficients are needed to identify the damage model along with 5 material coefficients:

- 2 Young's moduli: E_T and E_F

- 1 shear modulus : G_{FT}

- 2 Poisson's ratio : ν_{TT} and ν_{TF}

- 2 threshold strains : ε_{d0}^F and ε_{d0}^T

- 2 fracture strains : ε_R^F and ε_R^T

6.2.4.1 Results with one yarn

Some preliminary results are presented here in the case of a contact between a spherical indent of radius $R = 20$ mm and a half-space with one yarn. The normal load is $W = 50$ N and both parts are made of the same material with $E = 114600$ MPa. The yarn is embedded just below the surface at a depth $z = 0.25a^*$. The yarn is made of small transverse isotropic cuboidal inclusions with material parameters arbitrarily choose to be $E_F = 120000$ MPa and $E_T = 20000$ MP ($E_F = 6 \times E_T$). For sake of simplicity, the yarn diameter is represented by only five cuboids (see Fig 6.20).

The presence of the yarn is strongly affecting both the stress field in the material and the contact pressure (see Fig. 6.22) since it is localized very close to the surface. A parametric study of the contact perturbation due to the presence of inclusions has already been performed by Leroux et al. [LER 10]. He showed that for an inclusion deeper than $h > 0.4a$, no effect on the contact pressure can be observed.
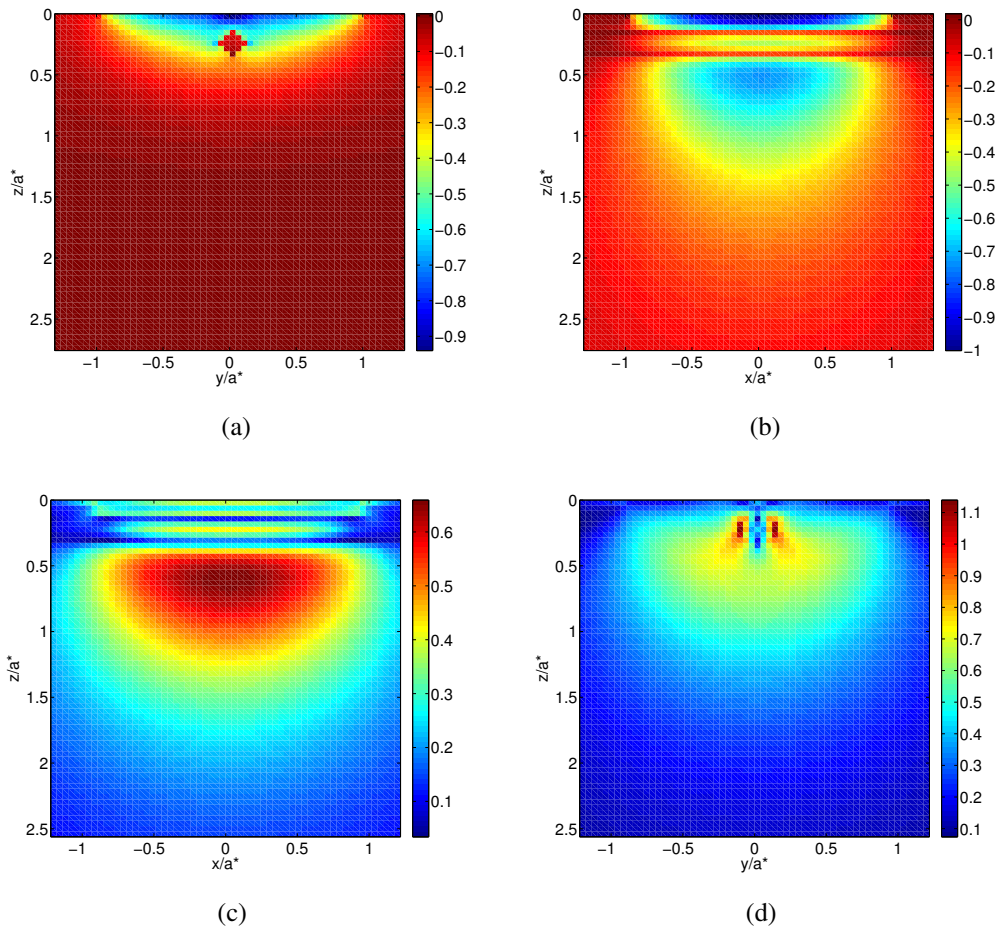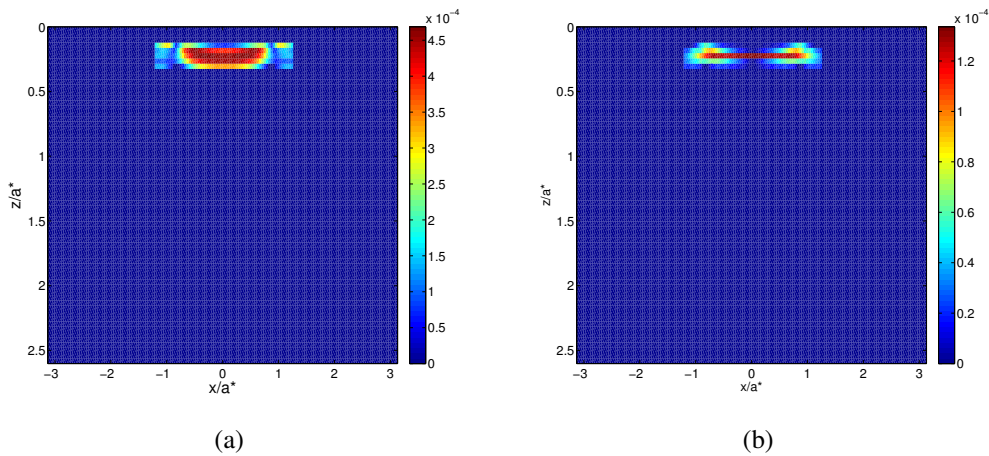
Figure 6.20: Dimensionless stress field in a unique yarn embedded into the matrix (a) σ_{11}/P_0 in the plane $x = 0$ (b) σ_{33}/P_0 in the plane $y = 0$ (c) σ_{VM}/P_0 in the plane $x = 0$ (d) and $y = 0$.

(a)

(b)
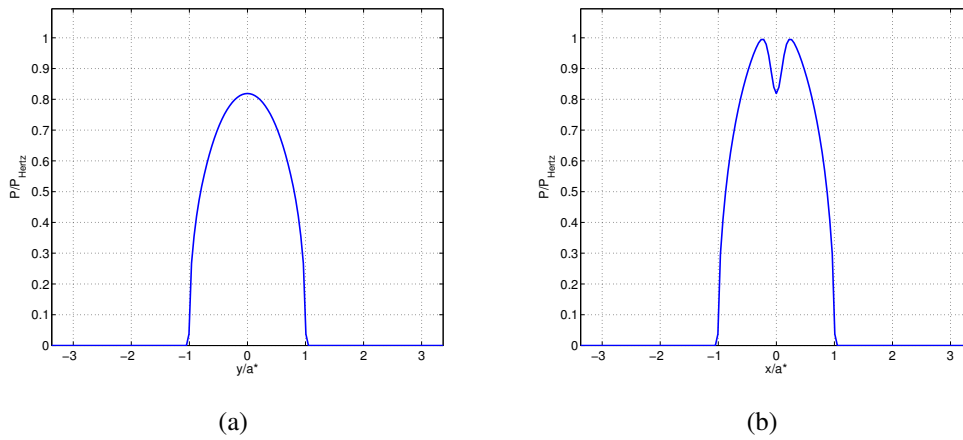
Figure 6.21: Contact pressure in the plane (a) $x = 0$ (b) $y = 0$.

The two equivalent strains defined in the previous section are calculated and presented in the plane $y = 0$ in Fig. 6.22.

(a)

(b)

Figure 6.22: Equivalent strain (a) in the direction of the fiber (b) in the direction transverse to the fiber in the plane $y = 0$.

The equivalent strain in the fiber direction is found to be higher than the equivalent strain in the transverse direction. It is because the yarn is very close to the maximum shear stress depth. In order to go further in the analysis of this model, more experimental investigations have to be realized. Future work is to identify the different parameters of the two damage laws of the model.

6.2.5 Partial Conclusion

This section has presented the limitation of the homogenization theory in presence of a contact loading. A voxelization method has been introduced to model the complex geometry of woven composite material with the semi-analytical solver. Results showed the presence of strong stress gradients at the interface between the yarns and the matrix. A modification of a previous damage model has been proposed to model the damage appearing in the yarns. More experimental results are needed to expend this work. In the following section, the voxelization technique is applied to model the microstructure of polycrystalline alloys. Finally the results are used to predict the fatigue life of rolling element bearings.

6.3 Effects of polycrystalline anisotropy on RCF

In the previous section, the semi-analytical method has permitted to simulate the behavior of woven composite material under contact loading at the mesoscopic scale. In this section, the semi-analytical solver is used to represent bearing steel at the micro-structural scale. A voxelization of the grain aggregate geometry is used to compute the stress in the material and to estimate the scatter in fatigue life of materials under rolling contact fatigue.

6.3.1 Microstructure of metallic alloys

The microstructure of steel used in roller bearings like AISI 52100 is composed of an aggregate of grains (Ferrite, Austenite, Martensite etc.). AISI 52100 is a steel with a high carbon and chromium concentration and several treatments by heating and quenching can affect the microstructure. The polycrystalline microstructure of AISI 52100 steel is observed on a fracture surface in Fig. 6.23(b). Fracture seems to happen at the grain boundaries [SAD 09]. These phenomena can not be taken into account in numerical simulation when considering a homogeneous material. The Voronoi tessellation method allows to accurately simulate this kind of material microstructure [ITO 93] and has been extensively used to account for microstructure typology randomness in materials under rolling contact fatigue [RAJ 08b, JAL 09, WEI 10, WEI 11, BOM 13b, PAU 14, VIJ 18].

6.3.2 Voronoi tessellation

The Voronoi tessellation is a numerical technique to divide a continuous space into regions following some principles detailed in Okabe and Boots [OKA 00] and recalled here:

- A set of not coinciding seed points $\gamma = \{p_1, p_2, ..., p_n\}$ are randomly placed in a three dimensional volume $V \in \mathbb{R}^3$.
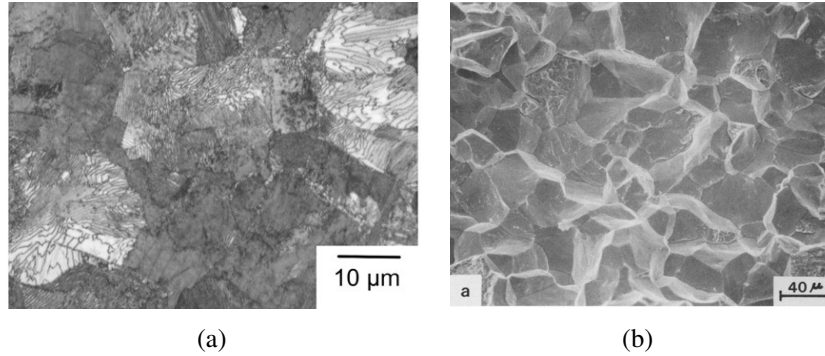
Figure 6.23: (a)Microstructure of bearing steel AISI 52100 [BHA 12]. (b) Fracture surface of AISI 52100 steel austenized at 800° [NAK 78].

- The volume V is divided into regions $V_{\{p_i\}}$, volume of influence associated with a seed point p_i. Each region is composed of every point closer (using euclidean distance) to the seed point p_i than to any other seed points of γ. This condition can be expressed for each point $x \in V$:

$$V_{\{p_i\}} = \left\{ d(p_i, x) \leq d(p_j, x), j \in [1, n], \forall x \in V \right\} \tag{6.13}$$

- Grain boundaries are the planes formed by the points equidistant from two generating points. Therefore Voronoi cells are convex close polyhedra covering the entire volume V and forming the Voronoi diagram.

The distribution of seed points in the volume allows to capture the randomness in the microstructure topology. Moreover, the density of seed point and its distribution is controlling the average grain size and shape. A Poisson process is often used to place the seed points because of its ability to accurately reproduce polycrystalline microstructures [WEI 10].

The Voronoi tessellation has been applied to model microstructure typology for homogenization computation [KUM 94, NYG 02] and for contact simulation in both fretting [DIC 06a, ZHA 09, ASH 17] and rolling contact fatigue [WEI 10, PAU 14, VIJ 18] with the finite element method and with multigrid method [BOF 15]. The representation of microstructure is limited to the volume where the gradient of stresses from the contact is significant regarding to the characteristic length of the microstructure. The grain diameter is an input of the algorithm to place the seed points of the Voronoi diagram and using the MATLAB's voronoin algorithm based on the software QHULL [BAR 96]. In this chapter, all the Voronoi diagrams have been generated using a MATLAB's algorithm developed at the METL laboratory of Purdue University.
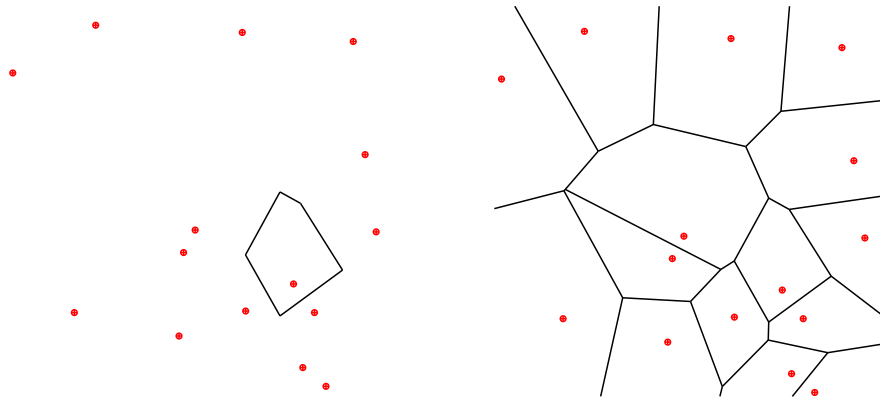
Figure 6.24: The Voronoi tessellation process: space partition from a 2D seed distribution.
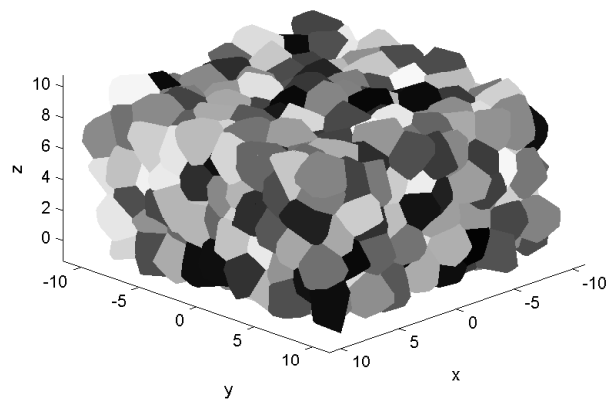
Figure 6.25: Example of a 3D Voronoi tessellation

6.3.2.1 Mesh building

In finite element, the mesh of the Voronoi diagram is often unstructured. Each Voronoi cell is meshed with tetrahedral elements to obtain a fine discretization of the grain boundaries [VIJ 18]. Other authors also used structured method with cube elements (voxel) [ZHA 09, ASH 17]. This is the same technique used in the previous section 6.2.2 and used in this section to simulate the microstructure.

The discretization grid of the semi analytical solver is superimposed on the Voronoi diagram (see Fig. 6.26). Each point is labeled with the Voronoi cell it belongs to. The labelization process is done from the calculation of the minimum distance between the point of the grid and one of the seed points.

6.3.2.2 Polycrystalline anisotropy

Most of the microstructure models in the literature are simulating isotropic materials but on the microstructural scale, steel is made of randomly oriented anisotropic crystal grains. If the loading conditions allow to consider the macroscale response of the material, the anisotropy of the grains is resulting in a isotropic global material behavior and stiffness. But considering the high stress gradient in contact loading, the grain orientation needs to be taken into account. A cubic anisotropy model is adopted here to simulate the crystalline elasticity of the material as in Vijay et al. [VIJ 18]. A single crystal structure is assumed here for sake of simplicity and each grain has the same elastic stiffness constants as recalled in Eq. 6.14. Each grain has the same stiffness in its local coordinate system but the macroscopic response of the material is evaluated in the cartesian reference frame. It is then necessary to rotate the local grain stiffness matrix C_{local} into the reference frame $C_{reference}$ following Eq. 6.15. Thus, the stiffness of each grain produces different values in the reference frame.

$$\begin{pmatrix} \sigma_{11} \\ \sigma_{22} \\ \sigma_{33} \\ \sigma_{23} \\ \sigma_{31} \\ \sigma_{12} \end{pmatrix} = \begin{pmatrix} C_{11} & C_{12} & C_{12} & 0 & 0 & 0 \\ C_{12} & C_{11} & C_{12} & 0 & 0 & 0 \\ C_{12} & C_{12} & C_{11} & 0 & 0 & 0 \\ 0 & 0 & 0 & C_{44} & 0 & 0 \\ 0 & 0 & 0 & 0 & C_{44} & 0 \\ 0 & 0 & 0 & 0 & 0 & C_{44} \end{pmatrix} \begin{pmatrix} \varepsilon_{11} \\ \varepsilon_{22} \\ \varepsilon_{33} \\ 2\varepsilon_{23} \\ 2\varepsilon_{31} \\ 2\varepsilon_{12} \end{pmatrix} \tag{6.14}$$

$$C_{reference} = R_{Z''} R_{X'} R_Z C_{local} R_Z^T R_{X'}^T R_{Z''}^T \tag{6.15}$$

In the simulation, random Euler angles are assigned to each cell of the Voronoi diagram. Each grain is discretized in small cuboidal inclusions with the same cubic elastic properties but rotated accordingly with the assigned angles of each grain. All the inclusions belonging to a specific grain have the same rotation angles. Vitos et al. [VIT 03] determined cubic material constants for stainless steel from quantum mechanical calculations and their results are used in the simulations (see Table 6.1).

A measure of anisotropy is defined through the parameter A [PAU 14] and is calculated to be 3.78 here:
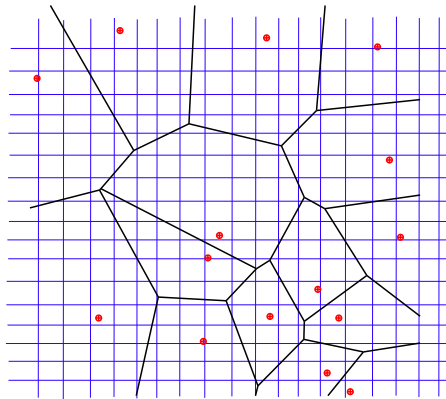
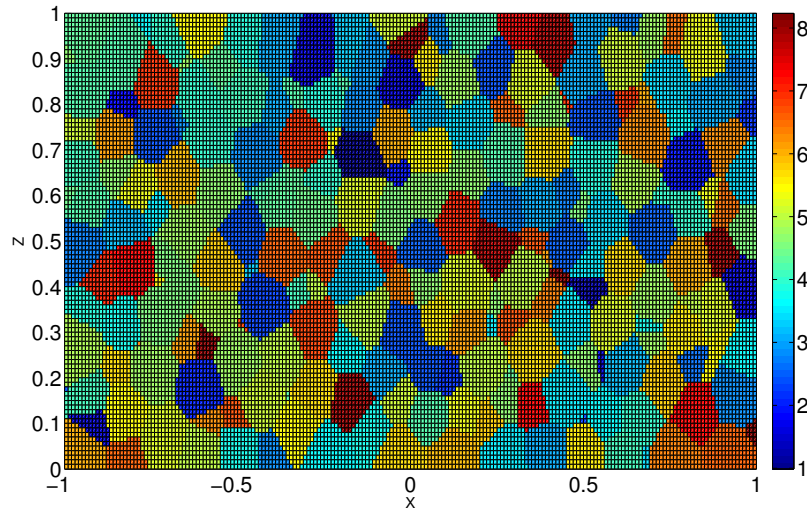**Figure 6.26:** Voxelization of the Voronoi tessellation

Elastic Constant	Stress (GPa)
C11	204.6
C12	137.7
C44	126.2

Table 6.1: Cubic elasticity constant for steel [VIT 03]

$$A = \frac{2C_{44}}{C_{11} - C_{12}} \tag{6.16}$$

In Fig. 6.27, the Voronoi diagram is voxelized and random Euler angles are assigned to each grain. It should be noted that this method is also able to simulate textured alloys by giving a principal orientation for every grain of the material.

Figure 6.27: Voxelization of the domain accordingly to the Voronoi tessellation. Amplitudes correspond to the sum of the Euler angles.

6.3.3 Contact stress field in polycrystalline materials

6.3.3.1 Description of the parameters of the simulation

The rolling of a 3D rigid cylinder on an elastic body enriched with cubic elastic inclusions is investigated (Fig. 4.7). The radius of the cylinder is $R = 2.78$ mm and a normal load $W = 25.5$ N is applied on the cylinder. The half-space Young's modulus and Poisson's ratio are chosen as $E_0 = 200$ GPa and $\nu_0 = 0.3$, respectively. For the homogeneous half-space, this load leads to a contact half width $a^* = 0.05$ mm and a Hertzian maximum contact pressure $P_H = 2$ GPa. The cylinder length in the Y-direction is $L_Y = 0.16$ mm which is more than three times larger than the contact half width in the x direction.

The loading moves from left ($x < 0$) to right ($x > 0$), maintaining the normal load constant, on a distance equal to $2a^*$ decomposed into 21 time steps. The tangential displacement at each time step is equal to $0.1a^*$. In this part, the effect of friction was neglected. The loading and material parameters are consistent with the ones from Vijay et al. [VIJ 18]. A Voronoi tessellation of the half-space is done and voxelized following the steps described in section 6.3.2.1. The average grain size in the Voronoi tessellation is around 10 μm [BOM 13a]. Note that the computation being elastic and without friction, only the randomly oriented microstructure has an influence on the results. The elastic constants of the inclusions are chosen to represent the same steel. The microstructure is made of around 600 000 inclusions. The half-space is discretized in $225 \times 115 \times 59$ computation points such that the space between points is $2\Delta x = 2\Delta y = 2\Delta z = 0.04a^*$. The proposed method allows to compute a rolling cycle in around 10 hours with 8 processors at 2.40 GHz and 8 GB RAM.

6.3.3.2   Stress field and contact pressure in the anisotropic domain

The stress field under the contact is strongly affected by the mismatch in the orientation of the cubic structure. The microstructure affects the depth and the amplitude of the maximum stress in the material during a loading cycle. The von Mises stress in the plane $y = 0$ is plotted in Fig. 6.28(b) and shows the stress rising effect of inclusion mismatch. The von Mises stress in the anisotropic and in the isotropic domain is plotted along the depth ($z > 0$) in ($x = 0; y = 0$). The von Mises stress amplitude in the anisotropic domain is locally higher than the one in the isotropic domain. The effect of the microstructure can also be observed on the contact pressure in Fig. 6.29. One may note that the maximum pressure is lower in the anisotropic domain than in the isotropic domain and the area of contact is larger in order to conserve the load equilibrium. This may come from the material orientation of the inclusions at the contact surface. The main difference with the work of Vijay et al. [VIJ 18] is the coupling between the contact solution and the heterogeneous material solver. In Vijay et al. [VIJ 18], the contact pressure is imposed and assumed Hertzian. In the present results, and with a same imposed normal load, the contact pressure is influenced by the microstructure resulting in a larger contact area and a lower maximum pressure. This larger distribution of pressure on the surface is responsible for a slightly lower stress distribution in the subsurface (see Fig. 6.28) than what can be observed in Vijay et al. [VIJ 18]. Finally, the results in Fig. 6.28 showed that the maximum von Mises stress in the anisotropic domain is resulting of the mismatch between the orientation of two grains but is not strongly affecting the contact pressure if it is localized far enough from the top surface.

(a)

(b)

(c)
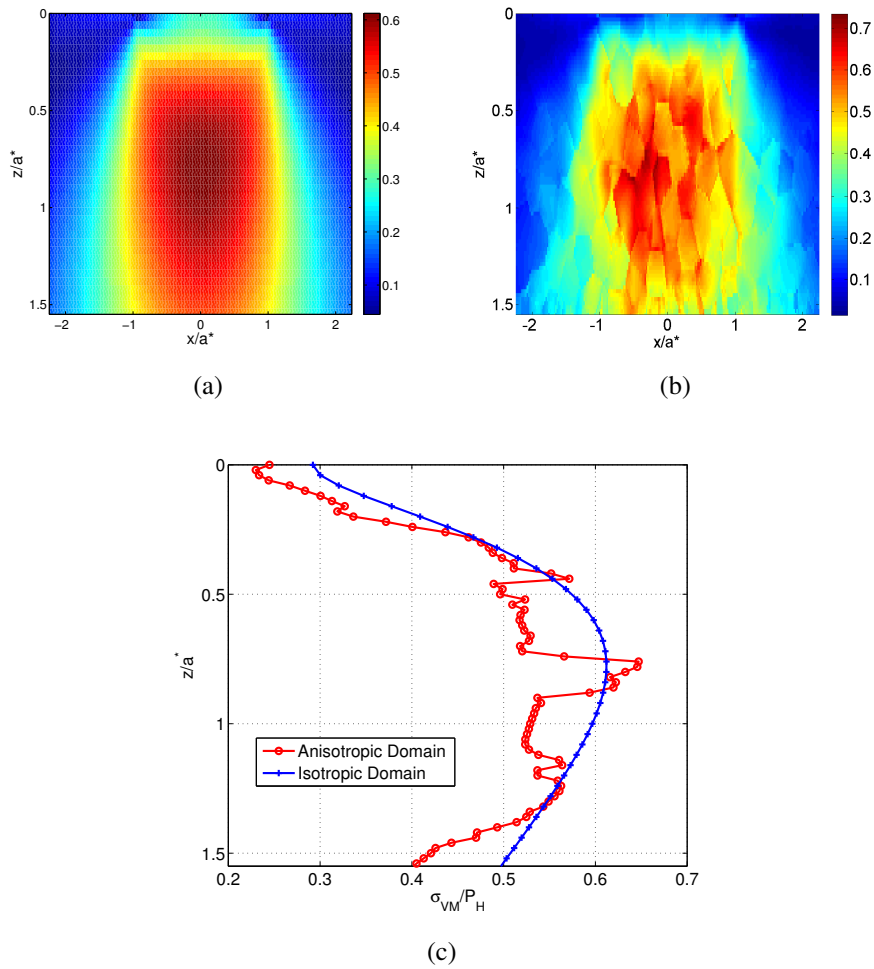
Figure 6.28: Dimensionless von Mises stress in the plane $y = 0$ (a) in an isotropic domain (b) in an anisotropic polycrystalline domain. (c) von Mises stress along z direction in the anisotropic domain and in the isotropic domain.
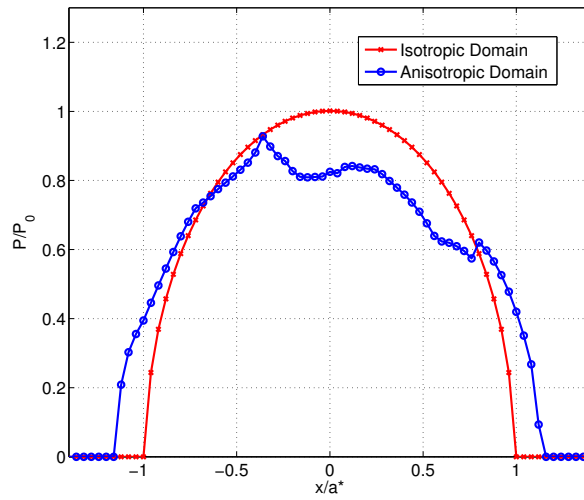
Figure 6.29: Contact pressure between the rigid cylinder and the isotropic domain and with the anisotropic domain.

6.3.4 Application to fatigue life of bearings

Fatigue is a process of damage accumulation manifesting through decreasing material properties in the solid. It can be decomposed in three steps: initiation of the crack, propagation of the crack and final rupture of the material. Each step is acting at different speeds depending of the material. The present work is focusing on the initiation of cracks because it is particularly affected by the random distribution of material properties and defects inside the material microstructure [ZHA 16]. The difference in elastic properties between the crystal acts as a stress raiser in solid and in particular at the grain boundaries [PER 93]. The previous microstructure model is used to predict the location of crack initiation in the material and its fatigue life under contact loading. In the following sections, classical methods to calculate the life of bearings are briefly recalled.

6.3.4.1 Weibull Statistical distribution

In order to estimate the life of manufactured bearings, experiments have emphasis the presence of a scatter in the results due to the presence of defects in the material. Weibull [WEI 39] proposed a statistical distribution often used to estimate the bearing life.

A two parameters Weibull probability function with k and λ positive constants can be expressed as:

$$f(x,\lambda,k) = \begin{cases} \frac{k}{\lambda}\left(\frac{x}{\lambda}\right)^{k-1} e^{-\left(\frac{x}{\lambda}\right)^k} & \forall x > 0 \\ 0 & \forall x \leq 0 \end{cases} \tag{6.17}$$

k is a shape parameter ($k = 1$ gives the exponential distribution) and λ is a scale parameter of the distribution.

By integrating Eq. 6.17, one can obtain the failure probability function:

$$F(x,\lambda,k) = \int_0^x f(t,\lambda,k)\mathrm{d}t = 1 - e^{-(\frac{x}{\lambda})^k} \tag{6.18}$$

With x representing the time leading to the failure of the component and F is the failure rate. If $k > 1$, the failure rate is increasing with time while $k < 1$ indicates that the failure rate is decreasing over time. Finally, for $k = 1$, the failure rate is constant over time.

A Weibull plot is representing the cumulative distribution of experimental data. In order to have a linear regression of the data, one can expressed Eq. 6.18 as following:

$$ln(1 - F(x,\lambda,k)) = -(\frac{x}{\lambda})^k \tag{6.19}$$

$$ln\left(ln\left(\frac{1}{1 - F(x,\lambda,k)}\right)\right) = kln(x) - kln(\lambda) \tag{6.20}$$

One can plot the Weibull linear plot on a logarithmic scale with k the slope of the line and λ the intercept. This tool is often used to estimate the population of rolling element bearings that fail before a given number of rolling cycles. It can be used to estimate the parameters of the Weibull distribution if a straight line is obtained from the data in the Weibull plot.

6.3.4.2 Lundberg-Palmgren Criterion

Based on the work of Weibull [WEI 39], Lundberg and Palmgren [LUN 47] proposed one of the first theories to estimate bearing life. This theory is based on the assumption that the most probable event leading to the bearing failure is subsurface crack initiation mainly due to the presence of a weak point in a volume of material. They assumed that the maximum shear stress coming from the contact loading is the main factor of bearing failure. The weak points are assumed to be randomly distributed in the material and the Weibull theory was applied to determine the probability of survival of the volume.

For a bearing under repeated rolling contact loading, the probability of survival S is expressed in the following equation:

$$ln\left(\frac{1}{S}\right) = A\frac{N^e\tau^cV}{z^h} \tag{6.21}$$

With N the number of repeated loading cycles, τ the maximum value of the shear stress over the stressed volume V and z the corresponding depth. e (the Weibull slope),c and h are material dependent parameters and A is an empirical constant. Ioannides and Harris [IOA 85] modified the Lundberg and Palmgren [LUN 47] equation to take into account infinite fatigue life by introducing a stress threshold.

Von Mises stress [IOA 85], unidirectional shear stress [ZAR 69] and octahedral shear stress [ZHO 93b] have been respectively used as the critical stress in the equation 6.21.

Replacing τ, z and V by the bearing basic dynamic load rating C and P the equivalent load on the bearing, one can obtain the equation giving the life for 10% of failure:

$$L_{10} = \left(\frac{C}{P}\right)^n \tag{6.22}$$

The exponent n was determined experimentally and is equal to 3 for ball bearings (elliptical contact area) and to 10/3 for roller bearings (line contact area).

This model assumes no shear traction and perfectly smooth surfaces leading to one of the main limitation of this formulation: no surface initiated failure of the bearings is considered.

Other modifications of the Lundberg Palmgren equation have been proposed by several authors in the literature [ZHO 93a, ZAR 94, CHE 95, HAR 99, MOR 18a]. In all these models, the critical stress and its depth are supposed constant to determine the bearing life. But several authors [CHE 89, YOS 93] found that, under the same experimental conditions, cracks occur at different depths.

6.3.4.3 Life scatter in rolling element bearings due to microstructure

Raje et al. [RAJ 08a] proposed an opposite viewpoint by considering that the variation in the critical stress and depth due to material microstructure are responsible for the dispersion in bearing life. Instead of assuming a Weibull distribution, they simulated randomly generated microstructure topology using Voronoi tessellation. Moreover, simulating a large number of microstructures allow to reproduce scatter in bearing life. In Raje et al. [RAJ 08a] formulation, the probability of survival and the bearing geometry are considered constant allowing to write a modified bearing life equation:

$$N \propto \frac{z^r}{\tau^q} \tag{6.23}$$

With $r = 2.33$ and $q = 10.33$ as in Lundberg-Palmgren theory. The critical stress and the corresponding depth are the variable parameters that need to be determined. Several microstructure simulations are giving life predictions and allow to determine the Weibull slope parameter e. The same approach has been used with 2D [JAL 09, PAU 14] and 3D [WEI 11, VIJ 18] finite element models. The same method has also been applied to the study of plasticity in rolling contact [WAR 14, GOL 18], fretting [GHO 13] and formation of butterfly wings [MOG 15b, MOG 15a, MOG 16b].

Critical stress computation

Numerical simulations have been performed on 30 domains to guarantee a good accuracy in the Weibull distribution (94% lower confidence limit [THO 70]). The Voronoi tessellation is the same in every domain and only the orientation angles of each crystal are changing. Effect of material orientation on the RCF life scatter is analyzed with three different critical stresses: maximum shear stress reversal, maximum Tresca stress and maximum Von Mises stress.

Amplitude and depth of the maximum critical stress in every domain are compared with the results obtained with an isotropic domain. Results for the maximum shear stress reversal are presented in Fig. 6.30, for the maximum Tresca stress in Fig. 6.31 and for the maximum Von Mises stress in Fig. 6.32. For every simulation, the maximum critical stress amplitude found is higher in the anisotropic domain than in the isotropic domain while the corresponding depth is varying around the reference homogeneous isotropic domain value. The mean amplitude of the maximum shear stress reversal is found to be $0.658P_H$ and their depth locations are found to vary between $0.36a^*$ and $0.68a^*$. The mean amplitude of the maximum Tresca stress is evaluated at $0.475P_H$ and their depth locations are found to vary between $0.52a^*$ and $1.04a^*$. Finally, the mean amplitude of the maximum Von Mises stress is found to be $0.849P_H$ and their depth locations are found to vary between $0.56a^*$ and $1.04a^*$. For all three critical stresses, results presented here are showing a scatter in the localization of the critical stress between the different anisotropic domains.
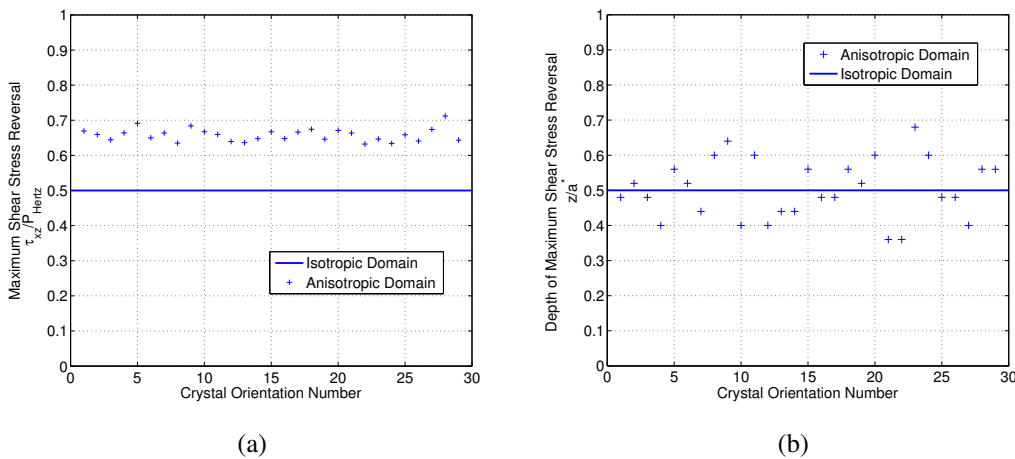
Figure 6.30: (a) Variation of magnitude in the maximum shear stress reversal in the 30 anisotropic domains. (b) Variation of the corresponding depth in the 30 anisotropic domains.

Fatigue criterion

According to Raje et al. [RAJ 08a] hypothesis, it is the variation in magnitude and depth of the critical stress that is responsible for the scatter in bearings life. The scatter in the results obtained with 30 different material's microstructures is used to create a Weibull plot of the probability of failure. One should note that no Weibull distribution of the fatigue lives is explicitly assumed here. 2 parameters and 3 parameters Weibull plots are realized with the three different critical stresses and are presented in Fig. 6.33, Fig. 6.34 and Fig. 6.35. The corresponding Weibull slopes can be found in Table 6.2. One can
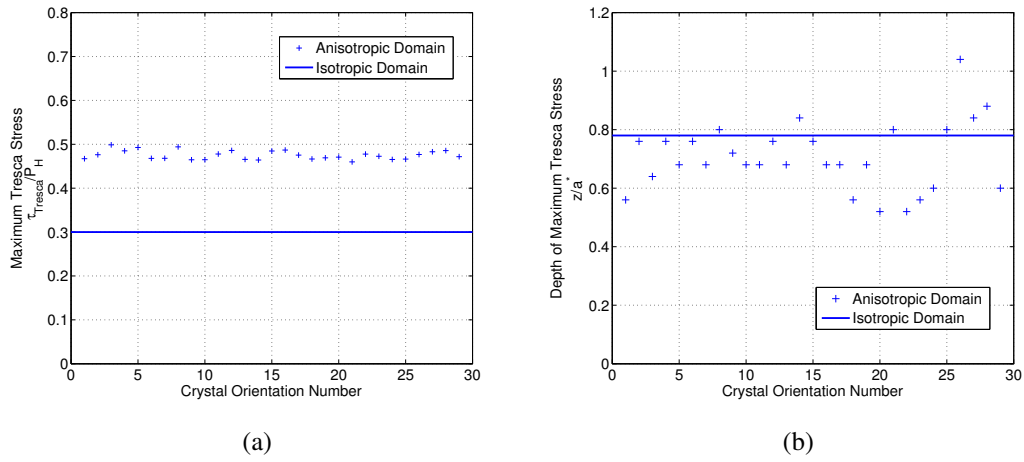
Figure 6.31: (a) Variation of magnitude in the maximum Tresca stress in the 30 anisotropic domains. (b) Variation of the corresponding depth in the 30 anisotropic domains.
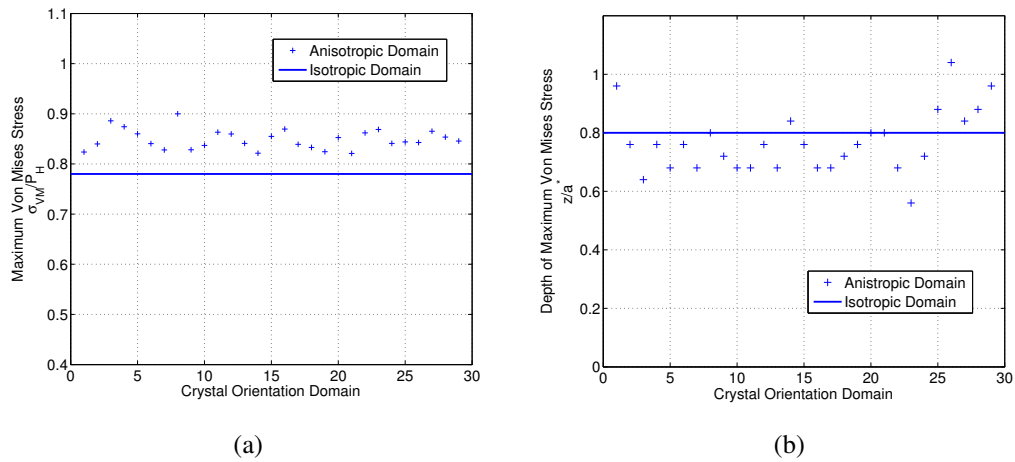
Figure 6.32: (a) Variation of magnitude in the maximum Von Mises stress in the 30 anisotropic domains. (b) Variation of the corresponding depth in the 30 anisotropic domains.
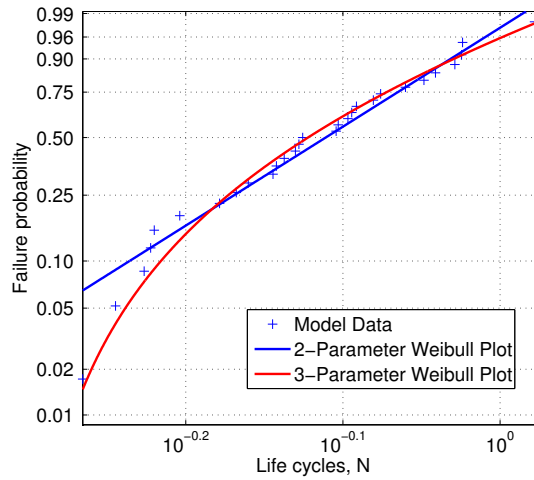
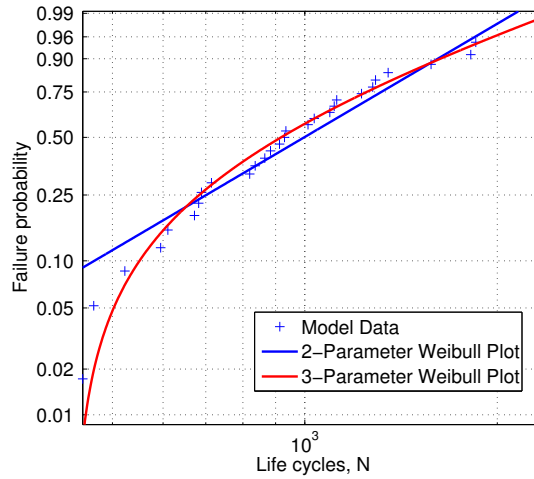**Figure 6.33:** 2 and 3 parameters Weibull plot superimposed on the data from the model for the maximum reversal shear stress criterion.

Stress Criterion	2 Parameters Weibull Slope	3 Parameters Weibull Slope
$\Delta\tau_{xz}$	6.5587	2.2899
τ_{Tresca}	2.4998	1.3268
τ_{VM}	2.4039	1.5534

Table 6.2: Weibull slopes for different stress criterion.

observed that the maximum shear stress reversal is showing a bigger Weibull slope than the two others critical stresses and is the more critical criteria for life prediction. These results are confirming the influence of material's microstructure in the life scatter of parts under RCF loading.

Weibull slope parameters with Finite Element Simulation

The Weibull slopes obtained with our results are compared with the Weibull slopes found in the literature in Table 6.3. The presented results are in the same range than the results obtained with finite element models for isotropic and anisotropic materials. Using the maximum shear stress reversal, Weibull slopes obtained with the semi-analytical solver exhibit a higher slope than the one found with finite element by Vijay et al. [VIJ 18]. One reason is that the voxelization of the microstructure doesn't allow to accurately reproduce the smooth grain boundaries [DOI 15b]. Moreover, the computational discretization of the semi-analytical solver is only able to compute the stress field on a regular grid of Gaussian points while the finite element model allow to mesh the grains to compute the shear stress reversal on the geometric grain boundary. This difference can be observed in lower amplitude of shear stress reversal in Fig. 6.30(a) than in Vijay et al. [VIJ 18]. Finally, the methodology presented here is showing the ability of the semi-analytical solver

Figure 6.34: 2 and 3 parameters Weibull plot superimposed on the data from the model for the maximum Tresca stress criterion.
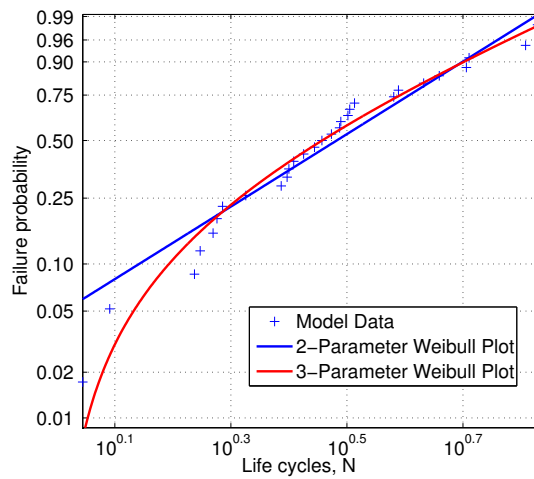
Figure 6.35: 2 and 3 parameters Weibull plot superimposed on the data from the model for the maximum Von Mises stress criterion.

Authors	Weibull Slope
Lundberg-Palmgren [LUN 47]	1.125
Raje et al. [RAJ 08a]	3.36
Paulson et al. [PAU 14]	1.18
Weinzapfel et al. [WEI 11]	4.55
Vijay et al. [VIJ 18]	0.95

Table 6.3: Weibull slopes from models in literature.

to capture the life scatter in rolling contact fatigue.

6.4 Partial Conclusion

This chapter has presented an application of the heterogeneous semi-analytical solver to microstructure modeling of two kinds of heterogeneous materials. Although a first part focused on the ability of the method to find the homogenized effective properties of heterogeneous materials, limitations of the homogenization theory for contact mechanics applications have been highlighted. A link between the scale of the contact and the scale of the material microstructure has been emphasized and showed the need to model material heterogeneous structure. In particular,the mesoscopic scale is preferred to model composite materials. A voxelization method is proposed using experimental data from tomography in order to model the woven complex geometry. The effect of the contact area and of the composite structure on the localization of maximum stress is highlighted. Moreover, a modification of the previous damage model is proposed to simulate the damage behavior of the anisotropic yarns. Finally, the same voxelization technique is used for bearing steel anisotropic microstructure based on a Voronoi tessellation and allow to exhibit the scatter in fatigue life prediction. One of the major contributions of this work is the ability of the semi-analytical method to solve a coupled contact problem along with the strongly heterogeneous material subsurface problem.

Conclusion and Prospects

Introduction of complex materials like woven composite materials in mechanical systems is a major trend in the aeronautical industry. Therefore, the development of fast and reliable tools to simulate the contact between composite and metallic parts is of major importance to predict the life of such components.

The present work used Semi-Analytical Methods (SAM) to solve three dimensional contact problem on heterogeneous materials as presented in Chapter 2. The first approach coupled the semi analytical solver with a continuum damage mechanics based model to reproduce the damage phenomena appearing in the contact area in fretting conditions (Chapter 3). Both gross slip regime and partial slip regime have been investigated. Results show a good agreement with experimental results that the appearance of wear and crack initiation is depending on the sliding conditions. Moreover, results showed that damage in contact area lead to a decrease of the contact pressure. An application to coated materials was also presented and the ability of hard coatings to protect the substrate is confirmed by the model. A damage model from the literature is implemented and a good agreement is found between results from both models. Moreover, the damage mechanics approach based on a three dimensional field computation is compared with the classical wear approach based on two dimensional field computation of the dissipated energy. Both methods are giving similar results in term of contact pressure evolution.

The approach has been extended to the modeling of microstructural alterations around nonmetallic inclusions in bearing steel (Chapter 4). SAM's is used to compute the stress field around the inclusion during a rolling cycle for the three dimensional propagation of butterfly wings. The model is using small cuboidal inclusions to represent the microstructural alterations. Whereas influence of an inclusion close to the surface on the contact pressure has already been highlighted, the effect of inclusion depth and rigidity on butterfly wings formation is emphasized. The computation speed and the low memory needed allow to execute the numerous simulations needed. In addition to this subsurface model, SAM is applied to surface initiated damage during the rolling over an artificial indent and show the capacity of this method to reproduce C-cracks around indent.

Whereas tribological behavior of metallic alloys has been studied for decades, composite material behavior is still not well understood. To this end, experimental tests have been realized and results are synthesized in Chapter 5. Pin-on-disk (POD) and fretting tests between a AISI 52100 steel ball and a woven composite material show the different wear behaviors of the matrix compared to the yarns. Coefficient of friction in the POD test corresponds to the average value of the respective coefficient of friction of each

constituent of the material. Specific wear rates for the whole material and for each of its constituents are identified. Finally, design of experimental test with a contact area closer to the scale of the composite material REV is presented along with preliminary results. The effect of damage on the normal behavior are clearly identified on the stress-displacement curve. Therefore, the results show the influence of the complex structure of the material on its mechanical and tribological behavior. Realization of a tomography of the part before and after the test would allow to identify composite damage mechanisms in contact loading.

The capacity of the semi-analytical method to model material's complex structure at the mesoscopic level for composite materials or at the microscopic level for bearing steel has been detailed in the Chapter 6. In the first place, limitation of the homogenization theory and of the scale separability when contact loading is applied is pointed out. Thus, a voxelization method using cuboidal inclusions with the properties of the yarns is used with the semi-analytical solver. Results showed the perturbation of the stress field in the contact area and in the volume below. The same technique is applied to bearing steel microstructure. Scatter in the rolling contact fatigue life is highlighted and results are compared with finite element models from the literature.

However, all the analyses performed in this work have been limited to elasticity coupled with a damage model. The additional effect of plasticity for the fretting behavior would need to be investigated through a fully coupled heterogeneous plastic damage model. It would allow to simulate the build-up effect on the side of the fretting zone. Effect of the presence of butterfly wings around hard inclusions in rolling contact fatigue would need to be analyzed at the light of micro plasticity due to the stress rising effect occurring in the vicinity of the inclusion [AMU 16]. To be more accurate in the simulation of composite materials, the visco-elastic behavior of the matrix as studied by Koumi [KOU 14a, KOU 15b] require more attention and a coupled visco-elastic damage model should be implemented. In order to represent composite damage mechanisms, development of a model for the complex structure of woven composite would need to take into account debonding between the yarns and the matrix. Finally, one should note that the results of this work proved the efficiency of the semi-analytical method to deal with complex physical phenomena and geometries. Furthermore, results presented in the last two chapters highlighted the limitation of homogeneous model for contact and damage simulation and the need for computational model of contact at the mesoscopic scale.

Ackowledgement

Appendix A

Influence Coefficients

The influence coefficients giving the elastic stresses in a semi infinite body generated by a uniform pressure are recalled here. Love [LOV 52] first developed the solution for the displacement of the surface with a patch of normal pressure and Vergne [VER 85] extended the solution to tangential loading.

Elastic stresses generated by a uniform pressure

Coefficients giving the stress field due to a uniform pressure applied on a rectangular surface of size $\Delta x \times \Delta y$ and centered in $(x,y) = (0,0)$. The coefficients are given as a function of the position of the calculation point (x,y,z), x and y being the directions parallel to the surface and z the depth, directed towards the body. E and ν are the Young modulus and the Poisson's ratio of the body respectively.

One can define $\rho = \sqrt{x^2 + y^2 + z^2}$ and I,J index referring to x, y or z.

$$\frac{\sigma_{IJ}}{p} = C_{IJ}^p(x,y,z,E,\nu) = S_{IJ}^p(x + \frac{\Delta_x}{2}, y + \frac{\Delta_y}{2}, z, E, \nu) + S_{IJ}^p(x - \frac{\Delta_x}{2}, y - \frac{\Delta_y}{2}, z, E, \nu)$$

$$- S_{IJ}^p(x + \frac{\Delta_x}{2}, y - \frac{\Delta_y}{2}, z, E, \nu) - S_{IJ}^p(x - \frac{\Delta_x}{2}, y + \frac{\Delta_y}{2}, z, E, \nu), \quad \text{(A.1)}$$

with

$$S_{xx}^p(x,y,z,E,\nu) = \frac{\nu}{\pi} \arctan\left(\frac{z^2 + y^2 - y\rho}{zx}\right) + \frac{1-2\nu}{\pi} \arctan\left(\frac{\rho - y + z}{x}\right) + \frac{z}{2\pi} \frac{xy}{(x^2 + z^2)\rho}, \quad \text{(A.2)}$$

$$S_{yy}^p(x,y,z,E,\nu) = \frac{\nu}{\pi} \arctan\left(\frac{z^2 + y^2 - y\rho}{zx}\right) + \frac{1-2\nu}{\pi} \arctan\left(\frac{\rho - x + z}{y}\right) + \frac{z}{2\pi} \frac{xy}{(y^2 + z^2)\rho}, \quad \text{(A.3)}$$

$$S_{zz}^p(x,y,z,E,\nu) = \frac{1}{2\pi} \arctan\left(\frac{z^2 + y^2 - y\rho}{zx}\right) - \frac{z}{2\pi} \frac{xy}{\rho} \left(\frac{1}{x^2 + z^2} + \frac{1}{y^2 + z^2}\right), \quad \text{(A.4)}$$

$$S^p_{xy}(x,y,z,E,\nu) = -\frac{z}{2\pi}\frac{1}{\rho} - \frac{1-2\nu}{2\pi}\ln(\rho+z), \tag{A.5}$$

$$S^p_{yz}(x,y,z,E,\nu) = \frac{z^2}{2\pi}\frac{x}{(y^2+z^2)\rho}, \tag{A.6}$$

$$S^p_{xz}(x,y,z,E,\nu) = \frac{z^2}{2\pi}\frac{y}{(x^2+z^2)\rho}. \tag{A.7}$$

Elastic stresses generated by a uniform shear in the x direction

Contribution of applied shear stress along the x direction are recalled here. The shear are applied on a rectangular surface of size $\Delta x \times \Delta y$ centered in $(x,y)=(0,0)$.

$$\frac{\sigma_{IJ}}{q_x} = C^{q_x}_{IJ}(x,y,z,E,\nu) = S^{q_x}_{IJ}(x+\frac{\Delta_x}{2},y+\frac{\Delta_y}{2},z,E,\nu) + S^{q_x}_{IJ}(x-\frac{\Delta_x}{2},y-\frac{\Delta_y}{2},z,E,\nu)$$
$$- S^{q_x}_{IJ}(x+\frac{\Delta_x}{2},y-\frac{\Delta_y}{2},z,E,\nu) - S^{q_x}_{IJ}(x-\frac{\Delta_x}{2},y+\frac{\Delta_y}{2},z,E,\nu), \tag{A.8}$$

with

$$S^{q_x}_{xx}(x,y,z,E,\nu) = -\frac{z}{2\pi}\frac{1}{\rho}\left(1+\frac{-x^2+zy}{(\rho+z)(\rho-y)}\right) + \frac{\nu}{\pi}\frac{y}{\rho+z} - \frac{1}{\pi}\ln(\rho-y), \tag{A.9}$$

$$S^{q_x}_{yy}(x,y,z,E,\nu) = -\frac{z}{2\pi}\frac{y}{\rho(\rho+z)} - \frac{\nu}{\pi}\left(\frac{y}{\rho+z}+\ln(\rho-y)\right), \tag{A.10}$$

$$S^{q_x}_{zz}(x,y,z,E,\nu) = \frac{z^2}{2\pi}\frac{y}{\rho(x^2+z^2)}, \tag{A.11}$$

$$S^{q_x}_{xy}(x,y,z,E,\nu) = -\frac{z}{2\pi}\frac{x}{\rho(\rho+z)} - \frac{\nu}{\pi}\frac{x}{\rho+z} - \frac{1}{2\pi}\ln(\rho-x), \tag{A.12}$$

$$S^{q_x}_{yz}(x,y,z,E,\nu) = -\frac{z}{2\pi}\frac{1}{\rho}, \tag{A.13}$$

$$S^{q_x}_{xz}(x,y,z,E,\nu) = \frac{z}{2\pi}\frac{xy}{\rho(x^2+z^2)} + \frac{1}{2\pi}\arctan\left(\frac{z^2+y^2-y\rho}{zx}\right). \tag{A.14}$$

Appendix B

Heterogeneity influence coefficients

The results presented here are limited to a uniform eigenstrain, therefore, only the calculation of the tensor D_{ijkl} is performed.

$$D_{ijkl} = \frac{1}{8\pi(1-\nu)} [\Psi_{,ijkl} - 2\nu\delta_{kl}\phi_{,ij} - (1-\nu)(\delta_{kl}\phi_{il} + \delta_{ki}\phi_{,jl} + \delta_{jl}\phi_{,ik} + \delta_{li}\phi_{,jk})] \quad \text{(B.1)}$$

Potential functions can be expressed as:

$$\phi = \pi a_1 a_2 a_3 \int_\lambda^\infty \frac{U \mathrm{d}s}{\Delta} \quad \text{(B.2)}$$

$$\psi = \pi a_1 a_2 a_3 \frac{1}{2} \int_\lambda^\infty \left[\frac{\partial}{\partial s}\left(\frac{s^2 U^2}{\Delta}\right) - \frac{1}{2}\frac{U^2 s}{\Delta}\right] \mathrm{d}s \quad \text{(B.3)}$$

with

$$U(s) = 1 - \frac{x_i x_i}{a_i^2 + s} \quad \text{(B.4)}$$

$$\Delta(s) = \sqrt{(a_1^2 + s) + (a_2^2 + s) + (a_3^2 + s)} \quad \text{(B.5)}$$

Integral's inferior born λ is the highest square root of equation $U(\lambda) = 0$ for the point outside of the inclusion and $\lambda = 0$ inside the inclusion. By defining the following integrals:

$$I(\lambda) = 2\pi a_1 a_2 a_3 \int_\lambda^\infty \frac{\mathrm{d}s}{\Delta(s)} \quad \text{(B.6)}$$

$$I_i(\lambda) = 2\pi a_1 a_2 a_3 \int_\lambda^\infty \frac{\mathrm{d}s}{(a_i^2 + s)\,\Delta(s)} \quad \text{(B.7)}$$

$$I_{ij}(\lambda) = 2\pi a_1 a_2 a_3 \int_\lambda^\infty \frac{\mathrm{d}s}{(a_i^2 + s)\left(a_j^2 + s\right)\Delta(s)} \quad \text{(B.8)}$$

Potential function can then be written as,

$$\phi = V \quad \text{(B.9)}$$

$$\psi_{,i} = x_i \left(V - a_i^2 V_i\right) \quad \text{(B.10)}$$

With,

$$V(x) = \pi a_1 a_2 a_3 \int_\lambda^\infty \frac{U(s)}{\Delta(s)} ds = \frac{1}{2}\left[I(\lambda) - x_r x_r I_r(\lambda)\right] \tag{B.11}$$

$$V_i(x) = \pi a_1 a_2 a_3 \int_\lambda^\infty \frac{U(s)}{(a_i^2 + s)\Delta(s)} ds = \frac{1}{2}\left[I_i(\lambda) - x_r x_r I_{ri}(\lambda)\right] \tag{B.12}$$

Expressions of I integrals depend on the geometry of the inclusion and in the case of a **spherical inclusion** $(a_1 = a_2 = a_3 = a)$ can be expressed as

$$I(\lambda) = \frac{4\pi a^3}{\sqrt{a^2 + \lambda}}, \tag{B.13}$$

$$I_1(\lambda) = I_2(\lambda) = I_3(\lambda) = \frac{4\pi a^3}{3(a^2 + \lambda)^{\frac{3}{2}}} \tag{B.14}$$

For a **cuboidal inclusion**, potential functions have been expressed by MacMillan [MAC 58] and recalled here:

$$\phi(x) = \sum_{n=1}^{8} E(c_n) \tag{B.15}$$

$$\psi(x) = \sum_{n=1}^{8} F(c_n) \tag{B.16}$$

With

$$E = c_1 c_2 \log(R + c_3) + c_2 c_3 \log(R + c_1) + c_3 c_1 \log(R + c_2) \tag{B.17}$$

$$- \frac{1}{2}\left\{c_1^2 \tan^{-1}\left(\frac{c_2 c_3}{c_1 R}\right) + c_2^2 \tan^{-1}\left(\frac{c_3 c_1}{c_2 R}\right) + c_3^2 \tan^{-1}\left(\frac{c_1 c_2}{c_3 R}\right)\right\} \tag{B.18}$$

$$F = \frac{1}{4} c_1 c_2 c_3 R + \frac{1}{6}\left\{\left(R^2 - c_1^2\right) c_2 c_3 \log(R + c_1)\right. \tag{B.19}$$

$$+ \left(R^2 - c_2^2\right) c_3 c_1 \log(R + c_2) + \left(R^2 - c_3^2\right) c_1 c_2 \log(R + c_3)\right\} \tag{B.20}$$

$$- \frac{1}{12}\left\{c_1^4 \tan^{-1}\left(\frac{c_2 c_3}{c_1 R}\right) + c_2^4 \tan^{-1}\left(\frac{c_3 c_1}{c_2 R}\right) + c_3^4 \tan^{-1}\left(\frac{c_1 c_2}{c_3 R}\right)\right\} \tag{B.21}$$

and

$$R = \sqrt{c_1^2 + c_2^2 + c_3^2} \tag{B.22}$$

Vector $c = (c_1, c_2, c_3)$ is defined for the following equations,
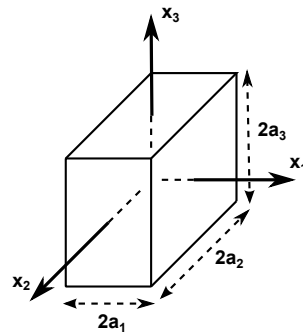
Figure B.1: Cuboidal heterogeneity [LER 13]

$$c_1 = (x_1 - a_1, x_2 - a_2, x_3 - a_3)$$
$$c_2 = (x_1 + a_1, x_2 - a_2, x_3 - a_3)$$
$$c_3 = (x_1 + a_1, x_2 + a_2, x_3 - a_3)$$
$$c_4 = (x_1 - a_1, x_2 + a_2, x_3 - a_3)$$
$$c_5 = (x_1 - a_1, x_2 + a_2, x_3 + a_3)$$
$$c_6 = (x_1 - a_1, x_2 - a_2, x_3 + a_3)$$
$$c_7 = (x_1 + a_1, x_2 - a_2, x_3 + a_3)$$
$$c_8 = (x_1 + a_1, x_2 + a_2, x_3 + a_3)$$

(B.23)

Appendix C

Zero-padding

This technique consists in extending the size of the sources (pressure here) defined on [0,N-1] to [0,2N+1] by setting their value to 0 on the zone [N, 2N+1]. No overlapping with the influence coefficients is then possible.

Wrap-around order

For the influence coefficients, the domain size [0, N-1] is also doubled and becomes [0, 2N-1]. The coefficient with index N is set equal to zero in order to avoid overlapping both domain. Coefficients from N+1 to 2N-1 are extended according to their parity properties. Details on the method can be found in [LIU 00, GAL 07b].

The FFT is then applied to the extended data, multiplication is made in the frequency domain and the inverse FFT allows to determine the final results with negligible error.
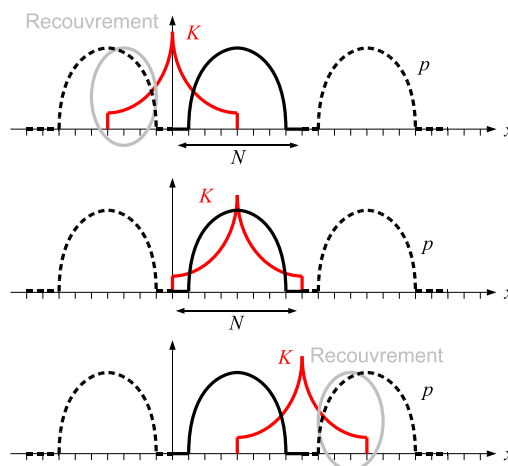
Figure C.1: Periodicity and overlapping created by the convolution product [GAL 07b]
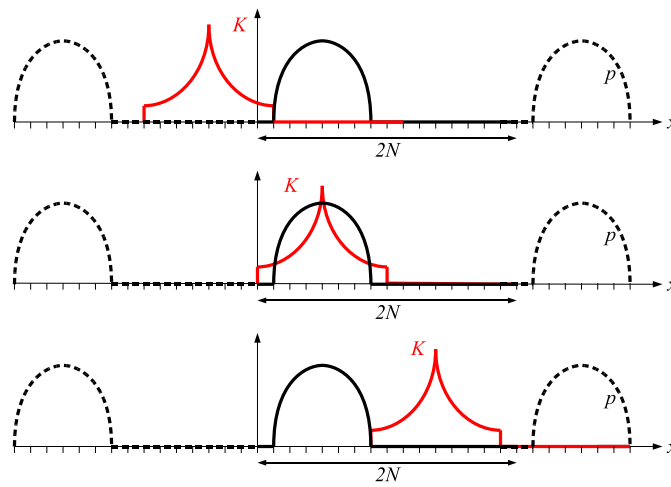
Figure C.2: Deleting overlapping using zero padding [GAL 07b]
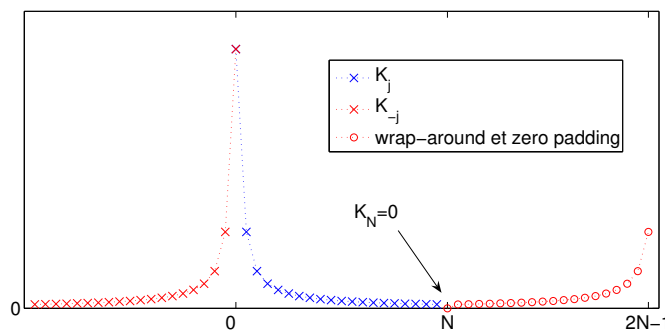
Figure C.3: Wrap-around and zero-padding for even coefficients [GAL 07b]
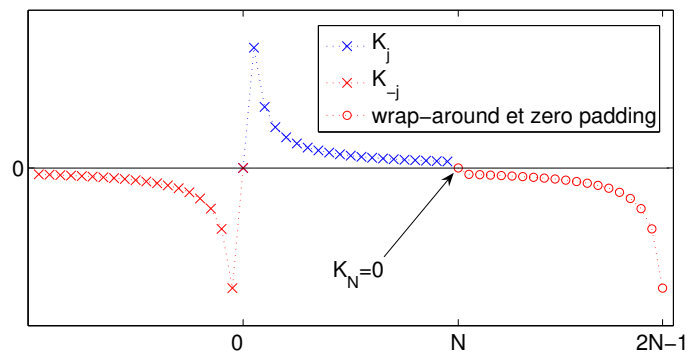
Figure C.4: Wrap-around and zero-padding for odd coefficients [GAL 07b]

Appendix D

Optical micrographs observations

Some observations of the contact tracks were conducted after the experiments using an optical micrograph to create a 3D surface reconstruction image. For different normal loading amplitudes, images have been taken on localization where the contact area is on yarn and where the contact area is on the matrix. One can noticed that the track width is larger when the contact is on the matrix than on the yarn due to its lower stiffness (see Fig. D.1, Fig. D.2). Moreover, the wear scar measured on the matrix (around $25\mu m$, see Fig. 6.2(a)) is deeper than the one on the yarn (around $4\mu m$, see Fig. 6.2(b)). It can be observed that each component of the composite material exhibit different wear mechanisms. Matrix wear mechanism seems to be adhesive wear while yarn has abrasive wear with creation of very thin wear particles. These mechanisms are in good agreement with what has been observed by Li et al. [LI 18b]. Moreover, observations show that debris particles migrate out of the contact during the test due to friction and the moving load. Because of the unilateral sliding, these particles are piling up on both side of the track (see Fig. 6.3(a) and Fig. 6.3(b)) and some debris particles are transferred on the steel ball (see Fig. D.3). One should note that the piling up effect is more likely to happen on the yarn (Fig. 6.1(b)) than on the matrix (Fig. 6.1(a)).
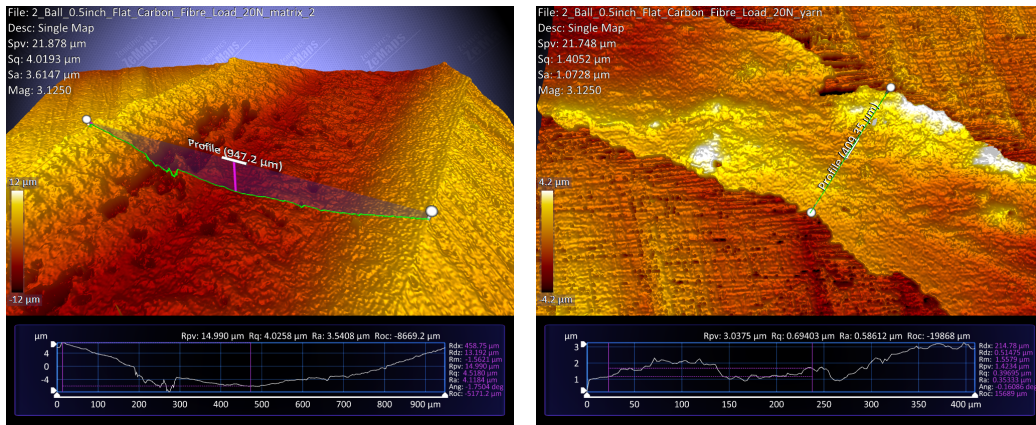
(a)

(b)

Figure D.1: N=5000 Cycles and W=20N (a) Contact surface on matrix. (b) Contact surface on yarn.
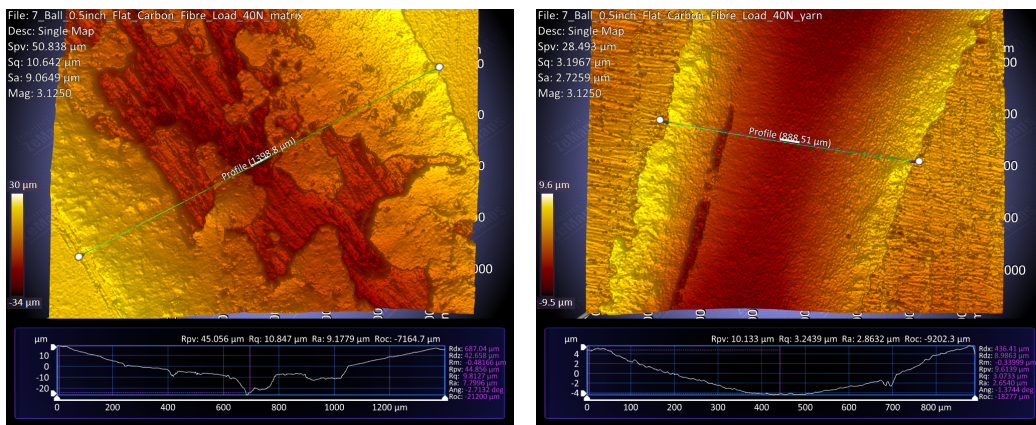
(a)

(b)

Figure D.2: N=5000 Cycles and W=40N (a) Contact surface on matrix. (b) Contact surface on yarn.
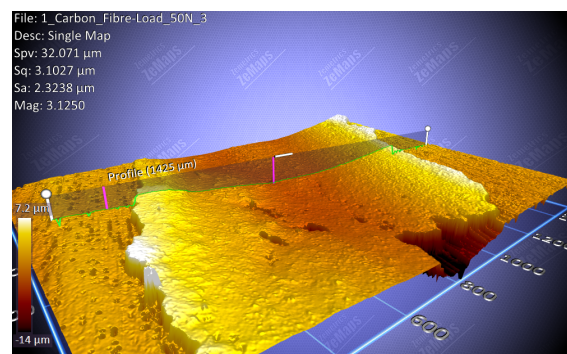
(a)
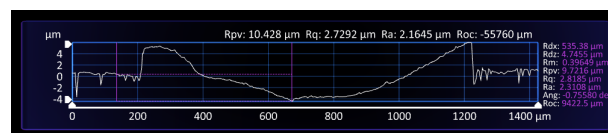
(b)
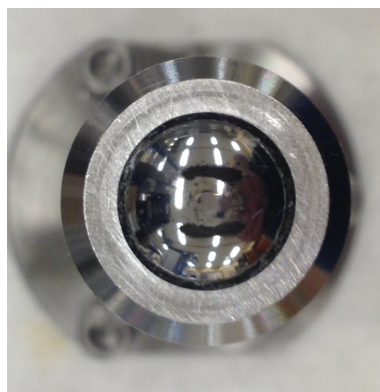
(c)

Figure D.3: N=5000 Cycles and W=50N (a) Contact surface on yarn. (b) Profile transverse to the contact track with pile up from wear debris. (c) Observation of wear debris on the ball after pin-on-disk experiment.

Comparison with steel on steel contact.

In order to compare the previous result of pin-on-disk experiments between a steel ball and a woven composite disk, tests have been performed in the same conditions between a 52100 AISI steel ball and a disk of the same steel. In-situ coefficient of friction and scar depth are measured for four different normal loading amplitudes and plotted in Fig. D.4 and D.5. The averaged coefficient of friction between two AISI 52100 bearing steel part is found to be $\mu \approx 0.75$. Moreover, the measured scar depth for the four different loading amplitudes have almost the same slope. Using the same approach than in section 5.2.4, the specific wear rate is calculated using a linear regression of the curve representing the wear volume function of the sliding distance time the normal load. Considering the hardness of AISI 52100 steel to be $H = 7.85$GPa, one can calculate the dimensionless Archard wear coefficient to be $K = 5.98 \times 10^{-7}$. This result is in the same range than what can be found in the literature [BHU 01]. The wear mechanisms between two steel parts are associated with plastic deformations and adhesive wear [ALO 14].
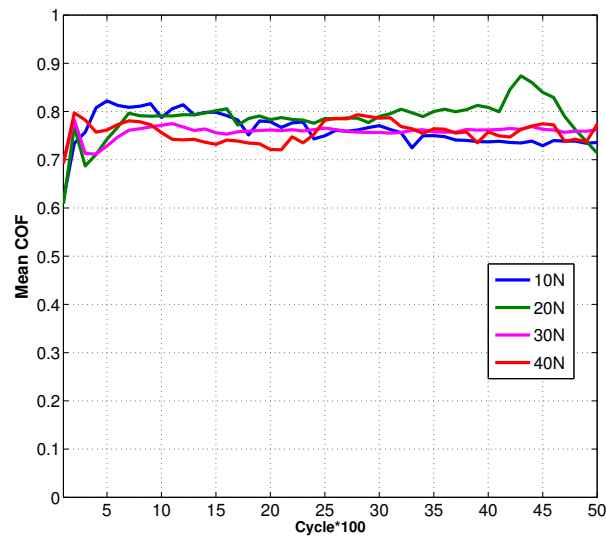
Figure D.4: In-situ coefficient of friction between AISI 52100 steel ball and disk for different normal loads.

Fretting experiment with METL test rig

A test rig designed at the METL to realize fretting wear test in various configuration [LEO 12a] was used in this section (see Fig. D.7). Fretting tests have been realized between the composite material and two flat parts made of steel. A small disk of composite was cut and machined to realized a crowning on both surfaces in contact. A linear actuator was used to impose a reciprocating movement through an arm holding the composite.
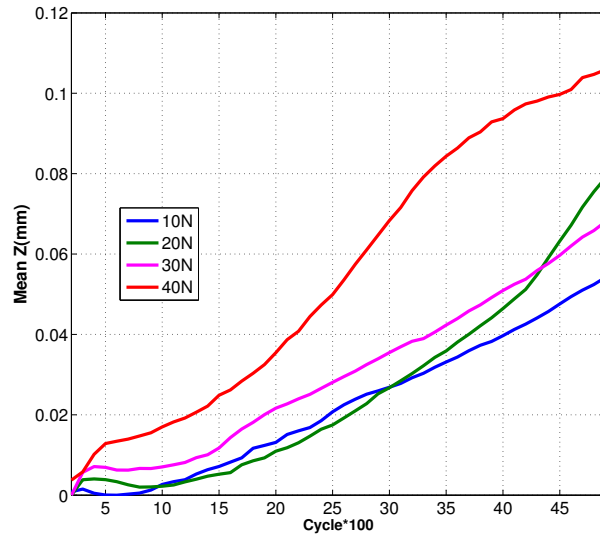
Figure D.5: In-situ wear depth between AISI 52100 steel ball and disk for different normal loads.
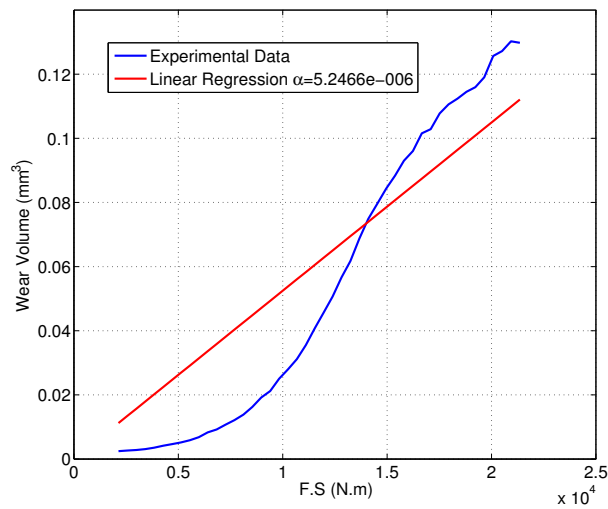
Figure D.6: Wear Volume between AISI 52100 steel ball and disk function of the sliding distance with W=40N. Obtention of the wear rate coefficient from a linear regression.

A load cell with a 222 N capacity is fixed on the arm between the composite part and the actuator and a dead weight is used to apply a normal load on the contact. Finally, a position sensor was used to measure the displacement of the moving arm as in Fig. 6.7(b). Both the friction force and the tangential measurement are measured during the test and fretting loops during the experiments are plotted in Fig. D.8. The wear scar obtained with this experiment was too large be observed with the profilometer as in the previous section. Some limitations of the sensors make it difficult to measure the fretting loop in partial slip conditions and further experiments with a modified test rig would be necessary to obtain a good measurement of the fretting behavior.

(a)   (b)

(c)
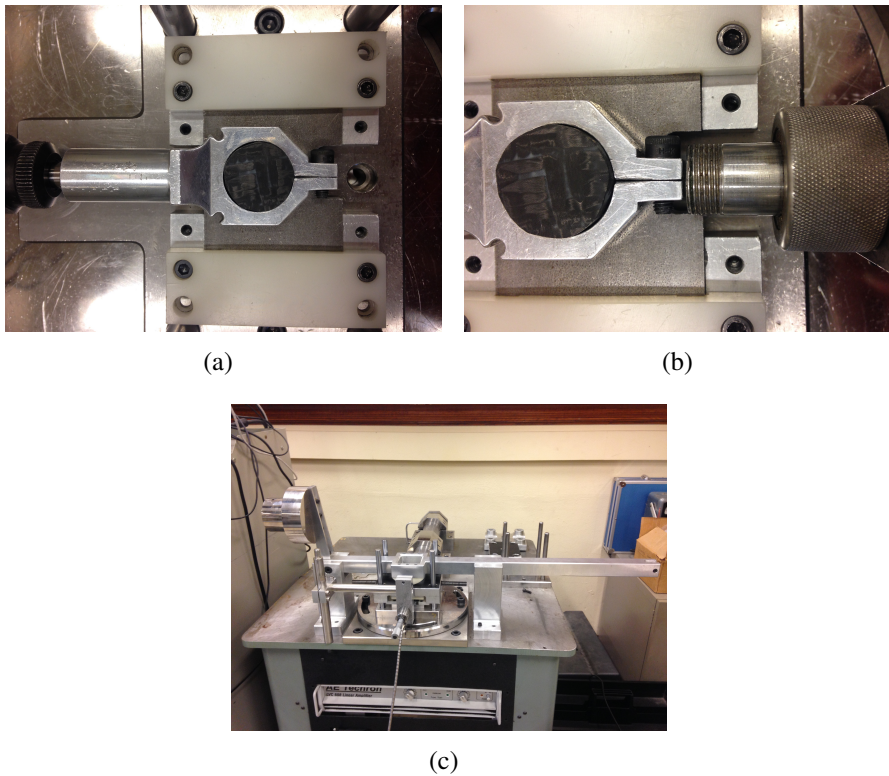
Figure D.7: Fretting experiment with METL test rig (a) Up view. (b) Displacement sensor (c) Global view of the experimental set up.
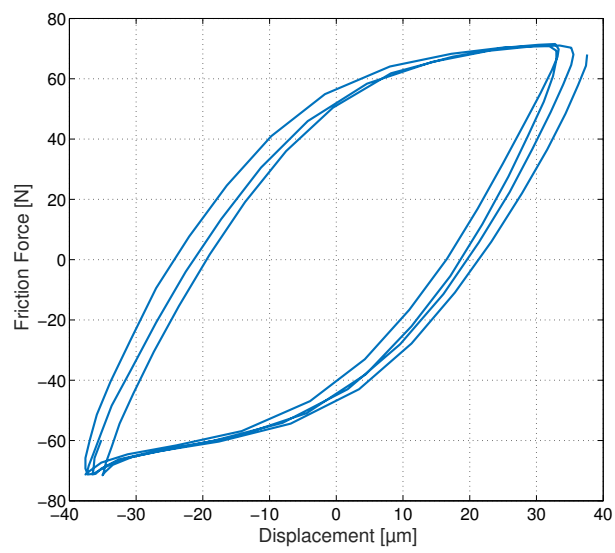
Figure D.8: Fretting Loop N=60000, W=125N and $\delta = 0.2$mm

Bibliography

[AHM 18] AHMADI A., SADEGHI F., SHAFFER S.
In-Situ Friction and Fretting Wear Measurements of Inconel 617 at Elevated Temperature. *Wear*, vol. 410-411, 2018, p. 110-118.

[AIE 01] AIELLO G.
Utilisation des composites à matrice céramique SiCf/SiC comme matériau de structure de composants internes du tore d'un réacteur en fusion. PhD Thesis, Université d'Evry Val d'Essone, 2001.

[ALE 86] ALEKSANDROV V., ROMALIS B.
Contact Problems in Mechanical Engineering. *Mashinostroenie, Moscow*, , 1986.

[ALL 93] ALLIX O., CLUZEL C., GASSER A., LADEVÈZE P.
Modélisation des composites céramique-céramique à différentes échelles. *Revue des composites et des matériaux avancés*, vol. 3, 1993.

[ALL 10] ALLEY E. S., NEU R. W.
Microstructure-sensitive modeling of rolling contact fatigue. *International Journal of Fatigue*, vol. 32, n° 5, 2010, p. 841 - 850.

[ALO 14] ALOTAIBI J., YOUSIF B., YUSAF T.
Wear Behaviour and mechanism of different metals sliding against stainless steel counterface. *Journal of Engineering Tribology*, vol. 228 (6), 2014, p. 692-704.

[ALT 18] AL-TAMEEMI H. A., LONG H., DWYER-JOYCE R. S.
Initiation of sub-surface micro-cracks and white etching areas from debonding at non-metallic inclusions in wind turbine gearbox bearing. *Wear*, vol. 406-407, 2018, p. 22-32.

[AMU 16] AMUZUGA K. V., CHAISE T., DUVAL A., NELIAS D.
Fully Coupled Resolution of Heterogeneous Elastic-Plastic Contact Problem. *Journal of Tribology*, vol. 138, 2016, p. 021403-1.

[ANG 16] ANGRAND L.
Modèle d'endommagement incrémental en temps pour la prévision de la durée de vie des composites tissés 3D en fatigue cyclique et en fatigue aléatoire. PhD Thesis, Université Paris - Saclay / ENS Cachan, 2016.

[ANT 08] ANTALUCA E., NELIAS D.
Contact fatigue analysis of a dented surface in a dry elastic-plastic circular point contact. *Tribology Letters*, vol. 29(2), 2008, p. 139-153.

[ARC 53] ARCHARD J.
Contact and rubbing of flat surfaces. *Journal of Applied Physics*, vol. 24 (8), 1953, p. 981-988.

[ARC 57] ARCHARD J.
Elastic deformation and the laws of friction. *Proceedings of the Royal Society of London*, vol. 243, 1957, p. 190-205.

[ASH 17] ASHTON P., HARTE A., LEEN S.
Statistical grain size effects in fretting crack initiation. *Tribology International*, vol. 108, 2017, p. 75-86.

[ATA 10] ATAG
A Beginner's Guide to Aviation Efficiency. ATAG, 2010.

[BAG 12] BAGAULT C., NELIAS D., BAIETTO M.-C.
Contact Analyses for Anisotropic Half Space : Effect of the Anisotropy on the Pressure Distribution and Contact Area. *Journal of tribology*, vol. 134, n° 3, 2012, Page 031401 (8 pages).

[BAG 13] BAGAULT C., NELIAS D., BAIETTO M.-C., OVAERT T.
Contact Analyses for Anisotropic half-space coated with an anisotropic layer : Effect of the anisotropy on the pressure distribution and contact area. *International Journal of Solids and Structures*, vol. 50, n° 5, 2013, p. 743-754.

[BAR 96] BARBER C., DOBKIN D. P., HUHDANPAA H. T.
The Quickhull Algorithm for Convex Hulls. *ACM Transactions on Mathematical Software*, vol. 22 (4), 1996, p. 469-483.

[BEA 87] BEARD J.
The Rational Selection of Palliatives for Avoidance of Fretting. *Proceedings of the Institution of Mechanical Engineers International Conference: Tribology - Friction, Lubrication and Wear Fifty Years On*, , 1987, p. 311-319.

[BEC 81] BECKER P. C.
Microstructural changes around non-metallic inclusions caused by rolling-contact fatigue of ball-bearing steels. *Metals Technology*, vol. 8, n° 1, 1981, p. 234-243, Taylor & Francis.

[BEN 67] BENTALL R. H., JOHNSON K. L.
Slip in the rolling contact fo two dissimilar elastic rollers. *International Journal of Mechanical Sciences*, vol. 9, 1967, p. 389-404.

[BEN 87] BENVENISTE Y.
A new approach to the application of Mori-Tanaka's theory in composite materials. *Mechanics of materials*, vol. 6, n° 2, 1987, p. 147–157, Elsevier.

[BER 90] BERTHIER Y.
Experimental Evidence For Friction and Wear Modelling. *Wear*, vol. 139, 1990, p. 77-92.

[BHA 12] BHADESHIA H.
Steels for bearings. *Progress in materials Science*, vol. 57, n° 2, 2012, p. 268–435, Elsevier.

[BHU 01] BHUSHAN B., Ed. *Modern Tribology Handbook*. CRC Press, 2001.

[BLA 91] BLANCHARD P., COLOMBIE C., PELLERIN V., FAYEULLE S., VINCENT L.
Material Effects in Fretting Wear : Application to Iron, Titanium and Aluminium Alloys. *Mettalurgical Transactions A*, vol. 22 (7), 1991, p. 1535-1544.

[BLA 16] BLASS T., DINKEL M., TROJAHN W.
Bearing Performance as a function of structure and heat treatment. *Materials Science and Technology*, vol. 32 (11), 2016, p. 1079-1085.

[BOF 12] BOFFY H.
Techniques multigrilles et raffinement pour un modèle 3D efficace de milieux hétérogènes sous sollicitations de contact. PhD Thesis, INSA Lyon, 2012.

[BOF 14] BOFFY H., VENNER H.
Multigrid solution of 3D stress field in strongly hetergeneous materials. *Tribology International*, vol. 74, 2014, p. 121-129.

[BOF 15] BOFFY H., VENNER H.
Multigrid numerical simulation of contact mechanics of elastic materials with 3D heterogeneous subsurface topology. *Tribology International*, vol. 92, 2015, p. 233-245.

[BOM 13a] BOMIDI J. A. R., WEINZAPFEL N., SADEGHI F., SLACK T., MOGHADDAM S. M., LIEBEL A., WEBER J., KREIS T.
Experimental and numerical investigation of torsion fatigue of bearing steel. *Journal of Tribology*, vol. 135(3), 2013, Page 031103.

[BOM 13b] BOMIDI J. A. R., WEINZAPFEL N., SADEGHI F., LIEBEL A., WEBER J.
An Improved Approach for 3D Rolling Contact Fatigue Simulations with Microstructure Topology. *Tribology Transactions*, vol. 56, n° 3, 2013, p. 385-399, Taylor & Francis.

[BOR 04] BORDREUIL C., HOCHARD C.
Rupture prediction of woven ply laminated plate with an open hole. *11th European Conference on Composites Materials (Greece Rhodes)*, 2004.

[BOU 85] BOUSSINESQ J.
Application des Potentiels à l'étude de l'équilibre et du mouvement des solides élastiques. Gauthiers-Villars, 1985.

[BOU 05] BOUCLY V., NELIAS D., LIU S., WANG Q., KEER L.
Contact analyses for bodies with frictional heating and plastic behavior. *Journal of tribology*, vol. 127, 2005, p. 355-364.

[BRA 90] BRANDT A., LUBRECHT A.
Multilevel matrix multiplication and fast solution of integral equations. *Journal of Computational Physics*, vol. 90, n° 2, 1990, p. 348–370, Elsevier.

[BRA 96] BRADGDON C., O'CONNOR D., LOWENSTEIN J., JASTY M., SYNIUTA W.
The importance of multidirectional motion on the wear of polyethylene. *Proceeding of the Institution of Mechanical Engineers, Part H: Journal of Engineering in Medicine*, vol. 210 (3), 1996, p. 157-165.

[BRY 88] BRYGGMAN U., SODERBERG S.
Contact conditions and surface degradation mechanisms in low amplitude fretting. *Wear*, vol. 125 (1-2), 1988, p. 39-52.

[CAR 12] CARRERE N., LAURIN F., MAIRE J.-F.
Micromechanical-based hybrid mesoscopic 3D approach for non-linear progressive failure analysis of composite structures. *Journal of Composite Materials*, vol. 46, 2012, p. 2389-2415.

[CAT 38] CATTANEO C.
Sul Contatto di Due Corpi Elasticiti : Distribuzion Locale Degli Sforzi. *Rendiconti dell'Academia Nazionalle dei Lincei*, vol. 27, 1938, p. 342-348,434-436,474-478.

[CER 82] CERRUTI V.
Ricerche intorno all'equilibrio de corpi elastici isotropi. *Rend. Accad. Naz. Lincei.*, vol. 3 (13), 1882, p. 81-122.

[CER 15] CERULLO M., TVEGAARD V.
Micromechanical study of the effect of inclusions on fatigue failure in a roller bearing. *International Journal of Sructural Integrity*, vol. 6(1), 2015, p. 124-141.

[CHA 74] CHABOCHE J. L.
Une loi différentielle d'endommagement de fatigue avec cumulation non linéaire. *Revue Française de Mécanique*, vol. 50-51, 1974, p. 71-82.

[CHA 88] CHABOCHE J.-L., LESNE P.
A Non-Linear Continuous Fatigue Damage Model. *Fatigue and Fracture of Engineering Materials and Structures*, vol. 11 (1), 1988, p. 1-17.

[CHA 95] CHABOCHE J. L., LESNE P. M., MAIRE J.-F.
Continuum Damage Mechanics, Anisotropy and Damage Deactivation for Brittle Materials like Concrete and Ceramic Composites. *International Journal of Damage Mechanic*, vol. 4, 1995, p. 5-22.

[CHA 11a] CHAISE T., NELIAS D.
Contact Pressure and Residual Strain in 3D Elasto-Plastic Rolling Contact for a Circular or Elliptical Point Contact. *Journal of Tribology*, vol. 133, n° 4, 2011, Page 041402.

[CHA 11b] CHAISE T., NELIAS D., SADEGHI F.
On the Effect of Isotropic Hardening on the Coeffcient of Restitution for Single or Repeated Impacts Using a Semi-Analytical Method. *Tribology Transactions*, vol. 54, n° 5, 2011, p. 714-722.

[CHA 11c] CHAISE T.
Mechanical simulation using a semi analytical method: from elasto-plastic rolling contact to multiple impacts. PhD Thesis, INSA Lyon, 2011.

[CHA 12] CHAISE T., LI J., NELIAS D., KUBLER R., TAHERI S., DOUCHET G., ROBIN V., GILLES P.
Modelling of multiple impacts for the prediction of distortions and residual stresses induced by ultrasonic shot peening (USP). *Journal of Materials Processing Technology*, vol. 212, 2012, p. 2080-2090.

[CHE 89] CHEN L., CHEN Q., SHAO E.
Study on initiation and propagation angles of sub-surface cracks in GCr15 bearing steel under rolling contact. *Wear*, vol. 133, 1989, p. 205-218.

[CHE 95] CHENG W., CHENG H.
Semi-analytical modeling of crack initiation dominant contact fatigue for roller bearings. *Proceedings of the 1995 Joint ASME/STLE Tribology Conference, Orlando, FL, Oct. 8-11.*, 1995.

[CHE 08a] CHEN W. W., WANG Q. J., WANG F., KEER L. M., CIAO J.
Three-Dimensional Repeated Elasto-Plastic Point Contacts, Rolling, and Sliding. *Journal od Applied Mechanics*, vol. 75, 2008, Page 021021.

[CHE 08b] CHEN W., LIU S., WANG Q.
FFT-based numerical methods for elasto-plastic contacts of nominally flat surfaces. *Journal of Applied Mechanics*, vol. 75, 2008, p. 011022-1-11.

[CHE 15] CHENG B., KORTSCHOT M.
Heterogeneous Surface Wear Models for the Prediction of the Specific Wear Rate of Woven Carbon Fibre Reinforced Epoxy Composites. *Polymers & Polymer Composites*, vol. 23 (6), 2015, p. 359-367.

[CHI 78] CHIU Y.
On the stress field and surface deformation in a half space with a cuboidal zone in which initial strains are uniform. *Journal of Applied Mechanics*, vol. 45, 1978, p. 302-306.

[CIA 98a] CIAVARELLA M.
The Generalized Cattaneo Partial Slip Plane Contact Problem I - Theory. *International Journal of Solids and Structures*, vol. 35 (18), 1998, p. 2349-2362.

[CIA 98b] CIAVARELLA M.
The Generalized Cattaneo Partial Slip Plane Contact Problem II - Examples. *International Journal of Solids and Structures*, vol. 35 (18), 1998, p. 2363-2378.

[COU 08] COUÉGNAT G.
Approche multiéchelle du comportement mécanique de matériaux composites à renfort tissé. PhD Thesis, Université Sciences et Technologies-Bordeaux I, 2008.

[COX 92] COX B. N., DADKHAH S., AL.
Mechanisms of compressive failure in 3D composite. *Acta metal mater*, vol. 40, 1992, p. 3285-3298.

[CRO 56] CROSSLAND B.
Effect of large hydrostatic pressures on the torsional fatigue strength of an alloy steel. *Proc. Int. Conf. on Fatigue of Metals*, vol. 138 Institution of Mechanical Engineers London, 1956.

[DAG 10] DAGGUMATI S., VAN PAEPEGEM W., AL.
Local damage in a 5-harness satin weave composite under static tension : Part II - Meso-FE modelling. *Composites Science and Technology*, vol. 70, 2010, p. 1934-1941.

[DAN 93] DANG VAN K.
Macro-micro approach in high-cycle multiaxial fatigue. *Advances in multiaxial fatigue (San Diego, 1991), ASTM, Philadelphia*, vol. 191, 1993, p. 120-130.

[DEC 11] DE CARVALHO N., PINHO S., ROBINSON P.
Reducing the domain in the mechanical analysis of periodic structures with application to woven composites. *Composites Science and Technology*, vol. 71, 2011, p. 969-979.

[DIC 06a] DICK T., CAILLETAUD G.
Fretting modelling with a crystal plasticity model of Ti6Al4V. *Computational Materials Science*, vol. 38, n° 1, 2006, p. 113–125.

[DIC 06b] DICK T., PAULIN C., CAILLETAUD G., FOUVRY S.
Experimental and numerical analysis of local and global plastic behaviour in fretting wear. *Tribology International*, vol. 39, n° 10, 2006, p. 1036–1044.

[DIN 03] DING Y., RIEGER N.
Spalling formation mechanism for gears. *Wear*, vol. 254 (12), 2003, p. 1307-1317.

[DOI 15a] DOITRAND A., FAGIANO C., CHIARUTTINI V., LEROY F., MAVEL A., HIRSEKORN M.
Experimental characterization and numerical modeling of damage at the mesoscopic scale of woven polymer matrix composites under quasi-static tensile loading. *Composites Science and Technology*, vol. 119, 2015, p. 1-11.

[DOI 15b] DOITRAND A., FAGIANO C., IRISARRI F.-X., HIRSEKORN M.
Comparison between voxel and consistent meso-scale models of woven composites. *Composites: Part A*, vol. 73, 2015, p. 143-154.

[DOI 17a] DOITRAND A., FAGIANO C., CARRERE N., CHIARUTTINI V., HIRSEKORN M.
Damage onset modeling in woven composites based on a coupled stress and energy criterion. *Engineering Fracture Mechanics*, vol. 169, 2017, p. 189-200.

[DOI 17b] DOITRAND A., FAGIANO C., HILD F., CHIARUTTINI V., MAVEL A., HIRSEKORN M.
Mesoscale analysis of damage growth in woven composites. *Composites Part A: Applied Science and Manufacturing*, vol. 96, 2017, p. 77-88.

[DON 16] DONG Q., ZHOU K., CHEN W. W., FAN Q.
Partial slip contact modeling of heterogeneous elasto-plastic materials. *International Journal of Mechanical Sciences*, vol. 114, 2016, p. 98 - 110.

[DON 17] DONE V., KESAVAN D., MURALI KRISHNA R., CHAISE T., NELIAS D.
Semi analytical fretting wear simulation including wear debris. *Tribology International*, vol. 109, 2017, p. 1-9.

[DUR 07] DURVILLE D.
Finite Element Simulation of Textile Materials at Mesoscopic Scale. *Finite element modelling of textiles and textile composites, St Petersburg, 26-28 September*, 2007.

[DUR 10] DURVILLE D.
Simulation of the mechanical behaviour of woven fabrics at the scale of the fibers. *International Journal of Material Forming*, vol. 3-S2, 2010, p. 1241-1251.

[ELI 15] ELIAS A.
Nocivité des défauts induits par impact pour les structures composites tissées 3D à matrice organique. PhD Thesis, Ecole Centrale de Nantes / Onera, 2015.

[ELI 17] ELIAS A., LAURIN F., KAMINSKI M., GORNET L.
Experimental and numerical investigations of low energy/velocity impact damage generated in 3D woven composite with polymer matrix. *Composites Structures*, vol. 159, 2017, p. 228-239.

[ESH 57] ESHELBY J.
The determination of the elastic field of an ellipsoidal inclusion and related problems. *Proceedings of the Royal Society of London*, vol. A241, 1957, p. 376-396.

[ESH 61] ESHELBY J.
Elastic inclusions and inhomogeneities. *Progress in Solid Mechanics*, vol. 2, 1961, p. 89-140.

[EVA 12] EVANS M.-H.
White structure flaking (WSF) in wind turbine gearbox bearings: effects of butterflies and white etching cracks (WECs). *Materials Science and Technology*, vol. 28, n° 1, 2012, p. 3-22, Taylor & Francis.

[EVA 13a] EVANS M.-H., RICHARDSON A. D., WANG L., WOOD R. J. K.
Effect of Hydrogen on Butterfly and White Etching Crack (WEC) Formation Under Rolling Contact Fatigue (RCF). *Wear*, vol. 306(1-2), 2013, p. 1-16.

[EVA 13b] EVANS M.-H., RICHARDSON A. D., WANG L., WOOD R. J. K.
Serial Sectioning Investigation of Butterfly and White Etching Crack (WEC) Formation in Wind Turbine Gearbox Bearings. *Wear*, vol. 302(1-2), 2013, p. 1573-1582.

[EVA 13c] EVANS M.-H., WALKER J., MA C., WANG L., WOOD R.
A FIB/TEM study of butterfly crack formation and white etching area (WEA) microstructural changes under rolling contact fatigue in 100Cr6 bearing steel. *Materials Science and Engineering: A*, vol. 570, 2013, p. 127 - 134.

[FIN 58] FINDLEY W. N.
A theory for the effect of mean stress on fatigue of metals under combined torsion and axial load or bending. N° 6 Engineering Materials Research Laboratory, Division of Engineering, Brown University, 1958.

[FOR 61] FORSYTH P.
A two stage fatigue fracture mechanism. *Proc. Cranfield Symposium on Fatigue*, 1961.

[FOU 96] FOUVRY S., KAPSA P., VINCENT L.
Quantification of fretting damage. *Wear*, vol. 200, 1996, p. 186-205.

[FOU 97] FOUVRY S., KAPSA P., ZAHOUANI H., VINCENT L.
Wear analysis in Fretting of Hard Coatings Through a Dissipated Energy Concept. *Wear*, vol. 203-204, 1997, p. 393-403.

[FOU 03] FOUVRY S., LISKIEWICZ T., KAPSA P., HANNEL S., SAUGER E.
An energy description of wear mechanisms and its applications to oscillating sliding contacts. *Wear*, vol. 255, n° 1-6, 2003, p. 287–298, Elsevier.

[FOU 04] FOUVRY S., DUÒ P., PERRUCHAUT P.
A quantitative approach of Ti-6Al-4V fretting damage : friction, wear and crack nucleation. *Wear*, vol. 257(9-10), 2004, p. 916-929.

[FUL 10] FULLERINGER B., NELIAS D.
On the tangential displacement of a surface point due to a cuboid of uniform plastic strain in a half-space. *Journal of Applied Mechanics*, vol. 77(2), 2010, p. 021014-1/7.

[FUL 11] FULLERINGER B.
Semi-analytical modeling of complex mechanical contacts: Application to inclusions and wear of coated surfaces. PhD Thesis, INSA Lyon, 2011.

[GAL 06] GALLEGO L., NELIAS D., JACQ C.
A comprehensive method to predict wear and to define the optimum geometry of fretting surfaces. *ASME Journal of Tribology*, vol. 128, 2006, p. 476-485.

[GAL 07a] GALLEGO L., NELIAS D.
Modeling of fretting wear under gross slip and partial slip conditions. *Journal of Tribology*, vol. 129, n° 3, 2007, p. 528-535.

[GAL 07b] GALLEGO L.
Fretting et Usure des Contacts Mécaniques : Modélisation Numérique. PhD Thesis, INSA Lyon, 2007.

[GAL 10] GALLEGO L., NELIAS D., DEYBER S.
A fast and efficient contact algorithm for fretting problems applied to fretting modes I, II and III. *Wear*, vol. 268, n° 1, 2010, p. 208-222.

[GAR 15] GARCIN S., FOUVRY S., HEREDIA S.
A FEM fretting map modeling : Effect of surface wear on crack nucleation. *Wear*, vol. 330-331, 2015, p. 145-159.

[GAR 17] GARCIA C., LAURIN F., HURMANE A., IRISARRI F.-X., LECLERCQ S., DESMORAT R.
Proposition of a methodology for the identification of composite material out-of-plane elastic parameters. *Comptes Rendus des JNC 20 - Ecole des Ponts ParisTech - 28-30 Juin*, 2017.

[GHO 13] GHOSH A., LEONARD B., SADEGHI F.
A stress based damage mechanics model to simulate fretting wear of Hertzian line contact in partial slip. *Wear*, vol. 307, 2013, p. 87-99.

[GOD 84] GODET M.
The third-body approach: a mechanical view of wear. *Wear*, vol. 100, n° 1-3, 1984, p. 437–452, Elsevier.

[GOL 18] GOLMOHAMMADI Z., WALVEKAR A., SADEGHI F.
A 3D efficient finite element model to simulate rolling contact fatigue under high loading conditions. *Tribology International*, vol. 126, 2018, p. 258-269.

[GOR 79] GORDELIER S., CHIVERS T.
A Literature Review of Palliatives for Fretting Fatigue. *Wear*, vol. 56, 1979, p. 177-190.

[GRA 07] GRABULOV A., ZIESE U., ZANDBERGEN H.
TEM/SEM investigation of microstructural changes within the white etching area under rolling contact fatigue and 3-D crack reconstruction by focused ion beam. *Scripta Materialia*, vol. 57, n° 7, 2007, p. 635 - 638.

[GRA 10] GRABULOV A., PETROV R., ZANDBERGEN H. W.
EBSD Investigation of the Crack Initiation and TEM/FIB Analyses of the Microstructural Changes Around the Cracks Formed Under Rolling Contact Fatigue (RCF). *International Journal of Fatigue*, vol. 32(3), 2010, p. 576-583.

[GRA 13a] GRAIL G.
Approche multimodèle pour la conception de structures composites à renfort tissé. PhD Thesis, Université d'Orléans, 2013.

[GRA 13b] GRAIL G., HIRSEKORN M., WENDLING A., HIVET G., HAMBLI R.
Consistent Finite Element mesh generation for meso-scale modeling of textile composites with preformed and compacted reinforcements. *Composites: Part A*, vol. 55, 2013, p. 143-151.

[GU 16] GU H., RÉTHORE J., BAIETTO M.-C., SAINSOT P., LECOMTE-GROSBRAS P., C. V. H., LUBRECHT A.
An efficient MultiGrid solver for the 3D simulation of composite materials. *Computational Materials Science*, vol. 112, 2016, p. 230-237.

[GUA 17] GUAN J., WANG L., ZHANG C., MA X.
Effects of non-metallic inclusions on the crack propagation in bearing steel. *Tribology International*, vol. 106, 2017, p. 123-131.

[GUY 97] GUY P., MEYNAUD P., VINCENT A., DUDRAGNE G., BAUDRY G.
Sub-surface damage investigation by high frequency ultrasonic echography on 100Cr6 bearing steel. *Tribology International*, vol. 30, n° 4, 1997, p. 247 - 259.

[HAR 99] HARRIS T. A., YU W.
Lundberg-Palmgren Fatigue Theory: Considerations of Failure Stress and Stressed Volume. *Journal of Tribology*, vol. 121 (1), 1999, p. 85-89.

[HAR 01] HARRIS T. A.
Rolling bearing analysis. John Wiley and sons, 2001.

[HEN 11] HENRY J., ABOURA Z., KHELLIL K., OTIN S.
Fatigue damaging analysis of a carbon / epoxy 3D layer interlock with acoustic emission. *Comptes Rendus JNC 17*, , 2011.

[HEN 13] HENRY J.
Mécanisme d'endommagement en fatigue dans les tissus multicouches interlocks. PhD Thesis, Université de Technologie de Compiegne, 2013.

[HER 82] HERTZ H.
On the contact of elastic solids. *Journal fur die reine und angewandte Mathematik*, vol. 92 (156-171), 1882, p. 22-37.

[HES 52] HESTENES M., STIEFEL E.
Methods of Conjugate Gradients for Solving Linear Systems. *Journal of Research of the National Bureau of Standards*, vol. 49 (6), 1952.

[HES 80] HESTENES M.
Conjugate direction methods in optimization, vol. 175. Springer-Verlag New York, 1980.

[HIL 88] HILLS D. A., NOWELL D. O. J. J.
On the mechanics of fretting fatigue. *Wear*, vol. 125, 1988, p. 129-146.

[HIL 93] HILLS D. A., NOWELL D., SACKFIELD A.
Mechanics of Elastic Contacts. Butterworth-Heinemann Ldt, 1993.

[HIL 96] HILD F., BURR A., LECKIE F. A.
Matrix cracking and debonding of ceramic-matrix composites. *International Journal of solid structures*, vol. 33, 1996, p. 1209-1220.

[HIR 06] HIRAOKA K., NAGAO M., ISOMOTO T.
Study on Flaking Process in Bearings by White Etching Area Generation. *Journal of ASTM International*, vol. 3(5), 2006, p. 1-7.

[HOL 17] HOLMBERG K., ERDEMIR A.
Influence of tribology on global energy consumption, costs and emissions. *Friction*, vol. 5(3), 2017, p. 263-284.

[HUR 14] HURMANE A., IRISARRI F.-X., LAURIN F., LECLERCQ S., BENZEGGAGH M.
Strength analysis of woven interlock composites subjected to compressive loading : experiments and simulation. *ECCM16 - 16th European Conference on Composite Materials*, 2014.

[HUR 15] HURMANE A.
Analyse par un dialogue essais / calculs de la tenue en compression de structures composites tissées interlocks. PhD Thesis, Université de Technologie de Compiegne / Onera, 2015.

[IAR 09] IARVE E. V., MOLLENHAUER D. H., ZHOU E. G., BREITZMAN T., WHITNEY T. J.
Independent mesh method-based prediction of local and volume average fields in textile composites. *Composite Part A: Applied Science and Manufacturing*, vol. 40, 2009, p. 1880-1890.

[IOA 85] IOANNIDES E., HARRIS T. A.
A New Fatigue Life Model for Rolling Bearings. *ASME Journal of Tribology*, vol. 107 (3), 1985, p. 367-378.

[ITO 93] ITO O., FULLER E.
Computer modelling of anisotropic grain microstructure in two dimensions. *Acta Metallurgica Materialia*, vol. 41, 1993, p. 191-198.

[JAC 02] JACQ C., NELIAS D., LORMAND G., GIRODIN D.
Development of a three-dimensional semi-analytical elastic-plastic contact code. *Journal of Tribology*, vol. 124(4), 2002, p. 653-667.

[JAE 04] JAEGER J.
New solutions in contact mechanics. , 2004.

[JAL 09] JALALAHMADI B., SADEGHI F.
A Voronoi Finite Element Study of Fatigue Life Scatter in Rolling Contacts. *Journal of Tribology*, vol. 131, n° 2, 2009, p. 022203-15, ASME.

[JAL 11] JALALAHMADI B., SADEGHI F., BAKOLAS V.
Material Inclusion Factors for Lundberg-Palmgren Based RCF Life Equations. *Tribology Transactions*, vol. 54, n° 3, 2011, p. 457-469, Taylor & Francis.

[JER 16] JERBI H.
Modélisation de l'usure et l'endommagement des contacts nus et revetus sous chargement de fretting par méthode semi-analytique. PhD Thesis, INSA Lyon, 2016.

[JIN 89] JIN X., KANG N.
A study on rolling bearing contact fatigue failure by macro-observation and micro-analysis. *Wear of Materials*, vol. 1, 1989, p. 205-213.

[JOH 85] JOHNSON K.
Contact Mechanics. Press syndicate of the university of Cambridge, 1985.

[JON 47] JONES A. B.
Metallographic Observations of Ball Bearing Fatigue Phenomena. *American Society for Testing and Materials*, vol. STP 70, 1947, p. 35-52.

[JU 96] JU Y., FARRIS T.
Spectral Analysis of Two-Dimensional Contact Problems. *ASME Journal of Tribology*, vol. 118, 1996, p. 320-328.

[KAC 58] KACHANOV L. M.
Time of the rupture process under creep conditions. *Izvestia Akademii Nauk SSSR, Otdelenie tekhnicheskich nauk*, vol. 8, 1958, p. 26-31.

[KAL 90] KALKER J.
Three-dimensional elastic bodies in rolling contact, vol. 2. Springer, 1990.

[KAM 15] KAMINSKI M., LAURIN F., MAIRE J.-F., RAKOTOARISOA C., HÉMON E.
Fatigue Damage Modeling of Composite Structures: the ONERA Viewpoint. *Life Prediction Methodologies for Materials and Structures*, vol. Issue 9, 2015.

[KAN 13] KANG J.-H., HOSSEINKHANI B., WILLIAMS C., MOODY M., BAGOT P., DEL CASTILLO P. R.-D.
Solute redistribution in the nanocrystalline structure formed in bearing steels. *Scripta Materialia*, vol. 69, nº 8, 2013, p. 630 - 633.

[KER 06] KERRIGAN A., KUIJPERS J., GABELLI A., IOANNIDES E.
Cleanliness of Bearing Steels and Fatigue Life of Rolling Contacts. *Journal of ASTM International*, vol. 3, 2006, p. 2-7.

[KER 14] KERSANI M., LOMOV S. V., VUURE A. W. V., BOUABDALLAH A., VERPOEST I.
Damage in flat/epoxy quasi-unidirectionnal woven laminates under quasi-static tension. *Journal of composite materials*, vol. 4, 2014, p. 1-11.

[KOU 14a] KOUMI K., NELIAS D., CHAISE T., DUVAL A.
Modeling of the contact between a rigid indenter and a heteregeneous viscoelastic material. *Mechanics of Materials*, vol. 77, 2014, p. 28-42.

[KOU 14b] KOUMI K., ZHAO L., LEROUX J., CHAISE T., NELIAS D.
Contact analysis in the presence of an ellipsoidal inhomogeneity within a half space. *International Journal of Solids and Structures*, vol. 51, 2014, p. 1390-1402.

[KOU 14c] KOUMPIAS A., TSERPES K., PANTELAKIS S.
Progressive damage modelling of 3D fully interlaced woven composite materials. *Fatigue and Fracture of Engineering Materials and Structures*, vol. 37 (7), 2014, p. 696-706.

[KOU 15a] KOUMI K., CHAISE T., NELIAS D.
Rolling contact of a rigid sphere/sliding of a spherical indenter upon a viscoelastic half-space containing an ellipsoidal inhomogeneity. *Journal of the Mechanics and Physics of Solids*, vol. 80, 2015, p. 1-25.

[KOU 15b] KOUMI K. E.
Modélisation du contact entre matériaux hétérogènes : Application au contact Aube/Disque. PhD Thesis, INSA Lyon, 2015.

[KRE 16] KREWERTH D., LIPPMAN T., WEIDNER A., BIERMANN H.
Influence of non-metallic inclusions on fatigue life in the very high cycle fatigue regime. *International Journal of Fatigue*, vol. 84, 2016, p. 40-52.

[KUM 94] KUMAR S., KURTZ S. K.
Simulation of Material Microstructure using a 3D Voronoi Tessellation: Calculation of Effective Thermal Expansion Coefficient of Polycrystalline Materials. *Acta Metallurgica Materialia*, vol. 42(12), 1994, p. 3917-3927.

[LAD 94] LADEVÈZE P., GASSER A., ALLIX O.
Damage Mechanics Modeling for Ceramic Composites. *Journal of Engineering Materials and Technology*, vol. 116, 1994.

[LAU 03] LAURSEN T.
Computational contact and impact mechanics: fundamentals of modeling interfacial phenomena in nonlinear finite element analysis. Springer, 2003.

[LAU 07] LAURIN F., CARRRERE N., MAIRE J.
A multiscale progressive failure approach for composite laminates based on thermodynamical viscoelastic and damage models. *Composite Part A: Applied Science and Manufacturing*, vol. 38 (1), 2007, p. 198-209.

[LEC 74] LECKIE F., HAYHURST D.
Creep rupture of structures. *Proc. Roy.Soc. London*, vol. A340, 1974, p. 323-347.

[LEM 72] LEMAITRE J.
Evaluation of dissipation and damage in metals submitted to dynamic loading. *Mechanical behavior of materials*, , 1972, p. 540-549.

[LEM 77] LEMAITRE J., DUFAILLY J.
Modélisation et identification de l'endommagement plastique des métaux. *3ème Congrès Français de Mécanique, Grenoble, France*, , 1977.

[LEM 84] LEMAITRE J.
How to use damage mechanics. *Nuclear Engineering and Design*, vol. 80, 1984, p. 233-245.

[LEM 85] LEMAITRE J.
A Continuous Damage Mechanics Model for Ductile Fracture. *Journal of Engineering Materials and Technology*, vol. 107, 1985, p. 83-89.

[LEM 90] LEMAITRE J., CHABOCHE J.-L.
Mechanics of solid materials. Cambridge University Press, 1990.

[LEM 92] LEMAITRE J.
A course on damage mechanics. Springer-Verlag, 1992.

[LEM 05] LEMAITRE J., DESMORAT R.
Engineering Damage Mechanics: Ductile, Creep, Fatigue and Brittle Failures.
Springer-Verlag Berlin Heidelberg, 2005.

[LEO 12a] LEONARD B., SADEGHI F., SHINDE S., MITTELBACH M.
A novel modular fretting wear test rigid. *Wear*, vol. 274-275, 2012, p. 313-325.

[LEO 12b] LEONARD B. D., SADEGHI F., SHINDE S., MITTELBACH M.
A numerical and experimental investigation of fretting wear and a new procedure for
fretting wear maps. *Tribology Transactions*, vol. 55(3), 2012, p. 313-324.

[LER 10] LEROUX J., FULLERINGER B., NELIAS D.
Contact analysis in presence of spherical inhomogeneities within a half-space. *International Journal of Solids and Structures*, vol. 47, 2010, p. 3034-3049.

[LER 11] LEROUX J., NELIAS D.
Stick-slip analysis of a circular point contact between a rigid sphere and a flat unidirectional composite with cylindrical fibers. *International Journal of Solids and Structures*,
vol. 48, 2011, p. 3510-3520.

[LER 13] LEROUX J.
Modélisation numérique du contact pour matériaux composites. PhD Thesis, INSA
Lyon, 2013.

[LET 06] LETOMBE S., CLUZEL C., LADEVÈZE P.
A CMC damage based on micro and macromechanics for high temperature and complex loading. *High Temperature Ceramic Matrix Composites*, , 2006, p. 578-583.

[LI 15] LI L., SWOLFS Y., CARVELLI V., LOMOV S. V.
Identification of the damage in woven composites based on acoustic emission cluseter
analysis. *7th International Conference on Composites Testing and Model Identification*, 2015.

[LI 18a] LI D., WANG Z., YU H., WANG Q.
Elastic fields caused by eigenstrains in two joined half-spaces with an interface of coupled imperfections: Dislocation-like and force-like conditions. *International Journal
of Engineering Science*, vol. 126, 2018, p. 22 - 52.

[LI 18b] LI J., ZHANG K., LIU P., LI Y.
Tribological Behavior and Microstructure of carbon Fiber-Reinforced Polymer against
Ti6Al4V Alloy in Fretting Contact. *Tribology Transactions*, vol. 61 (2), 2018, p. 256-268.

[LI 18c] LI J., ZHANG K., LIU P., LI Y.
Tribological behavior and microstructure of carbon fiber-reinforced polymer against
Ti6Al4V in Fretting Contact. *Tribology Transactions*, vol. 61-2, 2018, p. 256-268.

[LI 19] LI D., WANG Z., WANG Q.
Explicit analytical solutions for elastic fields in two imperfectly bonded half-spaces with a thermal inclusion. *International Journal of Engineering Science*, vol. 135, 2019, p. 1 - 16.

[LIS 03] LISKIEWICZ T., FOUVRY S. WENDLER B.
Impact of variable loading condtions on fretting wear. *Surface and Coatings Technology*, vol. 163, 2003, p. 465-471.

[LIT 66] LITTMANN W., WIDNER R.
Propagation of Contact Fatigue From Surface and Subsurface Origins. *Journal of Basic Engineering*, vol. 88, 1966, p. 624-636.

[LIU 00] LIU S., WANG Q., LIU G.
A versatile method of Discrete Convolution and FFT (DC-FFT) for Contact Analyses. *Wear*, vol. 243 (1-2), 2000, p. 101-111.

[LIU 01] LIU S. Q. W., LIU G.
A Three-Dimensional Thermal-Mechanical Asperity Contact Model for Two Nominally Flat Surfaces in contact. *Journal of Tribology*, vol. 123, 2001, p. 595-602.

[LOM 00] LOMOV S. V., GUSAKOV A. V., HUYSMANS G., PRODROMOU A., VERPOEST I.
Textile geometry preprocessor for meso-mechanical models of woven composites. *Composite Science and Technology*, vol. 60-11, 2000, p. 2083-2095.

[LOM 07a] LOMOV S. V., IVANOV D. S., VERPOEST I., ZAKO M., KURASHIKI T., NAKAI H., HIROSAWA S.
Meso-FE modelling of textile composites: Road map, data flow and algorithms. *Composites Science and Technology*, vol. 67-9, 2007, p. 1870-1891.

[LOM 07b] LOMOV S., VERPOEST I.
Model of shear of woven fabric and parametric description of shear resistance of glass woven reinforcements. *Composite Science and Technology*, vol. 67-9, 2007, p. 1870-1891.

[LOM 08] LOMOV S., ISANOV D., TRUONG T., VERPOEST I., BAUDRY F., VANDEN BOSCHE K., XIE H.
Experimental methodology of study of damage initation and development in textile composites in uniaxial tensile test. *Composite Science and Technology*, vol. 68-12, 2008, p. 2340-2349.

[LOV 52] LOVE A.
A Treatise on the Mathematical Theory of Elasticity. Cambridge University Press, 4th edition édition, 1952.

[LUB 91] LUBRECHT A., IOANNIDES E.
A fast solution of the dry contact problem and the associated sub-surface stress field, using multilevel techniques. *Journal of tribology*, vol. 113, n° 1, 1991, p. 128–133, American Society of Mechanical Engineers.

[LUN 47] LUNDBERG G., PALMGREN A.
Dynamic capacity of rolling bearings. *Acta Polytechnica, Mechanical Engineering series 2*, vol. 1 (3), 1947, p. 7-53.

[LUN 10] LUND T.
Sub-Surface Initiated Rolling Contact Fatigue - Influence of Non-Metallic Inclusions, Processing History, and Operating Conditions. *Journal of ASTM International*, vol. 7(5), 2010, p. 1-12.

[MAC 58] MacMILLAN W.
The Theory of the Potential: Theoretical Mechanics. Dover publications, 1958.

[MAI 97a] MAIRE J.-F., CHABOCHE J. L.
A new formulation of continuum damage mechanics (CDM) for composite materials. *Aerospace Science and Technology*, vol. 4, 1997, p. 247-257.

[MAI 97b] MAIRE J.-F., LESNE P. M.
A Damage Model for Ceramic Matrix Composites. *Aerospace Science and Technology*, vol. 5, 1997, p. 259-266.

[MAN 19] MANIERI F., STADLER K., MORALES-ESPEJEL G., KADIRIC A.
The origin of white etching cracks and their significance to rolling bearing failures. *International Journal of Fatigue*, vol. 120, 2019, p. 107-133.

[MAR 66] MARTIN J., BORGESE S., EBERHARDT A.
Microstructural alterations of rolling-bearing steel undergoing cyclic stressing. *Journal of Fluids Engineering*, vol. 88 (3), 1966, p. 555-565.

[MAR 85] MARIGO J.
Modelling of brittle and fatigue damage for elastic material by growth of microvoids. *Engineering Fracture Mechanics*, vol. 21(4), 1985, p. 861-874.

[MAR 10] MARCIN L.
Modelisation du comportement, de l'endommagement et de la rupture de materiaux composites à renforts tisses pour le dimensionnement robuste de structures. PhD Thesis, Universite Bordeaux 1, 2010.

[MAT 77] MATAKE T.
An explanation on fatigue limit under combined stress. *Bulletin of JSME*, vol. 20, n° 141, 1977, p. 257–263.

[MAT 09] Mathew M., Padaki N., Alagirusamy R., Deopura B., Fangueiro R., Rocha L., Gomes J.
Tribological behaviour of multilayered textile composites: The effect of reciprocating sliding frequency. *Wear*, vol. 267, 2009, p. 26-33.

[MAZ 89] Mazars J., Pijaudier-Cabot G.
Continuum Damage Theroy - Application to Concrete. *Journal of Engineering Mechanics*, vol. 115 (2), 1989, p. 345-365.

[MBA 13] Mbacke M. A.
Caractérisation et modélisation du comportement mécanique des composites tressés 3D : Application à la conception de réservoirs GNV. PhD Thesis, Ecole nationale des Mines de Paris, 2013.

[MEN 19] Mendoza A., Schneider J., Parra E., Obert E., Roux S.
Differentiating 3D textile composites: A novel field of application for Digital Volume Correlation. *Composite Structures*, vol. 208, 2019, p. 735-743.

[MER 11] Meriaux J.
Etude expérimentale et modélisation de l'endommagement dún contact aube/disque de soufflante soumis à des chargement de fretting fatigue. PhD Thesis, Ecole Centrale de Lyon, 2011.

[MIN 49] Mindlin R. D.
Compliance of elastic bodies. *Journal of Applied Mechanics*, vol. 71, 1949, p. 259-268.

[MOG 15a] Moghaddam S. M., Sadeghi F., Paulson K., Weinzapfel N., Correns M., Bakolas V., Dinkel M.
Effect of non-metallic inclusions on butterfly wing initiation, crack formation, and spall geometry in bearing steels. *International Journal of Fatigue*, vol. 80, 2015, p. 203 - 215.

[MOG 15b] Moghaddam S. M., Sadeghi F., Weinzapfel N., Liebel A.
A Damage Mechanics Approach to Simulate Butterfly Wing Formation Around Non-metallic Inclusions. *Journal of Tribology*, vol. 137, n⁰ 1, 2015, p. 011404–011404-13, ASME.

[MOG 16a] Moghaddam S. M., Sadeghi F.
A Review of Microstructural Alterations around Nonmetallic Inclusions in Bearing Steel during Rolling Contact Fatigue. *Tribology Transactions*, vol. 59, n⁰ 6, 2016, p. 1142-1156, Taylor & Francis.

[MOG 16b] Moghaddam S. M., Sadeghi F., Paulson K., Weinzapfel N., Correns M., Dinkel M.
A 3D numerical and experimental investigation of microstructural alterations around

non-metallic inclusions in bearing steel. *International Journal of Fatigue*, vol. 88, 2016, p. 29 - 41.

[MOH 95] MOHRBACHER H., CELIS J., ROOS J.
Laboratory testing of displacement and load induced fretting. *Tribology International*, vol. 28, 1995, p. 269-278.

[MON 15] MONTEBELLO C.
Analysis of the stress gradient effect in Fretting-Fatigue through a description based on nonlocal intensity factors. PhD Thesis, ENS Paris Saclay, 2015.

[MOR 73] MORI T., TANAKA K.
Average stress in matrix and average elastic energy of materials with misfitting inclusions. *Acta metallurgica*, vol. 21, nᵒ 5, 1973, p. 571–574, Elsevier.

[MOR 15] MORALES-ESPEJEL G., GABELLI A.
The Progression of Surface Rolling Contact Fatigue Damage of Rolling Bearings with Artificial Dents. *Tribology Transactions*, vol. 58, 2015, p. 418-431.

[MOR 17] MORALES-ESPEJEL G., BOFFY H., C. V. H.
Effect of material heterogeneity on surface fatigue for rough lubricated rolling sliding contacts. *Journal of Engineering Tribology*, vol. 231 (2), 2017, p. 274-290.

[MOR 18a] MORALES-ESPEJEL G., GABELLI A.
A model for gear life with surface and subsurface survival: Tribological effects. *Wear*, vol. 404-405, 2018, p. 133-142.

[MOR 18b] MORRIS D., SADEGHI F., CHEN Y.-C., WANG C., WANG B.
Effect of Residual Stresses on Microstructural Evolution Due to Rolling Contact Fatigue. *Journal of Tribology*, vol. 140, nᵒ 6, 2018, p. 061402–061402-9, ASME.

[MOS 75] MOSCHOVIDIS Z., MURA T.
Two-ellipsoidal inhomogeneities by the equivalent inclusion method. *Journal of Applied Mechanics*, vol. 42, 1975, p. 847-852.

[MUR 87] MURA T.
Micromechanics of Defects in Solids. Kluwer Academic Publishers, 2nd édition, 1987.

[NAK 78] NAKAZAWA K., KRAUSS G.
Microstructure and Fracture of 52100 Steel. *Metallurgical Transactions A*, vol. 9 (5), 1978, p. 681-689.

[NAO 14] NAOUAR N., VIDAL SALLE E., SCHNEIDER J., MAIRE E., BOISSE P.
Meso-scale FE analyses of textile composite reinforcement deformation based on X-ray computed tomography. *Composite Structures*, vol. 116, 2014, p. 165-176.

[NAO 15a] NAOUAR N.
Analyse mésoscopique par éléments finis de la déformation de renforts fibreux 2D et 3D à partir de microtomographies X. PhD Thesis, INSA de Lyon, 2015.

[NAO 15b] NAOUAR N., VIDAL SALLE E., SCHNEIDER J., MAIRE E., BOISSE P.
3D composite reinforcement meso F.E. analyses based on X-ray computed tomography. *Composite Structures*, vol. 132, 2015, p. 1094-1104.

[NEL 99] NELIAS D., DUMONT M. L., CHAMPIOT F., VINCENT A., GIRODIN D., FOUGÉRES R., FLAMAND L.
Role of Inclusions, Surface Roughness and Operating Conditions on Rolling Contact Fatigue. *Journal of Tribology*, vol. 121, n° 2, 1999, p. 240–251, ASME.

[NEL 00] NELIAS D., VILLE F.
Detrimental effects of debris dents on rolling contact fatigue. *Journal of Tribology*, vol. 122(1), 2000, p. 55-64.

[NEL 07] NELIAS D., ANTALUCA D., BOUCLY V.
Rolling of an elastic ellipsoid upon an elastic-plastic flat. *ASME Journal of Tribology*, vol. 129, n° 4, 2007, p. 791-800.

[NIX 88] NIX K. J., LINDLEY T. C.
The influence of relative slip range and contact material on the fretting properties of 3.5NiCrMoV rotor steel. *Wear*, vol. 125, 1988, p. 147-162.

[NOW 98] NOWELL D., DAI D. N.
Analysis of surface traction in complex fretting fatigue cycles using quadratic programming. *Journal of Tribology - Transaction of ASME*, vol. 120, 1998, p. 744-749.

[NYG 02] NYGÅRDS M., GUDMUNDSON P.
Three-Dimensional Periodic Voronoi Grain Models and Micromechanical FE-Simulations of a Two-Phase Steel. *Computer Materials Science*, vol. 24(4), 2002, p. 513-519.

[OKA 00] OKABE A., BOOTS B., SUGIHARA K., CHIU S. N.
Spatial Tessellations: Concepts and Applications of Voronoi Diagrams. Wiley, West Sussex, UK., 2000.

[ORT 85] ORTIZ M.
A constitutive theory for the inelastic behavior of concrete. *Mechanics of Materials*, vol. 4, 1985, p. 67-93.

[PAN 85] PANAGIOTOPOULOS P.
Inequality Problems in Mechanics and Applications: Convex and Nonconvex Energy Functions. Birkhauser, 1985.

[PAN 18] DE PANNEMAECKER A., FOUVRY S., BUFFIERE J.-Y., BROCHU M.
Modelling the fretting crack growth: from short crack correction strategies to microstructural approaches. *International Journal of Fatigue*, vol. 117, 2018, p. 75-89.

[PAU 81] PAUL B., HASHEMI J.
Contact pressure on closely conforming elastic bodies. *ASME Journal of Applied Mechanics*, , 1981, p. 543-5548.

[PAU 14] PAULSON N., BOMIDI J. A. R., SADEGHI F., EVANS R.
Effects of crystal elasticity on rolling contact fatigue. *International Journal of Fatigue*, vol. 61, 2014, p. 67-75.

[PAU 17a] PAULSON N. R., SADEGHI F.
EHL modeling of nonhomogeneous materials : The effects of polycristalline anisotropy on RCF. *Tribology International*, vol. 112, 2017, p. 137-146.

[PAU 17b] PAULSON N. R., SADEGHI F., HABCHI W.
A coupled finite element EHL continuum damage mechanics model for rolling contact fatigue. *Tribology International*, vol. 107, 2017, p. 173-183.

[PEA 07] PEARSON J., ZIKRY M., PRABHUGOUD M., PETERS K.
Global-local assessment of low-velocity impact damage in woven composites. *Journal of Composite Materials*, vol. 41, 2007, p. 2759-2783.

[PER 93] PERALTA P., SCHOBER A., LAIRD C.
Elastic stresses in anisotropic bicrystals. *Materials Science & Engineering, A: Structural Materials: Properties, Microstructure and Processing*, vol. 169, 1993, p. 43-51.

[POL 95] POLONSKY I., KEER L.
On white etching band formation in rolling bearings. *Journal of the Mechanics and Physics of Solids*, vol. 43, n° 4, 1995, p. 637 - 669.

[POL 99] POLONSKY I., KEER L.
A numerical method for solving rough contact problems based on the multi-level multi-summation and conjugate gradient techniques. *Wear*, vol. 231, n° 2, 1999, p. 206-219, Elsevier.

[POL 00] POLONSKY I.
Fast methods for solving rough contact problems: a comparative study. *Journal of tribology*, vol. 122, 2000, Page 36.

[POT 12] POTTER E., PINHO S., ROBINSON P., IANNUCI L., MCMILLAN A.
Mesh generation and geometrical modelling of 3D woven composites with variable tow cross-sections. *Computational Materials Science*, vol. 51-1, 2012, p. 103-111.

[QUI 19] QUIÑONEZ A., MORALES-ESPEJEL G.
Theoretical analysis of a rolling-sliding elastohydrodynamic lubrication line contact with a subsurface inclusion. *Journal of Engineering Tribology*, , 2019.

[RAB 69] RABOTNOV Y.
Creep problemes in structural members. Amsterdam: North Holland, 1969.

[RAH 09] RAHMAN Z., OHBA H., YOSHIOKA T., YAMAMOTO T.
Incipient damage detection and its propagation monitoring of rolling contact fatigue by acoustic emission. *Tribology International*, vol. 42, nº 6, 2009, p. 807 - 815.

[RAJ 06] RAJASEKARAN R., NOWELL D.
Fretting fatigue in dovetail blade roots: Experiment and analysis. *Tribology International*, vol. 39, nº 10, 2006, p. 1277–1285.

[RAJ 08a] RAJE N., SADEGHI F., RATEICK R. G.
A statistical damage mechanics model for subsurface initiatied spalling in rolling contacts. *Journal of Tribology*, vol. 130(4), 2008, Page 042201.

[RAJ 08b] RAJE N., SADEGHI F., RATEICK R. G., G. R., HOEPRICH M. R.
A numerical model for life scatter in rolling element bearings. *Journal of Tribology*, vol. 130, 2008, p. 011011-011011.

[RAK 13] RAKOTOARISOA C.
Prévision de la durée de vie en fatigue des composites à matrice organique tissés interlock. PhD Thesis, Université de Technologie de Compiegne, 2013.

[REN 09] REN N., ZHU D., CHEN W., LIU Y., WANG Q.
A Three-Dimensional Deterministic Model for Rough Surface Line-Contact EHL Problems. *Journal of Tribology*, vol. 131, 2009, p. 011501-1.

[REU 29] REUSS A.
Berechnung der Fließgrenze von Mischkristallen auf Grund der Plastizitätsbedingung für Einkristalle. *ZAMM-Journal of Applied Mathematics and Mechanics/Zeitschrift für Angewandte Mathematik und Mechanik*, vol. 9, nº 1, 1929, p. 49–58, Wiley Online Library.

[ROM 15] ROMANOV V. S., LOMOV S. V., VERPOEST I., GORBATIKH L.
Modelling evidence of stress concentration mitigation at the micro-scale in polymer composites by the addition of carbon nanotubes. *Carbon*, vol. 82, 2015, p. 184-194.

[RUE 14] RUELLAN A., VILLE F., KLEBER X., AMAUDON A., GIRODIN D.
Understanding White etching cracks in rolling element bearings: the effect of hydrogen chargin on the formation mechanisms. *Proc. Inst. Mech. Eng. Part J J; Eng. Tribol.*, 2014.

[RYC 12] RYCERZ P., KADIRIC A., PASARIBU R., MORALES-ESPEJEL G., OLVER A.
Effect of Additives on surface performance. *15th International Conference on Experimental Mechanics (ICEM)*, 2012.

[RYC 17] RYCERZ P., OLVER A., KADIRIC A.
Propagation of surface initiated rolling contact fatigue cracks in bearing steel. *International Journal of Fatigue*, vol. 97, 2017, p. 29-38.

[SAD 09] SADEGHI F., JALALAHMADI B., SLACK T., RAJE N., ARAKERE N.
A Review of Rolling Contact Fatigue. *Journal of Tribology*, vol. 131, 2009, p. 041403-1.

[SAL 92] SALEHIZADEH H., SAKA N.
The Mechanics of Crack Initiation at Hard Particles in Rolling Line Contacts. *Journal of Tribology*, vol. 114, n° 2, 1992, p. 341–347, ASME.

[SAL 03] SALVO L., CLOETENS P., MAIRE E., ZABLER S., BLANDIN J., BUFFIERE J.-Y., LUDWIG Y., BOLLER E., BELLET D., JOSSEROND C.
X-ray micro-tomography an attractive characterisation technique in materials science. *Nuclear Instruments & Methods in Physics Research, Section B: Beam Interactions with Materials and Atoms*, vol. 200, 2003, p. 273-286.

[SAL 18] SALLY O., JULIEN C., LAURIN F., DESMORAT R., BOUILLON F.
Fatigue lifetime modeling of oxide/oxide composites. *Procedia Engineering*, vol. 213, 2018, p. 797-803.

[SCH 88] SCHLICHT H., SCHREIBER E., ZWIRLEIN O.
Effects of Material Properties on Bearing Steel Fatigue Strength. J.J.C. H., Ed., *Effects of Steel Manufacturing Processes on the Quality of Bearing Steels*, p. 81-101 ASTM International, West Conshohocken, PA, 1988.

[SCH 06] SCHELL J., RENGGLI M., VAN LENTHE G., M'ULLER R., ERMANI P.
Micro-computed tomography determination of glass fiber reinforced polymer mesostructure. *Composite Science and Technology*, vol. 66, 2006, p. 2016-22.

[SCH 08] SCHNEIDER J., MARCIN L., ABOURA Z., MARSAL D.
Experimental investigation and behavior modeling of a 3D interlock woven fabric composite: Part 1. 2008, p. 380–388.

[SCH 09a] SCHNEIDER J.
A Meso-Voxel model of an interlock woven composite. *ICCM-17 Conference, Edinbourgh*, 2009.

[SCH 09b] SCHNEIDER J., ABOURA Z., KHELLIL K., BENZEGGAGH M., MARSAL D.
Off-plan behaviour investigation of an interlock fabric. *Comptes Rendus des JNC 16*, , 2009.

[SCI 99] SCIDA D., ABOURA Z., AL.
A micromechanics model for 3D elasticity and failure of woven-fibre composite materials. *Composite Science and Technology*, vol. 59, 1999, p. 505-517.

[SCO 67] SCOTT D.
Surface Studies in the Investigation of Failure Mechanisms. *Proceedings of the Institution of Mechanical Engineers, Conference Proceedings*, vol. 182(11), 1967, p. 56-64.

[SHE 07] SHERBURN M.
Geometric and mechanical modelling of textiles. PhD Thesis, The University of Nottingham, 2007.

[SHE 14] SHENGGUANG Z., WENZHONG W., ZIQIANG Z.
Elastohydrodynamic lubrication analysis of point contact with consideration of material inhomogeneity. *Journal of Tribology*, vol. 136 (4), 2014, Page 041501.

[SHE 15] SHEN F., HU W., MENG Q.
A damage mechanics approach to fretting fatigue life prediction with consideration of elastic-plastic damage model and wear. *Tribology International*, vol. 82, 2015, p. 176-190.

[SHI 09] SHIMIZU S., TSUCHIYA K., TOSHA K.
Probabilistic Stress-Life (P-S-N) Study on Bearing Steel Using Alternating Torsion Life Test. *Tribology Transactions*, vol. 52, n° 6, 2009, p. 807-816, Taylor & Francis.

[SIN 59] SINES G.
Behavior of metals under complex static and alternating stresses. *Metal fatigue*, vol. 1, 1959, p. 145–169, McGraw Hill, New York.

[SLA 10] SLACK T., SADEGHI F.
Explicit finite element modeling of subsurface initated spalling in rolling contacts. *Tribology International*, vol. 43 (9), 2010, p. 1693-1702.

[SOL 14] SOLANO-ALVAREZ W., BHADESHIA H.
White-etching matter in bearing steel. Part II: distinguishing cause and effect in bearing steel failure. *Metallurgical and Materials Transactions A*, vol. 45 (11), 2014, p. 4916-4931.

[STI 09] STIENON A., FAZEKAS A., BUFFIERE J.-Y., VINCENT A., DAGUIER P., MERCHI F.
A new methodology based on X-ray micro-tomography to estimate stress concentrations around inclusions in high strength steels. *Materials Science and Engineering: A*, vol. 513-514, 2009, p. 376 - 383.

[STY 51] STYRI H.
Fatigue Strength of ball bearings races and heat-treated 52100 steel specimens. *Proceedings of the American Society for Testing and Materials*, vol. 51, 1951, p. 682-700.

[SUH 73] Suh N.
The delamination theory of wear. *Wear*, vol. 25 (1), 1973, p. 111-124.

[TAK 01] Takemura H.
Development of New Life Equation for Ball and Roller Bearings. *SAE Paper*, vol. 2000-11-2601, 2001, p. 2117-2118.

[TAL 92] Tallian T.
Simplified contact fatigue life prediction model - Part III: New Model. *Journal of Tribology*, vol. 201 (1), 1992, p. 106-116.

[TAL 99] Tallian T.
Failure Atlas for Hertz Contact Machine Elements. 1999.

[TAN 00] Tan P., Tong L., Steven G., Ishikawa T.
Behavior of 3D orthogonal woven CFRP composites. Part I. Experimental investigation. *Composites Part A: Applied Science and Manufacturing*, vol. 31, n° 3, 2000, p. 259–271, Elsevier.

[TAR 14] Taro M., Chaise T., Nelias D.
A Methodology to Predict the Roughness of Shot Peened Surfaces. *Journal of Materials Processing Technology*, vol. 217, 2014, p. 65-76.

[THO 70] Thoman D., Bain L., Antler C.
Maximum likelihood estimation, exact confidence intervals for reliability and tolerance limits in the Weibull distribution. *Technometrics*, vol. 12, 1970, p. 363-371.

[TRI 72] Tricot R., Monnot J., Lluansi M.
How Microstructural Alterations Affect Fatigue Properties of 52100 Steel. *Metals Engineering Quarterly*, vol. 12.2, 1972, p. 39-47.

[TRI 10] Trinh P. V., Trung T. B., Thang N. B., Thang B. H., Tinh T. X., Quang L. D., Phuong D. D., Minh P. N.
Calculation of the friction coefficient of Cu matrix composite reinforced by carbon nanotubes. *Computational Materials Science*, vol. 49, 2010, p. S239 - S241.

[UME 09] Umezawa O., Nishikawa T., Tsuchida T., Hirakoa K.
Modelling of crack generation and growth under rolling contact fatigue in martensite steels. *Processing and Fabrication of Advanced Materials*, vol. XVIII, 2009, p. 555-564.

[UNA 04] Unal H., Sen U., Mimaroglu A.
Dry Sliding wear characteristics of some industrial polymers against steel counterface. *Tribology International*, vol. 37 (9), 2004, p. 727-732.

[VEN 00] Venner H. C., Lubrecht A.
Mulit-level Methods in Lubrication. Elsevier, 2000.

[VER 85] VERGNE F.
Calcul des déplacements et des contraintes dans un demi-espace élastique chargé en surface par des actions distribuées normales ou tangentielles quelconques. Master's thesis, INSA de Lyon, 1985.

[VIJ 18] VIJAY A., PAULSON K., SADEGHI F.
A 3D finite element modelling of crystalline anisotropy in rolling contact fatigue. *International Journal of Fatigue*, vol. 106, 2018, p. 92-102.

[VIN 88] VINGSBO O., SODERBERG S.
On fretting maps. *Wear*, vol. 126 (2), 1988, p. 131-147.

[VIN 92] VINCENT L., BERTHIER Y., GODET M.
Testing methods in fretting fatigue : a critical appraisal. *ASTM STP*, vol. 1159, 1992, p. 33-48.

[VIT 03] VITOS L., KORZHAVYI P., JOHANSSON B.
Stainless steel optimization from quantum mechanical calculations. *Nature Materials*, vol. 2, 2003, p. 25-28.

[VOI 89] VOIGT W.
Uber die Beziehung Zwischen den Beiden Elastizitats konstant en Isotroper Korper. *Wied. Ann*, vol. 38, nº 2, 1889, Page 573.

[VOR 92] VAN DER VORST H.
Bi-CGSTAB: A fast and smoothly converging variant of Bi-CG for the solution of nonsymmetric linear systems. *SIAM Journal on Scientific and Statistical Computing*, vol. 13 (2), 1992, p. 631-644.

[WAL 14] WALVEKAR A., LEONARD B., SADEGHI F., JALALAHMADI B., BOLANDER N.
An experimental study and fatigue damage model for fretting fatigue. *Tribology International*, vol. 79, 2014, p. 183-196.

[WAN 05] WANG F., KEER L.
Numerical simulation for three-dimensional elastic-plastic conact with hardening behavior. *ASME Journal of Tribology*, vol. 127(3), 2005, p. 494-502.

[WAN 13] WANG Z., ZHU D., WANG Q.
Elastohydrodynamic Lubrication of Inhomogeneous Materials using the equivalent inclusion method. *Journal of Tribo*, vol. 136 (2), 2013, Page 021501.

[WAR 13] WARHADPANDE A., SADEGHI F., EVANS R.
Microstructural alterations in bearing steels under rolling contact fatigue Part 1 - Historical Overview. *Tribology Transactions*, vol. 56(3), 2013, p. 349-358.

[WAR 14] WARHADPANDE A., SADEGHI F., KOTZALAS M., DOLL G.
Effects of plasticity on subsurface initiated spalling in rolling contact fatigue. *International Journal of Fatigue*, vol. 61, 2014, p. 67-75.

[WAR 16] WARREN K., LOPEZ-ANIDO R., VEL S., BAYRAKTAR H.
Progressive failure analysis of three-dimensional woven carbon composites in single-bolt double-shear bearing. *Composites Part B: Engineering*, vol. 84, 2016, p. 266-276.

[WEI 39] WEIBULL W.
A statistical theory of the strength of materials. *Royal Swedish Academy of Engineering Sciences Proc.*, vol. 151, 1939, p. 4-45.

[WEI 10] WEINZAPFEL N., SADEGHI F., BAKOLAS V.
An approach for modeling material grain structure in investigations of hertzian subsurface stresses and rolling contact fatigue. *Journal of Tribology*, vol. 132, 2010, p. 041404-1.

[WEI 11] WEINZAPFEL N., SADEGHI F., BAKOLAS V., LIEBEL A.
A 3D Finite Element Study of Fatigue Life Dispersion in Rolling Line Contacts. *Journal of Tribology*, vol. 133, n° 4, 2011, p. 042202–042202-10, ASME.

[WES 39] WESTERGAARD H. M.
Bearing pressures and cracks. *ASME Journal of Applied Mechanics*, vol. 6, 1939, Page 49.

[WIL 99] WILLIAMS J.
Wear modelling: analytical, computational and mapping: a continuum mechanics approach. *Wear*, vol. 225-229, 1999, p. 1-17.

[WRI 06] WRIGGERS P.
Computational contact mechanics. Springer, 2006.

[XIA 98] XIAO Y.-C., LI S., GAO Z.
A continuum damage mechanics model for high cycle fatigue. *International Journal of Fatigue*, vol. 20, n° 7, 1998, p. 503 - 508.

[XIN 17] XIN L., YANG B., LI J., LU Y., SHOJI T.
Wear damage of alloy 690TT in partial and gross slip fretting regimes at high temperature. *Wear*, vol. 390-391, 2017, p. 71-79.

[YAS 11] YASTREBOV V. A.
Computational contact mechanics: geometry, detection and numerical techniques. PhD Thesis, Ecole nationale supérieure des Mines de Paris, 2011.

[YOS 93] YOSHIOKA T.
Detection of Rolling contact sub-surface fatigue cracks using acoustic emission technique. *Lubrication Engineering*, vol. 49 (4), 1993, p. 303-308.

[ZAR 69] ZARETSKY E., PARKER R. J., ANDERSON W. J.
A study of residual stress induced during rolling. *ASME Journal of Lubrication Technology*, vol. 91, 1969, p. 314-319.

[ZAR 94] ZARETSKY E.
Design for Life, Plan for Death. *Machine Design*, vol. 66 (15), 1994, p. 55-59.

[ZAR 12] ZARETSKY E.
How to Determine Bearing System Life. rapport, 2012, Machinery Lubrication.

[ZHA 09] ZHANG M., NEU R. W., MCDOWELL D.
Microstructure-sensitive modeling: Application to fretting contacts. *International Journal of Fatigue*, vol. 31 (8-9), 2009, p. 1397-1406.

[ZHA 16] ZHAO L., NELIAS D., BARDEL D., MAYNADIER A., CHAUDET P., MARIE B.
On the fracture of multi-crystalline silicon wafer. *Journal of Physics D: Applied Physics*, vol. 49 (47), 2016, p. 475-601.

[ZHA 18] ZHANG X., WANG Q. J., WANG Y., WANG Z., SHEN H., LIU J.
Contact involving a functionally graded elastic thin film and considering surface effects. *International Journal of Solids and Structures*, vol. 150, 2018, p. 184 - 196.

[ZHO 93a] ZHOU R. S.
Surface Topography and Fatigue Life of Rolling Contact Bearings. *Tribology Transactions*, vol. 36, 1993, p. 329-340.

[ZHO 93b] ZHOU Z. R., VINCENT M.
Effect of external loading on wear maps of aluminium alloys. *Wear*, vol. 162-164, 1993, p. 619-623.

[ZHO 09] ZHOU K., CHEN W., KEER L., WANG Q.
A fast method for solving three-dimensional arbitrarily shaped inclusions in a half space. *Computer Methods in Applied Mechanics and Engineering*, vol. 198, n° 9-12, 2009, p. 885-892.

[ZHO 11a] ZHOU K., CHEN W., KEER L., AI X., SAWAMIPHAKDI K., GLAWS P., Q.WANG
Multiple 3D inhomogeneous inclusions in a half space under contact loading. *Mechanics of Materials*, vol. 43, 2011, p. 444-457.

[ZHO 11b] ZHOU K., KEER L. M., WANG Q. J.
Semi-Analytic solution for multiple interacting three-dimensional inhomogeneous inclusions of arbitrary shape in an infinite space. *International Journal for Numerical Methods in Engineering*, vol. 87, 2011, p. 617-638.

[ZHO 12] ZHOU K., KEER L. M., WANG Q. J., AI X., SAWAMIPHAKDI K., GLAWS P.
Interaction of multiple inhomogeneous inclusions beneath surface. *Comput. Methods Appl. Mech. Engrg.*, vol. 217-220, 2012, p. 25-33.

[ZHO 14] ZHOU Q., JIN X., WANG Z., WANG J., KEER L., WANG Q.
An efficient approximate numerical method for modeling contact of materials with distributed inhomogeneities. *International Journal of Solids and Structures*, vol. 51 (19-20), 2014, p. 3410-3421.

[ZHO 16] ZHOU K., DONG Q.
A Three-Dimensional Model of Line-Contact Elastohydrodynamic Lubrication for Heterogeneous Materials with Inclusions. *International Journal of Applied Mechanics*, vol. 8 (2), 2016, Page 1650014.

[ZWI 82] ZWIRLEIN O., SCHLICHT H.
Rolling contact fatigue mechanisms - accelerated testing versus field performance. *Rolling Contact Fatigue Testing of Bearing Steels*, vol. 771, 1982, p. 358-379.

List of Figures

UNIVERSITÉ DE LYON | INSA

FOLIO ADMINISTRATIF
THÈSE DE L'UNIVERSITE DE LYON OPEREE AU SEIN DE L'INSA LYON

NOM : BEYER

DATE de SOUTENANCE : 28 06 2019

Prénom : Thibault

TITRE : Semi-analytical modeling of damage under contact loading: Application to heterogeneous materials

NATURE : Doctorat

Numéro d'ordre : 2019LYSEI045

École doctorale : MEGA

Spécialité : Mécanique - Génie Mécanique - Génie Civil

RÉSUMÉ :

Les pieds d'aubes de soufflantes de turboréacteurs étant soumis à des sollicitations de type fretting, l'introduction de matériaux composites dans la nouvelle génération de moteur d'avion a rendu nécessaire le développement d'outils permettant de modéliser le contact entre des matériaux hétérogènes. En particulier, le comportement tribologique et l'endommagement de ces matériaux est encore mal compris. La mise en place de méthodes numériques capable de prédire les endommagements dans le contact permettrait de mieux prédire la durée de vie des pièces en service et de garantir la sécurité des passagers.
Cette thèse porte sur le développement de méthodes semi-analytiques pour la modé-lisation de l'endommagement dans des conditions de fretting et de roulement. Ceci est stratégique vu les temps de calculs prohibitifs des méthodes plus conventionnelles de type éléments finis. La méthode de l'inclusion équivalente d'Eshelby est utilisée pour modéliser des matériaux hétérogènes, de la présence de défauts jusqu'aux structures complexes des matériaux composites. Cette technique est aussi utilisée afin de représenter les dégradations des propriétés matériaux survenant au cours de l'endommagement. La méthode permet de prendre en compte plusieurs inclusions simultanément et les temps de calculs sont réduits grâce à l'utilisation massive de transformées de Fourier rapides (FFT). De premiers résultats permettent de montrer la capacité de cette méthode à représenter les endommagements apparaissant lors d'une sollicitation de fretting : l'usure et l'amorçage de fissures. Des applications aux matériaux revêtus sont proposées et la méthode est comparée à une méthode plus classique de modélisation de l'usure. Une bonne corrélation entre les deux approches a permis de valider la méthode. Dans un second temps, cette technique est adaptée à la modélisation de transformations microstructurales apparaissant dans les roulements autour de défauts proches de la surface de contact. Une campagne d'essais sous sollicitations de contact sur un matériau tissé 2D a permis de mieux comprendre son comportement tribologique. En particulier, l'effet des propriétés de chaque constituant sur le coefficient de frottement et sur l'évolution de l'usure dans le matériau est étudié. Finalement, une technique de discrétisation est utilisée afin de représenter la structure complexe des matériaux composites tissés dans le code de calcul semi-analytique. L'effet de la structure hétérogène sur la solution du contact est établi et la nécessité de représenter les matériaux hétérogènes à la bonne échelle est soulignée. Une application de cette technique à la microstructure des matériaux métalliques permet de prédire la durée de vie des aciers utilisés dans les roulements.

MOTS-CLÉS: Simulation numérique, contact, fretting, mécanique de l'endommagement, usure, fatigue de roulement, microstructure, matériaux composites...